Large Eddy simulation of the turbulent spark ignition and of the flame propagation in spark ignition engines

Sophie Mouriaux

NNT : 2016SACLC046

THÈSE DE DOCTORAT
DE
L'UNIVERSITÉ PARIS-SACLAY
PRÉPARÉE À
CENTRALESUPELEC

ÉCOLE DOCTORALE N°579

Sciences mécaniques et énergétiques, matériaux et géosciences.

Spécialité : Combustion

par MOURIAUX Sophie

Large Eddy Simulation of the turbulent spark ignition and flame propagation in spark ignition engines

Thèse soutenue à Rueil-Malmaison, le 14 Juin 2016

Composition du jury:

Mr. RENOU Bruno	Professeur	INSA Rouen	Président du Jury
Mme. DOMINGO Pascale	Directrice de recherche	INSA Rouen	Rapporteur
Mr. POINSOT Thierry	Directeur de recherche	IMFT	Rapporteur
Mr. KEMPF Andreas	Professeur	Université Duisburg-Essen	Examinateur
Mr. RICHARD Stéphane	Ingénieur de recherche	TURBOMECA	Examinateur
Mr. COLIN Olivier	Ingénieur de recherche	IFPEn	Directeur de thèse
Mr. VEYNANTE Denis	Directeur de recherche	EM2C	Co-directeur de thèse

Remerciements

"Tu vois cette pointe, ce sommet qui émerge de la nappe de nuages ? ... Tout au fond, par delà les plaines vertes et les douces collines qui s'étendent à nos pieds, par delà cette barre de rochers ocres, dans ce massif un peu grisâtre dont les contours semblent se fondre à l'azur du ciel ? - Heu...ah...oui, oui, je crois que je le vois, oui...- c'est ça, c'est là-bas que j'irai !". Ainsi s'exclamait le jeune compagnon. C'est le coeur plein de vaillance et d'enthousiasme qu'il regardait le chemin doucement serpentant vers le sommet à atteindre, car il ignorait encore tout de la longueur du périple et des obstacles à franchir !

Mes remerciements vont tout d'abord à mes deux rapporteurs, Mr. Thierry Poinsot et Mme Pascale Domingo, qui ont accepté de relire mon manuscrit. Je remercie également les membres du Jury ; la soutenance a été l'occasion d'un échange nourri, clôturant ces trois années de recherche. Celles-ci représentent une expérience des plus enrichissantes, que je ne saurais que trop recommander à tout futur docteur courageux mais aussi téméraire. Je remercie donc Antonio et Christian de m'avoir accueillie en R102, ainsi que toute l'équipe qui a contribué à faire de mon passage dans les murs d'IFPEn une aventure aussi pleine et agréable.

Aventure scientifique, qui n'aurait bien sûr pu se dérouler de la sorte sans les remarques et conseils de Denis, ni l'encadrement au quotidien d'Olivier. Les discussions auront été un (sacré !) moteur pour progresser toujours un peu plus loin, "petits pas à petits pas", comme aimait tant le dire un certain professeur de physique. Travailler avec eux a été un challenge toujours renouvelé, des premiers étonnements sur le modèle de Boger à la rédaction du manuscrit ; challenge positif qui m'a beaucoup apporté. J'ai toujours trouvé la porte d'Olivier ouverte pour discuter de mes très nombreuses interrogations et je tiens tout particulièrement à l'en remercier. J'en profite également pour saluer les ingénieurs de R10. Merci à JB pour sa bonne humeur et sa présence en CB307, Anthony pour ses séquences d'introduction puis de dépannage en GIT et problèmes de compilation - merci également à lui de m'avoir fait démonstration en ces occasions de son sens de l'humour à nul autre pareil. Merci à Nicolas, Karine et André qui m'ont donné de leur temps et toujours efficacement dépannée. Merci enfin à Christian et JB pour leurs précieux conseils lors des séances de répétition des présentations.
Mon séjour en IFPsie fut également une aventure humaine, une successions d'épisodes de courte mais intense jubilation - par exemple ayant cru, l'espace d'un instant et bien souvent à tort, avoir trouvé le moyen ultime de tordre le cou aux caprices du plissement dynamique ; ou avoir pensé à une n-ième possibilité d'explication

à cet allumage qui allume mais qui ne devrait pas allumer...Courts épisodes donc, suivis d'autres plus longs et plus nuageux, voire désespérément nébuleux...Ainsi s'est déroulé le périple de la thèse. Qu'aurait-il été, sans la joyeuse bande de compagnons de route qui en a égayé et partagé les étapes ? Je salue tous les thésards : les "anciens" Stéphane, Anthony, Oguz, Stavros, ceux de ma "promo" : Adam, Gorka, Benjamin, Nicolas et son attirance assumée pour les balles de tennis, et bien sûr Elias, embarqué le même jour que moi sur cette belle galère. Merci à Carlo, Damien et Anthony pour le support technique indispensable en début de thèse. Un merci et un salut tout spéciaux à Haifa, Betty et Lama, ainsi qu'à Federico, Valerio, Jan, Karl et Mickael, second QG d'adoption du premier étage. Grâce à eux, j'ai pu profiter de moments de digressions bien précieux et de beaucoup de capsules Nespresso. Merci à tous les participants des footings le long du bord de Seine, occasion de petits breaks parfois ensoleillés et toujours ressourçants. Mention spéciale à la chaise de CB180, toujours là pour m'accueillir ; un grand merci à l'occupant dudit bureau (qui cache des M&M's dans son tiroir) et à ses visiteurs pour leur écoute et leurs conseils, particulièrement pendant les derniers mois. Merci à mon bureau d'accueil CB307, Damien, Oguz et Guillaume (le Belge), rejoints ensuite par Jan. Ce bout de chemin a été des plus agréables. Je salue pour finir Jean-Charles dont j'ai partagé le bureau pendant ma dernière année et que je remercie pour sa bonne compagnie.

Enfin, je souhaite remercier tout particulièrement Riana, Thomas, Damien, Lucette et mes parents. C'est grâce à leur soutien et tout simplement à leur présence que j'ai pu parcourir, aussi sereinement et gaiement possible, le chemin serpentant de la thèse.

Bonne route aux nouveaux arrivés et à tous ceux qui suivront !

Contents

Nomenclature

Acronyms

AKTIM	:	Arc and Kernel Tracking Ignition Model
CA	:	Crank Angle
CCV	:	Cycle-to-Cycle Variability
CFD	:	Computational Fluid Dynamic
CPU	:	Central Processing Unit
DNS	:	Direct Numerical Simulation
ECFM-LES	:	Extended Coherent Flame Model for LES
ISSIM	:	Imposed Stretch Spark Ignition Model for LES
ITFNS	:	Intermittent Net Flame Stretch
KPP	:	Kolmogorov Petrovsky Pitsunov
LES	:	Large Eddy Simulation
RANS	:	Reynolds Average Navier Stokes
SI	:	Spark Ignition
HIT	:	Homegeneous Isotropic Turbulence

Roman Symbols

a_t	:	sub-grid stretch term
c	:	progress variable
C_{res}	:	resolved contribution of the curvature
C_{sgs}	:	unresolved contribution of the curvature
D	:	diffusivity coefficient
D_j	:	diffusivity coefficient for species j
D_{th}	:	diffusivity coefficient for the temperature T
D^u	:	diffusivity coefficient in the fresh gases side
e_t	:	total mass energy
E	:	efficiency function for the TF-LES model
E	:	activation energy of the reaction
f	:	flow field quantity
$\overline{f}$	:	averaged contribution of quantity f
$\tilde{f}$	:	Favre average
f''	:	fluctuation contribution to the Favre average
F	:	thickening factor
$\mathscr{F}$	:	LES filtering function
H	:	Heaviside function
J^k	:	diffusive flux of species
J^e	:	diffusive flux of heat
k	:	kinetic energy per unit of mass
l_t	:	integral length of turbulence
Le_k	:	Lewis number of species k
n	:	number of grid points to resolve the turbulent structures
n_{res}	:	number of points required to resolved the flame front
n_{spec}	:	number of species involved in the kinetic scheme
n_{reac}	:	number of reactions in the kinetic scheme
$\mathbf{N}$	:	normal to the iso-surfaces of c
$\overline{\mathbf{N}}$	:	normal to the resolved iso-surfaces of c at scale Δ
$\widehat{\overline{\mathbf{N}}}$	:	normal to the resolved iso-surfaces of c at scale $\widehat{\Delta}$
P	:	Pressure
P_{res}	:	resolved propagation term
P_{sgs}	:	unresolved propagation term
Pr	:	Prandtl number
r	:	radial coordinate
r	:	size of the turbulent structures
r_{bg}	:	burned gases radius
R	:	perfect gas constant
Sc_k	:	Schmidt number of species k
s_D	:	displacement speed
s_L	:	planar laminar flame speed
s_T	:	turbulent flame speed
S_m	:	mean flame surface
S_{res}	:	resolved flame surface
S_{res}	:	total flame surface
t	:	time
T	:	Temperature

T^{fg}	:	fresh gases temperature
T^{bg}	:	burned gases temperature
T_{max}	:	maximal temperature
$\mathbf{u}$	:	local velocity vector
u'	:	sub-grid turbulent velocity fluctuation
u'_{Δ}	:	turbulent velocity fluctuation at scale Δ
$\overline{V^b}$	:	mean burned gases volume
W	:	mean molar mass of the mixture
x	:	spatial coordinate
Y_j	:	mass fraction of species j
Y_F	:	fuel mass fraction

Greek symbols

α_t	:	parameter for the test-filter
β_0	:	constant for the sub-grid curvature term S_{sgs}
β	:	parameter of the dynamic wrinkling model
γ	:	parameter for the dynamic wrinkling model
Γ_1, Γ_2, Γ_3	:	efficiency function
δ_c	:	cut-off frequency in the fractal wrinkling expression
δ_L	:	laminar flame thickness
δ_θ	:	diffusive flame thickness
δ_r	:	reaction zone thickness
Δ	:	combustion filter
$\widehat{\Delta}$	:	effective filter
Δ_{ave}	:	average filter
$\overbrace{\Delta}$	:	test-filter operator
Δ_x	:	cell size
ϵ	:	dissipation rate of turbulent kinetic energy
η_k	:	Kolmogorov scale
k	:	turbulent kinetic energy per unite of mass
λ	:	thermal Fourier diffusivity coefficient
μ	:	laminar dynamic viscosity
ν	:	laminar kinematic viscosity
ν_t	:	subgrid turbulent kinematic viscosity at scale Δ_x
$\nu_{t,\Delta}$	:	subgrid turbulent kinematic viscosity at scale Δ
Ξ_Δ	:	subgrid wrinkling factor
Ξ_{ign}	:	flame wrinkling in the AKTIMeuler ignition model
Ξ_{res}	:	resolved flame wrinkling
Ξ_{tot}	:	total flame wrinkling in the AKTIMeuler ignition model
ρ	:	gas density
ρ^b	:	burned gases density
ρ^u	:	fresh gases density
σ_c	:	thickness control factor for the flame surface density transport equation
Σ	:	flame surface
$\overline{\Sigma}$ or $\overline{\Sigma}_{\tilde{c}}$	:	filtered flame surface
Σ_1, Σ_2, $\Sigma_{2,corr}$, Σ_3	:	flame surface at the effective scale $\widehat{\Delta}$
τ_{ij}	:	Reynolds stress tensor
τ	:	thermal expansion factor
τ_c	:	flame time
τ_k	:	Kolmogorov time
τ_t	:	turbulent time
ϕ	:	equivalence ratio
$\dot{\omega}$	:	reaction rate
$\overline{\dot{\omega}}$	:	chemical source term
$\overline{\dot{\omega}}_c$	:	chemical source term of the progress variable
$\overline{\Omega}_c$	:	reaction rate of an elementary chemical reaction

Superscript

^{u} : fresh gases

^{b} : burned gases

Subscript

$_{st}$: stoichiometric quantity

$_{F}$: fuel quantity

$_{O}$: oxidizer quantity

Introduction

Industrial context

Limitations of the world fossil fuel resources and climate change provoked by their intensive use led recently to growing research campaigns in the diversification of the energetic resources: wind, solar, biofuels, etc. Concerning the transportation domain, electrification of vehicles was recently introduced on the consumers market. However, processes based on liquid fuel combustion remain by far the most employed solution because of their very high calorific power. Therefore research efforts still need to be carried out to increase their energetic efficiency, both to preserve fuel resources and to limit the production of greenhouse gas (GHG) production. GHG are mainly CO_2 gases issued from the conversion of the fuel to energy and their emissions are therefore directly related to the fuel consumption rate. In Europe, transportation represents the second domain, after industry, that generates the largest amount of greenhouse gases: 20% of European CO_2 emissions are due to transportation vehicles and 80 % of these due to automotive vehicles [1]. To limit these emissions, European Union announced the reduction of the average CO_2 emissions to 80 g/km for the engines commercialized in 2020 (Fig. 1). Car manufacturers face then more and more severe regulations. In addition to this, pollutants are also regulated; among these, NOx including NO and NO_2 molecules, induce severe health and environmental damages. 50 % of European NOx emissions are generated by automotive vehicles and have therefore become a target in the Euros norms: the Euro norm 6c applied from 2017 requests that spark ignition engines present a maximal concentration of 60 mg/km. Improving engine efficiency, while decreasing pollutants emissions, represents an important technical challenge. In addition to this, car manufacturers must also deliver a product satisfying consumers in terms of power, reliability and drivability.

Research campaigns brought new technological solutions. Improvements concern the different elements of the vehicle power-train: optimization of combustion, choice of the fuel, choice of post-treatment systems...Thus, several new combustion engine concepts have been explored in recent years. For spark ignition (SI) engines, developments have focused on lean premixed combustion and dilution of stoichiometric mixtures by exhaust gas recirculation (EGR), eventually combined with direct injection. These techniques enable to limit the production of NOx while maximizing the engine efficiency. However they also lead to increased cycle-to-cycle variability (CCV), as illustrated in Fig. 2. CCV are caused by several factors, which have been object of numerous studies in the past years (Young, 1980; Ozdor et al., 1994)).

[1] *European Agency for Environment*

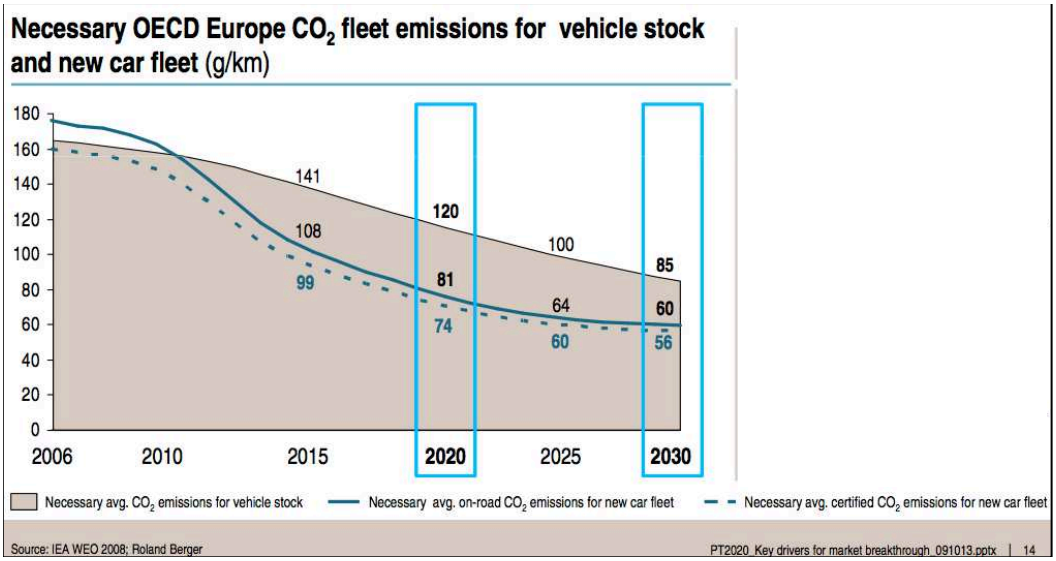

Figure 1: Evolution of target European $CO2$ emissions for vehicles. Source: *International Agency for energy* .

CCV are due to fluctuations of the velocity flow field and of the mixture composition (direct injection case) from one engine cycle to another. These fluctuations induce the variation of heat release, hence of the in-cylinder pressure, from one cycle to another. The ignition phase is a key element in CCV. For instance, cycle-to-cycle fluctuations of the velocity field generate cycle-to-cycle spark fluctuations, in terms of position and length (Aleiferis et al., 2000), as shown in Fig. 3. Local velocity, and eventually mixture fields are thus different when combustion initiates. The spark energy also varies in amount and in duration, as this energy depends on the spark length, leading to fluctuations of the flame development from one cycle to another (Fig. 4). For lean or diluted stoichiometric combustion, ignition becomes more difficult and a sufficiently fast propagation is not ensured, because of lower fuel consumption speeds (Young, 1981; Germane et al., 1983; Aleiferis et al., 2000). Therefore, a slight variation in local mixture composition or in velocity field may have a significant impact on the combustion initiation. A poor ignition due to unfavorable flow field conditions necessarily leads to a reduced global heat release rate in the cycle, far below the optimal one. An important cycle-to-cycle variability not only decreases the engine efficiency and increases pollutants emissions, but also reduces car drivability, which remains one of the major concerns for customers. Practically, ignition prevents today higher EGR rates or leaner combustion because of cycle-to-cycle variabilities. Controlling ignition is therefore a major topic for car manufacturers.

In this context, various solutions of ignition systems are proposed by constructors, to ensure an optimal combustion at each engine cycle. Conventional spark plug ignition systems are composed of a plug and an electrical ignition system which distributes electrical energy to the plug (Fig. 7-(a)). Typical energies delivered by the ignition circuit are of a few hundreds of mJ, while the duration of the spark discharge is less than one millisecond. For very lean or diluted stoichiometric combustion with possible mixture stratification (late direct injection), these systems tend to be replaced by more sophisticated electrical systems to promote ignition, for instance:

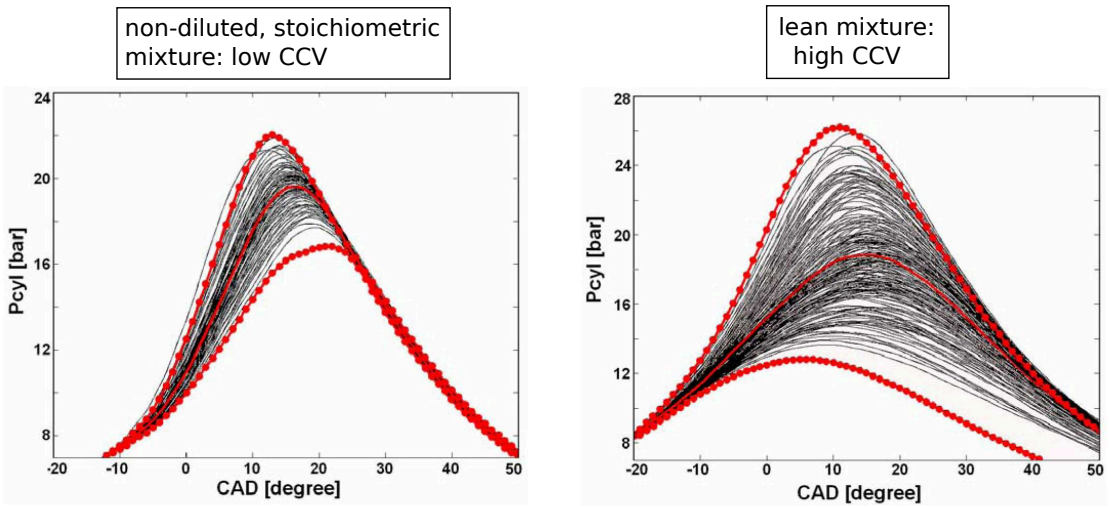

Figure 2: Measured in-cylinder pressure as a function of the crank angle (CAD). Non-diluted propane/air mixtures. (Left) 100 consecutive cycles, $\phi = 0.59$, (right) 200 consecutive cycles, $\phi = 1$. Bold red line is the ensemble averaged cycle. Lines with circles are the minimum and the maximum pressure cycles. From Lacour and Pera (2011)

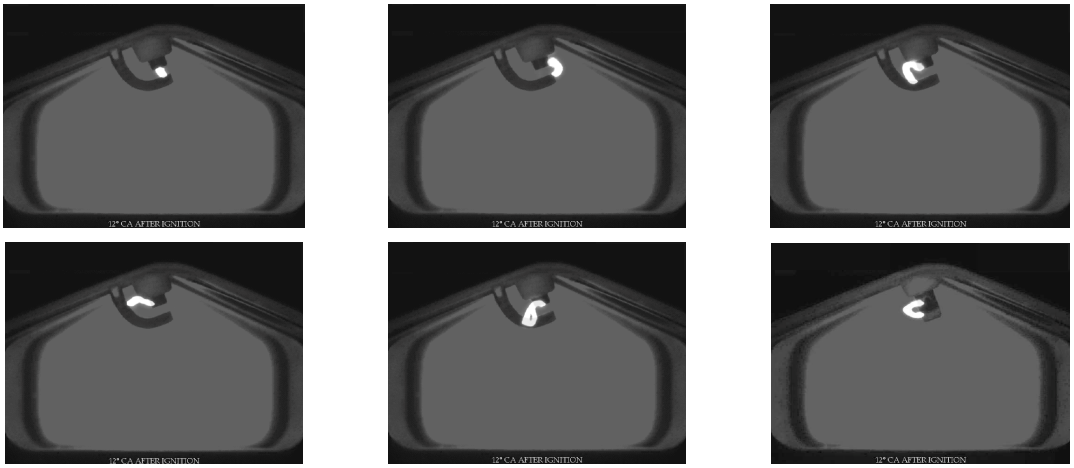

Figure 3: Images of spark for different engine cycles, recorded at the same instant (12° crank angle after ignition timing). Honda VTEC-E Lean-Burn Spark-Ignition Engine. From Aleiferis et al. (2000).

(i) high energy systems, to increase energy delivered to the gas mixture (several hundreds of mJ or up to 1 J stored in the secondary inductance); (ii) systems to distribute the energy during a longer time, such as the continuous current ignition (CCI) system of Continental (Fig. 7-(b)) or the SwRI system (Gukelberger et al., 2014); (iii) systems increasing the energy deposition volume: multiple sparks systems (Fig. 7-(b)) (Piock et al., 2010), multi-plug systems. Unconventional systems, are also tested: for instance Laser ignition (Yoshida and Soma, 2009), nanoseconds systems (Pancheshnyi et al., 2006; Domingues et al., 2008). If studies (Attard and Parsons, 2010; Chen et al., 2013; Gukelberger et al., 2014; Briggs et al., 2014; Pilla

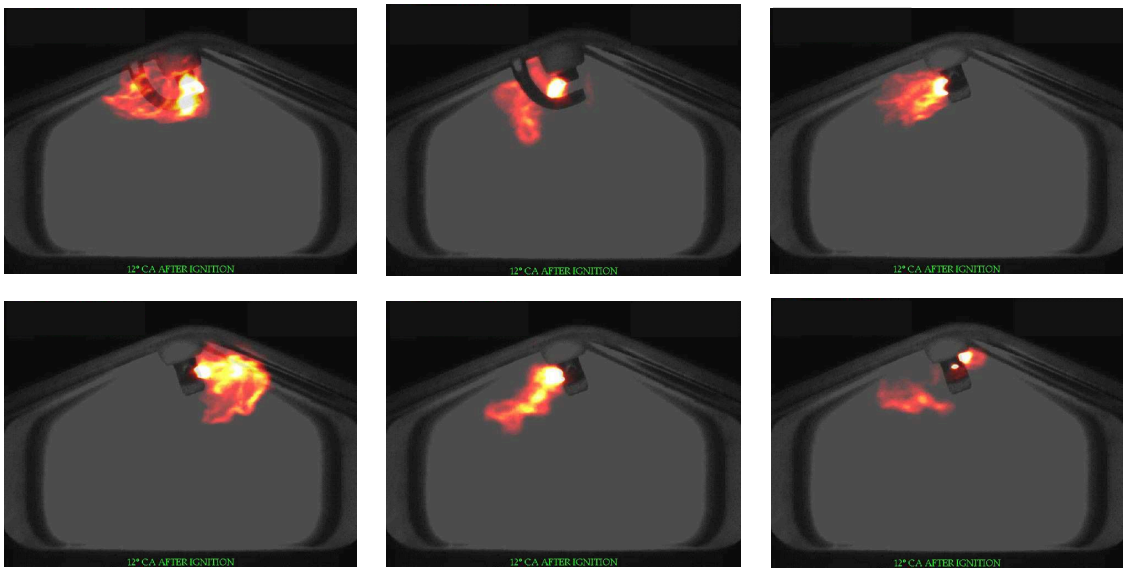

Figure 4: Images of the flame kernel for different engine cycles, recorded at the same timing (12 Crank Angles after ignition timing). Honda VTEC-E Lean-Burn Spark-Ignition Engine. (Aleiferis et al., 2000) .

and Francqueville, 2014) demonstrate that these more sophisticated ignition systems enable to use higher EGR rates or leaner fuel/air mixtures (as illustrated for instance in Fig. 5), their implantation in engines remains questionable due to costs and technical limitations. Besides, these studies remain limited to only a single or a few types of ignition devices and configurations. No clear conclusions can be established to favor one particular type of ignition system to another. In this context, the french ANR [2] FAMAC project gathers several academical partners, Continental and IFPEn, to characterize the ignition mechanisms, via different types of simulations and experimental validations. Results established in the project framework suggest that a key parameter to push back the lean or diluted EGR limit is the ignition energy, as illustrated in Fig.6. The present PhD contributes to this project, using large eddy simulation.

Large eddy simulation for spark ignition engines configurations

Efficient and affordable simulation tools such as RANS (Reynolds Averaged Navier Stokes) are successfully and widely used in the automotive industry to design combustion chambers. However, only information on an average cycle can be obtained because only averaged quantities of the flow field are resolved. The RANS approach is therefore not adapted to study cycle-to-cycle variability or any other physical phenomenon linked to fluctuations in the mixture composition, pressure, temperature or velocity of the flow field. Studying this type of phenomena is made possible by LES (Large Eddy Simulation). Now developed since a few decades, the ability of this method to predict cycle-to-cycle variability has been demonstrated (Richard

[2]National Agency for Research

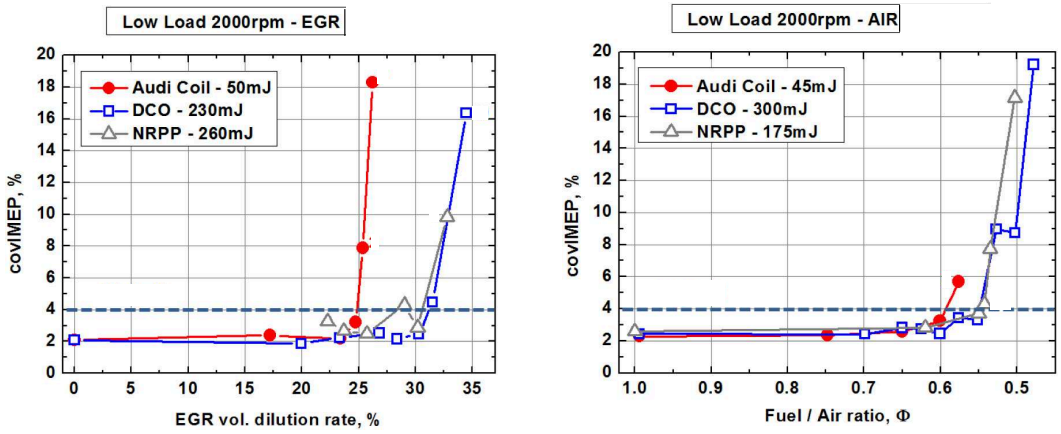

Figure 5: Influence of EGR (right) and air (left) dilution on engine stability (cov IMEP calculated for 200 engine cycles). Three ignition devices are compared: conventional system (Audi coil) and two unconventional systems: a Dual Coil system (Alger et al., 2013) and a Nanosecond Repetitively Pulsed Discharge system (NRPD) system (Pilla et al., 2006). The dashed line corresponds to the reference stability limit of the engine. Study of Pilla and Francqueville (2014)

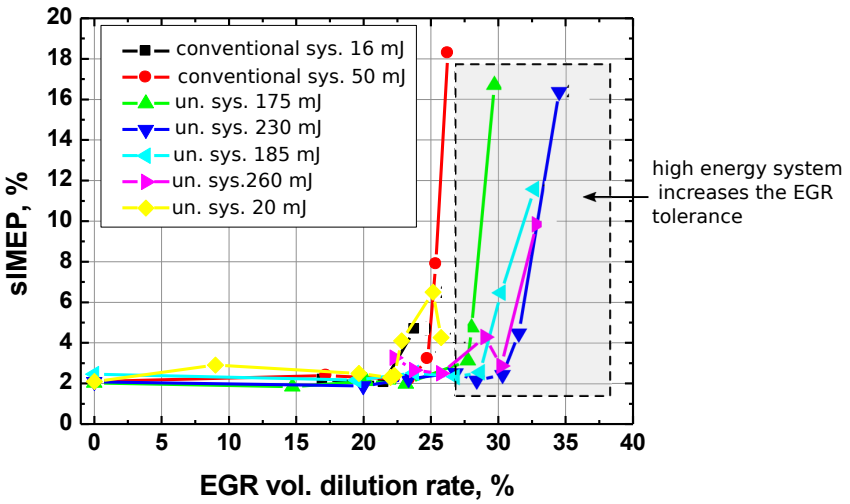

Figure 6: Influence of EGR dilution on engine stability (sIMEP) for different ignition systems corresponding to different energy. Conventional system and different types of unconventional systems. Study of G. Pilla and L. De Francqueville (IFPEn) for the FAMAC project, see also Pilla and Francqueville (2014).

et al., 2007; Vermorel et al., 2009; Goryntsev et al., 2009; Enaux et al., 2011; Truffin et al., 2015). LES resolves the large turbulent eddies of the flow field, while the effects of smallest eddies are modeled. This approach is particularly beneficial to the study of combustion processes, because combustion mostly results of the turbulent mixing processes controlled by the large turbulent eddies, which are resolved. Smallest eddies are well-adapted to modeling, as they present a more universal feature. Besides their contribution to the total turbulent energy is reduced. However LES precision has a CPU cost: fine meshes and high order numerical methods must

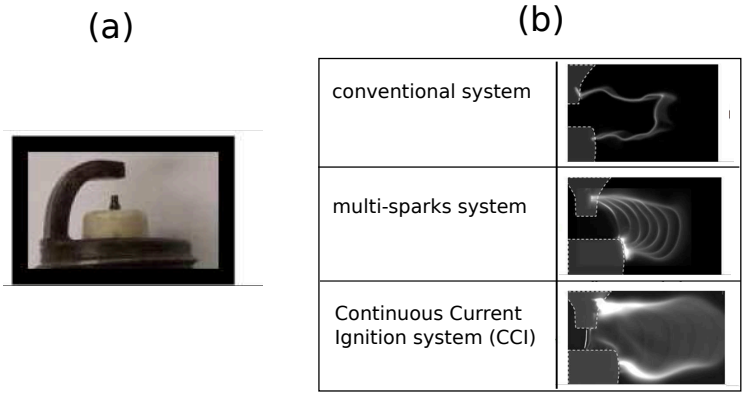

Figure 7: Different conventional ignition systems. (a): conventional plug. (b) images of spark generated by different types of conventional electrical ignition system.

be used. However, thanks to the constant increase of the CPU resources, LES can be used in complex industrial configurations, such as spark ignition engine configurations(Richard et al., 2007; Vermorel et al., 2009; Granet et al., 2012; Robert et al., 2015; Truffin et al., 2015) or aeronautical gas turbines configurations (Di Mare et al., 2004; Boileau et al., 2008; Staffelbach et al., 2009; Jones and Tyliszczak, 2010).

Motivations of the thesis

A major issue for LES of spark ignition engine configurations concerns the resolution on the LES grid of the thickness of premixed flames: a typical flame thickness in engine conditions is of a few tens of micrometers, while the cell size is usually limited to $\Delta_x \sim 0.5$ mm for CPU costs reasons. This means that a part of the flame-turbulence interactions occur at sub-grid scale and need to be modeled. Challenges to derive predictive combustion models adapted to spark ignition engines configurations are numerous, reflecting the complexity of the different physical phenomena at work in the engine combustion chamber: out-of-equilibrium flame development, mixture stratification (late direct injection case), flame-walls interactions, combustion instabilities (abnormal combustions such as knock or super-knock), pollutants formation and of course ignition. The ECFM-LES (extended coherent flame model for LES) model, proposed by Richard et al. (2007) and implemented in AVBP code (Colin and Rudgyard, 2000; Moureau et al., 2005), has been developed for ten years, based on the flame surface density (FSD) approach. However, this approach cannot reproduce complex ignitions (lean combustion regime or stoichiometric diluted regime, mixture stratifications), as the notion of flame surface becomes insufficient. Accordingly, a different path is explored in the present thesis, using the TF-LES approach (Colin, 2000). Lacaze et al. (2009) derived an ignition model for the TF-LES approach, the Energy Deposit model (ED), where ignition is modeled by a heat source term. In that case, the combustion initiation and the subsequent flame kernel growth are advantageously predicted by Arrhenius laws. This approach was already used to simulate the ignition and flame propagation sequences in gas turbine engines (Selle et al., 2004; Boileau et al., 2008; Staffelbach et al., 2009) and in spark ignition engine configurations (Thobois, 2006; Enaux et al., 2011; Granet et al., 2012; Misdariis, 2015). However, to simulate with accuracy engine cycles in

critical conditions, the description of ignition and of turbulent propagation phases demands additional developments, objects of this PhD thesis. Contributions are introduced below.

1. Spark ignition phase characterization: LES study of the ignition experiments of Cardin et al. (2013)

To finely characterize the ignition phase, interactions between chemistry and turbulence must be fully resolved. To do so, a sufficiently fine mesh must be used, so that the thickening factor of the TF-LES model can be set to unity, thus turning off the sub-grid turbulent combustion modeling contribution. Otherwise diffusion times, essential for ignition prediction, are modified. In spark ignition engines configurations, where pressure conditions induce a very thin flame of about 20 μm thickness, refining in the vicinity of spark plug to resolve the flame kernel requires a cell size of a few μm. As actual cell sizes are about 0.5 mm, refining the mesh locally during a short time (less than one millisecond) will become possible, thanks to the increase of super-computer power.
The long term objective of this part is thus to determine the numerical and physical parameters of the ED model which will allow to correctly represent the ignition phase of complex industrial devices. As ignitions are not accurately characterized in industrial devices, this work focuses on the calculation of laminar and turbulent ignitions in lean methane/air mixtures characterized by Cardin et al. (2013). Besides, these experiments were performed at atmospheric conditions, where the laminar flame thickness is of the order of magnitude of 0.5 -1 mm and can be resolved on the LES grid. These ignition cases are short duration spark ignition cases, which are today one of the preferred new ignition modes and on which research efforts are therefore focused on. The comparison with experiments is largely based on the ability of the simulations, using the ED model combined to reduced chemistry, to recover the experimental minimum ignition energy (MIE). The confrontation with experiments will also enable to improve the comprehension of ignition in critical conditions. In the middle term, the present ignition study can also serve to investigate gas turbine configurations, where ignition in critical conditions (low temperature and altitude) must be mastered. Conditions of pressure being severe than in SI engine configurations, the cell size required is about the hundreds of μs and such a strategy can be applied in a near future in real configurations, as shown in the pioneering work of Barré et al. (2014).

2. Modeling of the sub-grid wrinkling during the turbulent propagation phase

To capture CCV, both ignition and turbulent propagation phases must be well described. During the turbulent propagation phase, the essential feature governing combustion is the turbulent flame speed. Its prediction is particularly delicate in Spark Ignition engines because flame front wrinklings are not in equilibrium with turbulent motions. Just after ignition, the flame kernel is generally quasi-laminar and becomes progressively wrinkled under the action of turbulent structures when growing. Current wrinkling prediction models combined with the TF-LES approach correspond to algebraic closures, which assume an equilibrium wrinkling. Accord-

ingly, in order to use the TF-LES approach in spark ignition engine configurations, a wrinkling model accounting for the out-of-equilibrium flame development is required. Transport equations for wrinkling (Weller et al., 1998), which can predict out-of-equilibrium wrinkling values, are delicate to implement. Recently, a dynamic method was proposed by Wang et al. (2012) to predict without any parameter adjustment the out-of-equilibrium flame development and successfully tested in complex configurations (Schmitt et al., 2013; Veynante and Moureau, 2015). However, the model was not tested in SI engine configurations. Therefore, the second part of the thesis investigates the application of the dynamic wrinkling model of Wang et al. in an SI engine configuration. Some practical difficulties have been identified and modifications were therefore proposed.

Organization of the manuscript

The manuscript is organized as follows:

- **Part 1** presents essential notions to model premixed turbulent combustion and ignition in SI engines. The turbulent combustion models used in the study are described. Limitations of the current flame surface density ignition models are discussed, after having described the ignition mechanisms in SI engines. Finally, the choice of the simulation approach employed in the ignition study is justified.

- The dynamic wrinkling model of Wang et al. (2012) is studied in **Part 2**. First, specific issues to simulate SI engine configurations with the dynamic model are discussed. Modifications are then proposed and validated in simple configurations. Then, the modified dynamic wrinkling model is applied in a SI engine configuration and validated against experimental results and previous simulations results obtained using the ECFM-LES model (Robert et al., 2015).

- **Part 3** is dedicated to the simulations of Cardin et al. ignition experiments. Ignition parameters and their influence on minimum ignition energy are first determined for the laminar case. Then, results of the turbulent ignition cases are discussed. Comparisons to experimental data enable to assess the ignition strategy.

Part I

Modeling tools for turbulent premixed ignition and combustion in SI Engines

Chapter 1

Premixed turbulent combustion

Contents

In this chapter, general notions of numerical simulation of turbulent premixed flames are presented. Focus is then made on two LES turbulent combustion models which are used in this PhD thesis, the flame surface density (FSD) and the TF-LES approaches.

1.1 General notions for the numerical simulation of reactive flows

Governing equations for reactive flows are first presented. Essential notions of turbulent flows are recalled before presenting the numerical methods used to simulate reactive flows and describing the large eddy simulation (LES) formalism. Necessary notions of LES chemistry modeling are then briefly discussed.

1.1.1 Governing equations for reactive flows

Aerothermochemistry equations regroup the general equations of fluid mechanics and the transport equations of the species involved in the chemical reactions. Various formulations exist in the literature, for instance in Poinsot and Veynante (2005). In the following, equations are written using the conservative form and as implemented in the AVBP code.

1.1.1.1 Aerothermochemistry equations

- **Mass conservation**

$$\frac{\partial \rho}{\partial t} + \frac{\partial \rho u_i}{\partial x_i} = 0 \tag{1.1}$$

ρ is the gas density and u_i the component in direction i of the absolute flow velocity.

- **Species conservation**

$$\frac{\partial \rho Y_k}{\partial t} + \frac{\partial (\rho u_k Y_k)}{\partial x_i} = -\frac{\partial J_i^k}{\partial x_i} + \dot{\omega}_k \tag{1.2}$$

Y_k is the mass fraction of the species k (the total number of species is n_{spec}), $\dot{\omega}_k$ the species source term. J_i^k is expressed using the Hirschfelder et al. (1969) approximation:

$$J_i^k = -\rho \left(D_k \frac{W_k}{W} \frac{\partial X_k}{\partial x_i} - Y_k V_i^c \right) \tag{1.3}$$

where D_k is the diffusivity coefficient of species k, W_k the species molecular weight and W the mean molecular weight calculated according to:

$$\frac{1}{W} = \sum_{k=1}^{n_{spec}} \frac{Y_k}{W_k} \tag{1.4}$$

$X_k = Y_k W / W_k$ is the mole fraction of species k. Finally, V_i^c is a correction velocity to ensure the mass conservation (1.1), that is $\sum_{k=1}^{n_{spec}} J_i^k = 0$ and reads:

$$V_c^i = \sum_{1}^{n_{spec}} D_k \frac{W_k}{W} \frac{\partial X_k}{\partial x_i} \tag{1.5}$$

- **Momentum conservation**

$$\frac{\partial \rho u_j}{\partial t} + \frac{\partial \rho u_i u_j}{\partial x_i} = -\frac{\partial P}{\partial x_j} + \frac{\partial \tau_{ij}}{\partial x_i} \tag{1.6}$$

where P is the pressure, τ the viscous constraints tensor given by Newton's law:

$$\tau_{i,j} = -\frac{2}{3}\mu \frac{\partial u_k}{\partial x_k} \delta_{i,j} + \mu \left(\frac{\partial u_i}{\partial x_j} + \frac{\partial u_j}{\partial x_i} \right) \tag{1.7}$$

μ is the molecular viscosity, calculated according to temperature laws such as the Sutherland's law.

- **Energy conservation**

$$\frac{\partial \rho e_t}{\partial t} + \frac{\partial}{\partial x_i}((\rho e_t + P)u_i) = \frac{\partial}{\partial x_i}(\tau_{ij} u_i) - \frac{\partial J_i^e}{\partial x_i} + \dot{\omega}_e \tag{1.8}$$

where e_t is the total energy, $\dot{\omega}_e$ the heat release rate of chemical reactions and J_i^e the heat flux in the direction i, generally expressed with the Fourier law such as:

$$J_i^e = -\lambda \frac{\partial T}{\partial x_i} + \sum_{k=1}^{n_{spec}} J_i^k h_s^k \tag{1.9}$$

with T the temperature and λ the Fourier heat coefficient (section 1.1.1.2). h_s^k is the sensible enthalpy of species k.

- To complete the equations system, a final relation is used, relating the pressure P, density ρ and temperature T. The **perfect gas equation of state** is generally employed:

$$P = \rho \frac{R}{W} T \tag{1.10}$$

R is the perfect gas constant $R = 8.3143 \text{J.mol}^{-1}.\text{K}^{-1}$.

1.1.1.2 Non-dimensional numbers

In CFD codes, simplified diffusion laws are used, species diffusivity and thermal diffusivity coefficients used in Eqs. (1.2) and (1.8) respectively, are then expressed using non-dimensional numbers:

- The species diffusivity coefficient D_k is expressed introducing the species Schmidt number Sc_k such as:

$$D_k = \frac{\nu}{Sc_k} = \frac{\mu}{\rho Sc_k} \tag{1.11}$$

where ν is the kinematic viscosity defined as $\nu = \mu/\rho$. Sc_k is constant and extrapolated from complex transport coefficient calculations.

- The Fourier heat coefficient λ is expressed with the Prandtl number Pr, assumed to be constant:

$$\lambda = \frac{\mu}{C_p Pr} \tag{1.12}$$

$C_p = \sum_{k=1}^{n_spec} Y_k C_{p,k}$ is the constant pressure thermal capacity of the mixture, with $C_{p,k}$ the species constant pressure thermal capacity.

Finally, the species Lewis number Le_k can be introduced, comparing the thermal diffusivity D_{th} with the species diffusivity D_k:

$$Le_k = \frac{D_{th}}{D_k} = \frac{Sc_k}{Pr} \tag{1.13}$$

1.1.2 Turbulent flows characteristics

A turbulent flow regime is defined when all quantities characterizing the flow (pressure, velocity, temperature fields...) randomly fluctuate. Any turbulent quantity f may be written as the sum of its time average $\overline{f}$ value and of its fluctuation part f':

$$f = \overline{f} + f' \tag{1.14}$$

The turbulent flow is commonly described as a collection of vortices, of various size and life characteristic times, interacting with each other. The Reynolds number Re, that compares the inertia forces and the viscous dissipation forces, quantifies the level of turbulence:

$$Re = \frac{uL}{\nu} \tag{1.15}$$

where u and L are a characteristic velocity and length of the flow.
Considering an homogeneous isotropic turbulent flow (HIT), Kolmogorov suggests that most turbulence scales range between two fundamental scales: the integral scale l_t and the Kolmogorv scale η_k. l_t represents the characteristic scale of the most energetic vortices, while the Kolmogorov scale η_k defines the scale of the smallest vortices. The turbulent energy is transferred from the largest eddies to the smallest eddies (cascade of Kolmogorov), as illustrated in Fig. 1.1. The energy transfer takes place in the *inertial zone*. The dissipation rate ϵ is estimated as the ratio of the kinetic energy $k = 3u'(r)^2/2$ to the turbulent time $r/u'(r)$, as the energy transfer is assumed to take place without loss:

$$\epsilon = \frac{u'(r)^3}{r} \tag{1.16}$$

The Kolmogorov scale η_k and the integral scale l_t are related to each other by:

$$\frac{l_t}{\eta_k} = Re_t^{3/4} \tag{1.17}$$

where Re_t is the turbulent Reynolds number, based on the integral length properties is defined by:

$$Re_t = \frac{u' l_t}{\nu} \tag{1.18}$$

1.1.3 DNS, LES and RANS approaches

The most natural way to numerically resolve the aerothermochemistry equations established in section 1.1.1 would be to discretize all scales of combustion and turbulence, as in the **Direct Numerical Simulation (DNS)** approach. In that case, the cell size Δ_x is smaller than the Kolmogorov scale η_k and smaller than δ_L/n_{res}, where n_{res} is the number of grid points necessary to the resolution of the gradients within the flame front. However, this strategy demands very important CPU resources and can be employed in practice only in academical configurations: simple geometry, reduced turbulent Reynolds number Re_t and adequate conditions (temperature, pressure, chemical description) to resolve the flame front. This is the reason why RANS and LES approaches are considered for practical systems simulations.

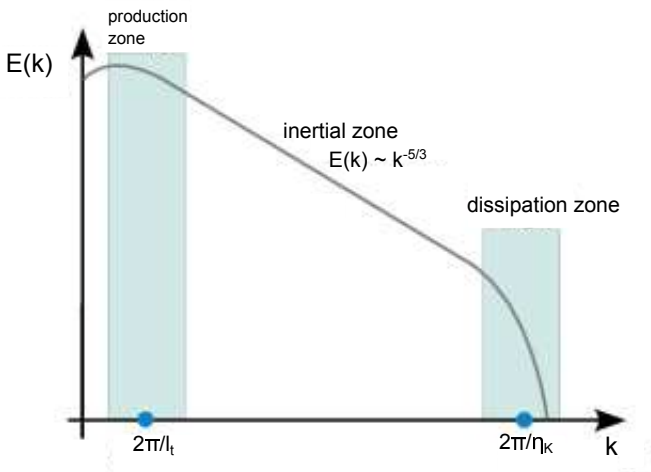

Figure 1.1: Turbulent energy spectrum according to the theory of Kolmogorov. k is the wave number.

RANS approach (Reynolds Average Navier Stockes). In this approach, only averaged quantities $\overline{f}$ are resolved. The averaging operation corresponds to a statistical average over a certain number N of realizations of the same physical event, for instance a certain number of engine cycles. Any quantity f is then written using the Reynolds decomposition between its average contribution $\overline{f}$ and its fluctuations f':

$$f = \overline{f} + f' \tag{1.19}$$

The balance equations for averaged quantities are obtained averaging the aerothermochemistry equations presented in section 1.1.1. The averaging operations introduce unresolved terms, containing the information on the fluctuations part. Such terms require specific closures, where the whole turbulence spectrum must be modeled. Accordingly it is not adequate to use RANS methods to analyze engine cycle-to-cycle variability or any phenomenon requiring an accurate description of the flow field fluctuations. However RANS accepts rather coarse meshes because only averages gradients need to be resolved and it does not require too costly and elaborate numerics. This explains why RANS approach is widely used in industry. Typical cell size is $\Delta_x = 0.5 - 1$ mm while simulation times take 12 hours.

LES method (Large Eddy Simulation). This approach resolves the largest scales of turbulence, while smaller scales are modeled. To do so, the cell size Δ_x must be chosen such as:

$$\eta_k < \Delta_x < l_t/n \tag{1.20}$$

n being the number of discretization points in the largest turbulence structures. The closer Δ_x from η_k is, the more turbulence structures are resolved, the finer the LES is. Estimating the Kolmogorov scale in a real engine is delicate, as turbulence is not homogeneous nor isotropic but a typical value, according to Haworth is 25 μm.
In LES, the aerothermochemistry equations system is filtered with a spatial filter of width Δ_{LES}, related to the cell size Δ_x. As in RANS, the filtering procedure bring unresolved terms containing information at the unresolved scales and information

relative to energy transfers between resolved and unresolved scales. These unresolved terms are closed using sub-grid models (section 1.1.4.2).

Figure 1.2 illustrates the principle of the 3 classes of numerical simulations.

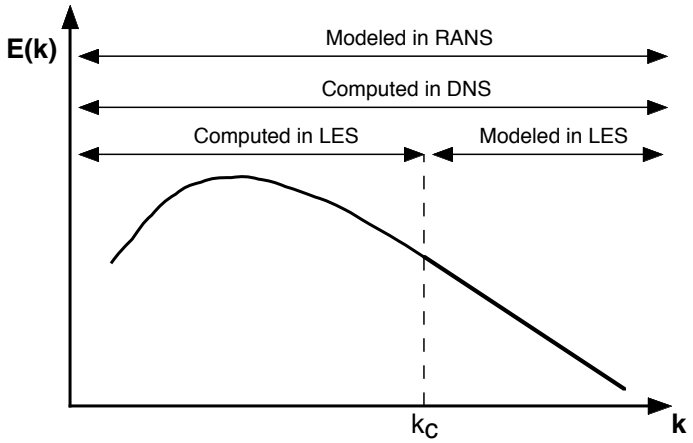

Figure 1.2: Turbulent energy spectrum illustrating the principle of RANS, LES and DNS methods (Poinsot and Veynante, 2005). k_c is the cut-off wave length of the LES filter.

1.1.4 LES formalism

1.1.4.1 LES filters

In LES, each physical quantity f is written as the sum of its filtered part $\overline{f}$, resolved on the LES mesh, and of its unresolved part f'. The analytical expression of any LES filtered quantity $\overline{f}$ is given by:

$$\overline{f}(\mathbf{x}) = \int f(\mathbf{x}')\mathscr{F}(\mathbf{x}-\mathbf{x}')\mathrm{d}\mathbf{x}' \tag{1.21}$$

where $\mathscr{F}$ is the LES filtering function of width Δ_{LES}.
The filtering operator must possess the following fundamental properties:

- Normalisation:

$$\int \mathscr{F}(\mathbf{x})\mathrm{d}\mathbf{x}' = 1 \tag{1.22}$$

- Commutation with the derivative operators, in order to establish the balance equations for the filtered variables. The commutativity is not ensured when the size Δ of the filter varies with time and/or space, which is the case for all engine simulations. Previous studies (Ghosal, 2004; Moureau et al., 2005) have characterized the commutativity errors, demonstrating that in most cases errors were not significant.

The LES Favre or mass weighted filtering is also defined as :

$$\tilde{f} = \frac{\overline{\rho f}}{\overline{\rho}} \tag{1.23}$$

with the decomposition between the Favre resolved part $\tilde{f}$ and the Favre unresolved part f'':

$$f = \tilde{f} + f'' \tag{1.24}$$

1.1.4.2 Filtered equations

Filtering the reactive fluid mechanics equations established in section 1.1.1 gives:

- Mass conservation:

$$\frac{\partial \overline{\rho}}{\partial t} + \frac{\partial (\overline{\rho}\tilde{u}_i)}{\partial x_i} = 0 \tag{1.25}$$

- Momentum conservation:

$$\frac{\partial \overline{\rho}\tilde{u}_j}{\partial t} + \frac{\partial \overline{\rho}\tilde{u}_i\tilde{u}_j}{\partial x_i} = -\frac{\partial \overline{P}}{\partial x_j} + \frac{\partial}{\partial x_i}\left(\overline{\tau}_{ij} - \overline{\rho}(\widetilde{u_i u_j} - \tilde{u}_i\tilde{u}_j)\right) \tag{1.26}$$

- Transport equation for species:

$$\frac{\partial \overline{\rho}\tilde{Y}_k}{\partial t} + \frac{\partial (\overline{\rho}\tilde{u}_i\tilde{Y}_k)}{\partial x_i} + \frac{\overline{\rho}(\widetilde{u_i Y_k} - \tilde{u}_i\tilde{Y}_k)}{\partial x_i} = -\frac{\partial \overline{J_i^k}}{\partial x_i} + \overline{\dot{\omega}}_k \tag{1.27}$$

- Transport equation for the total energy:

$$\frac{\partial \overline{\rho}\tilde{e}_t}{\partial t} + \frac{\partial \left(\overline{\rho}\tilde{e}_t + \overline{P}\right)\tilde{u}_i}{\partial x_i} = \frac{\partial}{\partial x_i}\left(\overline{\tilde{u}_j\tau_{ij}} - \left[\,\overline{(\rho e_t)\,\tilde{u}_i} - (\overline{\rho}\tilde{e}_t)\,\tilde{u}_i\right]\right) - \frac{\partial \overline{J_i^e}}{\partial x_i} + \overline{\dot{\omega}}_e \tag{1.28}$$

The equations system present filtered laminar fluxes and unresolved terms, corresponding to the small scales contribution, that must be closed in order to solve the equations system.
Filtered laminar fluxes for species and energy are closed using a gradient hypothesis:

$$\overline{J}_i^k \approx -\overline{\rho}\left(\overline{D}_k\frac{W_k}{W}\frac{\partial \widetilde{X}_k}{\partial x_i} - \tilde{Y}_k\tilde{V}_i^c\right) \tag{1.29}$$

$$\overline{J}_i^e \approx -\overline{\lambda}\frac{\partial \tilde{T}}{\partial x_i} + \sum_{k=1}^{n_{spec}} \overline{J}_i^k\tilde{h}_s^k \tag{1.30}$$

The laminar viscous tensor $\overline{\tau}_{ij}$ is approximated as:

$$\overline{\tau}_{ij} \approx 2\overline{\mu}\left(\tilde{S}_{ij} - \frac{1}{3}\delta_{ij}\tilde{S}_{ij}\right) \tag{1.31}$$

with $\overline{\mu} \approx \mu(\tilde{T})$ and $\tilde{S}_{ij}$ given by:

$$\tilde{S}_{ij} = \frac{1}{2}\left(\frac{\partial}{\partial x_i} + \frac{\partial}{\partial x_j}\right) \tag{1.32}$$

The unresolved terms are the following:

- **The sub-grid Reynolds stress tensor**: $\mathscr{T}_{ij} = \widetilde{u_i u_j} - \tilde{u}_i \tilde{u}_j$.
  Numerous closures exist in the literature: Smagorinsky model, the dynamic model of Germano (Germano et al., 1991; Germano, 1992), models with a transport equation for k_{sgs}. The most popular model remains the Smagorinsky model as its implementation is simple. According to Boussinesq assumption (Pope, 2001), the unresolved stress tensor is written such as:

$$\mathscr{T}_{ij} - \frac{\delta_{ij}}{3}\mathscr{T}_{kk} = -\nu_t \left(\frac{\partial \tilde{u}_i}{\partial x_j} + \frac{\partial \tilde{u}_j}{\partial x_i} \right) = -2\nu_t \tilde{S}_{ij} \tag{1.33}$$

  where ν_t is a sub-grid scale viscosity, modeled from dimensional arguments as:

$$\nu_t = C_S^2 \Delta_{LES}^2 \sqrt{2\tilde{S}_{ij}\tilde{S}_{ij}} \tag{1.34}$$

  C_S is a model constant.

- **The term of unresolved transport for species** is closed using a gradient hypothesis, introducing a turbulent diffusivity coefficient D_k^t:

$$\widetilde{u_i Y_k} - \tilde{u}_i \tilde{Y}_k = -\overline{\rho} \left(\overline{D}_k^t \frac{W_k}{W} \frac{\partial \widetilde{X}_k}{\partial x_i} - \tilde{Y}_k \tilde{V}_i^{c,t} \right) \tag{1.35}$$

  D_k^t is calculated with a turbulent Schmidt number Sc_k^t such as $D_k^t = \nu_t / Sc_k^t$.

- **The term of unresolved transport of energy** is also closed using a gradient hypothesis, introducing a turbulent Prandtl number Pr_t:

$$\frac{\partial}{\partial x_i} \left(\overline{\rho e_t \tilde{u}_i} - \overline{\rho} \tilde{e}_t \tilde{u}_i \right) = -\overline{\rho} c_p \frac{\nu_t}{Pr_t} \frac{\partial \tilde{T}}{\partial x_i} \tag{1.36}$$

  .

- **The filtered reaction rate** $\overline{\dot{\omega}}_k$: closures of this term are discussed in section 1.3 (turbulent combustion modeling).

1.1.5 Chemistry modeling in LES

Detailed chemistry The most direct manner to describe chemistry is to account for all elementary chemical reactions, as described in *detailed kinetic mechanism*. These kinetic mechanisms are validated against experimental data for a large variety of phenomena: auto-ignition, premixed and non-premixed planar flames, etc. and for a given range of pressure, temperature and composition. Detailed mechanisms are a collection of N_{reac} elementary reactions between two or three species, representing molecular interactions. For instance, the j^{th} elementary reaction involving species R_1, R_2, P_1 and P_2 reads:

$$R_1 + R_2 \rightarrow P_1 + P_2 \tag{1.37}$$

Then, the reaction rate Q_j of reaction j is written with an Arrhenius law such as:

$$Q_j = A_j [R_1][R_2] T^{\beta_j} \exp\left(\frac{-E_a}{\mathscr{R} T} \right) \tag{1.38}$$

where E_a is the activation energy, A_j the pre-exeponential factor and β_j an exponent. $[R_1] = \rho Y_{R_1}/W_{R_1}$ (resp. $[R_2]$) are the species concentrations $[R_1]$ (resp. $[R_2]$). Detailed mechanisms are not affordable in 3D calculations of industrial configurations, because this implies to use a very important numbers of grid points in the flame front (about 100 grid points), to correctly capture all intermediate and radicals species presenting very stiff profiles. This implies also to solve n_{spec} transport equations for the n_{spec} species of the detailed mechanism. For instance, the GRI mechanism used for methane/air chemistry (Smith et al., 2012) presents 325 reactions and 53 transported species. For larger hydrocarbons chains, this number increases: the Dagaut et al. (1994) mechanism for kerosene/air presents 225 species and 3493 irreversible reactions. Note that even if such resolution were possible, the use of detailed mechanisms in industrial configurations would not be straightforward: mechanisms are valid only over a certain range of thermodynamic conditions which, even if they are large, do not necessarily correspond to the whole range of operating conditions of the configuration. Various strategies are therefore used to describe chemistry: (i) to consider a global single-step reaction as in the flame surface density approach (section 1.3.1), (ii) to use tabulated chemistry, not detailed here; (iii) to use reduced kinetic schemes (as in the TF-LES approach presented in section 1.3.4). The different types of reduced schemes are described in the following.

Simplified schemes. These schemes present a very limited number of species (generally around 6) and of reactions (generally 2 to 4) (Jones and Lindstedt, 1988; Franzelli et al., 2010). Reactions do not correspond to elementary reactions but to global reactions, written with Arrhenius-like laws, calibrated to reproduce some essential features of the flame (usually laminar flame speed or auto-ignition delays), over a given range of temperature, pressure, equivalence ratio, more restrained that detailed mechanisms one. Thanks to their affordable CPU costs, simplified schemes are widely used for LES of industrial configurations (Di Mare et al., 2004; Staffelbach et al., 2009; Granet et al., 2012; Franzelli et al., 2013). To extend the validity range of these schemes, on-the fly adjustment methods of the kinetic parameters (activation energy E_a and pre-exponential constant A) were recently proposed (Franzelli et al., 2010). However, as simplified schemes do not include intermediate nor radicals species, phenomena such as pollutant formation, ignition or phenomena requiring accurate flame response to strain, cannot be described.

Skeletal schemes Skeletal schemes are obtained by reduction methods of detailed mechanisms, based on the consideration that some phenomena described by detailed schemes are not relevant to the combustion problem considered. Then some species and reactions can be removed, while keeping the description of the quantities of interests. Recent methods were proposed by Lu and Law (2006); Pepiot-Desjardins and Pitsch (2008). A reference detailed scheme (n_{det} species, N_{det} elementary reactions) is first chosen. Species and corresponding reactions, that have a negligible contribution to the phenomena of interest are explicitly removed from the detailed mechanism. To perform this operation, a set of targets is chosen. These targets correspond to chemical features that the reduced mechanism is expected to reproduce over a predefined range of physical conditions. In order to determine which are the species that have a negligible contribution to these targets, the reference solution is analyzed using for instance the directed relation graph (DRGEP) method (Pepiot-

Desjardins and Pitsch, 2008).
However, the CPU time of this type of scheme remains prohibitive to apply it to industrial configurations, as the number of species may remain high: for instance the Jerzembeck et al. (2009) scheme for n-heptane and iso-octane presents 203 species and 1071 reactions. Above all, species conserved in the skeletal mechanism may still present very short life time (typically of a few ns for highly reactive intermediate species or radicals), resulting in very steep profiles which cannot be resolved on the LES grid. This issue motivated recent derivations leading to *analytical schemes*, presented in the last paragraph.

Analytical schemes. A solution to avoid to transport very short life time species still present in skeletal schemes, consists to apply the QSSA (Quasi Stationnary State Assumption) to these species. Then, only remaining species are explicitly transported while the QSS species reaction rates are deduced from the composition of the transported species. To determine the QSS species, the LOI (Løvås et al., 2002) algorithm can be employed. As for the skeletal scheme, a set of targets must be specified to determine the QSS species in the analytical scheme.
First studies in industrial configurations using analytical schemes are very promising (Bauerheim et al., 2015).

1.2 Premixed turbulent flames

Classical combustion regimes encountered in SI engines correspond to the flamelets regime. In this regime, the turbulent flame is viewed a very thin interface between burned and fresh gases, wrinkled by turbulence. The flame structure is the same as the laminar flame one. One-dimensional laminar premixed flames are thus the basis element used to build the turbulent premixed combustion models in the flamelets regime. Essential notions are therefore presented in section 1.2.1, while flame-turbulence interactions characterizations using combustion diagram are briefly described in section 1.2.2. Finally, the transport equation for the progress variable c widely used to described turbulent premixed flames is recalled in section 1.2.3.

1.2.1 One-dimensional laminar premixed flames

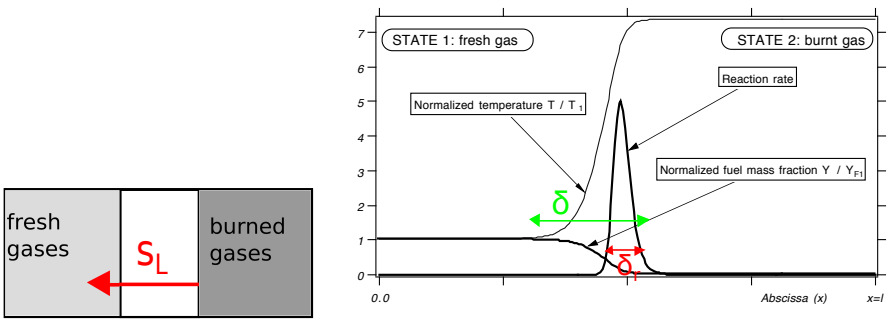

Figure 1.3: Sketch illustrating the propagation of a laminar premixed flame (Poinsot and Veynante, 2005)

The one-dimensional laminar premixed flame can be described as a wave propagating from the burned gases towards the fresh gases, at the laminar flame speed s_L, as illustrated in Fig. 1.3. Fresh gases consist of fuel and oxidizer, mixed prior to combustion, at a given temperature T^u, pressure P^u and composition. Fuel and oxidizer mass fractions (denoted respectively Y_F and Y_{O_2}) are related by the equivalence ratio ϕ such as:

$$\phi = s\frac{Y_F}{Y_{0_2}} = \left(\frac{Y_F}{Y_F}\right) / \left(\frac{Y_F}{Y_{0_2}}\right)_{st} \tag{1.39}$$

where $s = (Y_F/Y_{0_2})_{st}$ is the mass stoichiometric ratio.
The interface between the fresh gases and the burned gases corresponds to the flame front of laminar thickness denoted δ_L and is determined according to:

$$\delta_L = \frac{T^u - T^b}{\max\left|\frac{\partial T}{\partial x}\right|} \tag{1.40}$$

where T^b denotes the temperature in the burned gases. A characteristic time of the flame propagation τ_c (*flame time*) may be defined by:

$$\tau_c = \frac{\delta_L}{s_L} \tag{1.41}$$

Within the flame front, chemical reactions take place inside the *reaction zone* denoted δ_r, as illustrated in Fig. 1.3. The global reaction between the fuel F and the oxidizer O_2 is written as:

$$F + O_2 \rightarrow P \tag{1.42}$$

where P represents the products of combustion. The heat produced by combustion diffuses towards the fresh gases zone in front of the reaction zone, called *preheat zone*, while species diffuse within the flame front.

1.2.2 Turbulence/chemistry interactions

The premixed turbulent flame structure results of the interactions between chemistry and turbulence. To help understanding these complex interactions, combustion diagrams may be used (Borghi, 1988; Abdel-Gayed and Bradley, 1989; Peters, 1999). Different combustion regimes are defined, that correspond to different turbulent premixed flame structures, based on the comparison between the chemical characteristic time τ_c and different characteristic times of the turbulence. The Karlovitz number Ka is thus defined as the ratio of the chemical time τ_c by the characteristic time of the Kolmogorov scale, the Kolmogorov time τ_k:

$$Ka = \frac{\tau_c}{\tau_k} = \frac{u'(\eta_k)/\eta_k}{s_L/\delta_L} = \left(\frac{\delta_L}{\eta_k}\right)^2 \tag{1.43}$$

The Damköhler number Da corresponds to the ratio of the characteristic time of the integral scale τ_t out of the chemical time τ_c:

$$Da = \frac{\tau_t}{\tau_c} = \frac{l_t/u'(t_t)}{\delta_L/s_L} \tag{1.44}$$

Fig. 1.4 presents a combustion diagram according to Peters (1999), showing in ordinate the ratio u'/s_L and in abscissa the ratio l_t/δ_L. The Reynolds number Re_t, Karlovitz number Ka and Damköhler number Da are reported in the diagram, drawing the limits between the different turbulent regimes. The part where $Re_t < 1$ corresponds to the laminar combustion regime. The combustion regime of Spark Ignition engines lies between the *flamelet regime* and the *wrinkled thickened flame regime*, depending on the type of engine technology which is used:

- In the classical engine regime cases - that is stoichiometric combustion with low EGR rate - the combustion regime corresponds to the *flamelet regime*. In this regime, the Karlovitz number Ka is smaller than unity, which corresponds to $\delta_L < \eta_k$. No turbulent structures enter the flame front. Accordingly, the structure of the flame front keeps a structure close to the laminar flame front structure, turbulence and chemistry effects can be consequently decoupled. Flamelet models such as the flame surface density approach (section 1.3.3) are derived based on this assumption .

- In the case of lean combustion ($\phi < 0.7$) or in the case of a stoichiometric combustion associated to high EGR rates, the Karlovitz number increases, because the laminar flame speed s_L decreases. The combustion regime is close to the one of the *thickened wrinkled flamelet* regime, where $1 < Ka < 100$, which corresponds to $\delta_r < \eta_k < \delta_L$. Some turbulent structures can enter the preheat zone, enhancing the mixing but they do not enter the reaction zone δ_r of thickness $\delta_L/10$ approximately. However, chemical and turbulent effects cannot be entirely decoupled anymore.

- When $Ka > 100$, the regime is the *thickened flame* regime. Most turbulence scales can enter the flame front and some can even enter the reaction zone. The structure of the turbulent flame may be therefore very different from the laminar flame one. This regime does not likely correspond to SI engine combustion regimes.

1.2.3 Equation of the progress variable c

The balance equation for the progress variable c is very commonly used for premixed flames modeling. This equation is not solved in the AVBP code but is presented as some premixed combustion models (such as the flame surface density model presented in section 1.3.1) use this equation. The progress variable c equal to unity in burned gases and to zero in fresh gases is defined for homogeneous mixture by:

$$c = \frac{Y_{\mathrm{F}} - Y_{\mathrm{F}}^u}{Y_{\mathrm{F}}^u - Y_{\mathrm{F}}^b} \tag{1.45}$$

Assuming a Lewis number Le equal to unity, a single-step chemistry and isobaric flame ($\partial P/\partial t = 0$), a balance equation for the progress variable c can be derived and reads:

$$\frac{\partial \rho c}{\partial t} + \frac{\partial \rho u_i c}{\partial x_i} = \frac{\partial}{\partial x_i}\left(\rho D \frac{\partial c}{\partial x_i}\right) + \dot{\omega}_c \tag{1.46}$$

with D the diffusivity coefficient of the progress variable equal to the fuel diffusivity coefficient D_F and $\dot{\omega}_c$ is the reaction rate of the progress variable $\dot{\omega}_c = -\dot{\omega}_F/(Y_F^u - Y_F^b)$.

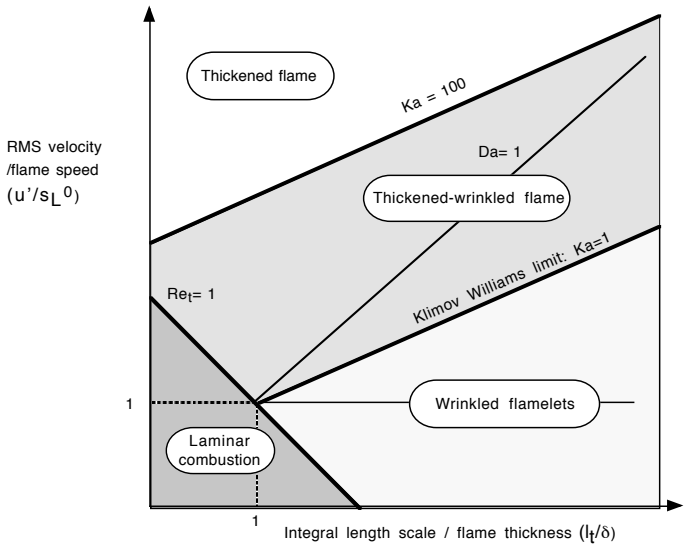

Figure 1.4: Combustion diagram according to Peters (1999), illustrating the different regimes of the turbulent premixed flames. Poinsot and Veynante (2005).

1.3 LES premixed combustion models

LES premixed combustion models are numerous, a classification can be found for instance in Poinsot and Veynante (2005). In this section, the presentation is restricted to two combustion models applicable to SI engine configurations and studied in the present thesis:

- Flame surface density (FSD) based models. General notions are first introduced in section 1.3.1. Then, the model with a balance equation is described in section 1.3.3 and the algebraic model in section 1.3.2.
- The LES-Thickened Flame model (TF-LES) is described in section 1.3.4.

This enables in section 1.3.5 to focus on the sub-grid wrinkling factor Ξ_Δ, which is a common notion to the FSD and TF-LES approach. The dynamic wrinkling model of Wang et al. (2012), studied in Part II of the manuscript is then introduced.

1.3.1 Flame surface density models

The flame surface density concept was originally proposed for RANS (Cant et al., 1990) and then adapted to LES, with algebraic closures (Boger et al., 1998), and balance equations (Hawkes and Cant, 2000; Richard, 2005). General notions of these models are first presented.

1.3.1.1 Equation of the filtered progress variable $\tilde{c}$

The flame surface density approach is derived under the flamelet regime assumption. Combustion is described by the progress variable c, under the assumptions presented in section 1.2.3. The flame front is viewed as a collection of laminar

flamelets wrinkled by the turbulent structures, but keeping a laminar flame structure. Accordingly, chemical effects can be decoupled from turbulence effects. The reaction rate of the progress variable $\dot{\omega}_c$ is in that case expressed as the product of the flame surface density Σ by the local consumption rate per unit of flame surface. Theoretical developments not detailed here led Boger et al. (1998) to establish the following expression for the balance equation of the filtered progress variable:

$$\frac{\partial \overline{\rho}\tilde{c}}{\partial t} + \frac{\partial \overline{\rho}\tilde{u}_i\tilde{c}}{\partial x_i} + \frac{\partial}{\partial x_i}\left(\overline{\rho u_i c} - \overline{\rho}\tilde{u}_i\tilde{c}\right) = \rho^u s_L \overline{\Sigma} \tag{1.47}$$

where $\overline{\Sigma}$ is the filtered flame surface, accounting for the flame-turbulence interactions, and $\rho^u s_L$ corresponds to the local gas consumption rate per unite of flame surface, accounting for the chemical effects. Practically, the laminar flame speed s_L can be tabulated from 1D flame calculations or computed from correlations such as the correlation of Metghalchi and Keck (1982).
Terms requiring a closure in Eq. (1.47) are the unresolved transport term $\widetilde{u_i c} - \tilde{u}_i\tilde{c}$ (this aspect was studied for instance by Rymer (2001) or Boger (2000)) and the filtered flame surface density term $\overline{\Sigma}$. $\overline{\Sigma}$ may be closed using an algebraic expression (section 1.3.2) or a transport equation (section 1.3.3).

1.3.1.2 Introduction of a combustion filter

The filtered flame front described by the filtered progress variable $\tilde{c}$ remains too thin to be resolved on the LES mesh: see Fig. 1.5, right and middle images. Accordingly, the flame front is filtered using a filter larger than the LES filter. This filter is called combustion filter and is denoted Δ. The filtered flame front at scale Δ must contain enough grid points points for the resolution of the gradients, such as $\Delta = n_{res}\Delta_x$ with n_{res} number of grid points required for the resolution, typically 5-10 points, as shown in Fig. 1.5, left.

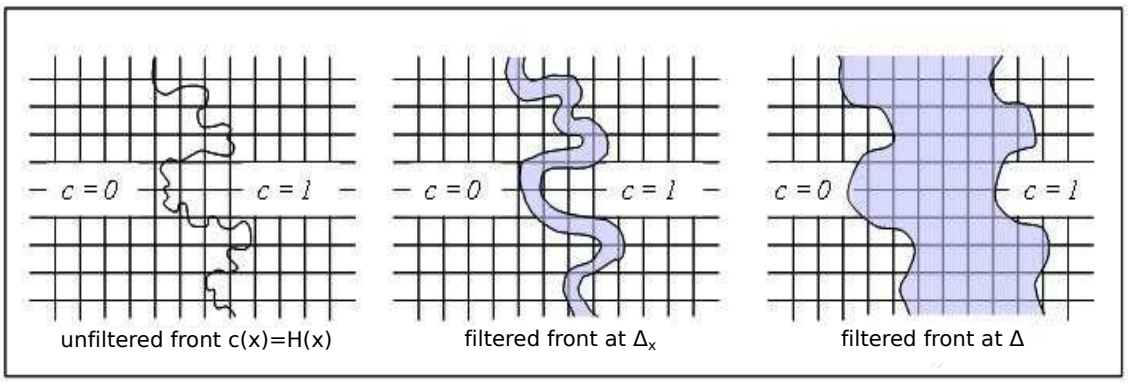

Figure 1.5: Left: infinitely thin flame front. Middle: filtering of the infinitely thin flame front at scale Δ_x. Right: filtering of the infinitely thin flame front at combustion filter scale Δ. Richard (2005).

1.3.2 The algebraic Flame Surface Density model of Boger et al.

To close the flame surface density $\overline{\Sigma}$, a simple algebraic closure may be used, such as the one proposed by Boger et al. (1998). Assuming an infinitely thin flame front (e.g. $\delta_L = 0$) $\overline{\Sigma}$ is recast as:

$$\overline{\Sigma} = \overline{|\nabla c|} \tag{1.48}$$

First, Boger et al. establish the analytical expression of $\overline{\Sigma}_{lam}$ for the 1D laminar flame, which reads in that case:

$$\overline{\Sigma}_{lam} = \overline{\left|\frac{\partial c}{\partial x}\right|} = \left|\frac{\partial \overline{c}}{\partial x}\right| \tag{1.49}$$

Authors describe the infinitely flame front by the progress variable $c(x) = H(x)$, where $H(x)$ is the Heavyside function. The analytical expression of the filtered progress variable $\overline{c}$ at the combustion filter scale Δ, which is assumed of a Gaussian shape, is then given by:

$$\begin{aligned} \overline{c}(x) &= \int_{-\infty}^{+\infty} H(x)\sqrt{\frac{6}{\pi}}\frac{1}{\Delta}\exp\left(-\frac{6}{\Delta^2}(x-x')^2\right)\mathrm{d}x' \\ &= \frac{1}{2} + \frac{1}{2}\mathrm{erf}\left(\frac{\sqrt{6}}{\Delta}x\right) \end{aligned} \tag{1.50}$$

with the erf function defined such as:

$$\mathrm{erf}(x) = \frac{2}{\sqrt{\pi}}\int_0^x \exp(-t^2)\mathrm{dt} \tag{1.51}$$

The 1D laminar filtered flame surface density $\overline{\Sigma}_{lam}$ at scale Δ then reads:

$$\overline{\Sigma}_{lam} = \overline{\left|\frac{\partial c}{\partial x}\right|} = \sqrt{\frac{6}{\pi}}\frac{1}{\Delta}\exp\left(-\frac{6}{\Delta^2}x^2\right) \tag{1.52}$$

This analytical expression of $\overline{\Sigma}_{lam}$ may be advantageously approximated using a function of $\overline{c}$, which form is then similar to the Bray Moss Libby model (Bray et al., 1987) developed for RANS, such as:

$$\overline{\Sigma}_{lam} \approx 4\sqrt{\frac{6}{\pi}}\frac{\overline{c}(1-\overline{c})}{\Delta} \tag{1.53}$$

The normalization constant $4\sqrt{6/\pi}\Delta$ enables to recover the total flame surface. Boger et al. define then a generalized flame surface density:

$$\overline{\Sigma} = \Xi_\Delta|\nabla\overline{c}| \approx \Xi_\Delta 4\sqrt{\frac{6}{\pi}}\frac{\overline{c}(1-\overline{c})}{\Delta} \tag{1.54}$$

where the sub-grid wrinkling factor Ξ_Δ is introduced, as defined by Weller et al. (1998). The wrinkling factor represents the ratio of the flame surface to its projection along the mean propagation direction in the filter volume:

$$\Xi_\Delta = \frac{\overline{|\nabla c|}}{|\nabla\overline{c}|} \tag{1.55}$$

Boger et al. also derived a closure for the unresolved transport term, which is not detailed here. The final transport equation for $\tilde{c}$ is recast by Boger et al. (1998) as:

$$\frac{\partial \overline{\rho}\tilde{c}}{\partial t} + \frac{\partial}{\partial x_i}\left(\overline{\rho}\tilde{u}\tilde{c}\right) = \rho^u D^u \Xi_\Delta \frac{\partial^2 \tilde{c}}{\partial x_i^2} + \rho^u s_L \Xi_\Delta \frac{4\sqrt{6/\pi}}{\Delta}\tilde{c}(1-\tilde{c}) \tag{1.56}$$

The diffusion term $\rho^u D^u \Xi_\Delta \Delta \tilde{c}$ accounts for the unresolved transport term. It enables to ensure the propagation of the laminar 1D flame at the laminar flame speed s_L and of a turbulent flame at $\Xi_\Delta s_L$. The diffusivity coefficient D^u is obtained by Boger (2000) following a KPP (Kolmogorov-Petrovski-Piskunov) analysis. It reads:

$$D^u = \frac{s_L \Xi_\Delta \Delta}{16\sqrt{6/\pi}} \tag{1.57}$$

Closures for the sgs wrinkling Ξ_Δ factor will be discussed in section 1.3.5.

1.3.3 Transported flame surface density model

The transport equation of $\overline{\Sigma}$ for LES has been discussed in several studies: Hawkes and Cant (2000); Richard et al. (2007). The formulation of the transport equation for $\overline{\Sigma}$ is given here according to the formulation established by Richard et al. (2007), corresponding to the ECFM-LES model implemented in the AVBP code. Details of corresponding derivations may be found also in Richard (2005).

Richard et al. (2007) write the transport equation for the filtered variable $\tilde{c}$ such as:

$$\frac{\partial \overline{\rho}\tilde{c}}{\partial t} + \frac{\partial}{\partial x_i}\left(\overline{\rho}\tilde{u}\tilde{c}\right) = \frac{\partial}{\partial x_i}\left(\frac{\overline{\rho}\nu_{t,\Delta}}{Sc_t}\frac{\partial \tilde{c}}{\partial x_i}\right) + \rho^u s_L \overline{\Sigma}_{\tilde{c}} \tag{1.58}$$

where $\nu_{t,\Delta}$ is the turbulent viscosity at the scale of the combustion filter Δ and the filtered flame surface $\overline{\Sigma}_{\tilde{c}}$ defined by:

$$\overline{\Sigma}_{\tilde{c}} = \overline{\Sigma} + \nabla.\left((\overline{c}-\tilde{c})\overline{\mathbf{N}}\right) \tag{1.59}$$

where $\overline{\mathbf{N}}$ is the normal to the iso-surfaces of the resolved progress variable $\overline{c}$, defined by:

$$\overline{\mathbf{N}} = -\frac{\nabla \overline{c}}{|\nabla \overline{c}|} \tag{1.60}$$

To close the filtered flame surface $\overline{\Sigma}_{\tilde{c}}$, Richard (2005) write the following balance equation:

$$\underbrace{\frac{\partial \overline{\Sigma}_{\tilde{c}}}{\partial t}}_{\text{unsteady effects}} + \underbrace{\nabla.\left[\langle \mathbf{u} \rangle_s \overline{\Sigma}_{\tilde{c}}\right]}_{\text{convective transport T}} = \underbrace{\langle \nabla.\mathbf{u} - \mathbf{N}\mathbf{N} : \nabla \mathbf{u} \rangle_s \overline{\Sigma}_{\tilde{c}}}_{\text{strain S}} - \underbrace{\left(\nabla.\langle s_d \mathbf{N} \rangle_s \overline{\Sigma}_{\tilde{c}}\right)}_{\text{planar propagation P}} + \underbrace{\langle s_d \nabla.\mathbf{N} \rangle_s \overline{\Sigma}_{\tilde{c}}}_{\text{curvature C}} \tag{1.61}$$

where operator $<>_s$ corresponds to the conditioned average to the filtered flame surface and $\mathbf{N}$ is the local normal to the c isosurface. Each term of Eq. (1.61) can be classically separated between a resolved contribution and an unresolved contribution. Unresolved contributions are closed using adequate sub-grid models

- **Strain term S**: $S_{res} + S_{sgs}$, with:

$$S_{res} = (\nabla.\tilde{\mathbf{u}} - \overline{\mathbf{N}}\ \overline{\mathbf{N}} : \nabla\tilde{\mathbf{u}})\overline{\Sigma}_{\tilde{c}} \tag{1.62}$$

The sgs strain term S_{sgs} is modeled as:

$$S_{sgs} = \frac{\alpha_1}{\sigma_c}\Gamma_1\left(\frac{\Delta}{\delta_L}, \frac{u'_\Delta}{s_L^0}, Re_\Delta\right)\frac{u'_\Delta}{s_L}\overline{\Sigma}_{\tilde{c}} \tag{1.63}$$

The efficiency function Γ_1 measures the strain of the flame by the unresolved turbulence structures (e.g. vortices smaller than Δ) and is given by the function of Charlette et al. (2002a), modified by Richard (2005). u'_Δ is the sub-grid scale velocity fluctuation, estimated using the method proposed by Colin (2000). α_1 is a model parameter, σ_c a correction factor proposed by Richard (2005) to control the thickness of the filtered flame front profile.

- **Propagation and Curvature terms**: $P_{res} + C_{res} + (P + C)_{sgs}$, with:

$$P_{res} = -\nabla.\left(s_d\overline{\mathbf{N}}\ \overline{\Sigma}_{\tilde{c}}\right) \tag{1.64}$$

$$C_{res} = s_d(\nabla.\overline{\mathbf{N}})\overline{\Sigma}_{\tilde{c}} \tag{1.65}$$

with s_d displacement speed of the front given by $s_d = (1 + \tau\tilde{c})s_L$, τ being the thermal expansion ratio defined by $\tau = \rho^u/\rho^b - 1$ (ρ^b burned gases density). The sub-grid scale contribution of the joined propagation and curvature terms $(P + C)_{sgs}$ is closed according to:

$$(P + C)_{sgs} = \beta s_L\frac{c^* - \overline{c}}{\overline{c}(1 - \overline{c})}(\overline{\Sigma}_{\tilde{c}} - \overline{\Sigma}^{lam})\overline{\Sigma}_{\tilde{c}} \tag{1.66}$$

where $\overline{\Sigma}^{lam}$ is the laminar contribution of the flame surface, expressed by $\overline{\Sigma}^{lam} = |\nabla\tilde{c}| + (\overline{c} - \tilde{c})\nabla.\overline{\mathbf{N}}$.

- **Transport term** T: $T_{res} + T_{sgs}$, with:

$$T_{res} = \nabla.(\tilde{\mathbf{u}}\overline{\Sigma}_{\tilde{c}}) \tag{1.67}$$

$$T_{sgs} = -\nabla.\left(\frac{\sigma_c\nu_{t,\Delta}}{Sc_t}\nabla\overline{\Sigma}_{\tilde{c}}\right) \tag{1.68}$$

The transport equation for $\overline{\Sigma}$ is by construction well adapted to describe the out-of-equilibrium wrinkling behavior of the flame in the engine combustion chamber, because there is no assumption of equilibrium between the flame surface production term and the flame surface destruction term, as it is done in other approaches (for instance in the Boger et al. and in the TF-LES models). The transported FSD approach presents other advantages for SI engine configurations: description of ignition with adequate sub-models (Richard et al., 2007; Colin and Truffin, 2011) (these models will be presented in section 3.2.3); description of the knock (**?**). The approach was successfully validated in several SI engine configurations (Richard et al., 2007; Vermorel et al., 2009; Robert et al., 2015). However, the approach presents following drawbacks:

- The closure of certain of the sub-grid contributions of the transport equation for $\overline{\Sigma}$ presents some difficulties, among which:
  - a correction factor σ_c is required to control the thickness of the resolved front, but this factor modifies the sgs strain term S_{sgs} by a factor $1/\sigma_c$ (see Eq. (1.63)). However, practically the resolved front has no time to diffuse or to become steep because the propagation time of the flame inside the combustion chamber is very short. This is why the correction factor σ_c can be set equal to unity.
  - the term S_{sgs} includes a modeling constant α_1 which often needs some small adjustments from one configuration to the other. This need for an adjustment probably reflects the fact that the formulation for S_{sgs} is not predictive enough.
- The notion of flame surface is insufficient to predict complex ignitions (lean or diluted stochioemetric combustion regimes, long electrical arcs, see section 3.2.3). This latter point represents the main limitation of the FSD approach and motivates the use of the TF-LES approach in the present work.

1.3.4 TF-LES model

To correctly resolve the gradients on the LES mesh, the flame front may be artificially thickened by a factor F, while propagating at the same laminar flame speed s_L as the non-thickened flame front as illustrated in Fig. 1.6.

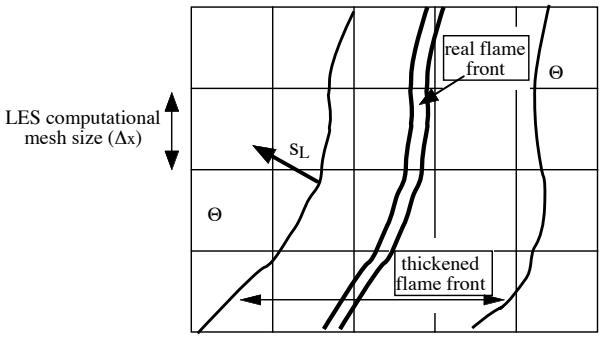

Figure 1.6: the flame front is thickened by a factor F while the laminar flame speed S_L is conserved. (Poinsot and Veynante, 2005)

The Thickened Flame model was originally proposed by Butler and O'Rourke (1977). Their analysis is based on laminar premixed flame considerations, which led them to modify the reaction and diffusive terms in the transport species equation, in order to keep unchanged the laminar flame speed s_L of the thickened flame, Classical theories for premixed flames (Williams, 1985; Kuo, 1986) are used to express the laminar flame s_L as:

$$s_L \propto \sqrt{D_{th}\dot{\omega}} \tag{1.69}$$

While the laminar flame thickness δ_L is expressed by:

$$\delta_L \propto \frac{D_{th}}{s_L} \tag{1.70}$$

According to relations (1.70) and (1.69), in order to keep the laminar flame speed s_L unchanged while thickening the laminar flame front by a factor F, the diffusivity coefficient must become FD_{th} and the reaction rate $\dot{\omega}/F$.

Colin et al. (2000) adapted the TF model to the LES formalism, demonstrating that, as the flame front is thickened, the interactions between the thickened flame front and the turbulence are changed.Then, when the flame front is thickened by a F factor, the Damköhler number Da is divided by F. In practice vortices of size smaller than $F\delta_L$ cannot wrinkle the thickened flame front, while they are able to wrinkle the non-thickened flame front. The other vortices affect the thickened flame front in a way that is also different from the way it affects the real flame. As a result, the thickened flame is less wrinkled than the non-thickened flame. To account for the lost flame surface, an efficiency function E (Angelberger et al., 1998; Colin et al., 2000) is introduced. The transport equation for the species is then recast as:

$$\frac{\partial \bar{\rho}\tilde{Y}_k}{\partial t} + \frac{\partial(\bar{\rho}\tilde{u}_i\tilde{Y}_k)}{\partial x_i} = \frac{\partial}{\partial x_i}\left(\bar{\rho}EFD_k\frac{\partial \tilde{Y}_k}{\partial x_i}\right) + \frac{E\dot{\omega}_k(\tilde{T},\tilde{Y}_k)}{F} \tag{1.71}$$

Similar modifications are made to the energy transport equation.
The efficiency function E which compensates the loss of flame surface induced by the thickening is defined as the ratio of the wrinkling of the non-thickened flame by that of the wrinkling of the thickened flame:

$$E = \frac{\Xi(\delta_L)}{\Xi(F\delta_L)} \tag{1.72}$$

Several closures for the wrinkling factor Ξ_Δ can be employed, for instance Colin et al. (2000) or the Charlette et al. (2002a) functions (see dedicated section 1.3.5 for the detailed expressions).
In practice, the thickening factor F is chosen to ensure:

$$F\delta_L = n_{res}\Delta_x \tag{1.73}$$

with n_{res} the number of grid points required to resolve gradients within the flame front. This number increases when gradients are steeper, for instance when intermediate species are described in the kinetic scheme.

The TF-LES model was already applied in SI engine configurations (Thobois, 2006; Enaux et al., 2011; Granet et al., 2012; Misdariis et al., 2015) and in gas turbines configurations (Boileau et al., 2008; Staffelbach et al., 2009). Its advantages are listed below:

- Its implementation is simple.
- The chemistry is directly resolved with the Arrhenius law. Therefore:

  - important phenomena, such as ignition, pollutants formation, flame stabilization, flame-walls interactions can be directly predicted, but with corrections taking into account the fact that the flame is thickened, which is not straightforward.
  - the description of the chemistry is only limited by the CPU resources and by the domain of validity of the kinetic schemes (temperature, pressure, equivalence ratio). This enables in theory to account for the description of intermediate species, which are for instance essential to describe phenomena such as pollutants formation. However in practice, using detailed kinetic mechanisms is not possible: in addition to the prohibitive CPU costs induced by these schemes, the resolution required to resolve the steepest intermediate species profiles would lead to increased thickening factors F, which needs to be avoided.This is the reason why simplified schemes are widely used. These mechanisms contain a very limited number of species, typically less than 10. This chemical description may however not be sufficient to describe phenomena such as ignition or pollutants formation, which require a more accurate chemical description. The possibility to use analytical schemes represents thus today a major improvement: when using this type of scheme, certain intermediate and radical species are transported, thus improving the chemical description, but the resolution required remains close to the one of simplified mechanisms.

However, the following drawbacks of the model must be mentioned:

- Because of the thickening factor, the flame response to strain is modified.
- To perform predictive simulations of SI engines configurations with the TF-LES model is delicate. Indeed, in order to correctly resolve the flame front, the thickening factor F remains very important: with a laminar flame thickness of 20 μm, a minimum of $n_{res} = 7$ points of resolution and a cell size $\Delta_x = 0.2$ mm (corresponding to a stoichiometric isooctane/air mixture a p=20 bars), then the thickening factor should be $F \approx 65$. When the thickening factor is so important, predicting with accuracy ignition and wall-flame interactions is not possible. To predict with accuracy the ignition using the TF-LES approach, the initial flame kernel cannot be thickened (Chapter 3). This implies for SI engine configurations an important refinement of the mesh with a cell size of 0.2 mm to 2 μm in the vicinity of the spark plug. The resolution required is today not possible. A solution could be to implement a coupling method between the calculation of the ignition in the ignition zone - with the adequate resolution - and the calculation of the whole combustion chamber. The coupling would be only required until the flame kernel has the sufficient size to be resolved on the coarse grid of the whole combustion chamber. Another option would be to use a code allowing adaptive mesh refinement (AMR), that refines where and when it is required.
  Regarding the wall-flame interactions, as the flame reaches the walls of the combustion chamber, either the thickening factor is conserved and the resulting estimation of the thermal flux is not correct, either the thickening factor is set equal to unity and the flame front becomes under-resolved, if the grid cell size is kept unchanged.

- Closures of the sgs wrinkling factor Ξ_Δ demand a specific modeling. This issue, which is common to the TF-LES and Boger models (and to all other approaches using the notion of sub-grid wrinkling) is detailed in the next section.

1.3.5 Sub-grid wrinkling modeling

The sgs wrinkling factor Ξ_Δ was introduced in section 1.3.2 when presenting the propagation model of Boger et al. (Eq. 1.55). The wrinkling factor may be also found in the expression of the efficiency function E of the TF-LES model (Eq. 1.71). The notion of sub-grid wrinkling factor is used in all models based on a geometrical description of the flame. In those approaches, assuming a flamelet regime, the sub-grid turbulence flame speed may be defined as:

$$s_T = \Xi_\Delta s_L \tag{1.74}$$

where s_L accounts for chemical effects, while Ξ_Δ for the flame turbulence interactions. Wrinkling is recast in terms of flame surface by Weller et al. (1998):

$$\Xi_\Delta = \frac{\overline{|\nabla c|}}{|\nabla \bar{c}|} \tag{1.75}$$

Several types of closures for the sgs wrinkling factor exist in the literature: algebraic closure, transport equation and dynamic closure. In the following, a brief literature survey is provided, introducing the dynamic wrinkling model of Wang et al. (2012) studied in Part II.

1.3.5.1 Brief literature survey of sub-grid wrinkling closures

Algebraic formulations of the wrinkling factor are the most easy to handle. Examples of such closures are listed below:

- equilibrium wrinkling of the flame surface density balance Eq. (1.61), obtained by a KPP analysis of Eq. (1.61) (see corresponding derivations in the PhD manuscrit of Richard (2005)):

$$\Xi_\Delta = \sqrt{1 + (4\nu_{t,\Delta} + \nu_l)\frac{\alpha_1 \Gamma_1}{{s_L}^2}\frac{u'_\Delta}{\Delta}} \tag{1.76}$$

  where α_1 is the model parameter and Γ_1 the efficiency function introduced in Eq. (1.63).

- Colin et al. (2000) formulation:

$$\Xi_\Delta = 1 + \alpha_2 \Gamma_2\left(\frac{\Delta}{\delta_L}, \frac{u'_\Delta}{s_L}\right)\frac{u'_\Delta}{s_L} \tag{1.77}$$

  where α_2 is an a priori unknown parameter and Γ_2 the efficiency function proposed by Colin et al. (2000), describing the ability of vortices to wrinkle the flame front at scale Δ.

- Charlette et al. (2002a) propose a modified exponent formulation of Eq. (1.77) such as:

$$\Xi_\Delta = \left(1 + \min\left[\frac{\Delta}{\delta_L}, \Gamma_3\left(\frac{\Delta}{\delta_L}, \frac{u'_\Delta}{s_L}, Re_\Delta\right)\frac{u'_\Delta}{s_L}\right]\right)^\beta \tag{1.78}$$

  where Γ_3 is the efficiency function proposed by Charlette et al. (2002a). $Re_\Delta = u'_\Delta \Delta/\nu$ is the sgs Reynolds number. The β exponent is an a priori unknown parameter.

- Wang et al. (2011) slightly modified Eq. (1.78) according to:

$$\Xi_\Delta = \left(1 + \min\left[\left(\frac{\Delta}{\delta_L} - 1\right), \Gamma_3\left(\frac{\Delta}{\delta_L}, \frac{u'_\Delta}{s_L}, Re_\Delta\right)\frac{u'_\Delta}{s_L}\right]\right)^\beta \tag{1.79}$$

  This formulation enables to maximize the wrinkling factor Ξ_Δ for large turbulence intensities by the fractal expression:

$$\Xi_\Delta = \left(\frac{\Delta}{\delta_L}\right)^\beta \tag{1.80}$$

  The model parameter β is then related to the fractal dimension D of the flame surface (Gouldin, 1987; Gulder, 1991) through $\beta = D - 2$.

Algebraic closures present one major drawback: the analytical derivation of algebraic closures is based under the flame turbulence equilibrium assumption, that is the equilibrium between flame surface production term and flame surface destruction term of Eq. (1.61):

$$\langle \nabla \mathbf{u} - \mathbf{NN} : \nabla \mathbf{u} \rangle_s = - \langle s_d \nabla . \mathbf{N} \rangle_s \tag{1.81}$$

This equilibrium assumption infers in practice that the flame can adjust instantaneously to the fluctuations of the flow. But this assumption is not verified during most of the flame development in the SI engine combustion chamber, as evidenced experimentally by Bradley and numerically by Richard et al. (2007). Just after the ignition, the flame kernel is quasi laminar. Then, as the flame kernel grows it is progressively wrinkled by turbulence. Accordingly, the wrinkling of the flame kernel progressively increases from unity values until reaching its equilibrium value. Algebraic wrinkling closures can predict equilibrium wrinkling values only and would overestimate the wrinkling factor when the flame kernel is quasi laminar. Since predicting the correct growth of the flame kernel is crucial to recover the correct heat release rate during the combustion cycle, algebraic closures for the sub-grid wrinkling should not be used in SI engines configurations.
In addition to this, in closures (1.77), (1.76) and (1.78), the determination of the velocity fluctuations at the combustion filter scale Δ (term u'_Δ) can be in practice delicate, as explained by Colin et al. (2000).

Other types of wrinkling closures can be employed that do not assume the equilibrium between flame and turbulence, for instance closures using a balance equation for the wrinkling factor (Weller et al., 1998). But implementing a transport equation for the wrinkling remains delicate, because this equation presents problematic boundary conditions: the value of Ξ_Δ towards fresh gases is not known a priori while the flame surface goes to zero. An interesting alternative consists in using a

dynamic formulation (Charlette et al., 2002b), that determines on the fly the appropriate value of the modeling constant appearing in most wrinkling expressions: for instance parameters α_1 and α_2 in Eqs. (1.76),(1.77) or parameter β in Eqs.(1.79), (1.80). This method was successfully implemented and tested in complex configurations: (i) jet flame of Chen et al. (1996), studied by Wang et al. (2011); Schmitt et al. (2014), (ii) PRECCINSTA burner (Meier et al., 2007) studied by Schmitt et al. (2013); Veynante and Moureau (2015), (iii) Tecflam burner (Schneider et al., 2005) studied by Schmitt et al. (2013), (iv), the Cambridge stratified swirl burner (SWB) studied by Mercier et al. (2015), (v) Matrix burner (Zajadatz et al., 2013) studied by Hosseinzadeh et al. (2015). Also, Wang et al. (2012) used the dynamic wrinkling model to predict the transient growth of a flame kernel self-propagating in a decaying homogeneous isotropic turbulence (HIT). Results demonstrated that the dynamic model can self-adapt to the turbulence intensity, predicting wrinkling values close to unity when the flame kernel is laminar and then wrinkling values increasing with the turbulence intensity.

The dynamic wrinkling model represents an interesting method to predict the out-of-equilibrium flame development in SI engine configurations, with no need of parameter adjustment from one configuration to another. To our knowledge, no attempt has be made to apply this model in a SI engine configuration. Part II is therefore dedicated to the adaptation and evaluation of the dynamic wrinkling model of Wang et al., coupled to the algebraic model of Boger et al. in a SI engine configuration. The study will enable to validate the strategy proposed in the present PhD for SI engines, that is the use of the TF-LES model coupled to the dynamic wrinkling model, once CPU resources will enable a sufficiently fine mesh to apply reasonable thickening factors.

Chapter 2

Physics of spark ignition

Contents

Physics of spark ignition are described in this chapter. Full details of the different physical events involved in the spark ignition are not provided, some of them belonging to the electromagnetism or to plasma physics, which are far beyond the scope of the combustion field. Spark plug ignition is first described in section 2.1. Laser-induced spark ignition is also briefly described in section 2.2, asCardin et al. experiments are Laser-induced spark ignitions. Common elements between the two modes of ignition will be highlighted; the reasons why Laser-induced spark ignition experiments were chosen for the ignition study. Finally, an essential quantity to characterize ignition, the minimum ignition energy (MIE), is introduced in section 2.3.

2.1 Description of the physics of the spark plug ignition

Two types of mechanisms may be distinguished during a spark plug ignition. The first category of mechanisms, described in section 2.1.1, is related to the formation of the spark and the way the energy of the spark is transferred to the gas. The second category of mechanisms, described in section 2.1.2, is related to the formation of the flame kernel and its development into a self-propagating flame kernel.

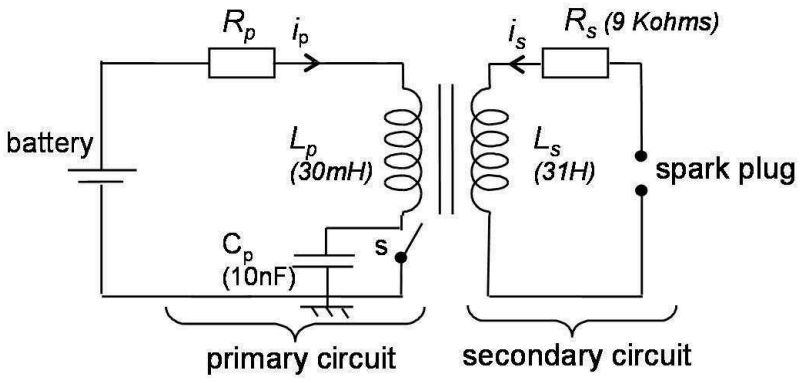

Figure 2.1: simplified electrical scheme for an inductive system

2.1.1 The spark energy deposit

Most automotive electrical ignition circuits can be modeled as the inductive ignition circuit presented in Fig. 2.1. At the ignition time, the switch of the ignition circuit is opened and the electric energy stored in the primary inductance is transferred to the secondary inductance by induction. The voltage at the plug electrodes rises very quickly ($< ns$). If the voltage reaches the breakdown voltage value, the spark formation process starts. Maly and Vogel (1979)describe the formation of an electric spark in four steps, which are illustrated in Fig. 2.2 and are detailed in the following.

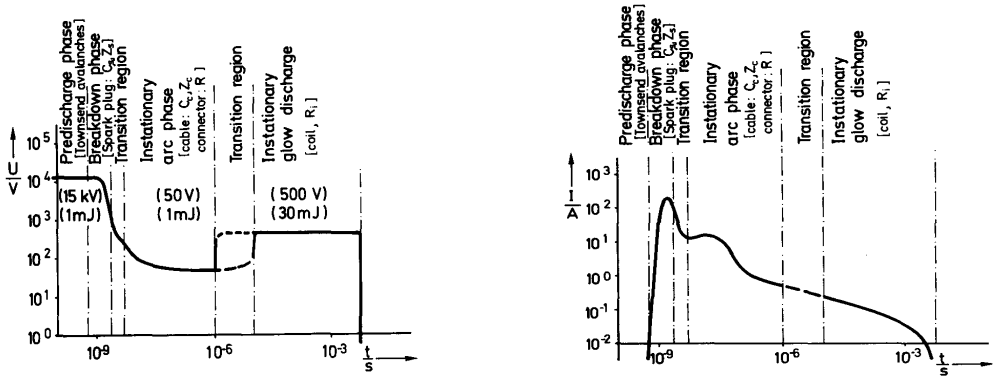

Figure 2.2: Schematic temporal evolution of the voltage (left) and current (right) of the spark during ignition, according to Maly and Vogel (1979).

- During the **predischarge phase** which lasts less than 1 ns, the air between the electrodes is ionized, becoming a conductor. An electron avalanche takes place, leading to the breakdown.
- The **breakdown phase** is characterized by a high peak of current in the spark gap, while the electrodes voltage suddenly drops. Because the air is a conductor, the electrical energy of the spark is transferred to the gas, which is

thus heated up in a few nanoseconds to very high temperatures (above 40 000 K). A plasma phase is formed, developing in a cylindrical channel of 20 μm diameter approximately. The energy released by the breakdown is transferred to the plasma with almost no loss (6 % according to Maly and Vogel (1979)) and is stored in the plasma in the form of dissociation and ionization energy (the plasma is then a non-equilibrium plasma).

- Transition phase (from $t \sim 1$ ns to $t \sim 1$ μs): due to the intense energy released during the breakdown, the pressure inside the plasma channel rises to $P \sim 200$ bar, causing the formation of a shock wave. The shock wave propagates and detaches rapidly from the hot gas kernel (around 100-200 ns according to Maly and Vogel (1979)). The plasma channel expands and the temperature decreases. The plasma, which was a non-equilibrium plasma during the breakdown, transitions toward a thermal plasma state (or equilibrium plasma state): the dissociation and ionization energy are largely converted to thermal energy.

- The **arc phase** which follows lasts a few μs and is characterized by a very low arc voltage(< 100 V). Temperature is maintained to 6000-7000K in the center of the spark channel, so that fusion points appear on the electrodes, possibly causing erosion of the electrode surface. The cathode and anode fall voltage are high, and the energy is dissipated by conduction to the electrodes, causing important losses. The arc expands and the thermal energy is transferred to the surrounding gas by heat and mass diffusion, mainly in the external zones of the plasma which are cooler. According to Maly and Vogel, the energy transfer during this phase has a 50 % efficiency.

- The **glow discharge** is the longest phase, lasting up to 2-3 ms, depending on the charge time of the electric circuit. The efficiency of the energy transfer during this phase is low (30 % efficiency according to Maly and Vogel), because of the strong fall voltage at electrodes. It corresponds thus to a much less intense energy transfer to the gas than the arc phase. During the glow phase, the excited species relax, while temperature decreases. The voltage remains constant (500 V) and the current decreases toward zero, until the spark ends.

  remark concerning the glow phase: the glow phase may not be observed in every ignition case, depending in fact on the electrical ignition circuit. Short duration sparks present no glow phase. Many studies (experimental or numerical) consider short duration sparks only because the key phases for the flame kernel formation and the flame kernel growth are the breakdown and arc phase.

The three modes of the spark discharge, e.g. the breakdown, the arc and the glow discharge, correspond to three different types of energy transfer from the spark to the gas. The transition between these modes is continuous, as the transition between the thermal plasma phase and the apparition of the flame kernel.

2.1.2 Combustion initiation and growth of the flame kernel

Combustion initiation The plasma relaxation brings thermal energy and radicals required to initiate combustion. The shock wave induced by the pressure rise inside the plasma channel (200 bars, according to Maly and Vogel (1979)) has a very limited effect on the initiation of chemical reactions: the shock wave expends much faster than the kernel of hot gases, detaching after $t \sim 0.5\ \mu s$, as illustrated in Fig. 2.3. The time evolution of the pressure wave and flame kernel are displayed, according to Kravchik and Sher (1994). Besides, the pressure wave is not sufficiently energetic to initiate the chemical reactions before detaching from the flame kernel (Maly and Vogel, 1979). However, the shock wave induces high velocities with recirculation zones at the tip of the electrodes, which promotes the mixing of hot burned gases with the surrounding fresh mixture. Also, the gas motion induced by the shock wave causes the kernel to develop into a torus shape (Ishii et al., 1992). As an illustration of this effect, Fig. 2.4 presents Schlieren images from the recent study of Bane et al. (2015), showing the effect of the pressure wave on the kernel development: the hot gas kernel, initially cylindrical because of the cylindrical shape of the spark between the electrodes, develops afterwards perpendicularly.

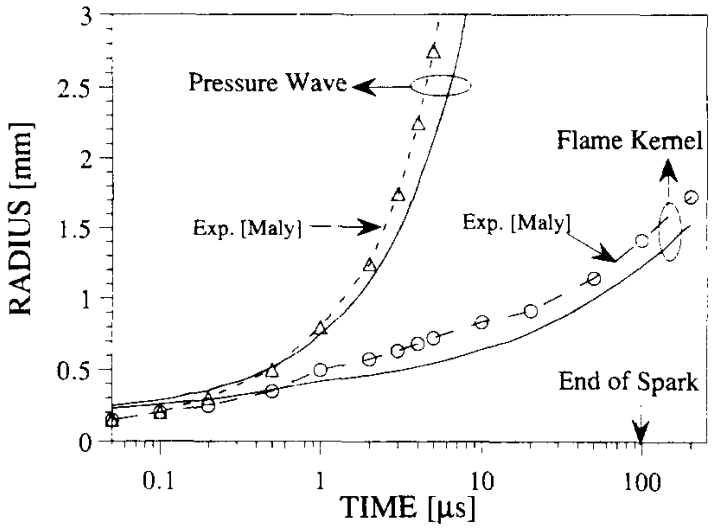

Figure 2.3: Flame kernel and pressure wave radii for stoichiometric CH_4-air mixture at 101.3 kPa. Gap between electrodes $d_{elec} = 1$ mm, spark duration $\tau_{spk} = 100\ \mu s$. Solid lines: prediction of the simulation of Kravchik and Sher (1994), dashed lines and marks: experimental results of Maly (1981).

At the end of the arc phase, the flame kernel has started to develop, the glow phase brings an additional heat supply and radicals to assist the combustion. As explained in section 2.1.1, the energetic transfer to the gas during the glow phase is less intense than during the arc phase, with a lower efficiency: its impact on the flame kernel development remains limited (Ishii et al., 1992). In practice, the glow phase can help to sustain the flame kernel for cases near flammability limits, that is very lean cases or with high EGR rate (Verhoeven, 1997).

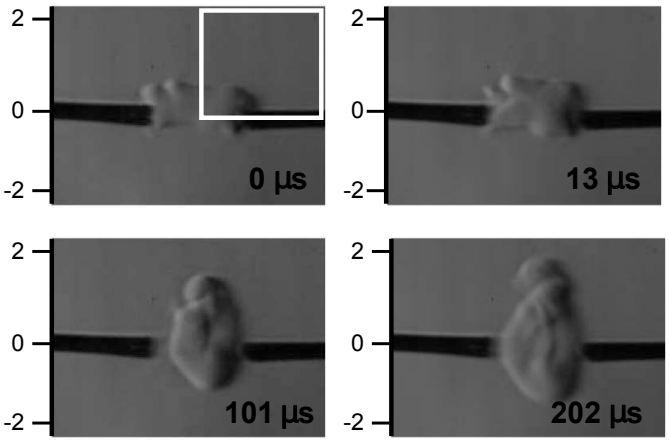

Figure 2.4: Images from high-speed schlieren visualization of a 2 mJ spark discharge in quiescent air, atmospheric conditions. Duration of the spark $\tau_{spk} < 1$ μs, inter electrodes distance $d_{elec} = 2$ mm. Distances shown are in mm. $t = 0$ μs corresponds to 12.6 μs after the breakdown. Study of Bane et al. (2015) (The white square corresponds to the calculation domain used in the simulation part of this experiment by the same authors, not shown here).

Growth of the flame kernel Even if a spark is formed, leading to the formation of a flame kernel, the flame kernel may not propagate. Figure 2.5 displays images of a flame kernel at different instants, in the case of unsuccessful and successful ignition. In the ignition failure case (top row), the flame kernel forms but starts cooling down after 300 μs. In the ignition success case (bottom row), the flame kernel forms and then grows into a self propagating flame kernel. Note that in the first 100 μs, there is almost no difference in the aspect of the flame kernel, wether it propagates after or not. The aspect of the flame kernel is also unchanged during the first 100 μs if varying the equivalence ratio (Akindele et al., 1982). To become a self-propagating flame kernel, the heat produced by the chemical reactions must balance the heat losses, mostly the conduction to electrodes and thermal diffusion at the surface of the flame kernel. This balance takes place only if the flame kernel has reached a certain size, denoted *critical size* (or *critical volume*) (Lewis and von Elbe, 1947). Note that the size of the initial flame kernel may be smaller than the critical size. In that case, the energy transferred by the spark to the gas must be sufficient to compensate the losses and to sustain the flame kernel until it reaches the critical volume.

Effect of turbulence on ignition Before the smallest characteristic time of turbulence is reached, that is the Komologorov time τ_k, turbulence has no effect on the ignition and the flame kernel remains laminar. This conclusion can be established from a simple characteristic time analysis and was confirmed by several experimental studies. Thus, Akindele et al. (1982) did experimental observations of spark ignition in quiescent and turbulent flows, generated by means of rotating fans. They observed no difference in the development of the flame kernel during the first 100 μs, whether there was turbulence or not. Figure 2.6 presents the temporal evolution of the flame kernel equivalent radius for quiescent and turbulent mixtures of increasing

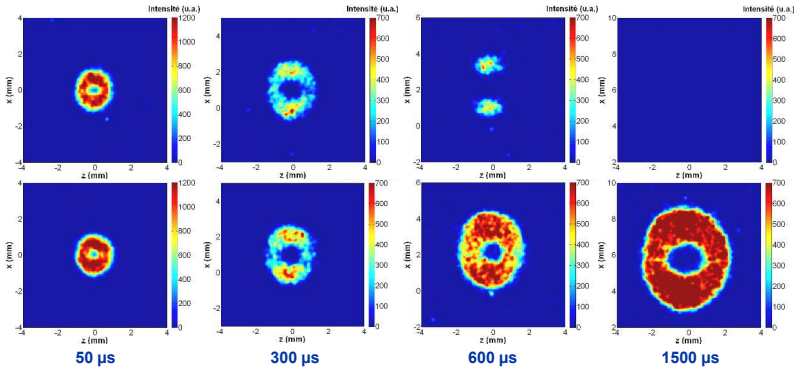

Figure 2.5: Instantaneous images of emissions (total radiations spectrum) of flame kernel (Laser-induced spark ignition), for a laminar premixed CH4/air mixture. $\phi = 0.65$. Atmospheric conditions. Top: ignition failure, the flame kernel cools down. Bottom: ignition success, the flame kernel propagates. Study of Cardin (2013).

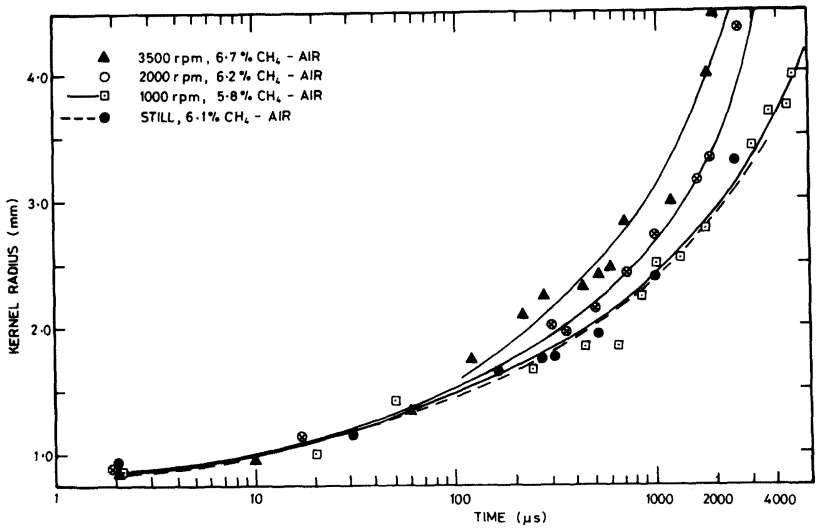

Figure 2.6: Kernel radius versus time for methane/air mixture at different fan speeds, corresponding to different turbulence intensities, according to Akindele et al. (1982).

turbulence intensity, clearly showing that the evolution of the radius is similar until $t \approx 100$ μs. Bradley and Lung (1987) did very similar experiments of spark ignition in a fan-stirred bomb in quiescent and turbulent flows and also established that turbulence had no effect during the first 200 μs.
When the smallest characteristic time of turbulence is reached, typically around 100-200 μs, turbulence acts both on the electrical arc and on the flame kernel.

- *Effects of turbulence on the electrical arc*: the electrical arc is deformed and convected by the flow. This results not only in changing the location of the arc in the flow but also in changing the amount of energy transferred to the gas. Indeed, when the arc is elongated, the proportion of energy inside the gas column between the electrodes increases, because the proportion of energy lost

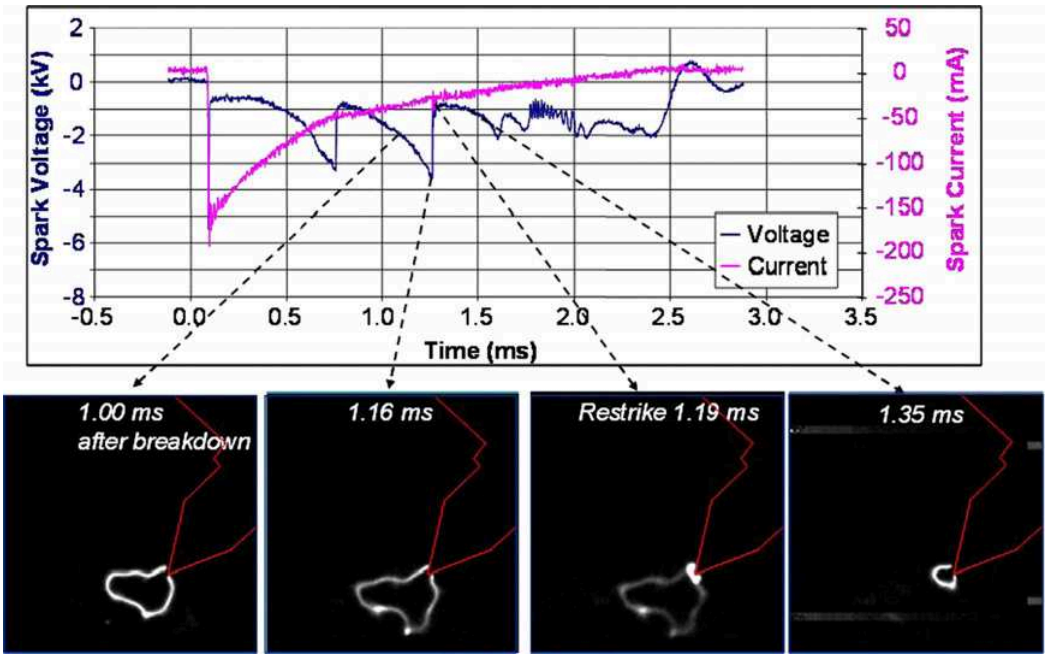

Figure 2.7: Spark voltage and current traces versus time (top) and a sequence of spark imaging illustrating spark stretching and a re-strike. Dahms et al. (2009)

by conduction to the electrodes decreases. A strong elongation of the arc may even cause a restrike, if the voltage in the elongated arc reaches the breakdown value. If so, a second breakdown takes place and a new electric arc is formed. Figure 2.7 illustrates an example of such a situation in a spray-guided gasoline engine. As the arc elongates (up to 10 mm after 1 ms), the spark voltage increases and reaches the breakdown value ($t = 1.16\ ms$). A new spark is then created ($t = 1.19\ ms$). In the case of short-duration sparks (a few hundreds of μs), the deformation of the arc is less important, because the arc has no time to be deformed by the flow.

- *Effects of turbulence on the flame kernel*: the turbulence structures wrinkle the flame kernel, as in the experimental visualizations of Akindele et al. (1982) in Fig. 2.8. In a more recent work, Kaminski et al. (2000)) performed PLIF visualization of the development of a turbulent flame kernel in an homogeneous methane/air mixture in a closed vessel. Figure 2.9 presents the temporal evolution of OH concentration fields for three ignitions, corresponding to the laminar case (a) and to two different turbulence intensity levels: (b) and (c). The progressive wrinkling of the flame kernel with turbulence can be observed. Also, when the turbulence intensity increases, as in case (c), the flame kernel is more wrinkled and is disrupted into pockets of burned gases. In the lower turbulence intensity case (b), the flame kernel keeps a global spherical shape. This difference of behavior during ignition between two turbulence regimes is today a topic of discussions, which will be presented in details in section 2.3.2.

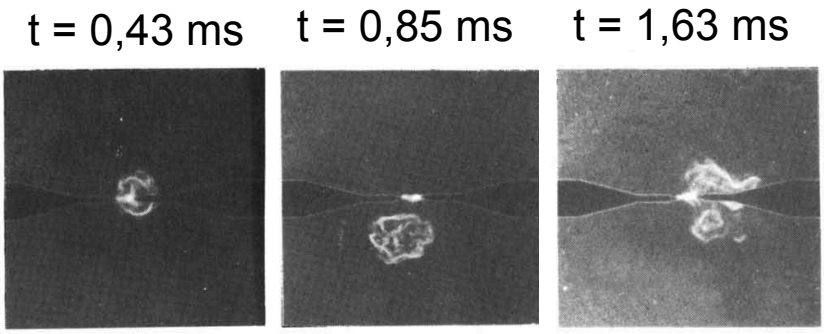

Figure 2.8: Photographs of turbulent spark kernel from the work of Akindele et al. (1982). Each photograph corresponds to a different spark. Spark duration: 130 μs, spark gap: 2 mm. Timing are given in reference to the ignition time. lean methane/air mixture $\phi = 0.8$.

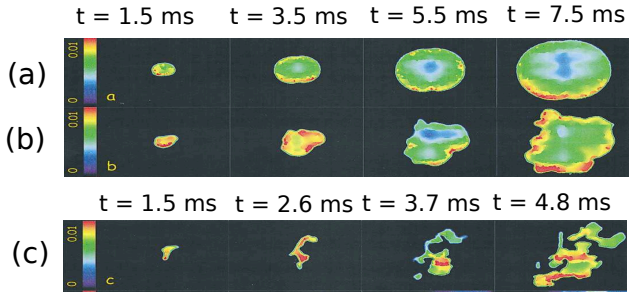

Figure 2.9: Evolution of OH concentration fields for three different spark ignition events corresponding to rotor speeds of 0 (a), 1000 (b) and 3000 rpm (c). The color scales correspond to the species mole fractions. Images from the work of Kaminski et al. (2000). Time is given to reference to the spark occurence.

The global action of the flow on ignition in a real engine chamber can be both favorable or unfavorable to the flame kernel development. For instance, if the flow convects the flame kernel away from the plug, the conduction losses at the electrodes are reduced and the combustion is enhanced. Figure 2.10 presents results of engine simulations by Pischinger and Heywood (1990) on two different engine cycles. In one case (cycle 8), the flame kernel stays centered on the electrodes gap, so that a large fraction of its surface is in contact with the electrodes. As a result, the heat losses to the electrodes are very important and are not compensated by the electrical energy of the arc (which is reduced as well since in that case the arc is not much elongated). This affects the overall combustion release rate and leads to a low pressure engine cycle. In the other case (cycle 96), the flame kernel is convected rapidly away from the electrodes. The electrical energy release can compensate the heat losses to the electrodes and the flame can propagate as if it were almost adiabatic, leading to a fast engine cycle. The flow may also bring the kernel to a zone where the local equivalence ratio is more favorable to ignition and propagation - in the case of a direct injection engine. The flow may also convect the kernel towards the walls of the combustion chamber, causing early flame/wall interactions. Last but not least, as it was presented in Fig. 2.9, turbulence wrinkles the flame front and, if it is very intense, can tear it apart, leading to an eventual quenching of the flame kernel.

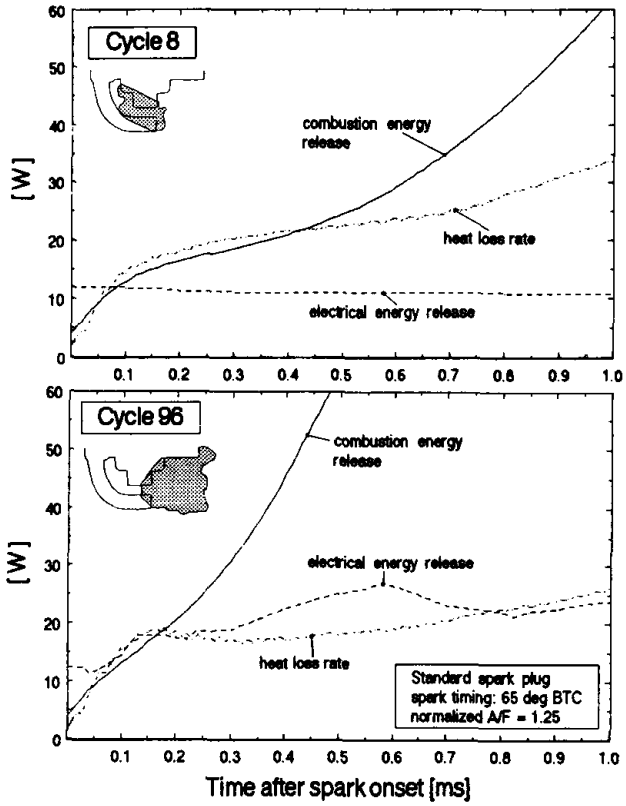

Figure 2.10: Electrical energy release rate, energy release rate by combustion and heat transfer loss rate for 2 different engine cycles, from the simulations of Pischinger and Heywood (1990).

Figure 2.11 summarizes the different stages of a spark plug ignition, according to the descriptions exposed in this section. Two main stages may be emphasized:

- **Phase A, "laminar", from t=0 to t≈ 100 – 200** μs: formation of the spark, breakdown and arc phase, shock wave formation and propagation, flame kernel starts to form.

- **Phase B, "turbulent", from t≈ 100 – 200** μs **to several ms**: development and growth of the flame kernel, assisted by the glow phase. Ignition depends on the balance between the energy released by the chemical reactions, the turbulent diffusion losses at the surface of the kernel and possible conduction losses to the electrodes. As turbulence wrinkles the flame kernel, the flame kernel development is strongly impacted. The energy supplied by the spark - mostly during phase A - must enable the flame kernel to reach the critical size for which the heat produced by the chemical reactions can balance the heat losses.

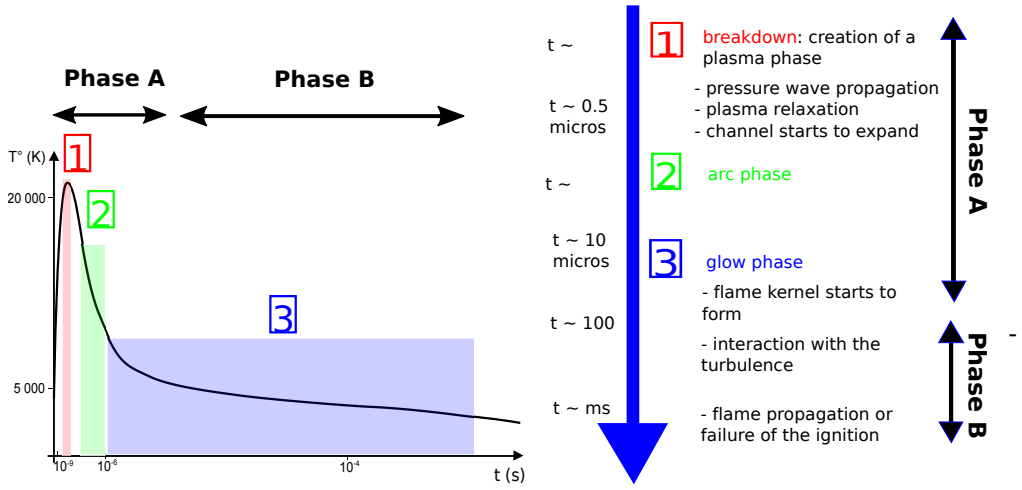

Figure 2.11: diagram illustrating the main stages of the ignition process

2.2 Brief description of the Laser-induced spark ignition

Even if Laser-induced spark ignition is not used in SI engines, this mode of ignition is briefly described in this section, because Part III is dedicated to simulations of the Laser-induced spark ignition experiments of Cardin et al. (2013). Reasons for this choice are:

- Mechanisms related to the flame kernel, development and interactions with turbulence are similar for Laser-induced spark and electric spark. Accordingly conclusions established in the ignition study can serve to improve both the understanding of Laser-induced spark ignition and spark plug ignition.
- The spark formed with both systems is similar, which explains why it is simulated in the same manner in the present work for both systems (this aspect will be developed in details in Chapter 3).
- Unlike with spark plug ignition, Laser ignition is a non-intrusive technique, therefore some difficulties for the comprehension (and for the simulation) of the ignition are removed: effects of the complex flow patterns between electrodes and of the thermal losses to the electrodes are avoided.
- The Laser-induced spark experiments of Cardin et al. (2013) were conducted in a well-characterized flow for simulations.

The Laser-induced spark is generated by focusing a laser beam through a lens with a typical pulse duration of a few nanoseconds. The spark forms when the energy density at the focal point reaches the breakdown threshold. The spark consists of a plasma that provides energy and highly reactive radicals. The process of the breakdown and of the spark formation is not detailed (see details for instance in Cardin (2013)). Once the spark is formed, mechanisms of the combustion initiation and of the kernel growth in the Laser induced spark case are very similar to the ones following the electric spark, probably because these mechanisms do not depend

on the way the energy is deposited by the ignition device. The success or failure of ignition can be characterized both for Laser-induced spark ignition and spark plug ignition with the notion of the minimum ignition energy (MIE), which will be introduced in section 2.3.

To complete this section, main differences between Laser-induced spark ignition and spark plug ignition which may have an impact on the flame development are mentioned:

- **Origin of the losses.** The breakdown phase of a Laser induced spark is shorter and more intense than the breakdown of an electric spark. Accordingly, the pressure wave formed in the case of a Laser induced spark is stronger. A detailed description of the effects of the pressure wave on the kernel development can be found for instance in Bradley et al. (2004). The authors explain how the pressure wave induces the formation of a third lobe of the hot gas kernel, helping to its development. Also, the energy losses due to the propagation of the shock wave are very important: about 70% according to Phuoc and White (2002), 85% according to Bradley et al. (2004). On the contrary, in the case of the spark plug ignition, the energy losses due to the shock wave are very low. According to Maly and Vogel (1979), 30% only of the input energy is dissipated as the shock wave propagates. On the other hand, Laser ignition being a non intrusive ignition technique, no conduction losses at the electrodes take place and the mixture can be ignited anywhere in the combustion chamber, in particular far away from the walls. In the spark plug ignition case, the conduction losses at the electrodes are very important, 70% according to Maly and Vogel (1979). Furthermore, the early interactions of the flame kernel with the plug and the walls can lead to extinctions.

- **Spark location.** The Laser induced spark is localized in a small volume, which location is reproducible from one Laser pulse to another in a quiescent and in a turbulent flow, as the Laser beam is focused by a given lens. On the contrary, the electric spark location is not reproducible in a turbulent flow, because the electric arc is then deformed by the turbulent structures (Fig. 2.7).

- **Spark duration.** The duration of the Laser induced spark is extremely short, generally a few nanoseconds, while it can last up to several milliseconds for an electrical spark. In the latter case, because the duration of the spark is long, the electrical arc is elongated by turbulence, which results in changing the shape and the location of the spark.

2.3 Minimum Ignition Energy

The minimum ignition energy (MIE) provides information on the necessary amount of energy required to successfully ignite a given mixture. Although a fundamental comprehension of the mechanisms detailed in section 2.1 and 2.2 (spark formation, energy transfer to the gas, initiation of the combustion, early stages of the kernel development) are required to understand what contributes to the success or failure

of the ignition, a more macroscopical approach such as determining the minimum ignition energy of a mixture for different conditions (pressure, equivalence ratio, turbulence intensity...) also brings useful informations. Numerous experimental, theoretical and numerical works are thus dedicated to the study of the MIE. From an experimental point of view, the minimum ignition energy is commonly defined as the amount of energy deposited by the ignition device leading to a probability of ignition of 50 %. For instance, Ballal and Lefebvre (1974); Ballal and Lefevbre (1975) measured the minimum ignition energy of a propane/air mixture ignited by spark plug ignition on a dedicated experimental configuration (closed-circuit tunnel with turbulence generated by fans). They found the MIE depends on numerous parameters:

- **Characteristics of the ignition device**: duration of the spark (for instance an optimal value of MIE was found according to the duration of the spark: Fig. 2.12), form of the electrodes, width of the electrode gap, material of the electrodes, position of the electrodes in the flow.

- **Characteristics of the mixture**: equivalence ratio, pressure and temperature. For instance, they established that the MIE was minimal near stoichiometry, as shown in Fig. 2.13.

- **Characteristics of the velocity field**: convective flow velocity, turbulence intensity and turbulence scale. MIE increases with convective flow velocity: (Fig. 2.13-(left) and with the turbulence intensity (Fig. 2.13-(right)).

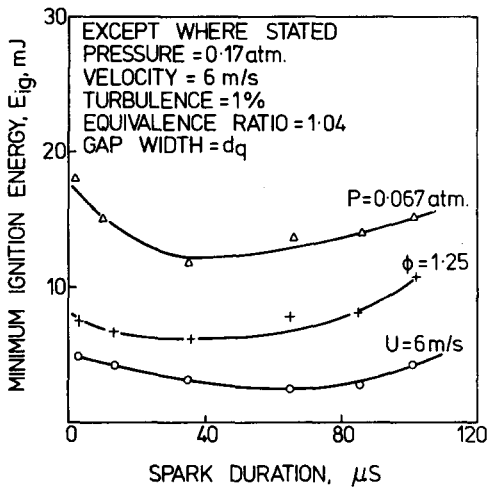

Figure 2.12: Measured MIE for different spark duration. Propane/air mixture. d_q corresponds to the quenching distance, see details in Ballal and Lefevbre (1975).

MIE studies are commonly classified in laminar ignition cases and turbulent ignition cases. Section 2.3.1 gives thus an overview of the fundamental notions related to the prediction of MIE in the laminar case, while section 2.3.2 is dedicated to the analysis in turbulent flows.

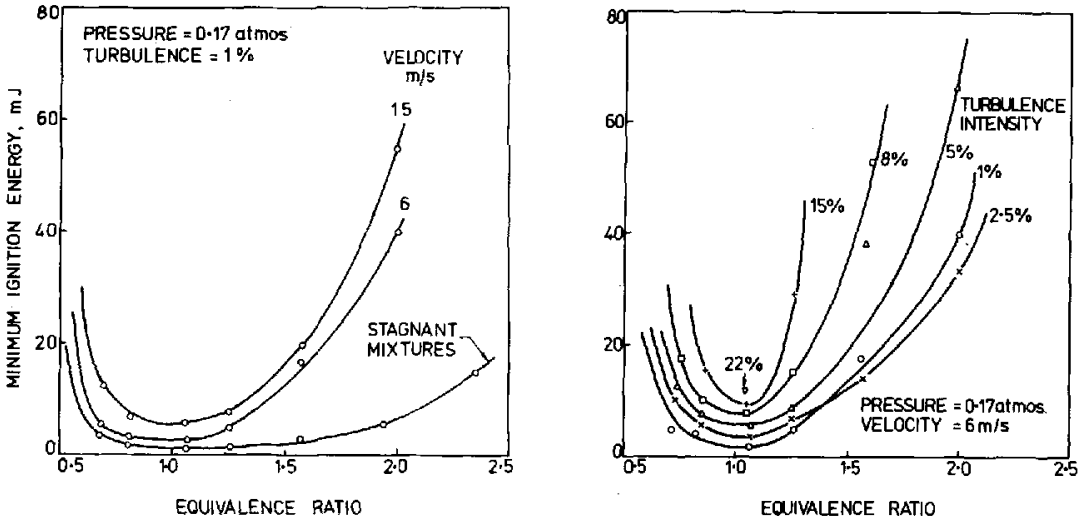

Figure 2.13: Measured MIE of propane/air mixture as a function of equivalence ratio ϕ and of mean velocity (left); of equivalence ratio and of turbulence intensity (right). Experiments of Ballal and Lefebvre (1974).

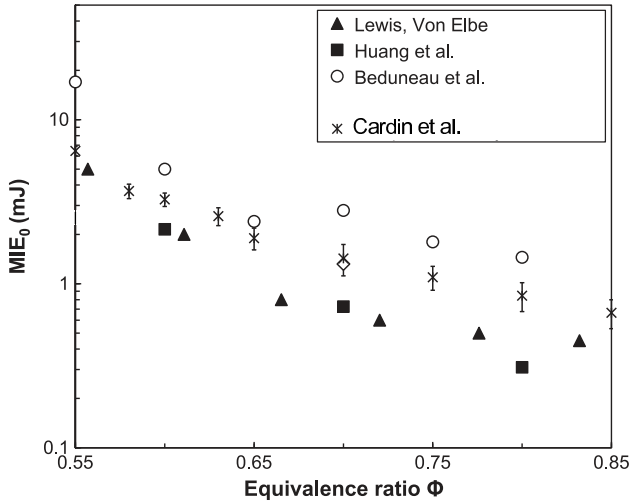

Figure 2.14: Different measurements of laminar MIE (MIE_0) of methane/air mixture as a function of equivalence ratio ϕ, for electric spark (Lewis von Elbe, Huang et al.) and Laser-induced spark ignition (Beduneau et al., Cardin et al.). Atmospheric conditions. Graph from Cardin (2013).

2.3.1 MIE in laminar ignition cases

All laminar MIE experiments confirm the results established by Ballal and Lefebvre. For instance, Ziegler et al. (1985) measured the MIE of quiescent lean methane-air mixtures at ambient temperature and a pressure of 2 bars, with arc and glow discharges. They showed that MIE depends on the electrode material and distance, spark type (arc or glow). Ishii et al. (1992) studied also the effect of the spark duration of the MIE, Bane et al. (2015) the effect of the forms of electrodes on the spark formation. MIE of Laser-induced spark ignition were also measured, for instance

in the work of Beduneau et al. (2003) and of Cardin (2013). MIE of Laser-induced spark ignition was found to present the same trend as MIE of spark plug ignition regarding for instance the equivalence ratio, as illustrated in Fig. 2.14. These measurements confirm that the success or failure of the ignition is not governed by the way the energy is deposited but by the balance between heat release and thermal losses, once the combustion reactions have been initiated. This explanation was first proposed by Lewis and von Elbe (1947), who introduced the notion of critical radius and established the following necessary condition for the flame kernel to become a self-propagating flame kernel: a critical radius $r = r_c$ must be reached, above which the heat produced by the chemical reactions can balance the heat losses. From there, 0D models (Ballal and Lefebvre, 1974; Akindele et al., 1982) or asymptotical analysis (Champion et al., 1986) have been derived. Several expressions for the critical radius r_c have been proposed but it is always related to the laminar flame thickness δ_L since it is the characteristic length for heat production and diffusion. Ballal and Lefebvre; Akindele et al. propose for instance:

$$r_c = \frac{D_{th}}{s_L} \tag{2.1}$$

D_{th} is the thermal diffusion coefficient, equal to $\lambda/\rho C_p$. With this definition, r_c is equal to the diffusive thickness, related to the laminar flame thickness and defined by:

$$\delta_\theta = \frac{D_{th}}{s_L} \tag{2.2}$$

In these approaches, the minimum ignition energy is defined as the total amount of energy required to heat a sphere of cold fresh gases of radius r_c to the adiabatic temperature of the laminar flame, so that:

$$\text{MIE} = \frac{4}{3}\pi r_c^3 \rho_u (T_{adiab} - T_0) \tag{2.3}$$

Accordingly, MIE is proportional to δ_L^3 (since thermal and laminar flame thicknesses are related) and also to $(1/s_L)^3$, using Eq. (2.2). These two last relations explain why MIE is minimal near stoichiometry and follows the trend such as the one observed in Fig. 2.13 and 2.14. To go further in the analysis, Champion et al. (1986) derived the 1D spherical equations for the problem of an already established steady spherical flame kernel of given radius r, with no external heat source term:

$$\begin{cases} \frac{1}{r^2}\frac{\partial}{\partial r}\left(r^2\lambda\frac{\partial T}{\partial r}\right) + Q_A w_A &= 0 \\ \frac{1}{r^2}\frac{\partial}{\partial r}\left(r^2\rho D_A\frac{\partial Y_A}{\partial r}\right) - w_A &= 0 \end{cases} \tag{2.4}$$

λ and D_A are the heat conductivity and the diffusion coefficient of the reactant A, Q_A the heat of reaction per unit of mass of reactant A and w_A the reaction rate (the authors assume a one-step chemistry), following the Arrhenius law. Champion et al. demonstrated the existence of an unstable solution to the equations system (2.4), corresponding to the spherical flame of radius $r = r_c$. If $r < r_c$, the flame collapses (the diffusive term is preponderant), if $r > r_c$ the flame can expand (the reaction rate term is preponderant). r_c is derived from the equations system and reads :

$$r_c = \frac{\lambda(T_{ad})}{\rho^u C_p(T_{ad}) s_L^0}\frac{T_{ad}}{T_b Le_A}\exp\left(\frac{E_a}{2RT_{ad}}\frac{T_{ad}-T_b}{T_b}\right) \tag{2.5}$$

The authors introduce the adiabatic combustion temperature T_{ad} and the burned gas temperature inside the flame kernel T_b, which are different if the Lewis number of the fuel Le_A is not equal to unity. When $Le_A = 1$, Eq. (2.5) becomes identical to Eq. (2.1). Numerical studies also investigated the determination of the laminar MIE, to reproduce and complete the results predicted by the asymptotical analysis. They will be presented in Chapter 3, dedicated to the ignition simulation studies.

2.3.2 Turbulent MIE and ignition regimes

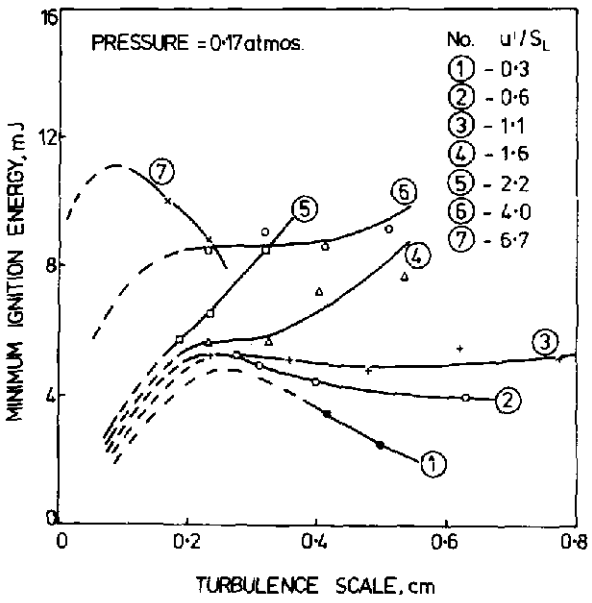

Figure 2.15: measured MIE of a propane/air mixture, $\phi = 1$ as a function of turbulence integral length scale and turbulence intensity. Experiments of Ballal and Lefebvre (1974)

From their experiments of turbulent spark ignitions, Ballal and Lefebvre (1974) established that MIE increased with the turbulence intensity, as seen in Fig. 2.13-(right). As the flame surface is wrinkled by turbulent structures, thermal losses strongly increase, more than consumption speeds s_c also enhanced by turbulence. Ballal and Lefebvre also investigated the effect of the turbulence integral length scale l_t on MIE, as presented in Fig. 2.15. From these observations, the relation between the turbulent MIE, the turbulence intensity and the turbulence scale cannot easily be characterized. However, Ballal and Lefebvre highlighted the existence of a transition region between a low intensity regime ($u'/s_L = 1$, curves 1, 2 and 3 in Fig. 2.15) and a high intensity regime ($u'/s_L > 4$, curves 4, 5, 6 in Fig. 2.15), for which the behavior of MIE appears to be very different. The authors proposed to extend their 0D analysis of the laminar case to turbulent cases: the critical ignition energy is still related to a critical ignition volume using Eq.(2.3), but the critical radius r_c is expressed as a turbulent flame thickness δ_T, to account for the wrinkling of the flame front by turbulence:

$$\delta_T = \frac{\lambda}{\rho^u C_p S_T} \left(1 + c_1 \mathrm{Re}\left(\frac{u'}{s_L^0}\right)^{c_2}\right) \tag{2.6}$$

c_1 and c_2 are constants depending on the turbulence characteristics. The term in factor with the Reynolds number Re represent the additional diffusivity brought by turbulence. The definition of this term clearly depends on the turbulence regime but no universal formulation could be derived. Other experimental works, which are exposed hereafter, confirm the observations of Ballal and Lefevbre and attempted to provide further explanations to the ignition regimes.

For instance, Akindele et al. (1982) observed in their experiments that the spreading of the radius was very similar for quiescent and low turbulence intensity case (corresponding to the 1000 RPM fan case), as shown in Fig. 2.6. But the spreading of the radius increases with the turbulence for the higher turbulence intensity case (2000 and 3500 RPM). Their observations confirm the existence of a transition regime. Akindele et al. explain that for low turbulence intensities, the flame surface is wrinkled by turbulence but it remains as a collection of laminar flamelets. For the higher intensity cases, the authors suggest, as the spreading rate of the radius much increases, that the structure of the flame front has changed and cannot be considered anymore as a collection of laminar flamelet.

More recently, the work of Kaminski et al. (2000) gave experimental evidence of the change of flame structure. In Fig. 2.9, a change of flame structure occurs between case (b) (low turbulence intensity case) and case (c) (high turbulence intensity case). While in case (b) the flame front is wrinkled but is continuous, in case (c), the flame front is disrupted in several burnt gas pockets. The authors propose to analyze their results introducing the Karlovitz number. They calculated the Karlovitz number for case (b) and case (c) : $Ka_{(b)} = 2.44$ and $Ka_{(c)} = 12.75$. According to the diagram of Peters (1999) (see Fig. 1.4), $Ka = 2.44$ is situated in the region close of the wrinked flamelet regime. In this regime, the flame front is a collection of laminar flames, wrinkled and stretched by the turbulence but keeping their inner laminar structure. $Ka = 12.75$ rather belongs to the thickened wrinkled flame regime. Then some vortices may enter the thermal flame thickness (but not the reaction zone), which could explain the apparition of pockets of burned gases as the ones observed in the experiments, but this assumption remains to be demonstrated.

Following these investigations, Shy et al. (2008) measured the minimum ignition energy of lean methane/air mixtures under increasing turbulence intensities, using a very short-duration electrical spark (10 μs). The results of their measurements are presented in Fig. 2.16, showing the measured MIE versus the ratio u'/s_L (left) and the measured MIE versus the Karlovitz number Ka (right). Shy et al. highlighted that, for a ratio $u'/s_L < 12$ corresponding to $Ka < 26$, the MIE increases almost linearly with the turbulent intensity. For a ratio $u'/s_L > 12$ corresponding to $Ka > 26$, the MIE increases exponentially. As in the work of Kaminski et al. (2000) the authors identified a change in the flame structure, from ($Ka < 26$) to ($Ka > 26$). The dependency of the MIE on the turbulence characteristics is clearly related to this change of the flame structure.
Finally, Cardin et al. (2013) carried out similar MIE measurements of turbulent ignition cases, with Laser-induced spark ignition. They found very similar results concerning the dependency of the MIE to the turbulence intensity as the ones of Shy et al.. The results obtained by Cardin et al. are illustrated in Fig. 2.17, showing

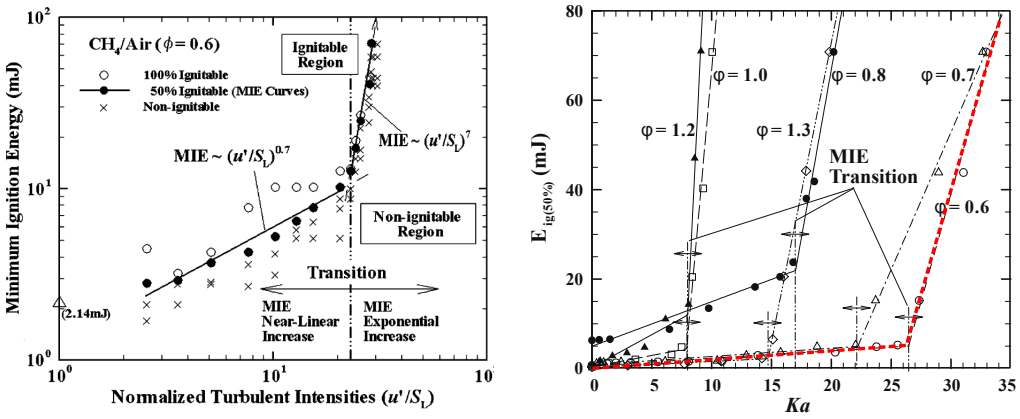

Figure 2.16: Measured MIE as a function of normalized turbulent intensities (left) and of the Karlovitz number (right) for methane-air mixtures at $\phi = 0.6$, according to the study of Shy et al. (2008)

the measured MIE versus the turbulence intensity u', for different lean equivalence ratios. Two zones are clearly distinguished: a zone where the MIE does not vary much with the turbulence intensity, corresponding to $u' < u'_{crit}$ and a zone where the MIE strongly increases with the turbulence intensity, corresponding to $u' > u'_{crit}$. The experimental visualization of the very early stages of the kernel development enabled also the authors to observe the change in the flame kernel structure. Figure 2.18 presents instantaneous images of the kernel emissions at various times after the laser pulse, for quiescent flow and increasing turbulence intensity flow. The left column corresponds to a turbulence intensity level situated in the second regime (after the transition), where the fragmentation of the kernel into pockets of burned gases can be clearly seen. This flame kernel shape corresponds to a high ratio $MIE_{turb}/MIE_{lam} \approx 5$ (Fig. 2.17), whereas a shape of flame kernel close to the laminar structure, such as the one observed in the middle column in Fig. 2.18, corresponds to a ratio MIE_{turb}/MIE_{lam} close to unity.

Note again that similar conclusions are established studying turbulent spark plug ignition cases (Kaminski et al., 2000; Shy et al., 2008) or Laser-induced spark ignition cases (Cardin et al., 2013).

To help understanding these different ignition regimes, numerical simulation would be a powerful tool of analysis but so far very few attempts have been made up to now to study this aspect: Chapter 3 presents in detail the different simulation approaches used for spark ignition, including the one retained for Part III dedicated to the simulation of Cardin et al. experiments.

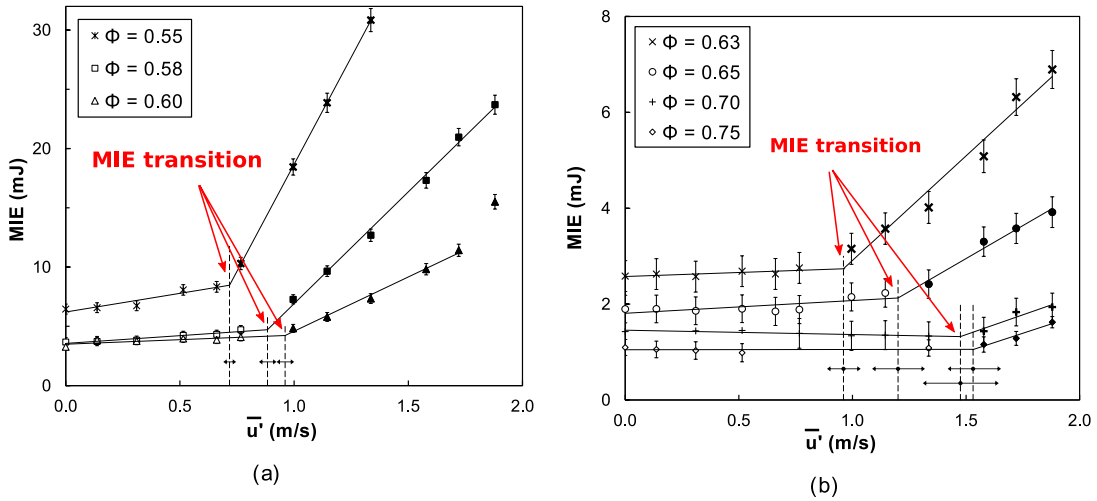

Figure 2.17: Measured MIE of Laser-induced spark ignition for methane-air mixtures as a function of turbulence intensity, for different equivalence ratios ϕ. Atmospheric conditions. Study of Cardin et al. (2013).

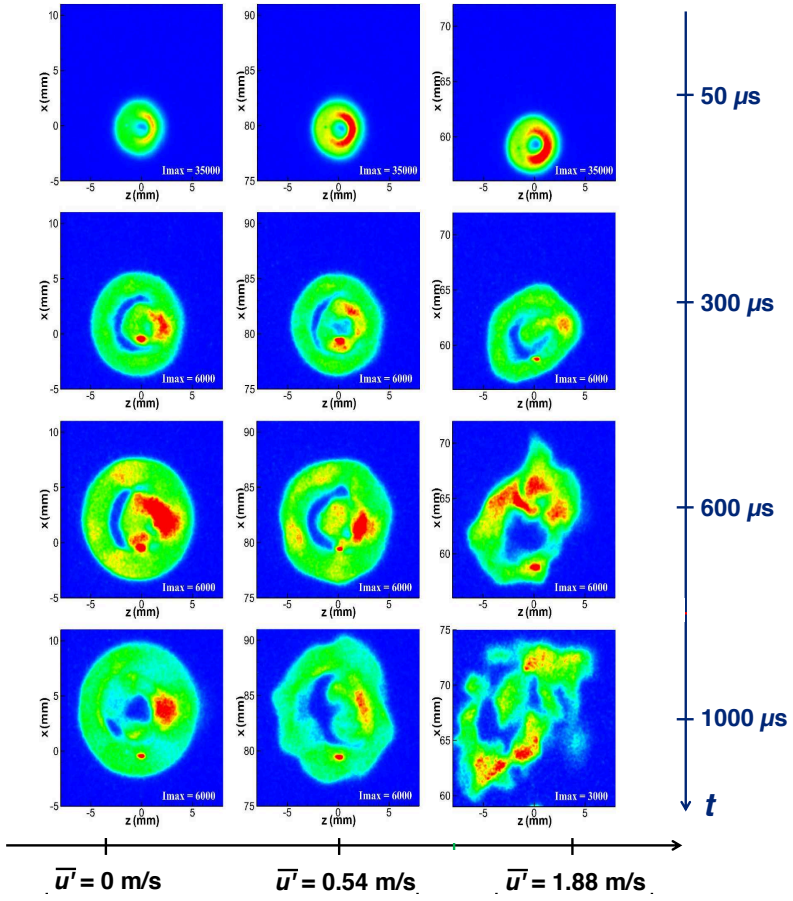

Figure 2.18: Evolution of kernel emissions (full radiation spectrum) at various times after the start of the laser pulse: 50 μs (row 1), 300 μs (row 2), 600 μs (row 3), 1000 μs (row 4). $\phi = 0.6$. Left column: laminar flow ($\overline{u'} = 0$) — Middle column: turbulent flow before the MIE transition in Fig. 2.17-left ($\overline{u'} = 0.54$ m/s) — Right column: turbulent flow after the MIE in Fig. 2.17-left ($\overline{u'} = 1.88$ m/s). Energy deposited by the Laser $E_d = 42\ mJ$. PhD Cardin (2013).

Chapter 3

Simulation approaches for spark ignition

Contents

Simulating the full ignition sequence, from the ignition electrical circuit to the flame kernel development and its interaction with turbulence, would provide very useful information to the understanding of ignition. Such simulations require the coupling of very different physical phenomena:

- *electromagnetism*: to calculate the exact variation of current and voltage in the electrical ignition circuit, before the breakdown and then during the breakdown, arc phase and glow phase.
- *plasma physics*: to describe the spark formation and the transfer of energy from the spark to the gas. Adapted plasma chemistry and thermodynamics must then be used. Physical timescales range between the ns and the μs; the spatial resolution required must be fine enough to capture the very short lifetime species ($\Delta_x < 1\ \mu m$).
- *thermal*: to accurately estimate the energy lost at electrodes
- *radiation*: to accurately estimate the losses of the flame kernel by radiation.
- *turbulent combustion*: to describe the flame kernel growth and the early interactions with turbulence.

Coupling all these phenomena would require to resolve very short time scales, with very fine mesh discretization, during a long time, which is impossible with the current CPU resources. Besides, there are still incertitudes concerning notably the plasma phase description: discussions are still open regarding the temperature, pressure, composition and size of the spark channel. Practically, spark ignition studies focus on distinct phases of the ignition, according to the mechanisms they aim at characterizing. On the one hand, DNS can provide detailed information on specific aspects of the ignition process, such as the role of the pressure wave propagation on the flame kernel formation, the influence of the electrodes geometry, the determination of the minimum ignition energy of a given mixture... These studies are presented in section 3.1, also introducing the modeling problematics addressed in the ignition study of Part III. On the other hand, LES can partly capture the interactions between flame kernel and turbulence and its impact on the flame development in complex configurations, but very strong simplifications of the ignition mechanisms are required: section 3.2 details the LES ignition models used with the TFLES and the FSD approach, stressing in which measure the models need to be improved for the prediction of critical ignition cases.

3.1 DNS of spark ignition

Among the DNS studies of ignition, several types must be distinguished, according to which part of the ignition process they focus on. Therefore section 3.1.1 first presents a classification of the different DNS categories, both in order to give a brief state of the art and to point out the different levels of assumptions required. Then section 3.1.2 details the approach in the DNS ignition study of Part III and presents the main problematics.

3.1.1 The different types of DNS of spark ignition

The classification presented in this section is illustrated in Figure 3.1.

Class 1 of DNS: "breakdown" simulations A first class of simulations focus only on the breakdown stage, to study the formation of the plasma phase and its transition to an equilibrium plasma (timescale: ns). For instance, Sher et al. (1992) determined the state at the end of the breakdown phase, e.g. the temperature inside the spark channel and the diameter of the channel. More recent works belong to plasma physics and are beyond the scope of the combustion field.

Classe 2 of DNS: "spark development and kernel formation simulations" A second category of simulations mostly discusses how the post-breakdown energy is transferred to the gas and how the flame kernel forms and develops. Initial conditions, corresponding to the end-breakdown state of the plasma, are required for these calculations: initial temperature, pressure and diameter of the spark channel. An exemple of initial conditions is displayed in Fig. 3.2 (Kravchik and Sher, 1994). Discussions are still opened regarding the exact post-breakdown initial state - temperature, pressure, size of the channel, composition of the plasma - and the chemistry of the plasma to be used. A description of the energy deposit during the

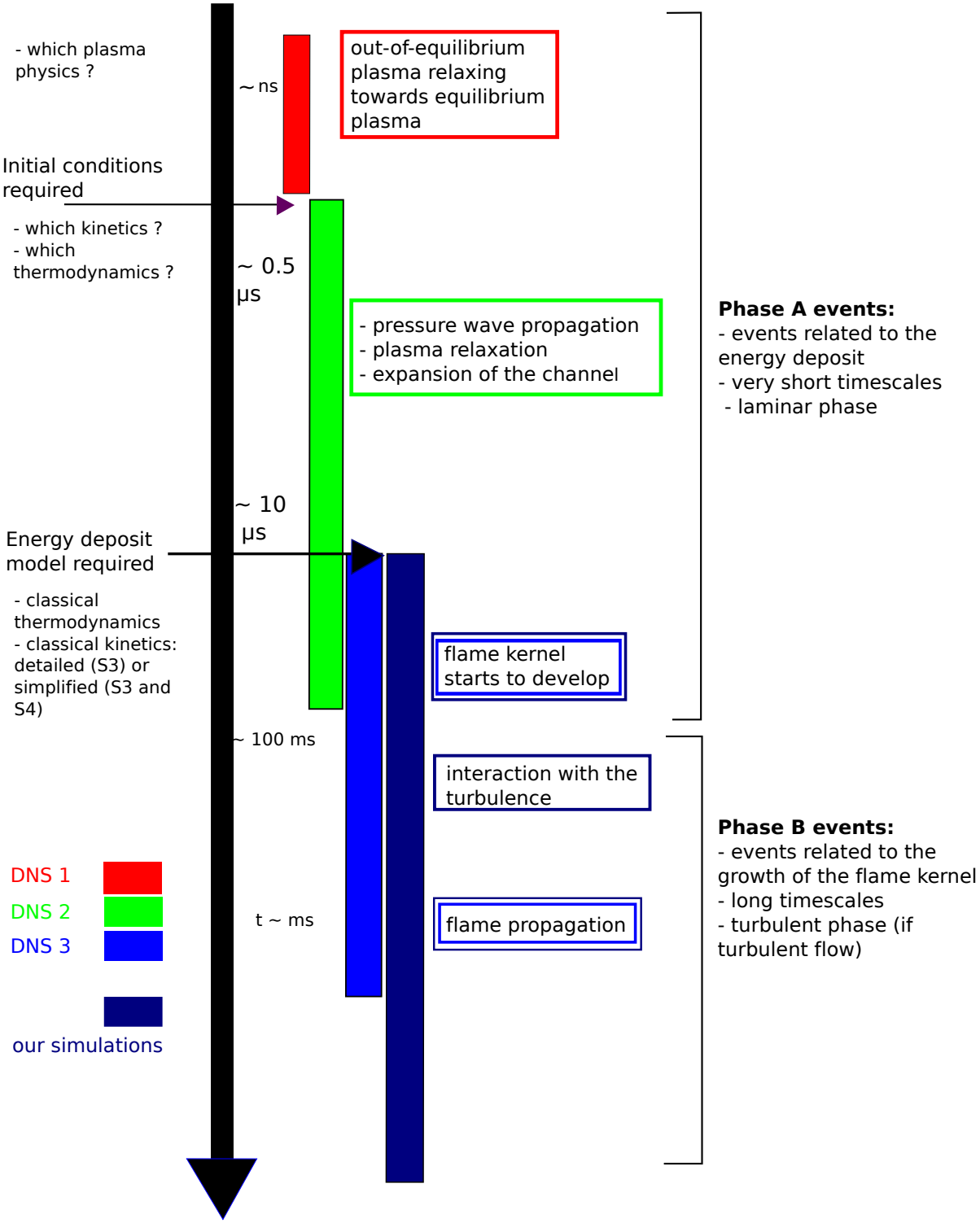

Figure 3.1: Sketch illustrating the different classes of simulations

arc phase and glow phase - if studying long duration sparks - is also required. These studies investigated various aspects: effect of the post-breakdown pressure wave on the kernel formation (Bradley and Lung, 1987; Sher and Keck, 1986; Kravchik and Sher, 1994; Thiele et al., 2000a; Morsy and Chung, 2002), effect of the plasma ionization (Thiele et al., 2000a), influence of the geometry of the electrodes on the kernel formation (Ishii et al., 1992; Thiele et al., 2000b; Bane et al.,

2015), effect of the temporal spark energy distribution (Sher and Keck, 1986; Ishii et al., 1992; Yuasa et al., 2002), estimation of the cathode/anode losses and of the radiation losses (Eisazadeh-Far et al., 2010). Most simulations are limited to two dimensions.

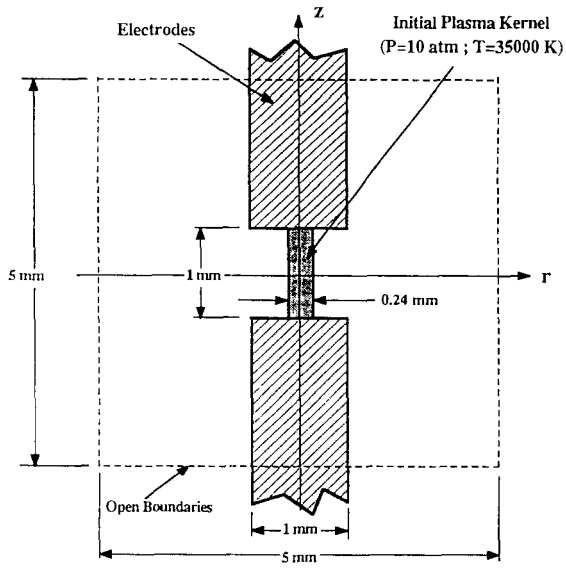

Figure 3.2: sketch illustrating the initial conditions and the boundary conditions in the simulation of Kravchik and Sher (1994)

Class 3 of DNS: "laminar MIE simulations" Some studies focus on the determination of the minimum ignition energy in the laminar case. Then, the physical time of the simulation must run until the flame kernel self-propagates. The order of magnitude of this time is the *ms*. Mechanisms governing the MIE in the laminar case are essentially the balance between the heat release by the combustion reactions and the thermal heat losses during the phase of growth of the flame kernel. Therefore corresponding studies do not focus on the phase of formation of the flame kernel (phase A in Fig. 3.1) but on the phase of the flame kernel growth (phase B in Fig. 3.1). Accordingly, the following phenomena are not accounted for: breakdown, arc phase, expansion of the plasma channel, pressure wave formation and propagation. It is also assumed in most studies that no initial radicals pool is present. Simplified chemistry is often used, for computational cost reasons but some studies used detailed kinetics (Sloane and Ronney, 1992; Han et al., 2010). The initiation of combustion is modeled by adding a heat source term in the energy equation. If temperature is raised and maintained to a sufficient level during a sufficient time, ignition takes place and a flame kernel is formed. Then, if the total energy of the heat source, denoted E_{ign}, is sufficient, the flame kernel develops and becomes a self-propagating flame kernel. The MIE in those simulations is then defined as the minimum value of total energy E_{ign}, ensuring the flame kernel propagation. Comparing the MIE predicted by simulations with experimental measurements of MIE is delicate. As explained in sections 2.1 and 2.2, an important part of the energy deposited by the ignition device is dissipated mostly by conduction losses at the

electrodes - in the case of spark plug ignitions - or by pressure losses - in the case of Laser-induced spark ignitions. Such simulations cannot well estimate these losses, as the spark energy input to the gas is modeled. However, despite the strong simplifications of the physics introduced by the model of energy deposit, using this approach enables to reproduce the dependency of the MIE on the equivalence ratio (Sloane and Schoene, 1988; Sloane, 1990; Wang and Sibulkin, 1993), or on the Lewis number (Tromans and Furzeland, 1986). Such results confirm that the thermal diffusive equilibrium process taking place during the kernel growth phase is a first order factor influencing the MIE as predicted in the theory of Lewis and von Elbe (section 2.3.1).

Class 4 of DNS: "Turbulent flame kernel development" Last type of DNS studies the interactions between the flame kernel and turbulence. In most cases, no ignition phase is accounted for: calculations start from an already self-propagating flame kernel. Accordingly no information on the minimum ignition energy can be provided. Most studies consider a spherical flame kernel developing in a decaying homogeneous isotropic turbulence flow field and investigate the influence of parameters such as turbulence intensity, integral length scale, mean curvature on the flame kernel growth: Kaminski et al. (2000); Gashi et al. (2005); Thévenin (2005); Bastiaans et al. (2007); Klein et al. (2008); Dunstan and Jenkins (2009).
To our knowledge, very few attempts have been made to perform turbulent DNS accounting for the ignition phase. Chakraborty et al. (2007) performed DNS simulations of turbulent ignition in inhomogeneous mixtures, using a heat source term to model ignition and a single-step chemistry. Authors evidenced that the mixture could not ignite for high turbulence intensity (corresponding to $u'/s_L = 12$), when using the same ignition energy as in the laminar case. However, the study largely focused on the effect of mixture stratifications on the flame kernel development, with fixed size and duration of the energy deposit. No minimum ignition energy was determined. Very recently, Patel and Chakraborty (2015) performed DNS of turbulent ignition in homogeneous mixtures, using a model of energy deposit and a single-step chemistry. Two equivalence ratios ($\phi = 0.8$ and $\phi = 1$) and different turbulence conditions were investigated. The study aimed at characterizing the effect of the turbulence intensity u' on the ignition energy, when varying the duration and the size of the energy deposit. Results are consistent with previous observations: ignition energy increases for leaner equivalence ratio $\phi = 0.8$, the increase of turbulent velocity fluctuations may lead to misfire. But no comparison with experimental data is made. Besides, the equivalence ratios considered in the study ($\phi = 1$ and $\phi = 0.8$) do not correspond to the very lean combustion regime where ignition becomes critical in SI engines ($\phi < 0.7$). The ignition study of Part III contributes therefore to DNS class 4, investigating lean equivalence ratios, using different types of kinetic schemes and comparing the simulation results to experimental data. However a certain number of issues must be first addressed in the laminar case, detailed in the following section 3.1.2.

3.1.2 Simulation approach for the ignition study

In the present ignition study, ignition is modeled by adding a heat source term $\dot{Q}_{ign}(\mathbf{x}, t)$ in the energy equation, as in the DNS class 3 described in section 3.1.1

and reduced kinetics are used. This strategy is adopted because the long term objective of the present work is to figure out if reduced chemistry with a simple thermal energy deposit can be a valid choice for complex engine configurations.
The parameters of the heat source term are the total energy E_{ign} distributed to the gas, the radius r_0 and the duration τ_{dep} of the deposit. The various hypothesis of this type of ignition modeling are first listed. Then, results of previous simulations are briefly discussed, as they motivated the parametric studies performed in Part III (Chapter 8).

3.1.2.1 Hypothesis of the ignition approach

1. The plasma phase is not solved. Accordingly a low energy density deposit should be used, to ensure low temperatures (typically around 2000 K) for which a chemical description of the plasma is not required. In simulations, the ignition energy E_{ign} and the deposit radius r_0 control the energy density deposit and must be therefore correctly chosen, this aspect is discussed in section 3.1.2.2.

2. The formation of the post-breakdown pressure wave is not accounted for. This implies that the duration of the deposit τ_{dep} is longer than the characteristic time of propagation of the pressure wave, which is of the order of magnitude of the microsecond. This aspect is discussed in section 3.1.2.2.

3. Reduced kinetics are used: intermediate and radicals species are not accounted for (simplified scheme) or only a part of them are described (skeletal or analytical scheme). Previous studies have shown that detailed kinetics are required to correctly estimate the MIE: this issue is described in section 3.1.2.3.

4. The radicals pool is not represented: ignition is triggered only by thermal energy. Sloane (1990) studied the effect of adding the initial ignition energy as pure heat or as a combination of dissociation of the fuel and oxygen with heat. The study demonstrates that accounting for the energy dissociation in the total ignition energy has a limited effect on ignition. This aspect was not further investigated in the present thesis.

5. The modeled energy deposit has a spherical shape, which implies that the flame kernel is supposed to grow with a spherical form. Some previous studies accounted for the initial cylindrical shape of the spark, but only in the case of spark plug ignition with long electrical arc (Han et al., 2010). To our knowledge, simulations of short duration of the laser induced spark type are all performed with a spherical deposit.

3.1.2.2 Parameters of the energy deposit

The choice of the ignition parameters E_{ign}, r_0 and τ_{dep} must be compatible with previous conclusions relatively to the choice of these parameters and their influence on MIE prediction are described in the following.

Energy density $D = E_{ign}/r_0^3$. The energy density governs the temperature in the ignition zone and must be limited to verify hypothesis 1. is no more verified. Practically, thermodynamics and kinetics of reduced schemes are valid only for a range of temperature that is generally close to 2000 K. Such temperatures correspond to a low energy density which is not representative of the physical energy deposit of the breakdown. These are the reasons why in most ignition studies using an energy deposit model, temperature observed in simulations can exceed 2000 K, some even reaching 8000 K (Wang and Sibulkin, 1993). The present study follows this path. However, to account for the fact that at high temperature the molecular diffusivity μ and the thermal conductivity λ are not well predicted by standard laws such as the Sutherland's law, a high temperature law is used: D'Angola law (Capitelli et al., 2001). In that case, coefficient μ is given by:

$$\log(\mu) = \log\left(\xi_0(T) + \sum_{j=1}^{5} a_j\sigma_j(T)\right) + \sum_{j=6}^{10} a_j\sigma_j(T) \tag{3.1}$$

where $\xi_0(T)$ and $\sigma_j(T)$ are function of the temperature T. Fourier coefficient λ is given by:

$$\log(\lambda) = a_0 + \sum_{j=1}^{6} a_j\sigma_j \log T + \sum_{j=7}^{10} a_j\gamma_j \log T \tag{3.2}$$

where $\sigma_j(T)$ and $\gamma_j(T)$ are functions of the temperature T.

Deposit radius r_0 Within the range of acceptable energy density values (respecting $T < 8000$ K within the ignition zone), MIE varies with the deposit radius r_0 (Frendi and Sibulkin, 1990; Sloane and Ronney, 1992; Wang and Sibulkin, 1993). For instance, Sloane and Ronney computed the MIE of a stoichiometric methane/air mixture for different deposit radius r_0, using two different simplified kinetics schemes, as shown in Fig. 3.3-right. The authors reported on the same graph results obtained by Frendi and Sibulkin (1990), displayed in Fig. 3.3-left. Finally Fig. 8.4 presents results of Wang and Sibulkin (1993), showing the MIE values they obtained as a function of the deposit radius r_0, for a propane/air mixture.
These results, obtained for different fuels and different kinetic schemes, show a similar trend: above a critical value of the deposit radius denoted $r_{0,crit}$, MIE increases with the volume of the energy deposit. For smaller radii ($r_0 < r_{0,crit}$), then MIE seems to be quasi-constant.

Deposit duration τ_{dep}. Frendi and Sibulkin (1990) and more recently Han et al. (2010) characterized the influence of the deposit duration τ_{dep} on MIE, when using a model of energy deposit. Frendi and Sibulkin (1990) determined the MIE of a stoichiometric methane/air mixture for different values of deposit duration τ_{dep}, keeping the value of the deposit radius r_0 constant, and using a one-step chemistry. Authors used two different sets of conservation equations in 1D spherical coordinates:

- (i) a set denoted *constant pressure model* where the pressure p is set constant and uniform.
- (ii) a set denoted *variable pressure model* corresponding to the classical balance equations described in 1.1.1.

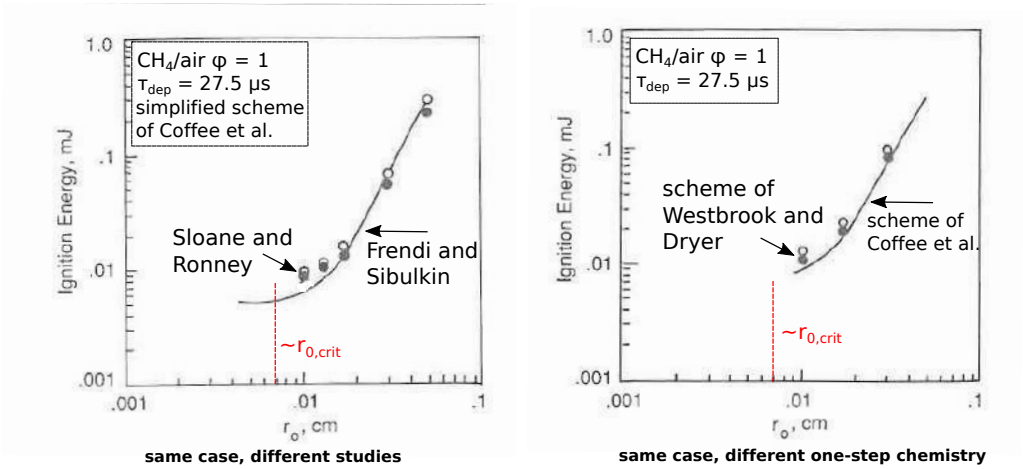

Figure 3.3: Figures from Sloane and Ronney (1992): MIE as a function of the energy deposit radius r_0. Atmospheric conditions. Filled symbols correspond to successful ignition and open symbols correspond to unsuccessful ignition. Left: symbols: results of Sloane and Ronney, solid line: results of Frendi and Sibulkin (1990). Right: results of Sloane and Ronney, using two different one-step kinetic scheme.

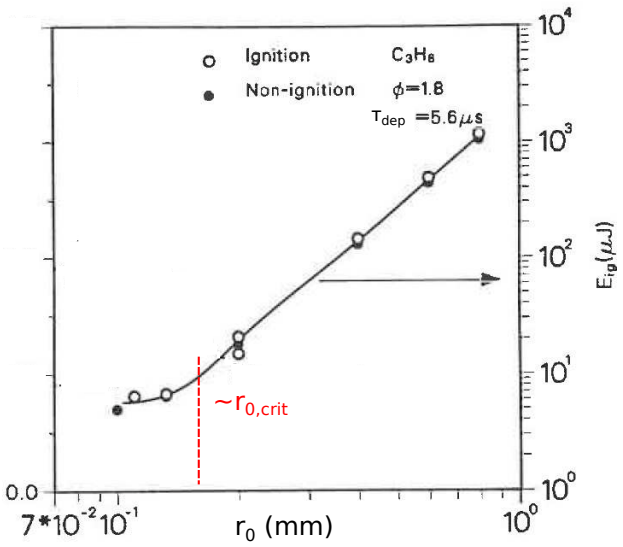

Figure 3.4: MIE as a function of the energy deposit radius r_0, according to Wang and Sibulkin (1993). Atmospheric conditions. Kinetic scheme: Jones and Lindstedt (1988).

The results of the calculations of Frendi and Sibulkin are presented in Fig. 3.5: values of MIE obtained using the *constant pressure model* and the *variable pressure model* are displayed against the deposit duration τ_{dep}, showing that:

- when $\tau_{dep} < \tau_1$, with $\tau_1 \sim 2\ \mu s$ as indicated in Fig. 3.5, the MIE predicted by the *variable pressure model* is larger than the MIE predicted by the *constant pressure model*, while when $\tau_{dep} > \tau_1$, both models predict similar values. This is due to the fact that when the power density becomes important enough (corresponding in that case to a duration $\tau_{dep} < 2\ \mu s$), a significant pressure wave is formed, dissipating a part of the deposited energy E_{ign}. Accordingly,

the temperature reached in the ignition zone using the *variable pressure model* is lower than the one obtained using the *constant pressure model*. Therefore, more energy is required to ignite with the *variable pressure model*.

- When $\tau_{dep} > \tau_1$, both models predict similar MIE values: as the power density becomes less important, the pressure rise is not significant anymore. The totality of the deposited energy E_{ign} remains in form of a thermal heat, both for the *constant pressure model* and for the *variable pressure model*. Note that the time τ_1 found by the authors is consistent with the characteristic time of the pressure wave propagation observed in experimental studies (Kono et al., 1989; Bradley et al., 2004).

- when $\tau_{dep} > \tau_2$, with $\tau_2 \sim 100\ \mu s$, MIE increases with τ_{dep}. Authors explain this finding by a more important contribution of the diffusion heat losses which can compete with the heat release during the energy deposit. Accordingly, more energy must be deposited to ignite.

According to these observations, to respect hypothesis 2 (pressure wave propagation is not accounted for), the deposit duration should be chosen longer than 5 μs. Also, when modeling a short-duration spark ignition, the deposit duration should be shorter than 100 μs because otherwise diffusion effects during the energy deposit phase become significant, which is not representative of a physical ignition.

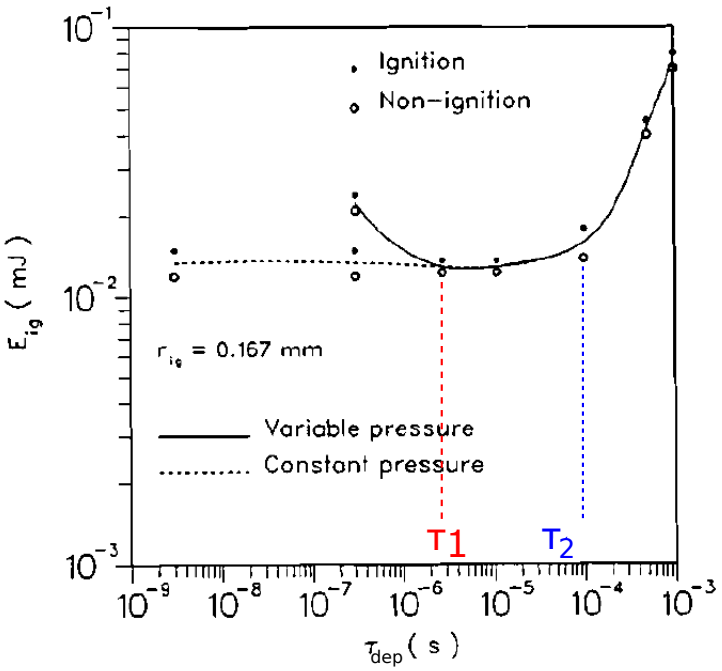

Figure 3.5: Minimum ignition energy (line) as a function of the deposit duration τ_{dep}, using the *variable pressure model* (plain line) and the *constant pressure model* (dashed line). Filled symbols correspond to successful ignition and open symbols correspond to unsuccessful ignition. Stoichiometric methane/air mixture. Figure from Frendi and Sibulkin (1990).

3.1.2.3 Choice of the kinetics

Simplified schemes recovering the laminar flame speed over a certain range of conditions cannot accurately describe other phenomena, in particular auto-ignition, curvature effects or differential diffusion effects. Besides radicals and intermediate species are not described. Simplified schemes may be therefore insufficient to describe ignition.
To evidence this aspect, Sloane and Ronney (1992) determined the MIE of a stoichiometric methane/air mixture using a detailed mechanism and compared the values to the ones obtained using a simplified scheme. Results are displayed in Fig. 3.6. Discrepancies of MIE prediction vary according to the size of the energy deposit r_0: when the deposit radius is smaller than a certain value ($r_0 < 0.3\ mm$), the MIE predicted using simplified chemistry is 20 times smaller than the MIE predicted using detailed chemistry, while for larger deposit radii ($r_0 > 0.3\ mm$), MIE values obtained using the simplified and detailed chemistry are of the same order of magnitude. Sloane and Ronney explain these observations as follows:

- when $r_0 < 0.3\ mm$, the characteristic diffusion time τ_{diff}, defined as $\tau_{diff} = r_0^2/D_{therm}$, is small enough for diffusive heat losses to compete with the heat released by the combustion reactions *during the energy deposit*. When this competition occurs, if the heat release is not significant enough to balance the decrease of the temperature due to heat losses *during the energy deposit*, then no ignition takes place. Because the detailed scheme describes the formation of a thermal radicals pool, the temperature observed during the ignition using detailed chemistry is much lower that the temperature during ignition obtained using the simplified scheme, which is exothermic: see Fig. 3.7, comparing radial profiles of temperature during the energy deposit for a given set of parameters (E_{ign}, r_0, τ_{dep}), for the detailed chemistry (right) and the simplified chemistry (left). From there, authors conclude that more energy is required to successfully ignite using the detailed kinetic scheme. The description of radicals in the detailed scheme results in the high discrepancy between the auto-ignition delay τ_{ai} of the detailed scheme and the ones of the simplified scheme, as evidenced in Table 3.1.

- when $r_0 > 0.3\ mm$, that is for larger energy deposit, the characteristic diffusion time τ_{diff} is longer. Accordingly, authors conclude that there is no competition between the heat diffusion and the heat release during the energy deposit phase and both kinetic mechanisms predict the same order of magnitude of MIE, even though auto-ignition delays are very different.

Based on their analysis, Sloane and Ronney recommend to use kinetic schemes predicting both the correct laminar flame speed and auto-ignition delays. As explained, detailed kinetics cannot be used to describe ignition in complex configurations (section 1.1.5). However the recent category of analytical schemes corresponds to the above prescription of Sloane and Ronney, as these schemes can reproduce both the correct laminar flame speed and auto-ignition delays, over a certain range of pressure, temperature and equivalence ratio conditions, while keeping affordable CPU costs. These conclusions motivated the choice to compare a simplified and an analytical scheme in the ignition study.

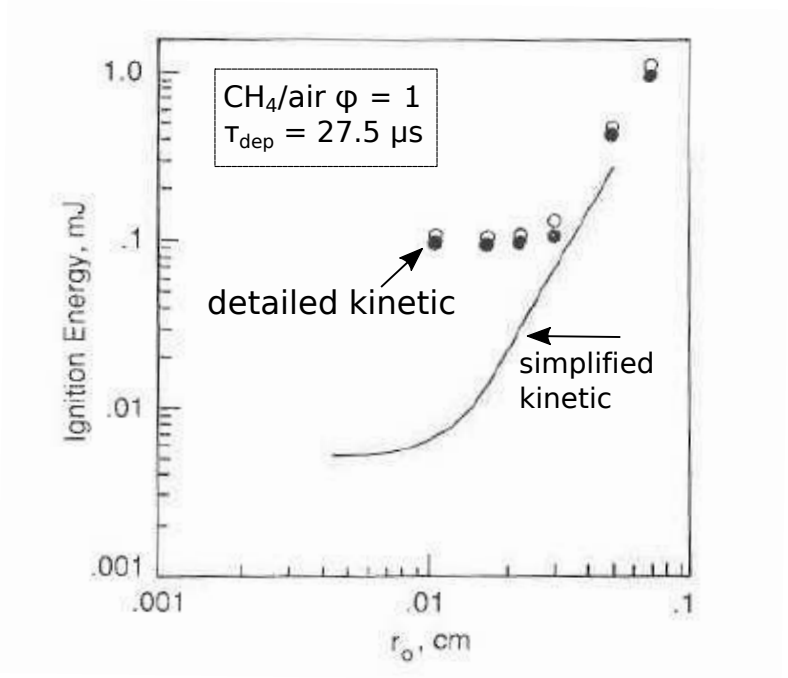

Figure 3.6: MIE as a function of the energy deposit radius r_0. Open circles: ignition occurred, filled circles: ignition did not occur. Symbols: results obtained by Sloane and Ronney (1992) using the detailed kinetic scheme of Sloane (1989). Solid line: results of Frendi and Sibulkin (1990) using the simplified kinetic scheme of Coffee et al. (1983)

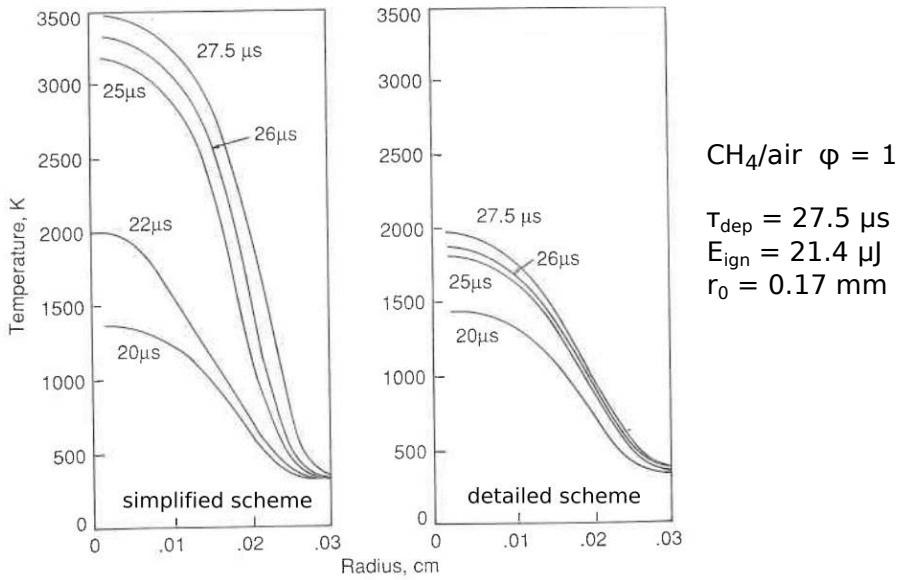

Figure 3.7: Temperature as a function of the radial coordinate r, at different instants of the energy deposit. Left: Simplified kinetic scheme of Coffee et al. (1983) (leading to successful ignition). Right: detailed kinetic scheme of Sloane (1989) (leading to ignition failure). Same ignition parameters in both cases. Study of Sloane and Ronney (1992).

	Auto-ignition delays τ_{ai} (μs) for $\phi = 1$		
Kinetic scheme	$T_i = 2222\ K$	$T_i = 2000\ K$	$T_i = 1500\ K$
Detailed	18.9	54.9	1500
Simplified	0.17	0.18	1.1

Table 3.1: Auto-ignition delays calculated in Sloane and Ronney (1992) for the detailed kinetic scheme of Sloane (1989) and the simplified kinetic scheme of Coffee et al. (1983) .

3.2 Modeling spark plug ignition with LES

Following sections present the actual LES ignition models of the FSD and TF-LES approaches.

3.2.1 Introduction to the LES ignition modeling

Figure 3.8 recalls the chain of the main physical events related to the spark formation which are not accounted for or modeled in LES, stressing out the difficulty to relate the input energy E_{ign} to the available experimental data (energy of the ignition device E_{device}). The exact locations and time distribution of the energy E_{ign} cannot be provided with details to the LES. But it will be shown in section 3.2.2 that E_{ign} can nevertheless be estimated from E_{device} using a 0D model, and also how the energy E_{ign} can be distributed in time with reasonable approximations. Then, sections 3.2.3 and 3.2.4 explain how, from the knowledge of $E_{ign}(t)$, combustion can be initiated and the flame kernel growth is predicted, using respectively the FSD approach and the TF-LES approach. It will be explained in particular that, the initial flame kernel being very small (in fact, smaller than the combustion filter size Δ or than the thickened laminar flame thickness $F\delta_L$), a specific treatment of the reaction rate is required, until the kernel has reached a certain size. Pros and cons of each approach will be discussed and the need of improving the modeling tools of ignition justified.

3.2.2 Estimation of the energy E_{ign}

Laser-induced spark ignition case As explained in section 2.2, an important part of the energy deposited during the breakdown is lost by the propagation of the shock wave ($\approx 85\%$ according to Bradley et al. (2004)). Therefore, the energy E_{ign} is usually estimated as 15% of the energy of the Laser E_{device}.

Spark plug ignition case In that case, a model of electrical circuit, such as the one proposed by Duclos and Colin (2001) is used to predict $E_{ign}(t)$. The electrical ignition circuit of the model is presented in Fig. 3.9. The inputs of the model are: the secondary inductance L_s, the secondary resistance R_s and the energy stored in the secondary inductance E_s. Experiments providing only the primary inductance value L_p, E_s is usually estimated following Verhoeven (1997) as

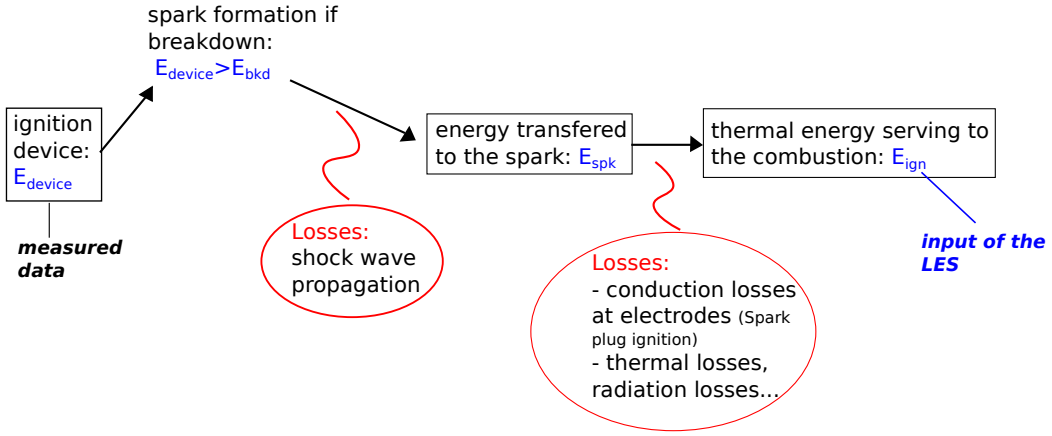

Figure 3.8: Sketch illustrating the chain of events, from the energy deposited by the ignition device (E_{device}) to the thermal energy input used in the LES (E_{ign}. Spark plug ignition case.)

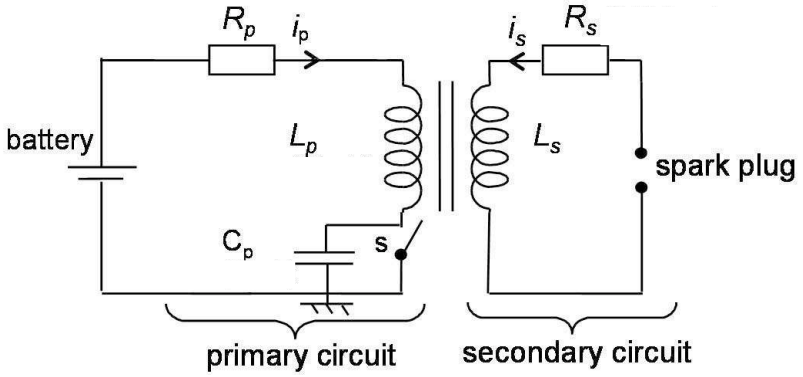

Figure 3.9: Simplified electrical ignition circuit of the AKTIM model. Figure from Truffin (2006).

$E_s = 0.6E_{mag,prim}$, where $E_{mag,prim}$ is the energy stored in the primary inductance given by $E_{mag,prim} = 1/2L_p i_p^2$. L_p is the primary inductance and i_p the primary current, which can be determined by experimental measurements. Then, the electrical circuit model predicts the temporal distribution of the thermal energy transferred to the gas $E_{ign}(t)$ during the spark plug ignition. 2 stages may be distinguished:

1. A first stage accounts for the voltage rise to the breakdown voltage V_{bd}. The voltage rise in the simulation lasts a few μs. V_{bd} is calculated using Pashen's law (Reinmann and Saitzkoff, 1998). If the voltage reaches V_{bd}, then a spark is formed and the energy released by the breakdown E_{bd} is estimated according to:

$$E_{bd} = \frac{1}{2} c_p V_{bd}^2 \tag{3.3}$$

where c_p is a capacity extrapolated from experimental measurements of E_{bd} and V_{bd}.

2. A second stage predicts the energy transfer during the glow phase. During

this phase, the total fall voltage between the electrodes can be written such as:

$$V_{spk}(t) = V_{cf} + V_{af} + V_{gc}(t) \tag{3.4}$$

V_{cf} and V_{af} are the cathode and anode voltage falls given by Kim and Anderson (1995). V_{gc} is the voltage in the gas column along the spark path and it is given, according to Kim and Anderson by:

$$V_{gc} = c_1 l_{spk} i_s^{c_2} p^{c_3} \tag{3.5}$$

l_{spk} is the spark length, i_s the current in the secondary circuit and p the average pressure in the vicinity of the spark channel. c_1, c_2 and c_3 are model constants. The secondary current i_s is calculated from:

$$i_s = \sqrt{\frac{2E_s}{L_s}} \tag{3.6}$$

E_s is the electrical energy of the secondary circuit, calculated according the classical law:

$$\frac{dE_s(t)}{dt} = -R_s i_s^2(t) - V_{spk} i_s(t) \tag{3.7}$$

The first right-hand side term represents the dissipation of electrical energy by Joule effect, where R_s is the secondary circuit total resistance. The second term represents the dissipation of energy between the electrodes.
The spark lasts until $E_s(t) = 0$.

Finally, the energy $E_{ign}(t)$ which serves to combustion is given by:

1. At spark timing (denoted t_{spk}), when the voltage V reaches the breakdown value V_{bd}, the input ignition energy E_{ign} is estimated from the breakdown energy E_{bd} such as (Verhoeven, 1997):

$$E_{ign} = 0.6 E_{bd} \tag{3.8}$$

The 0.6 factor accounts for losses during the breakdown and the arc phase, including losses to electrodes by conduction, by the pressure wave and by radiation.

2. During the glow phase, E_{ign} is estimated according to (Verhoeven, 1997):

$$\frac{dE_{ign}(t)}{dt} = V_{gc} i_s(t) \exp\left(-\frac{d}{2l_{spk}}\right) \tag{3.9}$$

d represents the diameter of the electrode. The exponential term accounts for the thermal losses of the arc at the electrodes. These losses increase with the diameter d of the electrode and decrease with the elongation of the arc.

3.2.3 Ignition modeling with the FSD approach

In the FSD approach, the flame surface needs to be initialized, practically by a deposit of burned gases. Then, the flame kernel is filtered with a combustion filter

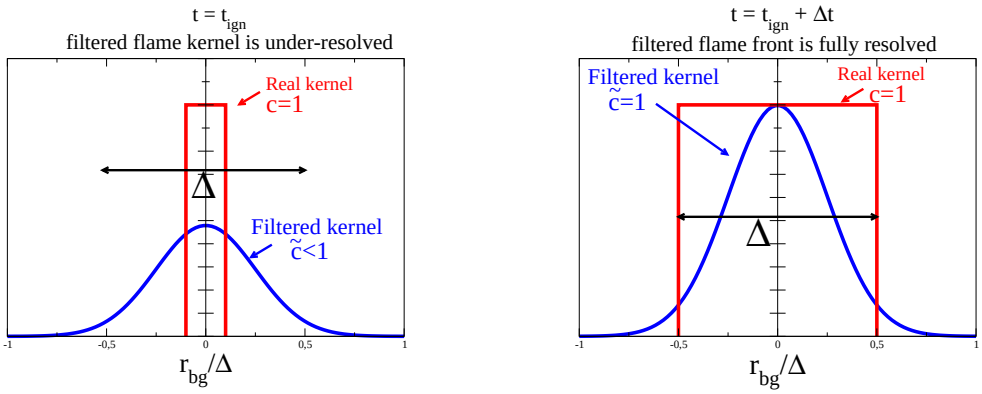

Figure 3.10: scheme of the real flame kernel and of the filtered flame kernel at ignition time t_{ign} (left) and at the transition time to the fully established filtered flame front $t_{ign} + \Delta t$ (right)

of size Δ (section 1.3.1.2). The burned gases radius r_{bg} of the flame kernel of volume V_{bg} is introduced and defined by:

$$V_{bg} = \frac{4}{3}\pi r_{bg}^3 = \int_\Omega \overline{c}\ dV \tag{3.10}$$

If the burned gases radius r_{bg} of the initial real flame kernel is smaller than the combustion filter width ($r_{bg} < \Delta$), then $\tilde{c}(t) < 1$, as illustrated in Fig. 3.10-left. Accordingly, the flame front is not fully established at scale Δ and the flame surface $\overline{\Sigma}$ entering the reaction rate cannot be estimated using the standard propagation models presented in section 1.3.1: the gradient based definition $\overline{\Sigma} = \Xi_\Delta |\nabla \overline{c}|$ cannot be used). Specific models are required, denoted *ignition model*, such as the AKTIMeuler model proposed by Richard et al. (2007) or the transport equation ISSIM model proposed by Colin and Truffin (2011). These LES combustion submodels are called *ignition models* in the sense that they provide a closure for the reaction rate during the early instants of the kernel development, that is until the filtered flame front is fully established at scale Δ, corresponding to the condition: $max(\tilde{c})(t) = 1$ (instant $t_{ign} + \Delta t$ in Fig. 3.10-right). This means that when using the FSD approach to predict ignition, 3 stages of modeling are required:

1. **Stage 1** Estimation of the energy E_{ign} that serves to combustion (see previous section 3.2.2).

2. **Stage 2** Deposit of initial burned gases, according to 0D criteria, described in section 3.2.3.1.

3. **Stage 3** Growth of the flame kernel modeled by the AKTIMeuler or the ISSIM model, until the flame kernel has a size close to the combustion filter size Δ. (The size Δ can be much larger than the critical size of the flame kernel defined in Chapter 2, section 2.3.1), described in section 3.2.3.2.

3.2.3.1 Deposit of the initial burned gases

The flame kernel is initialized by an instantaneous deposit of burned gases, when $E_{ign}(t)$ (predicted by the electrical circuit model presented in section 3.2.2) reaches

a critical value, denoted $E_{crit}(t)$. The corresponding timing is denoted t_{ign}, such as $E_{ign}(t_{ign}) = E_{crit}(t_{ign})$, where $E_{crit}(t)$ is given following the studies of Adelman (1981):

$$E_{crit}(t) = \frac{\gamma}{\gamma - 1} l_{spk}(t) p(t) \pi \delta_L^2 \tag{3.11}$$

Note that this expression is very similar to expression (2.3) proposed by Ballal and Lefebvre (1974), representing the energy required to heat and expand the kernel to the critical radius. Adelman assumes that the kernel has a cylindrical shape of length l_{spk}, instead of a spherical shape.
When criterion (3.11) is satisfied (instant t_{ign}) a mass of burned gases m_{bg}^{ign} is deposited in the vicinity of the spark plug, in the critical ignition cylinder of radius δ_L and of length l_{spk}, such as:

$$m_{bg}^{ign} = \langle \rho^u l_{spk} 4\pi \delta_L^2 \rangle \tag{3.12}$$

Brackets $<\quad>$ refers to an average in the spark plug vicinity. From the initial burned gases mass m_{bg}^{ign}, an initial burned gases volume is deduced. Its initial radius is denoted r_{ign} and is chosen in practice close to Δ. The initial $\overline{c}_{ign}$ profile is then determined, according to:

$$\overline{c}_{ign}(x, t_{ign}) = c_0 \exp\left(-\left(\frac{\mathbf{x} - \mathbf{x}_{spk}}{0.6\Delta}\right)^2\right) \tag{3.13}$$

The form of the initial $\overline{c}_{ign}$ profil is chosen so that the gradient of $\overline{c}$ is not too stiff, to enable a correct numerical resolution. The initial profile thickness is in practice close to the combustion filter Δ. c_0 is calculated to verify:

$$\int_\Omega \rho_b \overline{c}_{ign} \, dV = m_{bg}^{ign} \tag{3.14}$$

3.2.3.2 Growth of the flame kernel by AKTIM and ISSIM models

AKTIMEuler ignition model: it is is based on a 0D concept. During the ignition period, the reaction rate $\overline{\dot{\omega}}_{c,ign}$ is written using an algebraic closure similar to the one used in the algebraic model of Boger et al.:

$$\overline{\dot{\omega}}_{c,ign} = \rho^u s_L \Xi_{ign} \alpha_A \tilde{c}(1 - \tilde{c}) \tag{3.15}$$

The coefficient α_A is determined so that the total laminar flame surface equals the laminar flame surface S_m (Eq. 3.17). To account for the sgs wrinkling, the final reaction rate expression includes a wrinkling factor Ξ_{ign} that needs to be defined. Some definitions are first introduced. S_m, surface of the equivalent sphere of radius r_{bg} is given by:

$$S_m = 4\pi r_{\mathrm{bg}}^2 \tag{3.16}$$

The following condition on α can be now introduced, that imposes the filtered flame kernel to grow as the equivalent spherical flame kernel :

$$\int_\Omega \alpha_A \tilde{c}(1 - \tilde{c}) \mathrm{d}V = S_m \tag{3.17}$$

It is assumed during the kernel growth that, although the flame kernel is wrinkled by turbulence structures, a global spherical shape is kept. This assumption is valid

only for short electrical arcs, as in Fig. 2.8. For long electrical arcs, as in Fig. 2.7, this simplified approach is not adapted.
The global wrinkling Ξ_{ign} is illustrated in Fig. 3.11 and defined such as:

$$S_{tot} = S_m \Xi_{ign} \tag{3.18}$$

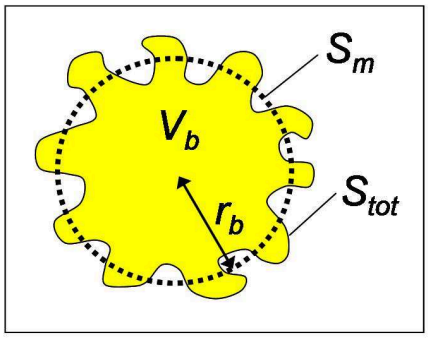

Figure 3.11: sketch illustrating the wrinkled flame kernel, showing S_{tot} (plain line), S_m (dotted line). Richard (2005).

During the ignition phase, the wrinkling Ξ_{ign} is separated in a resolved wrinkling contribution Ξ_{res}, corresponding to the wrinkling of the resolved flame front, and a sub-grid contribution Ξ_{sgs}, corresponding to the wrinkling information lost by to the filtering operation:

$$\Xi_{ign} = \Xi_{res} \Xi_{sgs} \tag{3.19}$$

Ξ_{res} is calculated based on the resolved front information and Ξ_{sgs} follows a 0D transport equation, details may be found in Richard (2005); Richard et al. (2007).

The AKTIMeuler ignition model presents some drawbacks to describe complex ignition cases. In the case of long electrical arcs, the flame is not spherical and the approach cannot correctly estimate the growth of the flame kernel. Besides, the 0D description of the sub-grid wrinkling can only be applied to moderate wrinkling situations. Finally, the AKTIMeuler model cannot describe multi-sparks ignition because the kernel growth rate is based on integral quantities. The ISSIM model (Colin and Truffin, 2011), using a transport equation, enables to describe the growth of the flame kernel in multi-spark ignition and to improve the description of turbulent ignition, thus solving a part of the modeling issues of the AKTIMeuler model.

ISSIM ignition model The reaction rate of the progress variable is modified according to:

$$\overline{\dot{\omega}}_c = \max\left(\rho^u s_L \overline{\Sigma}, \rho_b \frac{\overline{c}_{ign} - \overline{c}}{dt}\right) \tag{3.20}$$

where dt is the time-step of the computation. With this closure, the value $\overline{c}_{ign}$ (corresponding to the mass of burned gases m_{bg}^{ign} deposited) can be imposed and pre-existing flame kernels are also accounted for (via the term $\rho^u s_L \overline{\Sigma}$). To describe

the formation of a new flame kernel, a source term $\overline{\dot{\omega}}^{ign}_{\Sigma}$ is added in the FSD balance equation (1.61), defined such as:

$$\overline{\dot{\omega}}^{ign}_{\Sigma} = \max\left(\frac{\Sigma_{ign} - \overline{\Sigma}}{dt}, 0\right) \tag{3.21}$$

where Σ_{ign} recovers the surface of the equivalent sphere containing the volume of deposited burned gases m^{ign}_{bg}.
Because the flame front is not fully established during ignition (e.g. $max(\tilde{c}) < 1$), the resolved contribution $C_{res} + S_{res} + P_{res}$ in the FSD transport Eq. (1.61), as formulated respectively in Eqs. (1.65), (1.62) and (1.64), is not correct and must be modified. To do so, the flame kernel is locally assumed as a sphere of radius r_b and of surface $S_{tot} = 4\pi(r_b)^2\Xi_{\Delta}$. Then, the rate of growth of the local sphere of radius r_b is given by:

$$\frac{dr_b}{dt} = (1+\tau)\Xi_{\Delta}s_L \tag{3.22}$$

where τ is the expansion ratio ($\tau = \rho^u/\rho^b - 1$). Replacing S_{tot} in Eq. (3.22) gives:

$$\frac{1}{S_{tot}}\frac{dS_{tot}}{dt} = \underbrace{\frac{1}{\Xi_{\Delta}}\frac{d\Xi_{\Delta}}{dt}}_{turbulent\ \ stretch} + \underbrace{\frac{2}{r_b}(1+\tau)\Xi_{\Delta}s_L}_{curvature\ \ stretch}. \tag{3.23}$$

In Eq. (3.23), the turbulent stretch term is already modeled by terms $C_{sgs} + S_{sgs}$ in the FSD transport equation (1.61). The stretch term due to curvature must be then added in the FSD transport equation. Accordingly, the modified FSD transport equation is written as:

$$\frac{\partial\overline{\Sigma}}{\partial t} = T_{res} + T_{sgs} + S_{sgs} + \alpha C_{sgs} + \alpha P_{res} + \alpha(C_{res} + S_{res}) + (1-\alpha)\frac{2}{r_b}(1+\tau)\Xi_{\Delta}s_L + \overline{\dot{\omega}^{ign}_{\Sigma}} \tag{3.24}$$

Coefficient α tracks the instant when the flame front becomes established at scale Δ: α becomes equal to unity when $max(\tilde{c})$ becomes equal to unity. In that case, r_b is close to Δ (see Fig. 3.10) and α is thus defined according to:

$$\alpha = \frac{1}{2}\left[1 + \tanh\left(\frac{r_b/\Delta - 0.75}{0.15}\right)\right] \tag{3.25}$$

To enable the description of multi-spark ignitions, the radius r_b is not defined by a global relation like in the AKTIMEuler model (see Eq. (3.10)), but via a transport equation. r_b is not directly transported, the quantity ψ is, defined by:

$$\overline{\rho}\Psi = \overline{\rho}\tilde{c}\frac{2}{r_b} \tag{3.26}$$

The balance equation for Ψ reads (see Colin and Truffin (2011) for details):

$$\overline{\rho}\frac{\partial\Psi}{\partial t} = -\nabla.(\overline{\rho}\tilde{\mathbf{u}}\Psi) + \nabla.\left(\frac{\sigma_c\nu_{t,\Delta}}{Sc_t}\nabla\Psi\right) - (1+\tau)\frac{1}{r_b}\Xi_{\Delta}s_L\overline{\rho}\Psi + \frac{2}{r_b}\overline{\dot{\omega}_c} + \overline{\dot{\omega}}^{ign}_{\Psi} \tag{3.27}$$

In Eq. (3.27), the source term $\overline{\dot{\omega}}_{\Psi}^{ign}$ accounts for the creation of the flame kernel, which formulation is similar as in Eq. (3.21) and is given by:

$$\overline{\dot{\omega}}_{\Psi}^{ign} = \max\left(\frac{2\rho_b/(\overline{\rho}r_b)\overline{c}_{ign} - \overline{\rho}\Psi}{dt}, 0\right) \tag{3.28}$$

To close the sgs wrinkling factor Ξ_{Δ},Colin and Truffin (2011) first assumed a moderately wrinkled kernel and hence $\Xi_{\Delta} = 1$. Robert et al. (2015) proposed an expression for Ξ_{Δ} accounting for higher turbulence cases. But describing with accuracy the evolution of the wrinkling during the ignition phase with high turbulence intensity remains very delicate. However, the use of the transport equation (3.27) leads to major improvements:

- Multi-spark ignition (for instance in case of restrike or multi-spark ignition devices) for which multi-flame kernel are formed, can be described.

- An initial wrinkling can be accounted for: for instance, in the case of long duration and long electric arc cases, the initial flame kernel not being spherical but having a cylindrical shape, an initial wrinkling, corresponding to a form factor, can be then introduced.

3.2.3.3 Conclusions on flame surface density ignition models

In this section, limitations of the flame surface density approach to predict critical ignition cases (lean equivalence ratio, high turbulence intensity, inhomogeneous mixtures) are stressed out.
The kernel growth in high intensity turbulence cannot be well described because of the local sphericity assumption and because of the delicate closure of the sgs wrinkling. Besides, a very important limitation for the ignition prediction, if not the most important, concerns the deposit of the initial burned gases (section 3.2.3). The correlation of Adelman (3.11) is clearly not sufficient to predict with accuracy if ignition takes place or not. Main reasons are listed below:

- Even if the notion of critical ignition volume was investigated in numerous studies and even if the minimum ignition energy was found to vary with the laminar flame thickness, the exact relation between critical ignition energy and laminar flame thickness is uncertain. Besides, 0D correlations are based on the planar laminar flame thickness δ_L although during ignition the flame front is not established. Accordingly, the correlation of Adelman (3.11) (or any similar 0D criterion) can reproduce the correct trend regarding the variation of the equivalence ratio, but it cannot be quantitative.

- The flame kernel is assumed cylindrical, therefore the criterion does not account for the possible elongation of the arc by the flow.

- Effects of turbulence - even without considering the effect of the elongation of the arc, see the description of the ignition regimes in section 2.3.2) - on the estimation of ignition energy are not accounted for, since the Adelman criterion is based on laminar ignition considerations.

- In the case of a direct injection engine, the local equivalence ratio may vary a lot in the vicinity of the spark plug. Ignition does not take place everywhere as assumed in the above models but at certain locations favorable to ignition (Dahms et al., 2009). This behavior cannot be captured by the correlation because only homogenous mixtures are considered.

- The mass of deposited burned gases is also based on a correlation (see Eq. (3.12)), so that there is no physical relation between the ignition energy and the amount of burned gases.

All these reasons explain why, to simulate complex ignition cases a kinetic approach (such as the class 3 of DNS described in section 3.1.2 or the ignition model of the TF-LES approach described in next section 3.2.4) should be preferred. Effects of lean equivalence ratio, high turbulence intensity, two-phase flow on the ignition can be directly accounted for, since the reaction rate is closed using Arrhenius laws.

3.2.4 Ignition modeling with the TF-LES approach: Energy Deposit model

In the Energy Deposit (ED) model proposed by Lacaze et al. (2009), ignition is exactly modeled as in the DNS class 3 (see section 3.1.2): a heat source term $\dot{Q}_{ign}(\mathbf{X}, t)$ is added in the energy equation. Until the flame kernel reaches a certain size, the thickening factor F is set equal to unity, e.g. the flame front is fully resolved, which implies to use a mesh with the appropriate resolution. A strategy was proposed by Thobois (2006) and used by Enaux et al. (2011); Granet et al. (2012) in SI engine configurations, determining when the thickening factor could be activated.

3.2.4.1 Formulation of the heat source term $\dot{Q}_{ign}(\mathbf{X}, t)$

Laser-induced spark ignition case The Energy Deposit model was originally dedicated to simulate Laser-induced spark ignition. Lacaze et al. (2009) write a volumetric Gaussian source term in space and time such as:

$$\dot{Q}_{ign}(\mathbf{X}, t) = \frac{E_{ign}}{4\pi^2\sigma_r^3\sigma_t}\exp\left(-\frac{1}{2}\left(\frac{r-\mathbf{X}_0}{\sigma_r}\right)^2\right)\exp\left(-\frac{1}{2}\left(\frac{t-t_0}{\sigma_t}\right)^2\right) \tag{3.29}$$

where E_{ign} is the total amount of deposited energy, $\mathbf{X}_0$ the coordinates vector of the center of the deposit, t_0 the initial timing of the deposit. σ_r and σ_t control the size and the duration of the deposit, as introduced by Lacaze et al.:

$$\sigma_r = \frac{r_0}{2\sqrt{\ln(10)}} \tag{3.30}$$

and

$$\sigma_t = \frac{\tau_{dep}}{4\sqrt{\ln(10)}} \tag{3.31}$$

r_0 is the radius and τ_{dep} the duration of the deposit. The constant $4\sqrt{\ln(10)}$ ensures that 99% of the input energy E_{ign} is deposited in a duration τ_{dep} and in a zone of width d_0.

Adaptations of the ED model to spark plug ignition cases The ED model was coupled to the electrical circuit model described in section 3.2.2 (Truffin, 2006). In this case $\dot{Q}(\mathbf{X_0}, t)$ reads:

$$\dot{Q}(\mathbf{X_0}, t) = \frac{E_{ign}(t)}{(2\pi)^{3/2}\sigma_r^3 dt} \exp\left(-\frac{1}{2}\left(\frac{r - \mathbf{X}_0}{\sigma_r}\right)^2\right) \tag{3.32}$$

with dt the time-step of the simulation and $E_{ign}(t)$ given by the electrical circuit model of Duclos and Colin (2001) described in section 3.2.2.

3.2.4.2 Early instants of the growth of the flame kernel

Thickening is not applied in the energy deposit zone and this, until the flame kernel has reached a certain size. Indeed, if the flame kernel were thickened by a factor F, then the MIE would be multiplied at least by F^3 (since MIE would be proportional in that case to $(F\delta_L)^3$ according to Eq. (2.3)). Accordingly, the estimation of the MIE and the size of the initial flame kernel if applying a thickening factor above unity are not physical. It would be recommended to apply the thickening factor only once the flame kernel is self-propagating.
The constraint $F = 1$ implies the use of a very refined mesh satisfying at least $\Delta_x = \delta_L/n_{res}$ in the vicinity of the spark plug, which is today not affordable in SI engines.

3.3 Motivations for the ignition study of Part III

To enable a direct description of ignition, the ED ignition model is used, setting the thickening factor to unity. Indeed in that case combustion initiation and flame kernel growth are predicted by kinetics (directly using Arrhenius laws) and thermal diffusion. There is a direct relation between the amount of deposited energy E_{ign} and the mass of the resulting burned gases. Also, the flame kernel is fully resolved during the growth phase. This is not the case when using the FSD approach (section 3.2.3).
However, using the ED model to predict critical ignition cases (low laminar flame speed, high turbulence intensity) requires additional studies. To our knowledge, no attempts has been done so far to demonstrate the ability of the approach "*model for the spark energy deposit combined to reduced kinetics*" to predict the correct amount of ignition energy in critical conditions (section 3.1.1), nor to capture the transition in the ignition regimes, as evidenced in the experiments of Shy et al. (2008) or Cardin et al. (2013) (see Fig. 2.16 and 2.17). The objective of the present ignition study is therefore to determine the ignition parameters and the type of kinetic mechanisms, enabling an accurate prediction of the ignition energy in the laminar and different turbulent regimes experimentally characterized by Cardin et al.. Even though the study uses Laser-induced spark ignition experimental data, the modeling tools and the conclusions are the same for electric spark ignition cases:

- as pointed out in section 2.2, ignition regimes correspond to an universal phenomenon, which have been observed by different authors, in different configurations, using different ignition devices (Laser and spark plug ignition devices).

- the ED model can be used whether to simulate Laser-induced spark ignitions or very short spark plug ignitions. The spark energy deposit is modeled by a thermal energy deposit, accordingly the nature of the spark (Laser-induced spark or electric spark) is by construction not accounted for in simulations.

The study aims at bringing new elements on the understanding of the modeling of the ignition, considering only a short and localized energy deposit, in a lean premixed mixture. This represents a first step towards the understanding of more complex ignition cases: long duration electric spark, ignition in inhomogeneous mixtures.

Part II

Adaptation and evaluation of a dynamic wrinkling model in SI engines configurations

Introduction to Part II

As explained in section 1.3.5, modeling the sub-grid scale wrinkling factor in spark ignition engines is delicate: algebraic wrinkling closures are not adequate to describe the out-of-equilibrium flame kernel development. These closures are derived under the flame turbulence equilibrium assumption, which is not verified during the transient growth of the flame kernel: possibly quasi laminar during the first instants after spark ignition, the flame kernel is then progressively wrinkled by turbulence as it grows. In recent works (Wang et al., 2011, 2012; Schmitt et al., 2013, 2014; Veynante and Moureau, 2015; Mercier et al., 2015; Hosseinzadeh et al., 2015), a dynamic wrinkling closure, that determines the a priori unknown parameter of algebraic sgs wrinkling closure from the resolved fields, was successful employed to predict the progressive wrinkling of the flame by the turbulence. The method was implemented to be used in complex configurations requiring unstructured meshes and massively parallel calculations. According to these previous results, the dynamic wrinkling model is a promising method to describe the out-of-equilibrium flame development in SI engines configurations. It represents also an interesting alternative to the use of a transport equation for the flame surface density, which sgs closures are delicate to derive and require the adjustment of model parameter according to the level of turbulence intensity. The present part is therefore dedicated to the evaluation of the dynamic wrinkling in a SI engine configuration, as it was never applied so far to this kind of configuration. The specificities of SI engines configurations have revealed unphysical behavior of the dynamic model, requiring modifications prior to its use in such configurations.
This part is therefore organized in two chapters:

- Chapter 4 describes the additional studies and modifications of the dynamic wrinkling model.
- Chapter 5 validates the modified formulation of the dynamic model in the SI engine configuration. Several LES cycles were performed. Results obtained using the modified dynamic model are compared against experimental results and results of reference simulations performed with the ECFM-LES model, that use a transport equation for the flame surface density.

Chapter 4

Formulation of a dynamic wrinkling model adapted to SI engines configurations

Contents

The present study follows the work of Wang et al. (2012), who successfully reproduced the transient growth of the flame kernel in a decaying homogeneous isotropic turbulence, coupling the dynamic wrinkling model to the propagation model of Boger et al. (1998). Section 4.1 presents thus the dynamic wrinkling model as formulated by Wang et al.. Next sections are dedicated to the analysis of the dynamic model on issues specific to SI engines: the coupling of the dynamic wrinkling model with

the ignition model is discussed in section 4.2, the propagation of a laminar spherical flame is analyzed in section 4.3. Section 4.4 deals with the interactions of the flame front with the boundary of the computational domain and finally section 4.5 is dedicated to flame front interactions that occur when the flame is very wrinkled.

4.1 Dynamic wrinkling model of Wang et al. (2012)

Wang et al. (2012) base their study on the dynamic formulation proposed by Charlette et al. (2002b). Wang et al. apply a dynamic procedure on the following fractal closure of the sgs wrinkling (see also Eq.(1.80)):

$$\Xi_\Delta = \left(\frac{\Delta}{\delta_c}\right)^\beta \tag{4.1}$$

where δ_c is the inner cut-off scale of the flame front wrinkling (Gülder and Smallwood, 1995). Following the approach of Germano (1992), the unknown parameter, exponent β, is obtained by calculating in two different manners the reaction rate at a scale larger than the combustion filter scale Δ. To do so, Charlette et al. introduce a *test-filter*, denoted $\widehat{\Delta}$, which size is equal or larger than the combustion filter Δ:

$$\widehat{\Delta} = \alpha_t \Delta \quad \text{with } \alpha_t \geq 1 \tag{4.2}$$

Wang et al. (2012) use a Gaussian filter operator for the test-filtering operation, following the method proposed by Moureau et al. (2011) (see Annexe 9.4). When convoluting filters Δ and $\widehat{\Delta}$, assuming the two filters are Gaussian filtering operators, a Gaussian filtering operator, denoted $\widehat{\Delta}$ (*effective filter*) is obtained:

$$\widehat{\Delta} = \gamma\Delta = \sqrt{\Delta^2 + \widehat{\Delta}^2} \quad \text{with } \gamma \geq 1 \tag{4.3}$$

The following notations are also introduced:

- $\widehat{\overline{q}}$: the Reynolds filtered variable at scale $\widehat{\Delta}$, defined such as: $\widehat{\overline{q}} = \widehat{\overline{q}}$.
- $\widehat{\tilde{q}}$: the Favre filtered variable at scale $\widehat{\Delta}$, defined such as: $\widehat{\overline{\rho}\tilde{q}} = \hat{\overline{\rho}}\hat{\tilde{q}}$.
- $\widehat{Q}$: any Q quantity filtered using the test-filter $\widehat{\Delta}$

The "Germano-like" identity proposed by Charlette et al. expresses that the reaction rate averaged over a given domain (operator <>) is identical when directly estimating the model at the effective scale $\widehat{\Delta}$ (LHS) or by test-filtering the resolved reaction rate (RHS):

$$\left\langle \overline{\dot{\omega}}_{\widehat{\Delta}}(\tilde{\tilde{q}}) \right\rangle = \left\langle \widehat{\overline{\dot{\omega}}_\Delta(\tilde{q})} \right\rangle \tag{4.4}$$

Note that Eq. (4.4) is not locally verified because writing a local identity supposes that the shape of the reaction rate is the same at scale Δ and $\widehat{\Delta}$, which is not the case. Operator <> is a spatial averaging operator. (Practically, the averaging operation is performed using the same method as for the test-filter operation.)

To dynamically determine exponent β, Wang et al. propose to close the reaction rate using the generalized flame surface density (Boger et al., 1998):

$$\overline{\dot{\omega}}_{\Delta}(\tilde{c}) = \rho^u s_L \overline{\Sigma} = \rho^u s_L \Xi_{\Delta} |\nabla \overline{c}| \tag{4.5}$$

Eq. (4.4) is then recast as:

$$\langle \Xi_{\widehat{\Delta}} |\nabla \hat{\tilde{c}}| \rangle = \langle \widetilde{\Xi_{\Delta} |\nabla \overline{c}|} \rangle \tag{4.6}$$

Relation (4.6) recovers $\Xi_{\Delta} = 1 = \Xi_{\widehat{\Delta}}$ for laminar planar flame. This is not the case when using the Boger et al. algebraic expression or the Arrhenius form for the reaction rate, because the shape of the profiles are not conserved in the filtering operations (Wang et al., 2012; Veynante and Moureau, 2015).
Exponent β is finally recast as:

$$\beta \approx \frac{\log\left(\langle \widetilde{|\nabla \tilde{c}|} \rangle / \langle |\nabla \hat{\tilde{c}}| \rangle \right)}{\log(\gamma)} \tag{4.7}$$

The expression of exponent β provided by Eq. (4.7) will be denoted in the following *local formulation*. If averaging over the whole calculation domain, a *global formulation* is obtained for β, which reads in that case:

$$\beta = \frac{\log\left(\int_{\Omega} \widetilde{|\nabla \tilde{c}|} \, \mathrm{dV} / \int_{\Omega} |\nabla \hat{\tilde{c}}| \mathrm{dV} \right)}{\log(\gamma)} \tag{4.8}$$

Using this formulation, the dynamic wrinkling model verifies:

- The wrinkling factor Ξ_{Δ} always above unity: $\Delta > \delta_c$.
- The laminar degenerescence in the planar flame case: the formulation of exponent β (4.7) ensures that a unity wrinkling factor Ξ_{Δ} is recovered because in that case exponent β is equal to zero. Indeed, for 1D flames, operators norm, derivative and test-filter commute, so that Eq. (4.9) leading to $\beta = 0$ is verified:
$$\left| \frac{\partial \hat{\tilde{c}}}{\partial x} \right| = \widetilde{\left| \frac{\partial \tilde{c}}{\partial x} \right|} \tag{4.9}$$
- The degenerescence towards the DNS: then $\Delta \ll \delta_c$ and the sgs wrinkling factor Ξ_{Δ} tends toward unity.

4.2 Coupling of the dynamic wrinkling model with the ignition model

FSD ignition models, AKTIMEuler and ISSIM, were presented in section 3.2.3.2. Note that the ISSIM model is derived for the FSD transport model, therefore it is not adapted for a coupling with the algebraic model of Boger et al.. Only the algebraic

AKTIMEuler ignition model is considered for the coupling with the model of Boger and the dynamic wrinkling model. The coupling between the AKTIMEuler ignition model and the model of Boger et al. was explained in section 3.2.3: the ignition model is used until the filtered progress variable $\tilde{c}$ reaches unity, that is when the flame front is fully established at scale Δ. Then the propagation model of Boger et al. can be used. This coupling condition is modified when using the dynamic wrinkling model (section 4.2.1). Practical consequences of this modifications in SI engine simulations are discussed in section 4.2.2.

4.2.1 Definition of the coupling criterion

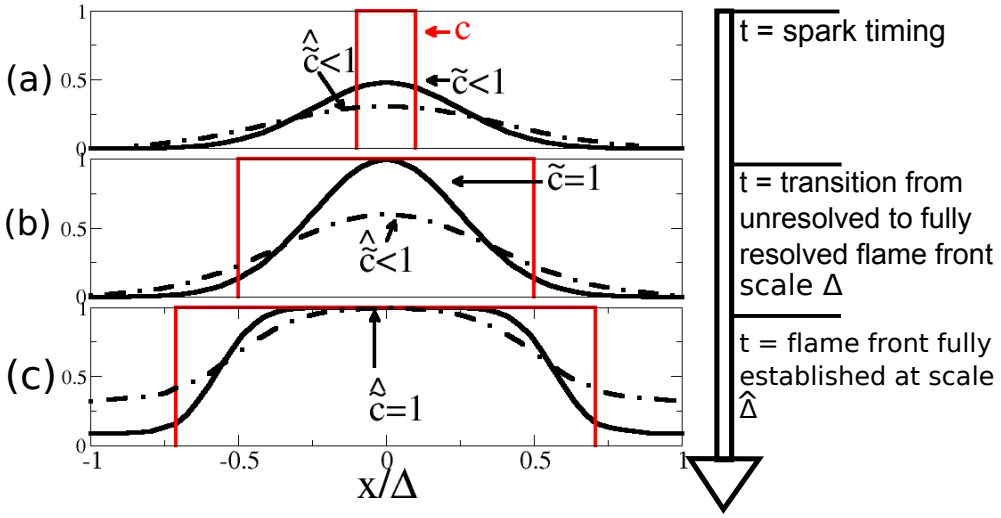

Figure 4.1: sketch of the profil of the progress variable c, $\tilde{c}$ and $\hat{\tilde{c}}$ for three different size of a laminar spherical flame kernel. (a): flame kernel but smaller than the combustion filter size Δ. (b) flame kernel larger than Δ but smaller than the effective filter size $\widehat{\Delta}$. (c) flame kernel larger than the effective filter size.

When using the dynamic wrinkling model, flame surfaces defined at scale $\widehat{\Delta}$, $|\nabla\hat{\tilde{c}}|$ and $\widehat{|\nabla\tilde{c}|}$, must be estimated. Accordingly, gradients based estimations of flame surface at scale $\widehat{\Delta}$ are not valid when $\hat{\tilde{c}} < 1$. This situation corresponds to a filtered spherical flame kernel of size smaller than scale $\widehat{\Delta}$ ($r_{bg} < \widehat{\Delta}$). As an illustration, Fig. 4.1 presents sketches of 1D profils of progress variable c, $\tilde{c}$ and $\hat{\tilde{c}}$ in a laminar spherical flame kernel of different sizes:

- (a) when $r_{bg} < \Delta < \widehat{\Delta}$, corresponding to $\hat{\tilde{c}} < \tilde{c} < 1$: the ignition model is required.
- (b) when $\Delta < r_{bg} < \widehat{\Delta}$, corresponding to $\tilde{c} = 1$ but $\hat{\tilde{c}} < 1$: flame surface $|\nabla\tilde{c}|$ can be correctly estimated but not flame surfaces $|\nabla\hat{\tilde{c}}|$ and $\widehat{|\nabla\tilde{c}|}$. The dynamic procedure cannot be use, the ignition model is still required.
- (c) when $r_{bg} > \widehat{\Delta}$, corresponding to $\hat{\tilde{c}} = 1$, then flame surfaces $|\nabla\hat{\tilde{c}}|$ and $\widehat{|\nabla\tilde{c}|}$ can be correctly estimated and the dynamic procedure can be applied.

Note that when the *local formulation* (Eq. (4.7)) of the dynamic wrinkling model is used, flame surfaces $|\nabla\hat{\tilde{c}}|$ and $\widehat{|\nabla\tilde{c}|}$ are then averaged in a zone of width Δ_{ave}, which corresponds to the width of the local averaging operator $<>$. Accordingly, quantities $<|\nabla\hat{\tilde{c}}|>$ and $<\widehat{|\nabla\tilde{c}|}>$ are not correctly estimated when $<\hat{\tilde{c}}>$ is smaller that unity. Denoting $\widehat{\Delta}_{\text{moy}}$ the resulting filtering scale after applying the test-filter operator $\widehat{\Delta}$ and the averaging operator Δ_{ave}, $\widehat{\Delta}_{\text{moy}}$ can be estimated according to:

$$\widehat{\Delta}_{\text{moy}} = \sqrt{\widehat{\Delta}^2 + \Delta_{\text{ave}}^2} = \Delta\sqrt{\gamma^2 + {\alpha_{ave}}^2} \tag{4.10}$$

Finally, the local dynamic model should be employed only if the flame kernel has an equivalent radius r_{bg} (calculated according to Eq. (3.10)) such as:

$$r_{bg} > \widehat{\Delta}_{\text{moy}} \tag{4.11}$$

For instance with $\Delta_{\text{ave}} = 2\Delta$ and $\widehat{\Delta} = 1.4\Delta$, Eq. (4.11) gives $r_{bg} > 2.45\Delta$, instead of $r_{bg} > \Delta$ when no dynamic procedure is applied (section 3.2.3).

4.2.2 Consequences of the coupling criterion in SI engine configuration

Condition (4.11) causes to extend the phase during which the FSD ignition model must be used: this phase lasts until the flame kernel has reached a size $r_{bg} \sim \widehat{\Delta}_{\text{moy}}$. A timing $t_{trans,dyn}$ may be introduced, that corresponds to the instant in the engine cycle when $r_{bg} \sim \widehat{\Delta}_{\text{moy}}$. When no dynamic procedure is applied, the ignition phase lasts only until $r_{bg} \sim \Delta$ (see Fig. 3.10): the corresponding instant in the engine cycle is denoted t_{trans}, with $t_{trans} < t_{trans,dyn}$. Practical tests in engine configuration have shown that the difference between t_{trans} and $t_{trans,dyn}$ can reach 1-2 CA, which is consequent considering that t_{trans} is usually equal to 2-4 CA and that the ignition phase has a major impact on the global flame development. To extend the ignition phase represents then a major drawback to the use of the dynamic wrinkling model in SI engines.

A solution to this issue consists in refining the mesh in the vicinity of the spark plug. The duration of the ignition phase would be shortened, hence reducing the dependency to the ignition model. Indeed when refining the mesh, then the transition burned gases radius $r_{bg,trans,dyn}$ is decreased and the instant when the dynamic procedure can be applied occurs sooner in the engine cycle. This strategy has a CPU cost, but it is expected that the benefice of using the dynamic method compensates the supplementary CPU cost.

4.3 Propagation of a laminar spherical flame using the dynamic wrinkling model

During the first instants of the flame kernel growth, the flame kernel may not be much wrinkled by turbulence. Accordingly, the dynamic model must predict wrinkling values close to unity when the flame kernel is quasi laminar. The laminar behavior of the dynamic model is verified for the planar flame but was never verified for

the spherical case. This section proposes thus to study the laminar degenerescence in the spherical case. Only the *local formulation* (4.7) is considered: conclusions using the *global formulation* (4.8) are similar but focus is on the *local formulation* which is preferred over the *global formulation* in SI engine configurations. Results of the simulations are analyzed in section 4.3.1, before defining a laminar degenerescence criterion in section 4.3.2.

4.3.1 Simulations: results and analysis

An already established laminar spherical flame is propagated in a 3D domain, using the propagation model of Boger et al. coupled to the dynamic wrinkling model. Parameters of the mixture are gathered in Tab. 4.1, the calculation domain is described in Tab. 4.2 and the parameters of the dynamic model are detailed in Tab. 4.3. The 3D laminar flame is initialized using a profile of the filtered progress variable $\overline{c}$ such as:

$$\overline{c}(r) = \frac{c_0}{2}\left(1 - \tanh\left(\frac{r}{\Delta}\right)\right) \tag{4.12}$$

where c_0 is calculated to recover $r_{bg,ini} = 7.4$ mm (see Eq. (3.10), the value of $r_{bg,ini}$ was chosen in practice to verify $r_{bg,ini} > \widehat{\Delta}$). Finally, surface averaged quantities β_s and $\Xi_{\Delta,s}$ are introduced:

$$\beta_s = \frac{\int_\Omega \beta\overline{\Sigma}\,\mathrm{dV}}{\int_\Omega \overline{\Sigma}\,\mathrm{dV}} \tag{4.13}$$

$$\Xi_{\Delta,s} = \frac{\int_\Omega \Xi_\Delta|\nabla\overline{c}|\,\mathrm{dV}}{\int_\Omega|\nabla\overline{c}|\,\mathrm{dV}} \tag{4.14}$$

Pressure P	Temperature T	Mixture	δ_L (Blint's correlation)
1.10^5 Pa	300 K	propane, $\phi = 1$	0.37 mm

Table 4.1: Mixture parameters

Length of the domain L	Cell size Δ_x	Boundary Conditions (NSCBC method)
60 mm	0.6 mm	outlet type with $P_{boundary} = 1.10^5$ Pa

Table 4.2: Parameters of the calculation domain

To correctly behave in the laminar spherical case, the dynamic procedure must predict a value of exponent β equal to zero, to ensure a wrinkling equal to unity. Unfortunately, simulation results demonstrated that this is not the case.

combustion filter Δ	test-filter $\widehat{\Delta}$	averaging filter Δ_{ave}	δ_c
$\Delta = 7\Delta_x$	Δ	2Δ	$3\delta_L$

Table 4.3: Parameters for the dynamic model

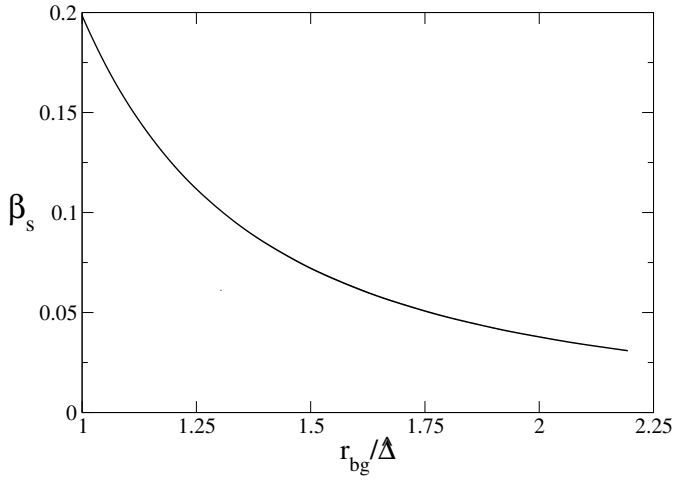

Figure 4.2: Evolution of the surface averaged exponent β_s as a function of $r_{bg}/\widehat{\Delta}$

Figure 4.2 presents the evolution of the surface averaged exponent β_s as a function of the adimensional burned gases radius $r_{bg}/\widehat{\Delta}$. Figure 4.3 presents the radial profil of exponent β in the flame front, at three different timings of the flame kernel growth, corresponding to three different values of the burned gases radius r_{bg}. These results clearly show that exponent β is not equal to zero as it would be required. Also exponent β decreases toward zero as the radius of the flame kernel increases, which suggests that β is governed by the curvature of the flame front. More precisely, curvature effects may be described as follows:

- *global curvature effects:* for a given position within the flame front (for instance position $\tilde{c} = 0.5$, as indicated in Fig. 4.3 by the filled circles), values of exponent β decrease when the burned gases radius r_{bg} increases, that is when the global curvature $curv_g = 2/r_{bg}$ decreases. This is also evidenced in Fig. 4.2: the surface averaged exponent β_s decreases as the global curvature $curv_g$ decreases. For small values of the global curvature $curv_g < 1/\widehat{\Delta}$ - that is when the spherical flame tends towards the planar flame -, β becomes very close to zero ($\beta < 0.03$), which is consistent with the fact that the dynamic model correctly degenerates for the planar flame. $\beta < 0.03$ corresponds to $\Xi_\Delta = 1.05$ at atmospheric conditions and $\Xi_\Delta = 1.15$ at engine conditions (the ratio Δ/δ_c entering the expression of the wrinkling changes with the laminar flame thickness). This value of exponent β can therefore be considered as an acceptable maximum value for a laminar flame. This leads to the conclusion that the dynamic model can predict a laminar spherical flame only for $r_{bg} > 2\widehat{\Delta}$ approximately.

- *local curvature effects:* for a given value of the burned gases radius r_{bg}, values

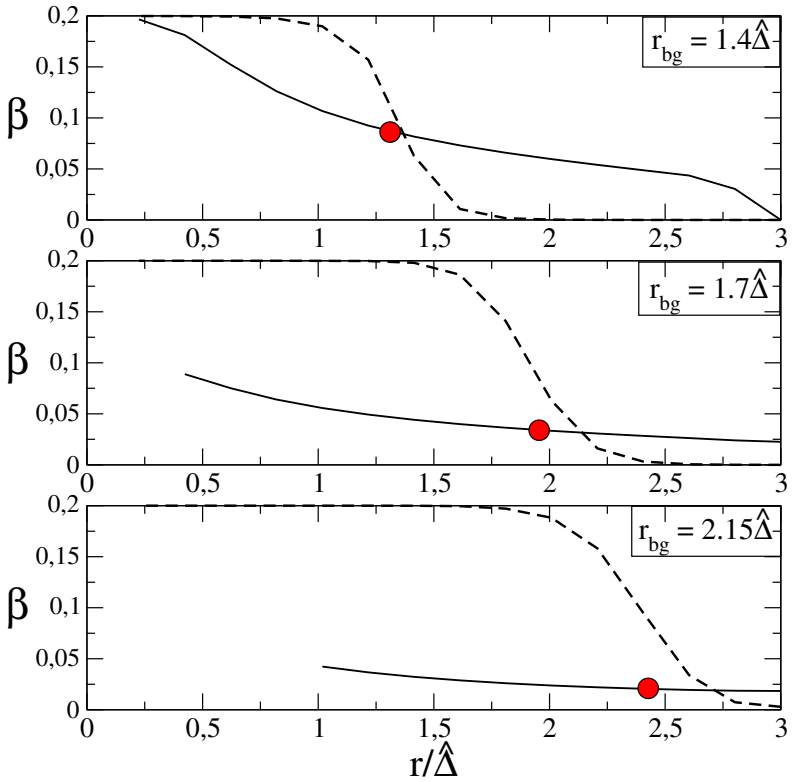

Figure 4.3: Plain line: radial profile of exponent β at three instants of the flame kernel growth, corresponding to three values of the burned gases radius r_{bg}. Dashed line: radial profile of $\tilde{c}$. Filled circles: values of exponent β corresponding to the position $\tilde{c} = 0.5$ in the flame front.

of exponent β decrease within the flame front when the radial coordinate r increases, that is when the local curvature $curv_l = 2/r$ decreases. This also implies that exponent β is not constant within the flame front, which would have been recommended in order to predict a constant value of wrinkling in the flame front. However, the local curvature effect becomes much less significant when the global curvature decreases, that is for larger flame kernels: when $curv_g < \widehat{\Delta}^{-1}$, β is quasi constant within the flame front.

According to these observations, exponent β clearly depends on the curvature of the flame front. The dynamic model interprets the curvature of the flame front as a wrinkling, whether the curvature is due to the action of the turbulence or whether the curvature is due to the laminar sphericity of the flame. However a criterion can be established, defining a minimal value of the burned gases radius r_{bg} above which curvature effects are not significant anymore (see next section 4.3.2). This conclusion is already suggested in Fig. 4.3: when $r_{bg} = 2.15\widehat{\Delta}$ then exponent β is very close to zero ($\beta \sim 0.03$). Corresponding values of wrinkling are then very close to unity.

4.3.2 A criterion for the laminar degeneration

To further analyze why the dynamic model interprets the laminar curvature as a wrinkling, the expression of exponent β (4.7) for a laminar spherical flame is

developed in spherical coordinates. Calculations are detailed in Annexe 9.4. The final expression of exponent β is reported below:

$$\beta(r) = \frac{\log\left(1 + \frac{\gamma^2 - 1}{12\gamma^2} \frac{\left\langle (c^+)^2 \left| \frac{\partial \tilde{c}}{\partial r} \right| \right\rangle}{\left\langle \left| \frac{\partial \hat{c}}{\partial r} \right| \right\rangle}\right)}{\log(\gamma)} \tag{4.15}$$

where the non-dimensional curvature c^+ is defined by:

$$c^+ = \frac{\widehat{\Delta}}{r} \tag{4.16}$$

Expression (4.15) shows that exponent β takes non-zero values when the curvature is non zero, accordingly the sgs wrinkling factor Ξ_Δ is larger than unity when the curvature c^+ is non-zero: the dynamic model interprets the curvature of the laminar flame front as a wrinkling. The larger the curvature c^+, the larger the value of β, as observed in Figs. 4.2 and 4.3. Writing the Taylor expansion of $\beta(r)$ given by Eq. (4.15) leads to the following observation: the degeneration towards the planar flame (i.e. when $c^+ \to 0$) goes in $(c^+)^2$. A minimal value of the burned gases radius $r_{\text{bg,min}}$ can be defined, from which exponent β becomes very close to zero. In practice, according to the results of the simulation, $r_{\text{bg,min}} = 1.5 - 2\widehat{\Delta}$. In that case, $\beta \sim 0.05$ (see Fig. 4.2), corresponding to $\Xi_\Delta \sim 1.08$ at atmospheric conditions and $\Xi_\Delta \sim 1.25$ at engine conditions. This implies that, to respect the laminar degeneration and avoid over predicted values of wrinkling factor, the dynamic wrinkling model must be employed only once the flame kernel has reached a size $r_{\text{bg,min}} = 1.5 - 2\widehat{\Delta}$. But in fact this condition is automatically verified, because of the ignition coupling criterion (section 4.2). The dynamic procedure can be applied to a flame kernel only of the size $\widehat{\Delta}_{moy}$. In practice, when $r_{bg} \sim \Delta_{moy}$, the laminar curvature effects described above are no more significant: the term $\langle |c^+|^2 |\nabla \tilde{c}| \rangle / \langle |\nabla \hat{c}| \rangle$ in the expression of exponent β (4.15) is much smaller than unity, so that the laminar degeneration is quasi verified. To illustrate these conclusions, Fig. 4.4 displays the evolution of β_s (4.4(a)) and of $\Xi_{\Delta,s}$ (4.4(b)) as a function of the non-dimensional burned gases radius $r_{bg}^+ = r_{\text{bg}}/\widehat{\Delta}$, for two different sizes of the combustion filter Δ (plain line $n_{res} = 5$, dashed line $n_{res} = 7$).

It can be observed that:

- when $r_{\text{bg}} > 0.75\widehat{\Delta}$, profiles of β function of $r_{bg}/\widehat{\Delta}$ are self-similar. This confirms that β varies with the curvature c^+ in expression (4.15).
- when $r_{\text{bg}} < 0.75\widehat{\Delta}$, self-similarity is not verified, because in that case the flame front is not fully established at scale $\widehat{\Delta}$: the gradients at scale $\widehat{\Delta}$ cannot be correctly estimated.
- when $r_{\text{bg}} > 2\widehat{\Delta}$, $\beta_s < 0.04$ and $\Xi_{\Delta,s} < 1.05$ at atmospheric conditions, which is very close to unity. Accordingly, when $r_{\text{bg}} > 2\widehat{\Delta}$, the laminar degeneration is quasi verified. The value $2\widehat{\Delta}$ is also very close to the minimal size of the flame kernel found in section 4.2 above which the dynamic procedure can be practically applied.

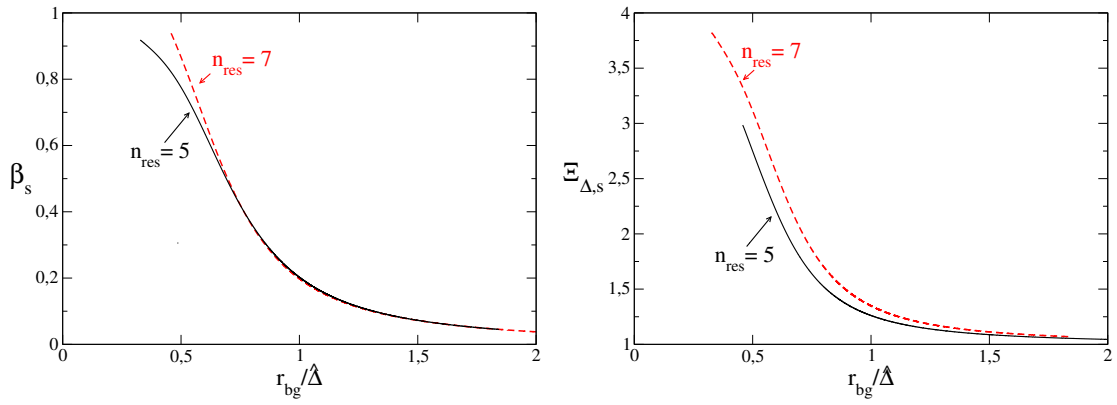

(a) (b)

Figure 4.4: Evolution of β_s (a) and $\Xi_{\Delta,s}$ (b) as a function of $r_{\mathrm{bg}}/\widehat{\Delta}$, for two different size of the combustion filter Δ. local formulation. $\widehat{\Delta} = \Delta$ and $\Delta_{\mathrm{ave}} = 2\Delta$.

These new investigations on the dynamic wrinkling model highlighted an undesired behavior of the dynamic model, which interprets the laminar curvature of the flame front as a wrinkling. However, it was also evidenced that the dynamic procedure can only be applied to a flame kernel of a certain size $r_{bg,trans,dyn}$, for which laminar curvature effects become insignificant on the wrinkling prediction. As a result, no correction of the dynamic model should be required, provided that the criterion on the size of the flame kernel is respected.

4.4 Flame front close to the boundaries of the computational domain

First tests of the dynamic model in the SI engine configuration - presented in details in Chapter 5 - highlighted limitations of the dynamic model as it was originally formulated by Wang et al. (2012). Unphysical behavior of the dynamic model, corresponding to very high values of the wrinkling (typically $\Xi_\Delta > 50$), was observed in two specific situations. The first situation is detailed in this section and occurs when the flame front is close to the boundary of the domain. The second situation will be detailed in section 4.5.

4.4.1 Description of the problem in the SI engine configuration

The boundary problem is illustrated in Fig. 4.5, showing an isosurface of the flame kernel ($\tilde{c} = 0.5$) inside the engine combustion chamber, colored by the wrinkling factor Ξ_Δ. The scale for the wrinkling Ξ_Δ was saturated to $\Xi_\Delta = 30$ in order to clearly evidence the zones of interest. The dynamic model predicts unphysical large values of the sgs wrinkling factor Ξ_Δ close to the boundary of the computational domain. The corresponding value of the exponent β is indicated. Such high values of wrinkling led to incoherent values of the reaction rate affecting the global evolution of the in-cylinder pressure. The phenomenon described above is obviously not compatible with engine simulations. To understand this problem, the

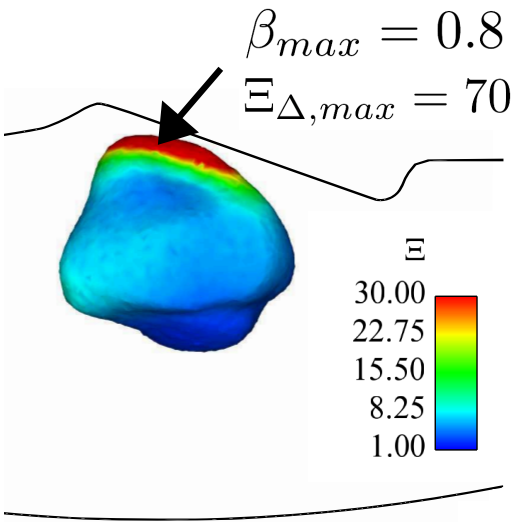

Figure 4.5: view of the flame kernel in the SI engine configuration (see description in section 5.1.2), isosurface of $\tilde{c} = 0.5$ colored by Ξ_{Δ}, black line: contour of the cut plane

propagation of a 1D planar flame is analyzed in section 4.4.2 and modifications of the dynamic model are proposed. Then, modifications are validated on non-planar flames in section 4.4.3.

4.4.2 Analysis of the 1D planar flame case

Section 4.4.2.1 presents a simple test case of a 1D planar flame, at atmospheric conditions, propagating towards the boundary of the calculation domain. Thanks to this analysis, a modified formulation for exponent β is proposed in section 4.4.2.2, to recover physical values of the wrinkling factor Ξ_{Δ}.

4.4.2.1 1D planar flame propagating towards the boundary of the computational domain

A 2D square domain of length $L = 20$ cm with a grid size $\Delta_x = 60$ mm is considered. Mixture and dynamic model parameters are those given in Tab. 4.1 in Tab. 4.3 respectively.
The 1D flame propagates towards the left boundary of the computational domain. Figure 4.6(a) shows flame surfaces $\Sigma_1 = \widetilde{|\nabla \tilde{c}|}$ and $\Sigma_2 = |\nabla \hat{\tilde{c}}|$, while Fig. 4.6(b) displays exponent β, when the flame front is at a distance d such as $d < \widehat{\Delta}$ from the boundary of the domain. It can be seen that for x such as $x < \widehat{\Delta}/2$ from the boundary, then $\Sigma_1 > \Sigma_2$ and $\beta > 0$. The difference between Σ_1 and Σ_2 increases as the position of the flame front gets closer to the boundary.

To understand why flame surfaces Σ_1 and Σ_2 are different close to the boundary, it is recalled that Σ_1 is obtained first calculating the gradient of $\tilde{c}$ and then test-

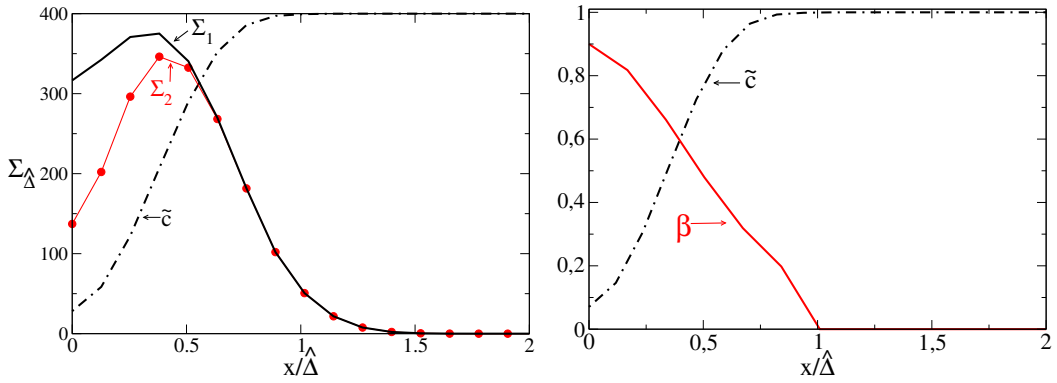

Figure 4.6: Behavior of the dynamic wrinkling when the flame front is at a distance $d < \widehat{\Delta}$ from the boundary: 1D profile of $\Sigma_1 = \widehat{|\nabla\tilde{c}|}$, $\Sigma_2 = |\nabla\hat{\tilde{c}}|$ (a) and β (Eq. (4.7)) (b). $x = 0$ corresponds to the boundary of the domain.

filtering, while Σ_2 is obtained first test-filtering $\tilde{c}$ and then calculating the gradient. Second, the numerical operators gradient and test-filter are centered operators. Accordingly, if Σ_1 and Σ_2 are different in the 1D planar case close to the boundary, this is because the commutation between the operator gradient - more precisely derivative - and test-filter is no more ensured, as these centered operators become truncated close to the boundary. To demonstrate this, numerical expressions of flame surfaces Σ_1 and Σ_2 are established for the 1D planar flame (see Annexe 9.4). To do so, an hexahedron mesh is considered. Expressions of operators derivative (denoted $\mathscr{D}$) and operator test-filter (denoted $\mathscr{T}$) correspond to the ones implemented in the AVBP code. Finally, the stencil $\mathscr{S}$ of operators $\mathscr{D} * \mathscr{T}$ (or $\mathscr{T} * \mathscr{D}$) is introduced, corresponding to the number of points required to complete the numerical calculation of operations test-filter and then derivative (respectively derivative and then test-filter). Conclusions of the calculations detailed in Annexe 9.4 are listed below:

1. when the stencil $\mathscr{S}$ of operators $\mathscr{D} * \mathscr{T}$ (or $\mathscr{D} * \mathscr{T}$) is truncated, then operators derivative and test-filter do not commute anymore: $\mathscr{D} * \mathscr{T} \neq \mathscr{D} * \mathscr{T}$. Accordingly, $\Sigma_1 \neq \Sigma_2$. It is also demonstrated that $\Sigma_1 > \Sigma_2$.

2. the more the stencil $\mathscr{S}$ is truncated, the more important is the numerical commutation error, the higher is the resulting exponent β, as also clearly evidenced in Fig. 4.6.

3. conclusions of points (1) and (2) do not depend on the shape of the test-filter and derivative operators. The commutation problem will be observed whenever these operators are centered operators.

4. the size of the zone impacted by the problem is close to $\widehat{\Delta}/2$.

Note that when calculating averaged quantities $< \Sigma_1 >$ and $< \Sigma_2 >$, the numerical problem described above is not restrained to the zone of width $\widehat{\Delta}$ but is spread over a larger zone by the averaging operation. In practice the width of this zone is therefore close to $\Delta_{ave}/2$. This is the reason why in Fig. 4.6 - (b), exponent β

is non-zero in the nodes situated at a distance $x > \widehat{\Delta}/2$ from the boundary, while when $x > \widehat{\Delta}/2$, $\Sigma_1 = \Sigma_2$.

Thanks to these analysis, a modified formulation of the exponent β is now proposed in the following section 4.4.2.2, that ensures $\Sigma_1 = \Sigma_2$ for the 1D planar flame, even close to the boundary of the domain.

4.4.2.2 Modified formulation for exponent β

To avoid unphysical values of wrinkling factor close to the domain boundary, several solutions can be considered:

- (i) To impose a law of the wall for the wrinkling, forcing the wrinkling towards unity at the wall. This implies to refine at the boundary in a zone of width at least $\widehat{\Delta}/2$, but this is not affordable in real engine configurations.
- (ii) To implement a new filtering operator that would ensure the numerical commutation everywhere in the calculation domain, but this strategy may not be compatible with massively parallel codes and unstructured meshes.
- (iii) To establish a modified formulation of exponent β where the numerical commutation operation - which causes the problem close to the boundary - is avoided. This last option is the one that was investigated and is now presented.

The modified formulation replaces $\Sigma_2 = |\nabla\hat{\tilde{c}}|$ by $\Sigma_{2,mod} = |\widehat{\nabla\tilde{c}}|$, leading to the following expression for exponent β, denoted now β_{mod}:

$$\beta_{mod} = \frac{\log\left(\langle|\widehat{\nabla\tilde{c}}|\rangle / \langle|\widehat{\nabla\tilde{c}}|\rangle\right)}{\log(\gamma)} \tag{4.17}$$

With this formulation, flame surfaces Σ_1 and $\Sigma_{2,mod}$ are equal for a 1D planar flame, because operators norm and test-filter commute in the 1D planar case. There is no more commutation required between operator derivative and test-filter as with the initial formulation of β Eq. (4.7). Figure. 4.7 displays the axial profiles of quantities β, β_{mod}, Σ_1, Σ_2 and $\Sigma_{2,mod}$, for the same 1D planar flame presented in section 4.4.2.1. It can be seen that:

- $\Sigma_1 = \Sigma_{2,mod}$ in the whole calculation domain, because operators norm and test-filter commute everywhere in the calculation domain for the 1D planar flame. Accordingly, $\beta_{mod} = 0$ in the whole calculation domain, ensuring that the wrinkling Ξ_{Δ} is equal everywhere to unity.
- far from the boundary, when $d > \widehat{\Delta}$ and when the mesh is regular, operators derivative and test-filter commute (Annexe 9.4), leading to:

$$\Sigma_2 = |\nabla\hat{\tilde{c}}| = |\widehat{\nabla\tilde{c}}| = \Sigma_{2,mod} \tag{4.18}$$

  Thanks to Eq. (4.18), the wrinkling factor Ξ_{Δ} is unchanged far from the boundary, when the mesh is regular. Demonstration can be found in Annexe

9.4 for the 1D planar flame case and can be extended to the 3D case. Note that Eq. (4.18) is not verified anymore for non-regular mesh. However, it will be explained in next section that practical tests evidenced in that case $\Sigma_2 \approx \Sigma_{2,mod}$.

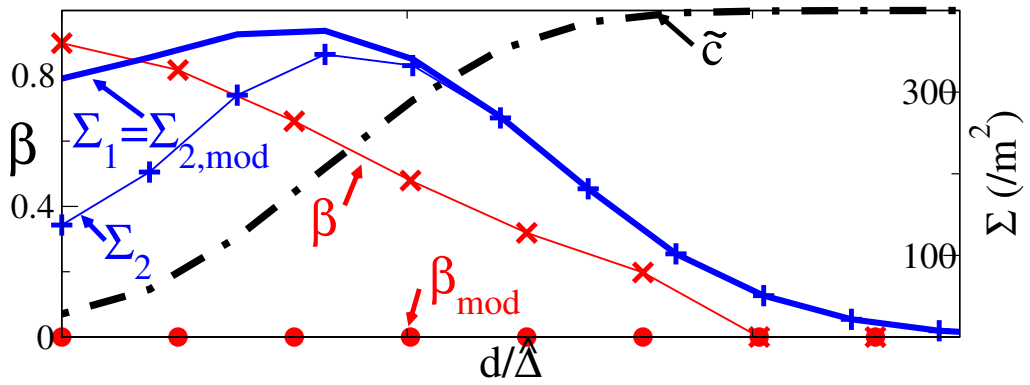

Figure 4.7: Axial profiles in a 1D planar flame of quantities $\tilde{c}$, Σ_1, Σ_2, $\Sigma_{2,mod}$, β (Eq. (4.7)) and β_{mod} (Eq. (4.17)). The 1D planar flame propagates towards the boundary of the domain ($d = 0$).

4.4.3 First tests of the modified formulation on non planar flames

The modified formulation (4.17) is now applied to the freely propagating laminar spherical flame described in section 4.3. This second validation verifies that the modified formation enables to recover a physical behavior of the sgs wrinkling factor Ξ_Δ when the flame is non planar and when using a regular mesh.
The spherical flame propagates until it reaches a distance $d < \widehat{\Delta}$ from the domain boundary. Figure 4.8 displays the profile of filtered progress variable $\tilde{c}$, exponent β_{mod} (Eq. (4.17)), compared to the profile of exponent β (Eq. (4.7)). Profiles are obtained from the same field of $\tilde{c}$. The effect of the correction is very clear:

- for the nodes situated at $d < \widehat{\Delta}/2$ from the boundary, β_{mod} tends toward zero as expected, because the local curvature of the flame front decreases (see section 4.3.1). On the contrary, values of exponent β according to the initial formulation Eq. (4.7) increase as the normalized distance $d/\widehat{\Delta}$ to the boundary of the domain decreases (as previously observed in Fig. 4.6-(b) for the planar flame).

- For the nodes situated at $d > \widehat{\Delta}/2$ from the boundary, values of β_{mod} and of β are the same, which confirms that $\Sigma_{2,mod} = \Sigma_2$ for the non planar flame, as predicted by Eq. (4.18).

Finally, the modification is tested in the case of 3D flame inside a SI engine combustion chamber. In this type of configuration, cells are tetrahedrons and are deformed as the piston moves. Accordingly, analytical derivations presented in section 4.4.2 are no more valid because the cell size Δ_x varies with time and space: this implies

that the commutation between filtering operator and derivative operator is never verified. Accordingly: $\Sigma_2 \neq \Sigma_{2,mod}$ and $\beta_2 \neq \beta_{2,mod}$ everywhere in the calculation domain. However, as it is often accepted in the LES community to neglect the numerical commutation errors when writing the LES equations (Ghosal, 2004; Moureau et al., 2005), commutation errors due to the irregularity of the mesh can be neglected. Therefore it can be considered that $\Sigma_{2,mod} \approx \Sigma_2$ far from the boundary. As an illustration, Fig. 4.9 presents a cut inside an engine combustion chamber, showing that when the flame front is at a distance $d > \widehat{\Delta}$, values of Ξ_{Δ} and $\Xi_{\Delta,mod}$ are very similar, thus confirming that despite the non-regular mesh, $\Sigma_{2,mod} \approx \Sigma_2$. When $d < \widehat{\Delta}$ the modified formulation ensures reasonable values of the wrinkling: using exponent β_{mod}, values of $\Xi_{\Delta,mod}$ close to the boundary of the domain are $\Xi_{\Delta,mod} \approx 5$, while using the initial formation for exponent β, values of $\Xi_{\Delta,mod} \approx 55$ are found.

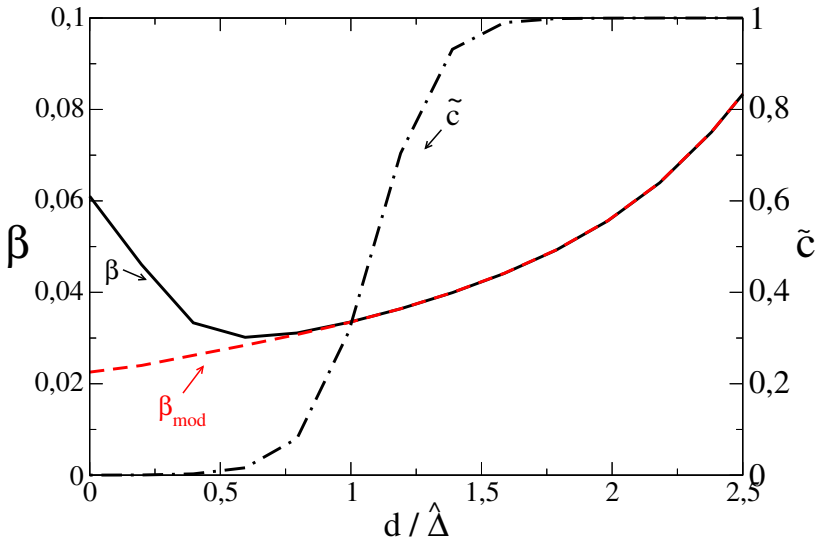

Figure 4.8: Radial profiles of exponent β_{mod} (Eq. (4.17)) (dashed line) and β (Eq(4.7)) (plain line), as a function of the normalized distance $d/\widehat{\Delta}$. The 1D spherical flame is at a distance $d < \widehat{\Delta}$ from the boundary of the domain ($d = 0$). The center of the spherical flame is situated at $d/\widehat{\Delta} = 5.1$.

The problem encountered when the flame front becomes close to the boundary of the computational domain was thus identified. It is due to a numerical issue: numerical operators test-filter and derivative employed for the calculation of flame surfaces Σ_1 and Σ_2 entering the expression of the exponent β do not commute anymore close to the boundary, as they are centered operators. A modified expression for the flame surface Σ_2 was proposed. Wrinkling factor values equal to unity were recovered for the 1D planar flame case and reasonable wrinkling values are obtained for 3D flames in the SI engine configuration. Next section 4.5 presents the last problem identified in the engine configuration and which concerns fronts interactions.

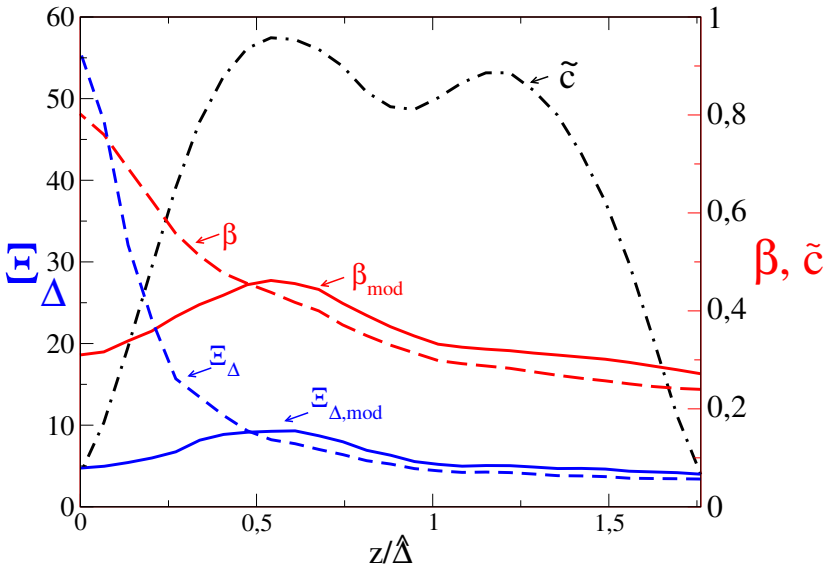

Figure 4.9: 1D profiles inside the combustion chamber of a SI engine configuration of exponent β_{mod} (Eq. (4.17)) (dashed line) and β (Eq. (4.7)) (plain line), of the corresponding sgs wrinkling factors $\Xi_{\Delta,mod}$ (plain line) and Ξ_{Δ} (dashed line). Profile of $\tilde{c}$: dotted/dashed black line. z=0 corresponds to the boundary of the computational domain.

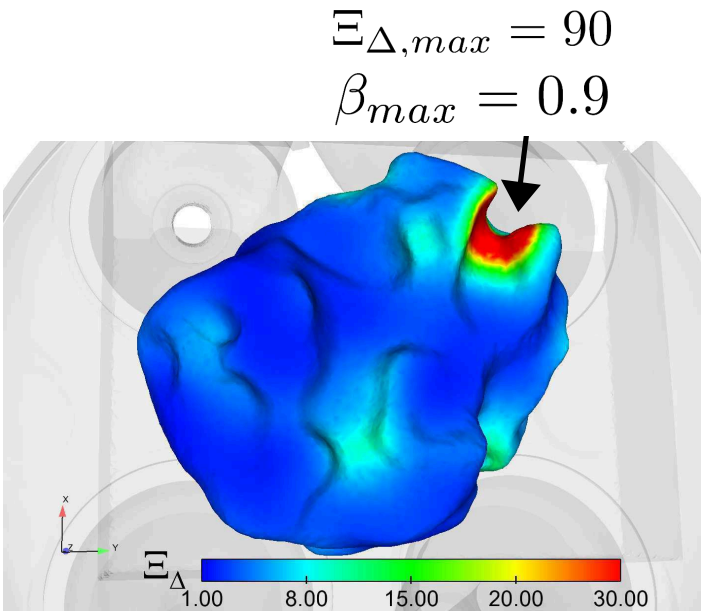

Figure 4.10: Front interactions in the SI engine configuration (see description in section 5.1.2), isosurface of $\tilde{c} = 0.5$ colored by the sgs factor Ξ_{Δ}.

4.5 Flame front interactions

The dynamic model was found to predict large values of the sgs wrinkling factor Ξ_{Δ} in certain zones of the flame kernel, where fronts are practically at a distance shorter than the test-filter width, as illustrated in Figure 4.10. The zone where $\Xi_{\Delta} > 30$ corresponds to a zone where two lobes of the flame front face each other. This large

values of $\Xi_{\widehat{\Delta}}$ lead to incoherent reaction rates values and a correction is required. The problem is characterized considering the interaction of two 1D planar flames. This simplified situation is analyzed in section 4.5.1 and modifications of the initial dynamic wrinkling model are discussed. Then a first test of the correction in the SI engine configuration is presented in section 4.5.2.

4.5.1 Flame fronts interactions in the 1D planar case

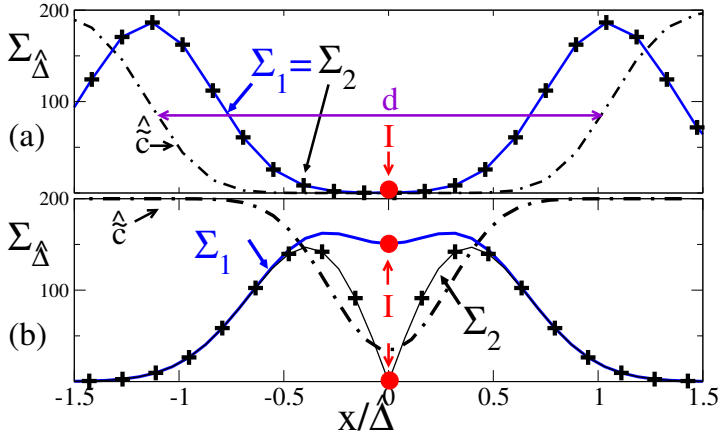

Figure 4.11: Two interacting one-dimensional planar flame fronts at a distance d, $\Sigma_1 = \widehat{|\nabla\tilde{c}|}$, $\Sigma_2 = |\nabla\hat{\tilde{c}}|$. (a): $d > \widehat{\Delta}$. (b): $d < \widehat{\Delta}$.

Fig. 4.11 illustrates the interaction of two 1D planar flames situated at a distance d from each other. Profiles of $\hat{\tilde{c}}$ and of flame surfaces $\Sigma_1 = \widehat{|\nabla\tilde{c}|}$ and $\Sigma_2 = |\nabla\hat{\tilde{c}}|$ are displayed. The symmetry point between the two flame fronts is indicated with letter I. Two cases are illustrated. Figure (4.11a) on top displays a situation without front interactions problem. The distance between fronts d is larger than $\widehat{\Delta}$, which allows the dynamic model to predict $\Sigma_1 = \Sigma_2$, i.e. to predict a wrinkling factor equal to unity. On the contrary, Fig. (4.11a) at the bottom illustrates a case where the two flame fronts interact. In this case, the distance d is smaller than $\widehat{\Delta}$, therefore $\tilde{c}$ is not null (nor equal to unity) in a zone of width $\widehat{\Delta}$ centered on point I, while $\nabla\hat{\tilde{c}}$ is null in point I. This leads to an ill-posed definition of the sgs wrinkling factor at scale $\widehat{\Delta}$:

$$\Xi_{\widehat{\Delta}} = \frac{\widehat{|\nabla c|}}{|\nabla\hat{\tilde{c}}|} \tag{4.19}$$

Figure (4.11b) also evidences that $\Sigma_1 \gg \Sigma_2$ in the zone of width $\widehat{\Delta}$ centered on point I. Accordingly the dynamic model predicts large values of the sgs wrinkling factor $\Xi_{\widehat{\Delta}}$ in this zone.

To avoid this problem, the estimation of the flame surface Σ_2 is modified in the locations of the flame front where fronts interact. Σ_2 is replaced by a flame surface Σ_3, defined at scale $\widehat{\Delta}$, but which does not tend toward zero where front interacts. The following expression for flame surface Σ_3 defined at scale $\widehat{\Delta}$ is proposed:

$$\Sigma_3 = \widehat{\mathbf{N}.\mathbf{N}|\nabla\tilde{c}|} \tag{4.20}$$

In this expression, $\mathbf{N}$ and $\widehat{\mathbf{N}}$ are the normal vectors to the resolved flame front at scale Δ and $\widehat{\Delta}$ respectively:

$$\mathbf{N} = -\frac{\nabla\tilde{c}}{|\nabla\tilde{c}|} \quad \text{and} \quad \widehat{\mathbf{N}} = -\frac{\nabla\hat{\tilde{c}}}{|\nabla\hat{\tilde{c}}|} \tag{4.21}$$

With expression 4.20, Σ_3 does not approach zero unlike Σ_2, where there are front interactions like in point I in Fig. 4.11.
Note that the normal $\widehat{\mathbf{N}}$ is not defined in point I, as the gradient $\nabla\hat{\tilde{c}}$ is null. It is practically set to zero in the code when the gradient $\nabla\hat{\tilde{c}}$ is null.

To recover the flame surface Σ_2 when there is no fronts interaction, Σ_2 is corrected according to:

$$\Sigma_{2,corr} = (1 - \hat{\zeta})\,\Sigma_2 + \hat{\zeta}\,\Sigma_3 \tag{4.22}$$

Flag $\hat{\zeta}$ is defined such as $\hat{\zeta} > 0$ where fronts interact and $\hat{\zeta} = 0$ elsewhere. To do so, a flag ζ is defined such as:

$$\zeta = \begin{cases} 1 \text{ if } \mathbf{N}.\widehat{\mathbf{N}} < 1 - \varepsilon \\ 0 \text{ if not} \end{cases} \tag{4.23}$$

This definition is based on following practical considerations on 3D flame fronts:

- when there is no front interaction at scale $\widehat{\Delta}$, then the zone of size $\widehat{\Delta}$ contains only one flame front: this situation is illustrated in Fig. 4.12-(a) and corresponds to a mildly wrinkled flame front. In that case normal vectors $\mathbf{N}$ and $\widehat{\mathbf{N}}$ are quasi collinear: $\zeta = 0$.

- when flame fronts interact at scale $\widehat{\Delta}$, the filtering zone of width $\widehat{\Delta}$ contains several flame fronts: this situation is illustrated in Fig. 4.12-(b). Accordingly, the smallest wrinkling scale is smaller than the test-filtering scale: $\lambda_{min} < \widehat{\Delta}$. Then $\mathbf{N}$ and $\widehat{\mathbf{N}}$ have different directions because some spatial frequencies of the resolved flame front are removed by the test-filtering operation: $\zeta = 1$.

The flag ζ is then test-filtered as flame front interactions induce high values of Ξ_Δ over a zone of characteristic length $\widehat{\Delta}$.

Test of the modified formulation in the 1D case The modified dynamic model is used on Fig. 4.11 1D fronts interactions canonical case. The following points must be validated:

1. the flag ζ corresponds to a Dirac function because $\widehat{\mathbf{N}}$=$\mathbf{N}$ everywhere, except in point I where $\widehat{\mathbf{N}}$ is practically set to zero when the gradient $\nabla\hat{\tilde{c}}$ is null. $\hat{\zeta}$ results thus of the test-filtering of the Dirac function.

2. since $\widehat{\mathbf{N}}$=$\mathbf{N}$ (except in point I), flame surfaces Σ_3 (Eq. 4.20) and $\Sigma_1 = \widehat{|\nabla\tilde{c}|}$ are equal.

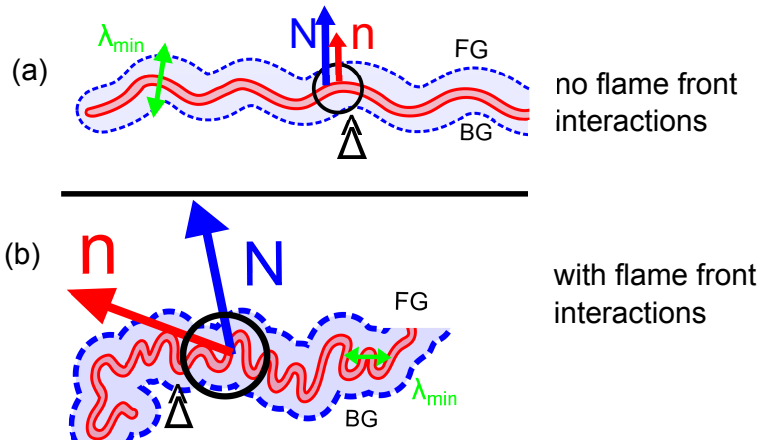

Figure 4.12: Sketch of flame fronts. Red surface: surface estimated at the combustion filter Δ scale — blue surface: surface estimated at the effective filter $\widehat{\Delta}$ scale — Black circle: effective filter $\widehat{\Delta}$. (a) Situation without front interactions at scale $\widehat{\Delta}$; (b): Situation with flame front interactions.

Profiles of flag $\hat{\zeta}$ and of flame surfaces Σ_1, Σ_2, $\Sigma_{2,corr}$ and Σ_3 are displayed in Fig. 4.13-(a). Points 1. and 2. are verified. Since Σ_3 is equal to Σ_1, the flame surface $\Sigma_{2,corr}$ reads:

$$\Sigma_{2,corr} = (1 - \hat{\zeta})\Sigma_2 + \hat{\zeta}\Sigma_1 \tag{4.24}$$

In the locations where flag $\hat{\zeta}$ is close to unity, Σ_2 is close to zero, thus $\Sigma_{2,corr} \approx \Sigma_1$, as shown in Fig. 4.13-(a). As a result, the wrinkling factor Ξ_Δ recovers values close to unity in the 1D planar case: $\Xi_\Delta \approx 1$ (Fig. 4.13-(b)).

4.5.2 Test in the SI engine configuration

The correction Eq. (4.24) is applied to a resolved flame kernel in the engine configuration exhibiting large values of wrinkling in certain locations, as in Fig. 4.14. The parameter ϵ in Eq. (4.23) is set to 0.1. Lower values of wrinkling factors Ξ_Δ are predicted in the corresponding locations, as seen in Fig. 4.14-b and c. These zones are detected by the sensor $\hat{\zeta}$, as shown in Fig. 4.14-a, which is equal to zero in the zone where no large values of wrinkling factors are present, showing that the correction is effective.

4.6 Conclusion

In this chapter, the dynamic wrinkling model of Wang et al. (2012) was studied, in view to its application in a SI engine configurations. Specific issues to SI engine were first addressed prior the tests in the engine configuration: (i) coupling with the ignition model, (ii) verification of the laminar degeneration for laminar spherical flames. Concerning (i), the dynamic procedure can be used only if the flame front is fully established at the scale of the effective filter $\widehat{\Delta}$, that is when the flame kernel has a size close to the effective filter width $\widehat{\Delta}$. Concerning (ii), the laminar degeneration is not ensured in the spherical case: the dynamic model predicts winkling values

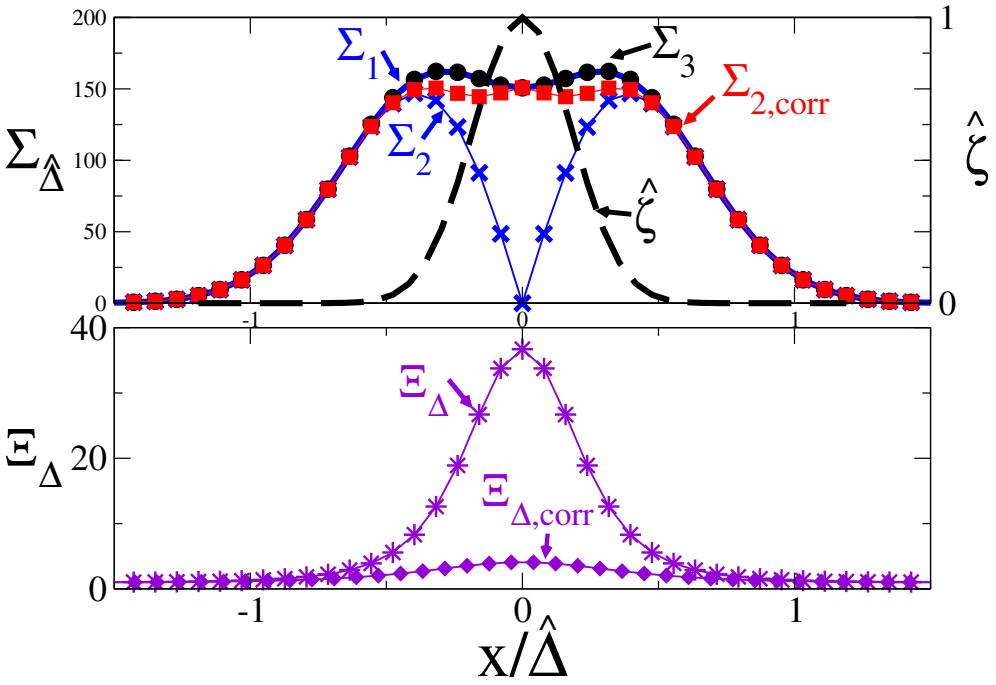

Figure 4.13: Effect of the correction (4.22) in the 1D planar flame interactions case (engine conditions). (a) profiles of flag $\hat{\zeta}$ and flame surfaces Σ_1, Σ_2, $\Sigma_{2,corr}$ and Σ_3. (b) 1D profiles the wrinkling without correction Ξ_Δ, and with correction $\Xi_{\Delta,corr}$.

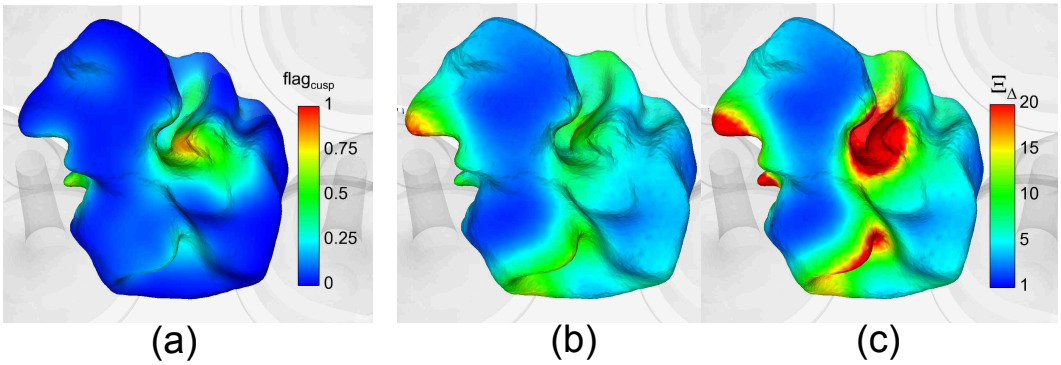

Figure 4.14: $\tilde{c} = 0.5$-isosurface of the flame kernel colored by (a): flag $\hat{\zeta}$; (b): corrected wrinkling $\Xi_{\Delta,corr}$; (c): original wrinkling Ξ_Δ.

higher than unity for laminar spherical flames. However, these values remain close to unity for kernels of size $\widehat{\Delta}$ and decrease quickly towards unity as the curvature of the front decreases.

The main drawback of the dynamic model is therefore that it can be applied only on a flame kernel of size close to $\widehat{\Delta}$. This implies to refine in the spark plug zone, in order to apply sooner in the cycle the dynamic procedure. Then, first tests in the SI engine configuration evidenced practical difficulties: the dynamic model predicts large values of wrinkling leading to incoherent reaction rate values, when the flame front is close to the domain boundary and when fronts interact. Modifications were proposed and tested on canonical cases. In the next chapter, the modified dynamic

model is applied to simulate several engine cycles and to assess its ability to predict out-of-equilibrium wrinkling values, with no need of parameter adjustment.

Chapter 5

Validation of the modified dynamic wrinkling model in the ICAMDAC engine configuration

Contents

In this chapter, the dynamic wrinkling model is applied in a spark ignition engine configuration, applying the two modifications proposed in sections 4.4 and 4.5. The numerical set-up is first presented, then results of simulations are analyzed in order to evaluate the ability of the dynamic wrinkling model to predict out-of-equilibrium wrinkling values, with no parameter adjustment.

5.1 Numerical set-up

5.1.1 Validation strategy

The validation of the modified dynamic model in the engine configuration has several objectives:

1. to verify that the modifications proposed in sections 4.4.2 and in 4.5 ensure a physical behavior of the dynamic model in engine conditions.

2. to confirm the ability of the modified dynamic model to predict out-of-equilibrium wrinkling factors values, that is to predict the transient growth of the flame kernel, first quasi-laminar after ignition and then progressively wrinkled by turbulence.

3. to evaluate the ability of the modified dynamic model to self-adapt, without case by case parameter adjustment.

4. to compare the local and the global formulations, as the turbulence inside the combustion chamber is not isotropic.

Accordingly, results obtained using the dynamic wrinkling model coupled to the Boger et al. (1998) propagation model are compared against:

- results obtained using the ECFM-LES model proposed by Richard et al. (2007) and modified by Robert et al. (2015), based on the transport equation for the flame surface density (3.24).

- results obtained using the equilibrium formulation of the wrinkling factor (1.76), coupled to the Boger et al. model.

Simulations were performed in the ICAMDAC engine configuration, described in next section. Table 5.1 summarizes the several types of simulations considered.

Simulations	model	study
A	ECFM-LES	Robert et al. (2015)
B	Boger et al. + eq. wrinkling Eq. (1.76)	present study
C	Boger et al + modified dyn. global wrinkling	present study
D	Boger et al.+ modified dyn. local wrinkling	present study

Table 5.1: The different types of simulations performed in the ICAMDAC engine configuration.

5.1.2 Description of the engine configuration

The ICAMDAC engine of IFPEn is a four-valve downsized single cylinder engine with direct injection. The engine is fueled with iso-octane and works under homogeneous conditions. The numerical strategy and the mesh for the ICAMDAC configuration were set up in the framework of the PhD works of A. Robert (IFPEn) and of A. Misdariis (CERFACS). Two engine regimes were characterized, corresponding to two different revolution per minute (RPM) (Table. 5.2). The computational domain is displayed in Fig. 5.1, while Fig. 5.2 shows a view of the mesh in the engine during the ignition phase. The spark plug is not meshed but the zone around the location of the spark plug is locally refined in order to initiate a flame kernel of reasonable size ($\approx 1\ mm$). Each cycle of the engine was divided into 44 phases, in order to ensure the quality of the mesh. Number of cells in the mesh varies between 1.07 to 12 millions (during the combustion), according to the position of the piston during the combustion cycle. Numerical settings are reported in Table 5.3.

Case	RPM	Spark Timing	IMEP
1	1800	8 CAD ATDC	19 bars
2	1300	13 CAD ATDC	20 bars

Table 5.2: specifications for the two engine regimes. CA ATDC: crank angle after top dead center.

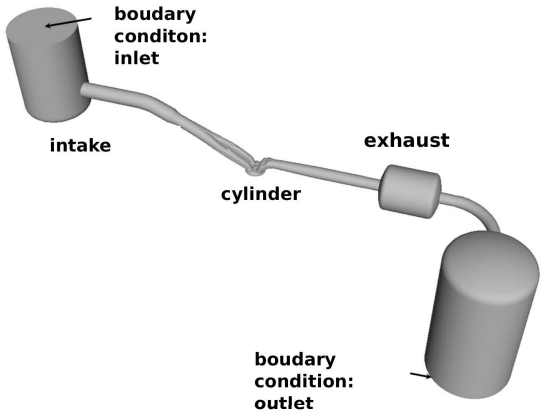

Figure 5.1: Representation of the calculation domain, from A. Robert (2014) .

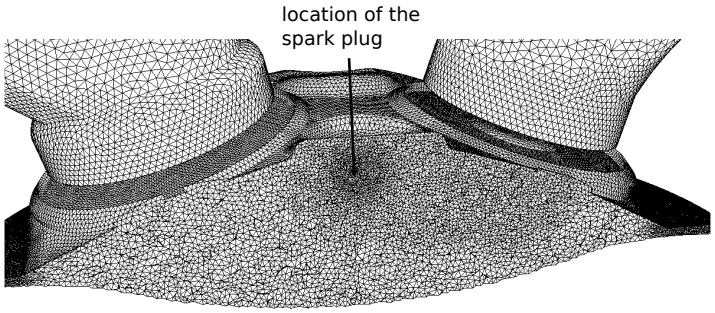

Figure 5.2: View of the mesh of the ICAMDAC engine during the phase of ignition, from Misdariis (2015).

numerical scheme	TTGC (during combustion phase)
sgs tensor model	Smagorinsky with $C_s = 0.18$
boundary conditions	NSCBC method

Table 5.3: Numerical parameters of simulations.

5.1.3 Choice of the simulated engine cycles

Robert et al. (2015) simulated 15 LES cycles, using the ECFM-LES model in the ICAMDAC engine configuration. Results obtained are displayed in Fig. 5.3, com-

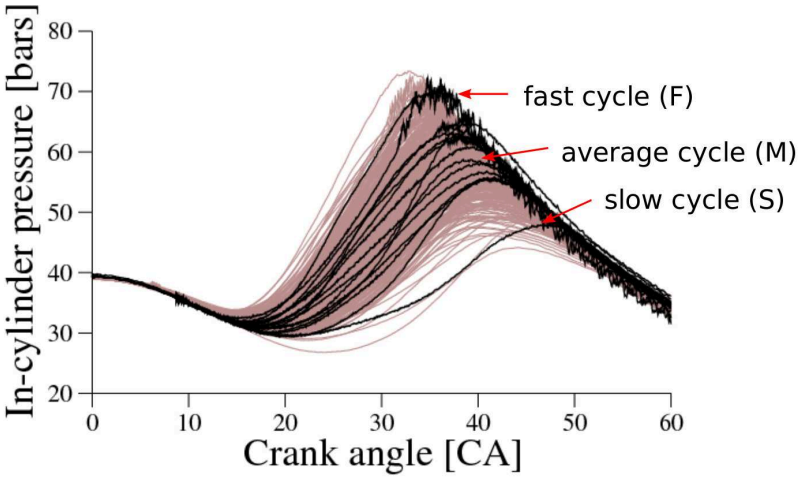

Figure 5.3: Instantaneous in-cylinder pressure for the ICAMDAC configuration (RPM = 1800, IMEP = 19 bars, spark timing = 8 CA ATDC). Experimental measurements (braun) and LES (black). Robert et al. (2015).

RPM	slow cycle.	average cycle	fast cycle
1800	1-S	1-M	1-F
1300	2-S	2-M	2-F

Table 5.4: Notations employed for the different cycles simulated in the present study.

paring the in-cylinder pressure predicted by the LES cycles and measured in the experiments. Robert et al. simulations were chosen as the reference simulations (simulations **A** in Table 5.1). The three other types of simulations (**B,C,D**) were performed in the present work using the same numerical settings as in Robert et al. (section 5.1.2). Only a reduced number of cycles were simulated, chosen among the cycles of simulations **A**. For each cycle, the initial solution was taken from the existing simulations **A** at a given timing which will be specified in the following. Chosen cycles correspond to a cycle presenting a high pressure peak (indicated as *fast cycle* in Fig. 5.3 and denoted in the following by letter F), an average pressure peak (*average cycle*, M) and a low pressure peak (*slow cycle*, S) inside the experimental envelope. Thus the cycle-to-cycle variability can be accounted for. Last but not least, the two engine regimes (Table 5.2) were investigated to vary the conditions of turbulence. In total 6 cycles (see notations in Table 5.4) are simulated, for the three types of simulations **B,C,D**.

The model parameters used in simulations are gathered in Table 5.5. Parameter $\alpha_{t,CFM}$ refers to parameter α_1 in the expression (1.63) of the sgs strain term, and parameter $\alpha_{t,Bog}$ refers to parameter α_1 in the expression (1.76) of the sgs equilibrium wrinkling factor formulation. Both parameters depends on the engine regime. $\alpha_{t,Bog}$ was adjusted to reproduce the pressure of cycle 1-M of the reference simulation **A**.

Simulations	Model	RPM	Parameters
A	ECFM-LES	1800	$\alpha_{t,CFM} = 1.8$
		1300	$\alpha_{t,CFM} = 1.4$

Simulations	Ξ_Δ	Parameters		
B	equilibrium Eq. (1.76)	$\alpha_{t,Bog} = 3.3$		
		δ_c	γ	α_{ave}
C	dynamic global	$3\delta_L$	1.42	-
D	dynamic local	$3\delta_L$	1.42	1.5

Table 5.5: Model parameters used for the reference simulations **A**, and present simulations **B, C, D**. Coefficient γ refers to the width of the effective filter $\hat{\Delta} = \gamma\Delta$ (Eq. (4.3)), and α_{ave} to the width of the local averaging operator, $\Delta_{ave} = \alpha_{ave}\Delta$ (see section 4.1). The combustion filter size is $\Delta = 8\Delta_x$.

RPM	slow cycle	ave cycle	fast cycle
1800	10.8	11.8	12.1
1300	16	15.8	15.52

Table 5.6: Start timing of the present simulations in CA ATDC

5.1.4 Initial solutions

As explained in section 4.2, the dynamic wrinkling model can be applied only to a kernel of size $r_{bg} \sim \widehat{\Delta}$. Two options may be considered for the simulations:

1. to use an ignition model - such as the AKTIMEuler ignition model - until the flame kernel has reached the sufficient size $r_{bg} \sim \widehat{\Delta}$. This option will be preferred in future but required further developments, as discussed in section 4.2.

2. to initiate the calculation with an already growing flame kernel of size $r_{bg} \sim \widehat{\Delta}$. This option is retained here as a first step. Accordingly, the initial solution of each cycle corresponds to a solution of simulation **A** verifying $r_{bg} \sim \widehat{\Delta}$. Timing of initial solutions for the different cycles and the different engine regime are gathered in Table 5.6.

5.2 Results and discussions

During the calculations exponent β is updated every 50 iterations. Tests showed that more frequent updates do not significantly change the results as the code time

step is based on acoustic CFL numbers while the model parameter is expected to evolve with convection times. The additional CPU cost induced by the dynamic procedure is about 20% compared to ECFM-LES computations. Fig. 5.4 presents the in-cylinder pressure predicted in simulations (**A, B ,C ,D**) for the different cycles and the different engine regimes. The experimental envelop is displayed in grey.

The in-cylinder pressure predicted by the dynamic model is within the experimental envelop and follows the cycle-to-cycle variations, for both local and global formulations. The local formulation shows even a better agreement with the ECFM-LES reference simulations from Robert et al. (2015) than the global one. The equilibrium formulation, with a model constant $\alpha_{t,Bog}$ adjusted to reproduce the pressure level of cycle 1-M, predicts pressure peaks outside the envelop for cycles 1-S, 2-M and 2-S.

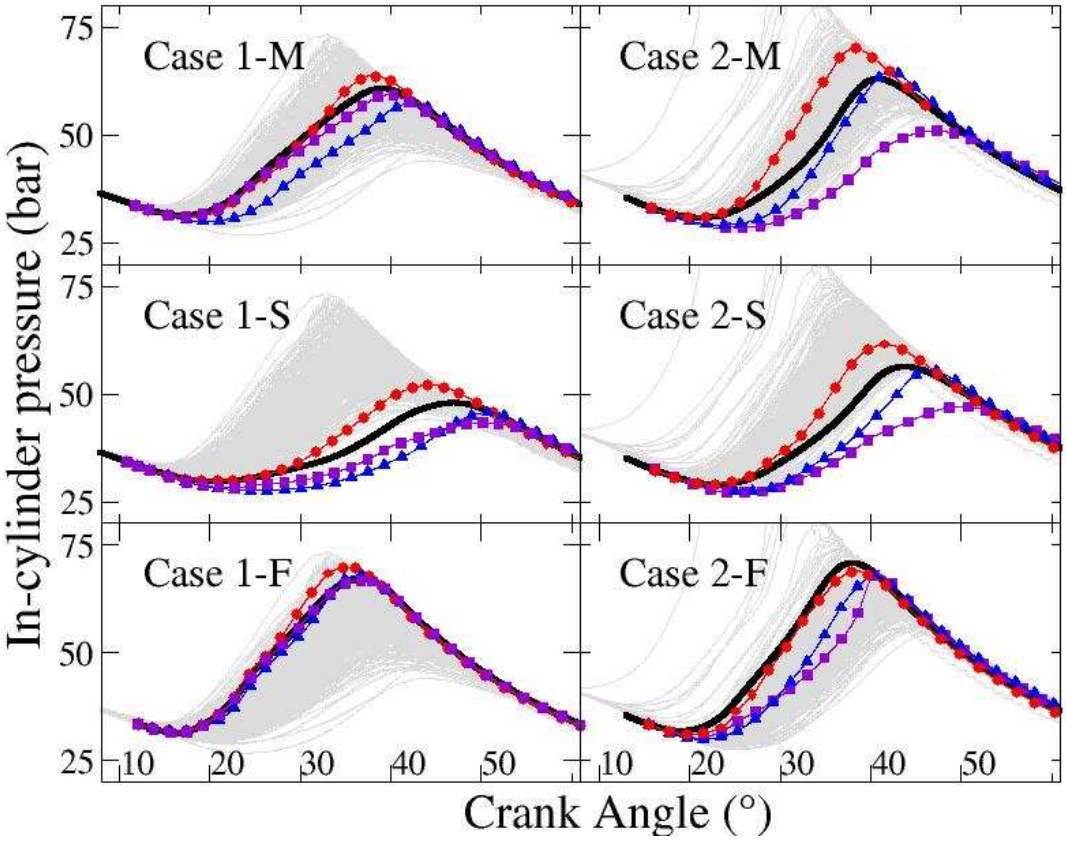

Figure 5.4: In-cylinder pressure vs crank angle for the different simulations cases detailed in Tab. 5.4. Black plain line: reference (**A**), squares: equilibrium formulation (**B**), triangles: global dynamic formulation (**C**), circles: local dynamic formulation (**D**).

Evolution of the mean wrinkling $< \Xi_\Delta >$ (Eq.(5.1)) and of the surface averaged velocity fluctuations at scale Δ $< u'_\Delta >$ (Eq.(5.2)) are analyzed.

$$< \Xi_\Delta > = \frac{\int_\Omega \Xi_\Delta |\nabla \tilde{c}| dV}{\int_\Omega |\nabla \tilde{c}| dV} \tag{5.1}$$

$$< u'_\Delta > = \frac{\int_\Omega u'_\Delta \Xi_\Delta |\nabla \tilde{c}| dV}{\int_\Omega \Xi_\Delta |\nabla \tilde{c}| dV} \tag{5.2}$$

Out-of-equilibrium flame development prediction Fig. 5.5 shows the mean wrinkling factor $< \Xi_\Delta >$, comparing total and resolved flame surface in the combustion chamber, for the four types of simulations. For the reference simulations **A** (ECFM-LES model), the mean wrinkling factor increases as the flame kernel grows and is wrinkled by turbulence, then it decreases as the flame surface is destroyed near the walls. Simulations **C** and **D** (dynamic model) predict exactly the same behavior, demonstrating that the dynamic model, computing exponent β on the fly, predicts out-of-equilibrium wrinkling values. Dynamic wrinkling factor values are also very similar to the ones predicted by the ECFM-LES model, excepted the peak observed near the end of the combustion, which has no impact on the overall consumption rate as corresponding to a time where less than 1 % of the initial fresh gases remain in the combustion chamber. On the other hand, simulations **B** (equilibrium formulation) are not as predictive. Derived assuming a flame-turbulence equilibrium, this formulation under-predicts the wrinkling after +38 CAD ATDC because u'_Δ has already strongly decreased: see Fig. 5.6 displaying the temporal evolution of the surface averaged sub-grid scale turbulence intensity u'_Δ calculated according to Colin et al. (2000). This explains the prediction of pressure levels outside the experimental envelope for cycles with a pressure peak occuring after +38 CAD ATDC, e.g. cycles $1-S$, $2-S$ and $2-A$.

Self-adaptation to the turbulence conditions The dynamic model is found to self-adapt to the turbulence intensity. Thus, Fig. 5.6 shows lower values of $< u'_\Delta >$ in Case 2 (RPM 1300) compared to Case 1 (RPM 1800). The dynamic model predicts accordingly lower $\langle \Xi_\Delta \rangle$ values for Case 2, but with no need of parameter adjustment, whereas the parameter $\alpha_{t,CFM}$ of the ECFM-LES model has been decreases from 1.8 to 1.4 from Case 1 to Case 2, to predict lower $\langle \Xi_\Delta \rangle$ values between Case 1 and Case 2.

Advantage of the *local formulation* Figure 5.4 shows that the pressure evolution between simulations **C** (global formulation) and **D** (local formulation) differs significantly, simulations **D** showing a better agreement with the reference simulations **A**. This confirms that, as turbulence inside the combustion chamber is not isotropic, a local determination of exponent β is required to correctly predict the growth of the flame kernel. To confirm this, the spatial distribution of β_{loc} is displayed in Fig. 5.7, for two different crank angle. The surface averaged value $\beta_{loc,s}$ is indicated by the red plain line while the value predicted by the global formulation (β_{glob}) is indicated by the dashed black line. Corresponding values of Ξ_Δ, $\Xi_{\Delta,s}$ and $\Xi_{\Delta,glob}$ are also presented (right).
The mean value of β_{loc} is close to β_{glob}, meaning that averaging surfaces Σ_1 and Σ_2

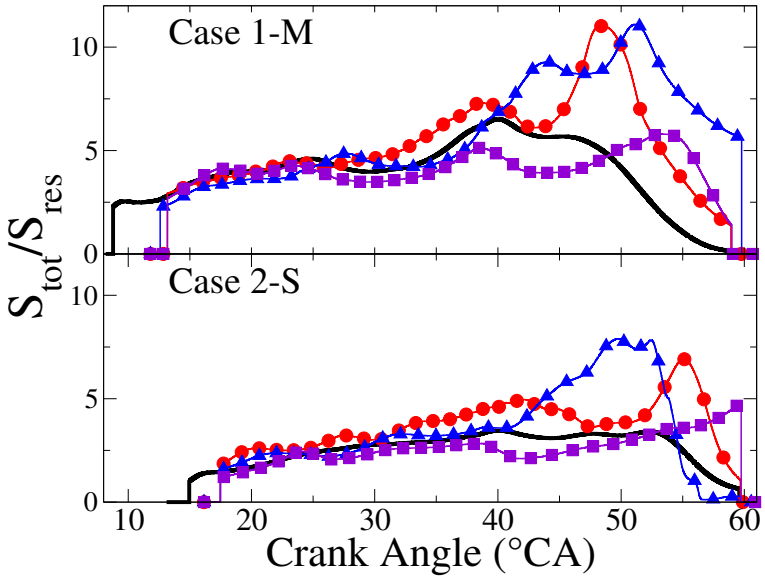

Figure 5.5: Temporal evolution of $\langle \Xi_\Delta \rangle = S_{tot}/S_{res}$, with $S_{res} = \int_\Omega |\nabla \tilde{c}| dV$ and $S_{tot} = \int_\Omega \Xi_\Delta |\nabla \tilde{c}| dV$. Black plain line: reference (**A**), squares: equilibrium formulation (**B**), triangles: global dynamic formulation (**C**), circles: local dynamic formulation (**D**). See Tab. 5.6 for cases correspondance.

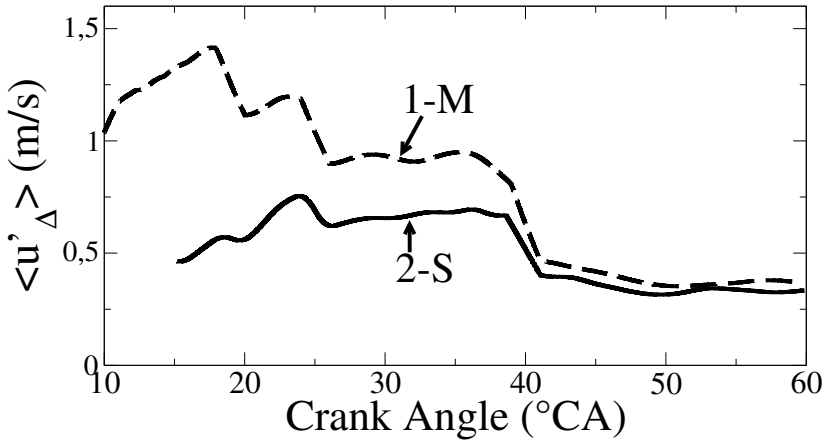

Figure 5.6: $< u'_\Delta >= \int_\Omega u'_\Delta \Sigma dV / S_{tot}$, the surface average turbulent intensity at scale Δ versus crank angle . See Tab. 5.6 for cases correspondance.

to calculate β_{glob} is similar to averaging local β_{loc} values. When the β_{loc} distribution is nearly symmetrical as at 22 CAD ATDC (Fig. 5.7b) $< \Xi_{glob} >$ is close to $< \Xi_{loc} >$. On the other hand, when the distribution presents a long tail towards large β_{loc} values as at 40 CAD ATDC, mean wrinkling factors estimated with the global formulation are substantially smaller than those using the local formulation (Fig. 5.7d). This finding is explained by the exponential relation between Ξ_Δ and β. Thus, the local formulation allows to account for the non-uniformity of the turbulence field in the engine, which is very significant considering the resulting difference of pressure levels predicted by the local and global formulations.

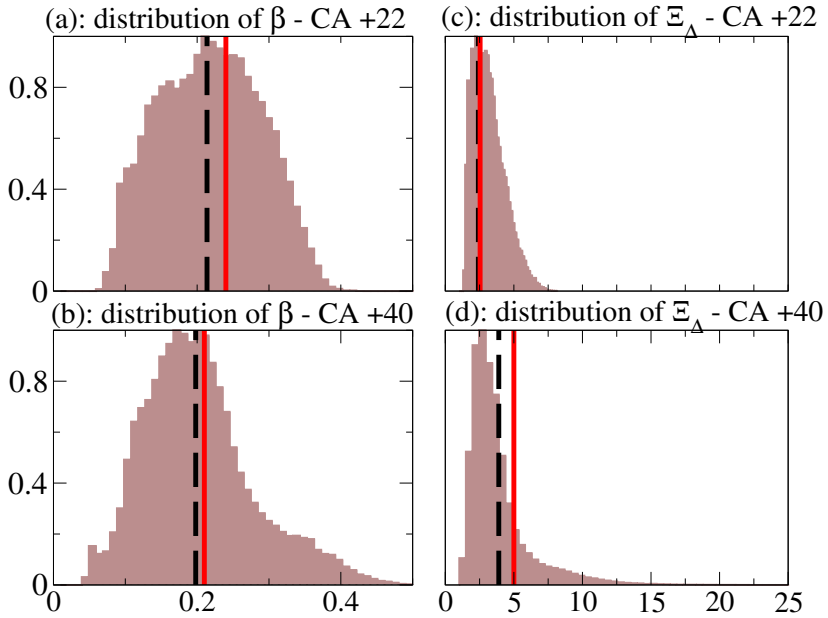

Figure 5.7: distributions of β_{loc} (a)-(b) and of $\Xi_{\Delta,loc}$ (c)-(d). Dashed black line: β_{glob} and $< \Xi_{\Delta,glob} >= \int_\Omega \Xi_{\Delta,glob} |\nabla \tilde{c}| dV / \int_\Omega |\nabla \tilde{c}| dV$ computed with the global formulation. Red plain line: surface average values $< \beta_{loc} >= \int_\Omega \beta_{loc} \Sigma dV / S_{tot}$ and $< \Xi_{\Delta,loc} >= S_{res}/S_{tot}$ computed with the local formulation. $\Sigma = \Xi_\Delta |\nabla \tilde{c}|$.

5.3 Conclusion

In this chapter, the modified dynamic wrinkling model coupled to the FSD algebraic Boger et al. model was applied in a spark ignition configuration. As a first validation step, calculations were started from an already grown and wrinkled flame kernel, as recommended by the analysis established in the previous chapter. Several engine cycles with strong cycle-to- cycle variability were simulated and results compared against results previously obtained with the reference ECFM-LES model. The dynamic model was proved to very well predict out-of-equilibrium wrinkling values and to account for the cycle-to-cycle variability, with no need for any model parameter adjustment and a moderate 20% CPU cost increase. These results confirm the strong potential of the dynamic approach .

Part III

Ignition study

Introduction to Part III

This part is dedicated to the simulations of the Laser-induced spark ignition cases experimentally investigated by Cardin et al. (2013). Motivations were presented in section 3.3.
The part is organized as follows:

- Chapter 6 describes the premixed methane/air Laser-induced spark ignition cases of Cardin et al. (2013). Main experimental results are presented.
- Chapter 7 presents the set-up employed in the simulations and discusses the parametric studies performed.
- Chapter 8 is dedicated to the simulations of the laminar ignition cases. The purpose of the study is to:
  - determine the ignition parameters (ignition energy, deposit radius...) and to characterize the role of kinetics (simplified and analytic schemes) in the laminar case.
  - better understand the ignition process in the laminar case observed in the experiments of Cardin et al. (2013).
- Chapter 9 is dedicated to the simulations of the turbulent ignition cases.

Chapter 6

Presentation of the Laser-induced spark ignition experiments

Contents

This chapter describes the Laser-induced spark ignition experiments of Cardin et al. (2013). The ignition trials were conducted in premixed methane/air mixtures at atmospheric conditions. Full details of the experiments can be found in the PhD manuscript of Cardin (2013). The experimental set-up and diagnostics that were employed are first briefly described in section 6.1.1. Main results are presented in section 6.2.

6.1 Experimental set-up and methods of measure

6.1.1 Description of the experimental set-up

All ignition trials were performed in a vertical wind tunnel, which is represented in the sketch of Fig. 6.1. It is composed of a vertical divergent-convergent chamber, containing a glass ball bed and a honeycomb to attenuate residual turbulent perturbations. The convergent provides a laminar and stationary flow with a flat velocity profile equal to 4 m/s. The MuSIG (Multi Scale Injection Grid, Mazellier et al.

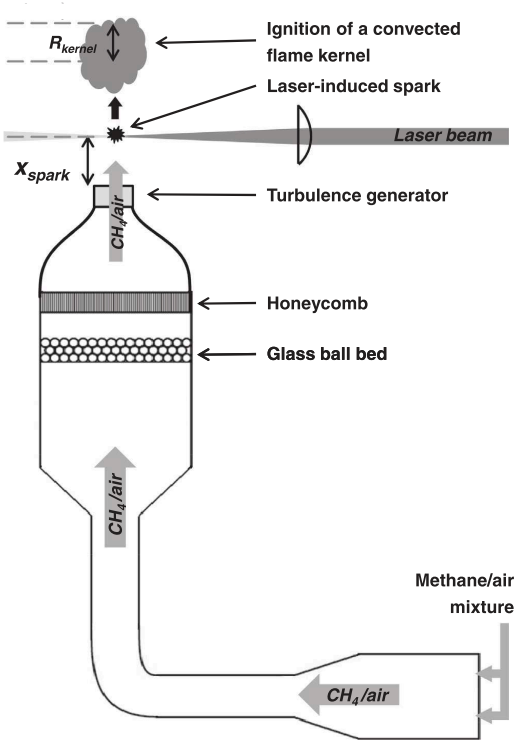

Figure 6.1: sketch illustrating the experimental set-up used by Cardin et al. (2013)

(2010)) is placed on the convergent to generate a homogeneous and isotropic turbulence with various turbulence characteristic (turbulence intensity u' and integral length l_t). Details will be given in next section 6.1.2.

This ignition system is illustrated in the sketch of Fig. 6.2, along with the different measurement devices:

- The spark is generated by a Laser Nd:Yag (wavelength is $\lambda = 532\ nm$). The duration of the pulse is $\tau_{pulse} = 8.2$ ns. To generate the spark at a given height x_{spark} above the turbulence grids, a system composed of a beam expander and a lens, with a focal length f of 200 mm, is used.

- The two energy meters determine the deposited energy E_d. Note that E_d is not equal to the energy of the Laser beam, therefore its determination requires a specific measurement procedure (which is not detailed here).

- A system including an intensified camera records images of the kernel development (kernel emission intensity), at times ranging from 20 μs to 3 ms after the breakdown. The camera is inclined from the laser beam with an angle of 24 degrees. The entire radiation spectrum emitted by the kernel is collected.

- The success or failure of an ignition trial is determined from the temporal evolution of the light that is emitted by the flame kernel is recorded during 30 ms. The detection system is placed 20 mm above the spark. When the ignition is successful, Cardin (2013) mentions that the passage of the flame

kernel in front of the detection system is observed around 10 ms after the start of the ignition laser, while when the ignition is not successful, no flame kernel passage is observed.

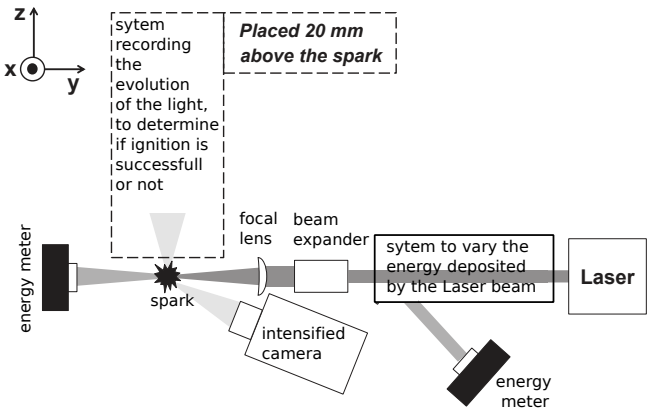

Figure 6.2: sketch of the ignition and measurement systems (top view). Cardin et al. (2013)

6.1.2 Properties of the turbulence generated by the MuSIG

Turbulence properties of the MuSIG are gathered in Tab. 6.1 (see Mazellier et al. (2010) for the details). As stressed by Cardin et al., grid turbulence decays spatially, between the moment of the energy deposition (corresponding to the position x_{spk} in Fig. 6.3) and the moment when the flame kernel has reached the position x_{kernel}. To account for this phenomenon, Cardin et al. spatially averaged all turbulence properties (operation denoted by $< \quad >$), between positions x_{spark} and $x_{spark} + H$ (see Fig. 6.3). Values obtained are reported in Tab. 6.1 as a function of the height of the energy deposition x_{spark} above the last grid of the MuSIG. The mean axial velocity U, the integral length scale l_t, the Kolmogorov length scale η_k, and the Kolmogorov time scale τ_k are also given. Values for η_k and τ_k were calculated based on the following relations:

$$\eta_k = \left(\frac{\nu^3}{\epsilon}\right)^{1/4} \tag{6.1}$$

and

$$\tau_k = \left(\frac{\nu}{\epsilon}\right)^{1/2} \tag{6.2}$$

where the kinematic viscosity ν and the turbulent dissipation rate ϵ were measured according to (Mazellier et al., 2010; Renou et al., 2002).

6.2 Experimental results

Section 6.2.1 presents the results of the laminar ignition cases, which are essential to understand the results established in the turbulent case, presented in section 6.2.2.

x_{spark} (mm)	$< U >$ (m/s)	$< u' >$ (m/s)	$< l_t >$ (mm)	$< \eta_k >$ (μm)	$< \tau_k >$ (μs)
60	6.36	1.88	4.91	50	128
65	6.05	1.72	4.96	51	136
70	5.78	1.58	5.06	54	148
80	5.36	1.34	5.35	59	181
90	4.08	1.14	6.75	65	222
100	4.89	1.00	6.21	71	268
124	4.66	0.77	7.38	85	379
144	4.55	0.66	8.25	94	460

Table 6.1: Properties of the turbulence generated by the MuSIG (Mazellier et al., 2010). Average quantities were obtained by spatial average (Cardin et al., 2013) .

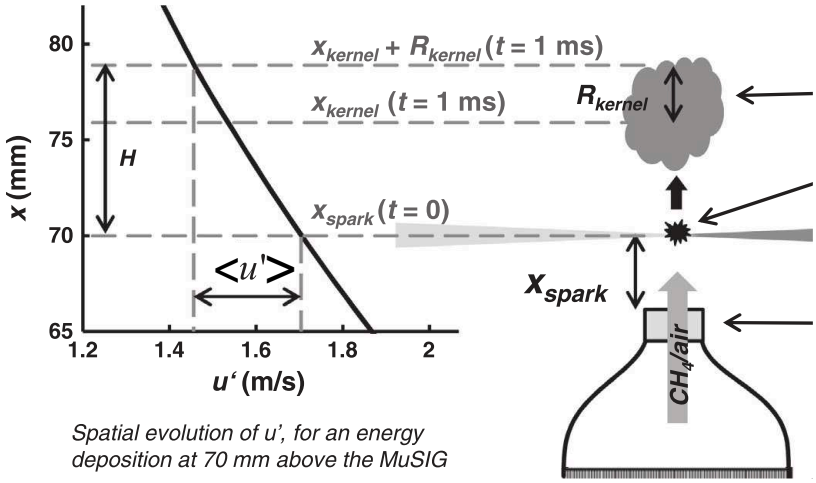

Figure 6.3: Sketch illustrating the spatial averaging operation $<\ >$ of the MuSIG turbulence properties displayed in Tab 6.1 (Cardin et al., 2013).

6.2.1 Laminar ignition cases

6.2.1.1 MIE measurements

Results of minimum ignition energy measurements in the laminar case (values are denoted MIE_0) for the different equivalence ratios are reported in Tab. 6.2. Values of the uncertainty on the MIE_0 values, ΔMIE_0, are also indicated. The method employed by Cardin et al. to measure MIE is explained in Annexe 9.4. To validate their results, the authors compared their measurements against values reported in the literature for the same pressure and temperature conditions: Lewis and Von Elbe (1987) and Huang et al. (2007) (spark plug ignition cases), Beduneau et al. (2003)

ϕ	0.55	0.58	0.6	0.63	0.65	0.7	0.75	0.8	0.85
MIE_0 (mJ)	6.25	3.68	3.27	2.58	1.9	0.7	1.10	0.85	0.6
ΔMIE_0	0.42	0.37	0.31	0.32	0.29	0.31	0.18	0.17	0.13

Table 6.2: Measurements of MIE in the laminar flow (denoted MIE_0) as a function of the equivalence ratio ϕ, premixed methane/air mixture. ΔMIE_0 is the uncertainty on the MIE_0 value. (Cardin, 2013)

(using two different focal length f) and Phuoc and White (1999) (Laser-induced spark ignition cases). The comparison is displayed in Fig. 6.4. All results are consistent: MIE_0 values decrease with the equivalence ratio ϕ. However, MIE values measured in the different studies differ. It is well known in the literature that MIE values determined in spark plug ignition cases are different from the ones of Laser-induced spark ignition cases (main reasons were mentioned in section 2.2). To explain the differences of the MIE values between the different Laser-induced spark ignition studies, Cardin et al. follow the conclusions established by Beduneau et al. (2003): the MIE depends on the volume of the energy deposited by the Laser beam, denoted V_d. The volume V_d is illustrated in the sketch of Fig. 6.5. According to Beduneau et al. (2003), when the volume V_d decreases, the energy density of the deposit increases, therefore the breakdown threshold is decreased and the MIE decreases. Cardin have thus estimated the volume of energy deposition volume in their study and the ignition volume in the study of Phuoc and White and of Beduneau et al.. They could establish that:

$$(V_d)_{Beduneau,f=50\ mm} < (V_d)_{Cardin} < (V_d)_{Beduneau,f=100\ mm} < (V_d)_{Phuoc} \tag{6.3}$$

which is consistent with the MIE results:

$$(MIE)_{Beduneau,f=50\ mm} < (MIE)_{Cardin} < (MIE)_{Beduneau,f=100\ mm} < (MIE)_{Phuoc} \tag{6.4}$$

These observations are important, because they highlight the fact that the MIE depends on the energy density deposited by the Laser, this energy density depending on the Laser wavelength and on the focal lens characteristics.

6.2.1.2 Evolution of the flame kernel characteristics during ignition

Prior to study ignition in turbulent mixtures, the flame kernel characteristics in laminar flow are determined. Attention is paid in particular to the evolution of the flame kernel: size, shape and emissions intensity.

Size of the flame kernel Figure 6.8 displays instantaneous images of the kernel, at times ranging from $t = 50\ \mu s$ to $t = 1500\ \mu s$, for different equivalence ratios. For each equivalence ratio, the MIE_0 is deposited value and a misfire and a fire case are displayed. The size of the kernel decreases as the equivalence ratio ϕ increases. This is because the deposited energy E_d decreases with the equivalence ratio. A smaller deposited energy E_d leads to the formation of a smaller plasma. This can be seen

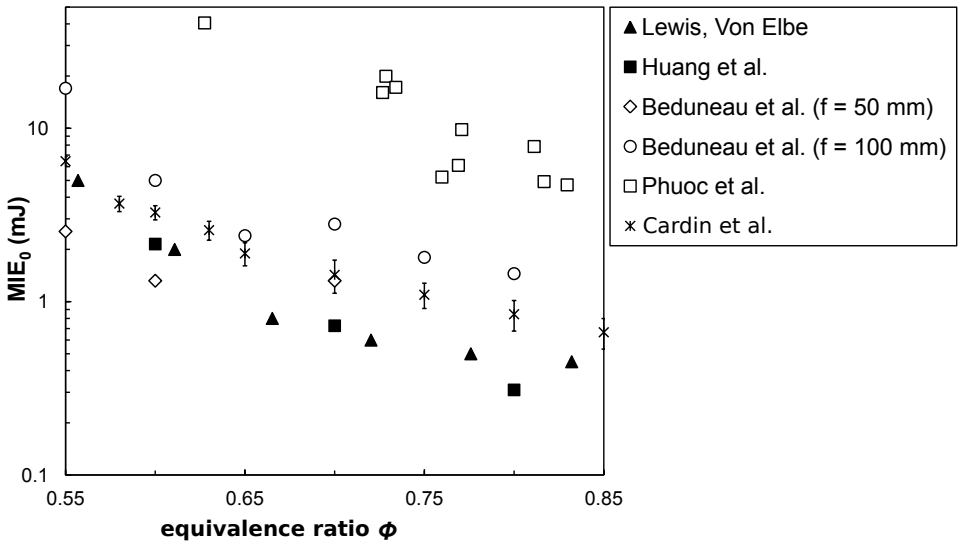

Figure 6.4: MIE measurements in the laminar case (MIE_0) as a function of the equivalence ratio ϕ in laminar methane/air mixtures. Comparison with data reported by Lewis and Von Elbe (1987), Phuoc and White (1999), Huang et al. (2007), Beduneau et al. (2003) and Cardin et al. (2013). Graph from Cardin et al. (2013).

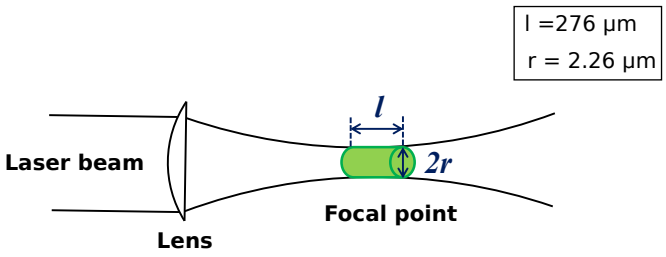

Figure 6.5: Sketch of the energy deposit volume V_d at the focal point, with the dimensions l and r measured by Cardin (2013).

in Fig. 6.6, showing images of the spark for different Laser energy and in Fig. 6.7 which displays the dimensions of the plasma (width and length) for different Laser energy and different focal length f: dimensions of the plasma decrease when the deposited energy E_d decreases. A smaller plasma leads to a smaller flame kernel.

Definition of the chain branching time τ_{CB} Figure 6.9 presents the temporal evolution of the kernel emission intensity, obtained by post-processing of the instantaneous emission images of the flame kernel recorded by the intensified camera (indicated in Fig. 6.2). In Fig. 6.9 a very high emission intensity peak is first seen, caused by the important concentration of radicals generated by the breakdown. Then, the mean emission intensity decreases. The authors suggest that this is because radicals recombine, leading to a decreased radical concentration in the hot kernel. The decrease of the mean intensity is globally the same for all cases, which means that the recombination process is independent of ignition success and of equivalence ratio. This is confirmed by observing the instant $t = 50\ \mu s$ in Fig. 6.8: the appearance of the kernel is very similar in the firing cases and the non-firing

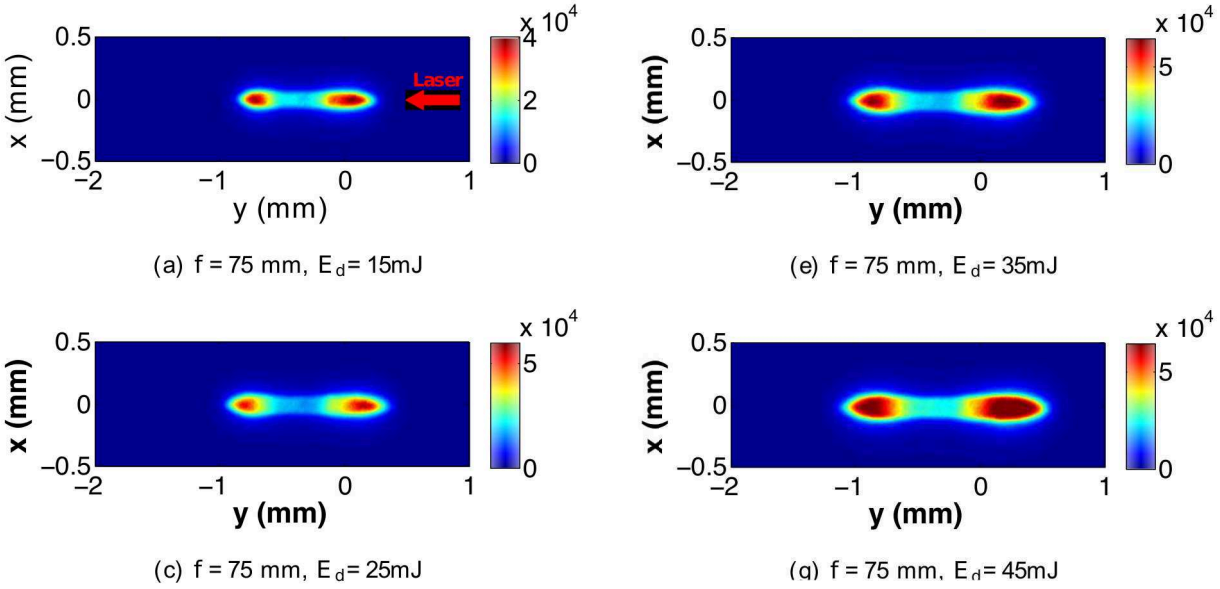

Figure 6.6: Recordings by ICCD camera of the spark in air, at $t = 11$ ns after the Laser shot, for different deposited energy E_d and same focal length f. Images from Cardin (2013).

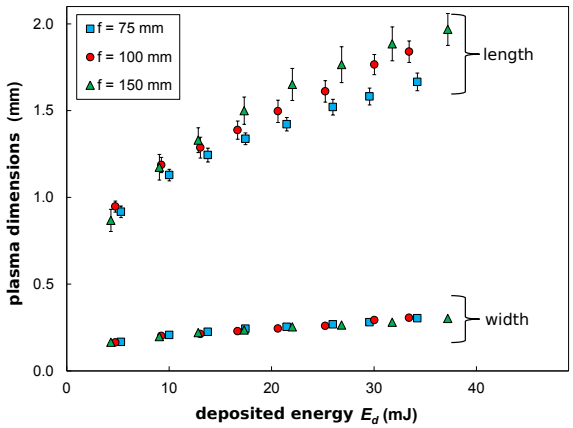

Figure 6.7: dimensions of the plasma (length and width) as a function of the deposited energy E_d, for three different focal length $f = 75$, 100 and 150 mm. Instant $t = 11$ ns. Graph from Cardin (2013).

cases. A few hundreds μs after the start of the breakdown process, the curves of firing and misfiring cases in Fig. 6.9 start to evolve differently. For firing cases, after a certain critical time, the mean intensity increases, while for the non-firing cases it keeps decreasing. This critical time, denoted by the authors τ_{CB}, depends on the equivalence ratio ϕ: when the equivalence ratio increases from $\phi = 0.58$ to $\phi = 0.75$, the critical time decreases from $\tau_{CB} = 820$ μs to $\tau_{CB} = 150$ μs. This is consistent with Fig. 6.8: for instance for $\phi = 0.75$, almost no kernel emission can be seen at $t = 300$ μs, while for $\phi = 0.55$, some emissions can still be observed at $t = 1500$ μs. The authors interpret the critical time τ_{CB} as a chemical time, which represents the time required for the chain branching reactions to develop. They explain that during this time, the number of radicals generated by the breakdown must be sufficiently high to generate enough chemical reactions to cause the hot kernel to release

a sufficient amount of energy to grow and compensate heat losses. Based on the mean intensity curves, the authors determine the critical time τ_{CB} for the different equivalence ratios: τ_{CB} is obtained intersecting the two parts of the mean emission intensity curves displayed in Fig. 6.9 (left part: exponential behavior, right part: quasi-linear behavior). Values of τ_{CB} are displayed in the graph of Fig. 6.10 and also reported in Tab. 6.3. Authors also indicated the value of τ_{CB} for equivalence ratio $\phi = 1$, extrapolated from the study of Beduneau et al. (2009). τ_{CB} is a key quantity, because as discussed in the next section 6.2.2, Cardin et al. suggest that the transition in the turbulent ignition regime occurs when the Kolmogorov time τ_k becomes smaller than the characteristic time τ_{CB}.

equivalence ratio ϕ	0.55	0.58	0.6	0.63	0.65	0.7	0.75	0.8	0.85
MIE_0 (mJ)	6.25	3.68	3.27	2.58	1.9	1.43	1.1	0.85	0.67
τ_{CB} (μs)	927	822	711	567	304	167	150	140	148

Table 6.3: Values of the chain-brainching time τ_{CB} determined by Cardin et al. (2013), for different equivalence ratios ϕ. Corresponding MIE_0 values are also reported.

6.2.2 Turbulent ignition cases

The results established in the turbulence case by Cardin et al. were presented in section 2.3.2, in Figs. 2.17 and 2.18. To interpret the ignition regimes, Cardin et al. explain that when the Kolmogorov time τ_k is of the same order of magnitude or larger than the chain-branching time τ_{CB}, then turbulence does not interfere with the initiation of the combustion reactions. This is why the MIE measured remains close the MIE value in the laminar case (MIE_0). In Fig. 2.18, left and middle columns correspond to this situation: the shape of the kernel remains spherical and is not much wrinkled. When the Kolmogorov time τ_k becomes smaller than the chain-branching time τ_{CB}, then turbulence does interfere with the initiation of the chain-branching reactions. The flame front is disrupted, as seen in Fig. 2.18-right column, more energy is required to ignite because of the increased energy dissipation by turbulence.

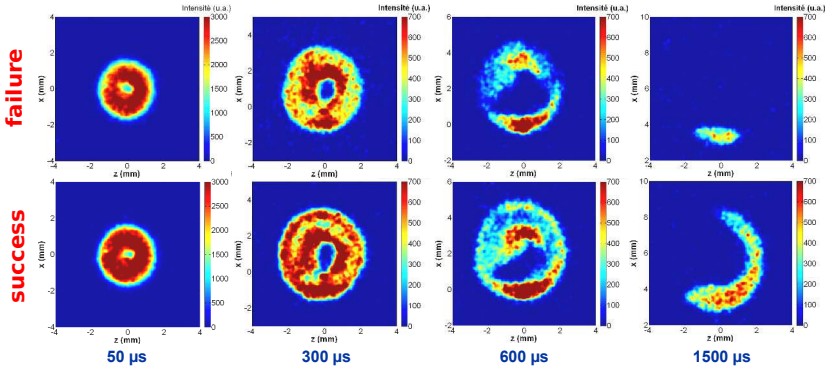

(a) φ = 0.55

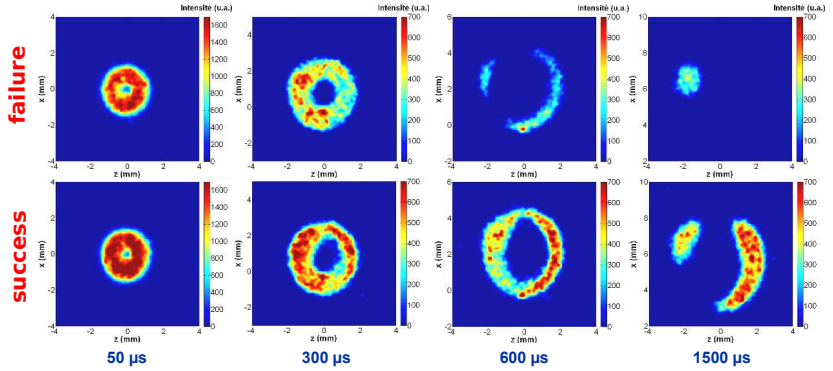

(b) φ = 0.60

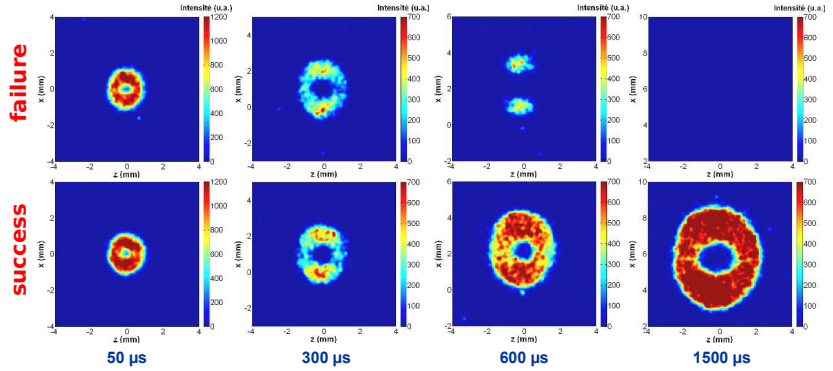

(c) φ = 0.65

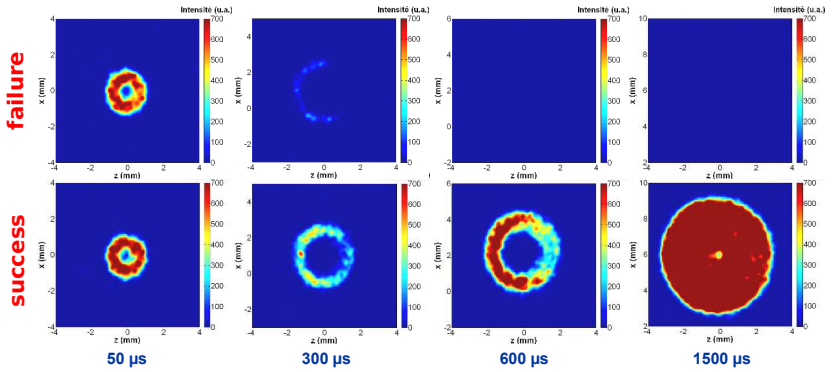

(d) φ = 0.75

Figure 6.8: Instantaneous emission (total spectrum) images of the kernel, for different equivalence ratios. The deposited energy E_d is the MIE_0 value of the corresponding equivalence ratio. The color scale is the same except for timing $t = 50\ \mu s$. Cardin (2013).

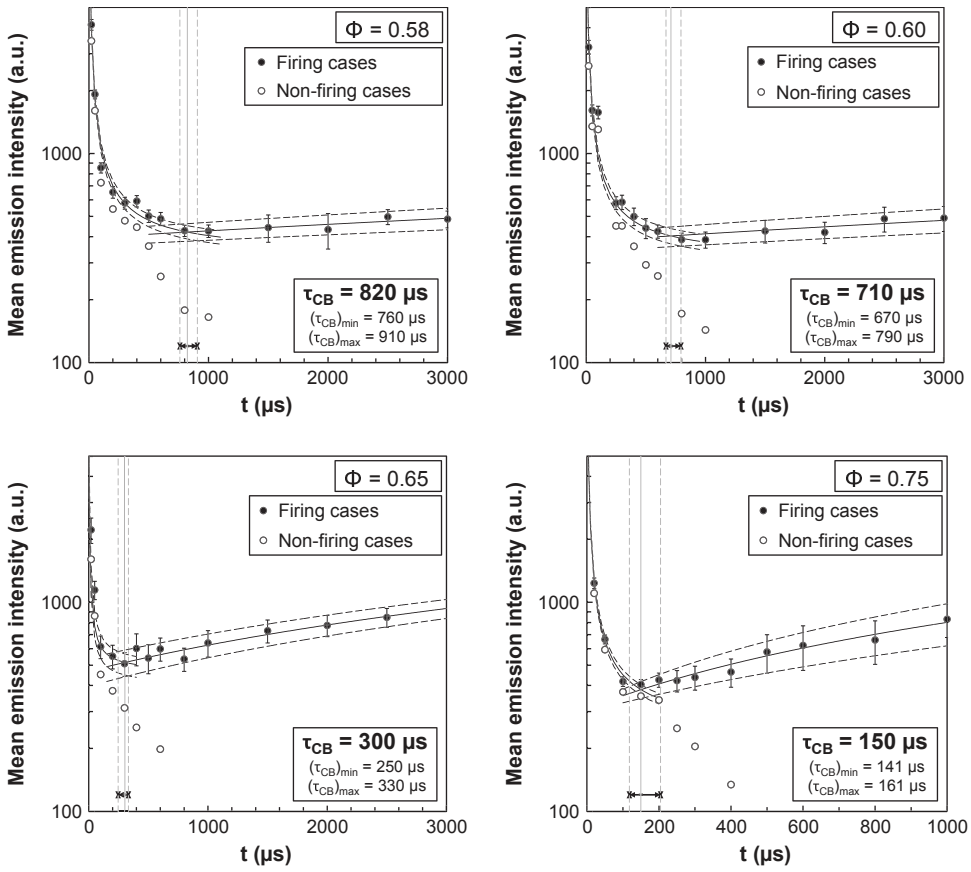

Figure 6.9: Temporal evolution of the mean emission intensity of the flame kernel for firing and nonfiring cases, for different equivalence ratios. The deposited energy is the MIE_0 value of the corresponding equivalence ratio. Cardin et al. (2013).

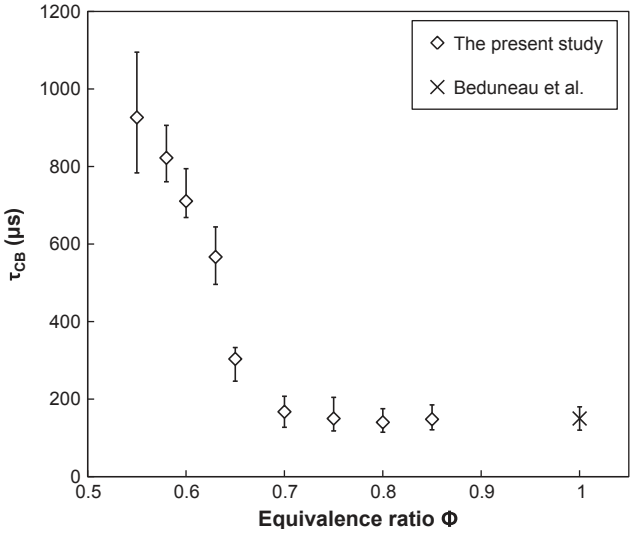

Figure 6.10: Chemical time τ_{CB} as a function of the equivalence ratios ϕ. At $\phi = 1$, τ_{CB} was determined based on the measurements by Beduneau et al. (2009). Graph from the study of Cardin et al. (2013) .

Chapter 7

Set up methods for the ignition study

Contents

In this chapter, set-up and methods employed in the ignition simulations are presented.

7.1 Presentation of the ignition cases

The different parameters used in the ignition simulations are presented and their choice justified when necessary: parameters of the mixture (equivalence ratio ϕ and Lewis numbers Le_k) in section 7.1.1, the energy deposit parameters (duration τ_{dep} and radius r_0) in section 7.1.2. The different kinetic schemes employed are presented in section 7.1.3 and the numerical set-up in section 7.1.4.

7.1.1 Mixture parameters

7.1.1.1 Equivalence ratio ϕ

The ignition study aims at improving the understanding of critical ignition cases with low laminar flame s_L. These ignition cases correspond to engine conditions with very lean equivalence ratio or with stoichiometric equivalence ratio and high EGR rate. To facilitate the calculation in terms of CPU resources, ignition cases with very lean equivalence ratios were investigated because these cases present a laminar flame thickness that is larger than cases near the stoichiometry: then the cell size Δ_x required to simulate lean equivalence ratio ignition case can be larger. Accordingly, among the different equivalence ratios investigated in the experiments of Cardin et al. (2013), the very lean equivalence ratio case $\phi = 0.6$ was chosen. The case $\phi = 0.55$ was also considered, closest equivalence ratio to the lean flammability limit for which experimental measurements are provided. Finally, the equivalence ratio $\phi = 0.85$ was investigated as well, as a reference of non-critical ignition case.

7.1.1.2 Species Lewis number Le_k

Lewis numbers are essential to determine the MIE, as pointed out in studies considering (Champion et al., 1986; Tromans and Furzeland, 1986; Chen et al., 2011). Effects of the Lewis number on the MIE when using the 2-step kinetic scheme and the analytic scheme must be therefore evaluated. Besides, when using the high temperature D'Angola law (section 3.1.2.2), Lewis numbers are governed by temperature and vary with space and time. A parametric study is then also required to characterize these effects.

According to its definition, Lewis numbers $Le_k = D_{th}/D_k$ depend on the law employed to calculate the laminar viscosity $\mu(T)$, entering the species diffusivity coefficient D_k, and to calculate the thermal Fourier coefficient $\lambda(T)$, entering the thermal diffusivity D_{th}. As explained in section 3.1.2.2, the D'Angola law is used to correctly estimate the laminar viscosity μ and the thermal Fourier coefficient λ. But using D'Angola Eqs. (3.1) and (3.2) to respectively compute coefficients μ and λ implies that the resulting Lewis number Le_k locally depends on the temperature T, leading to:

$$Le_k(T) = \frac{D_{th}(T)}{D_k(T)} = \frac{\lambda(T) Sc_k}{\mu(T) C_p(T)} \tag{7.1}$$

where the Schmidt number Sc_k is constant and extrapolated from 1D flame calculations using complex transport coefficients. In order to characterize the effect of the Lewis number Le_k on the MIE estimation, but still correctly estimating the

diffusivity at high temperature, different groups of simulations are considered, corresponding to different values of Lewis number Le_k (see Table 7.1):

1. **Diffusion 1 (D1)**: both coefficients μ and λ are calculated using the D'Angola law (Eqs. (3.1) and (3.2)). The species Schmidt number Sc_k are for all species: $Sc_k = 0.7$. Accordingly, the Lewis number Le_k locally depends on the temperature and is the same for all species.

2. **Diffusion 2 (D2)**: coefficient μ is calculated using the D'Angola law (Equation (3.1)) but the thermal Fourier coefficient λ is calculated according to the classical relation:
$$\lambda(T) = \frac{\mu(T)C_p(T)}{Pr} \tag{7.2}$$
and following relation is imposed, to ensure unity Lewis numbers ($Le_k = 1$):
$$Sc_k = Pr \tag{7.3}$$
Performing 1D methane/air flame complex chemistry calculations, $Pr = 0.7$ was found the best fit to complex diffusion law.

3. **Diffusion 3 (D3)**: coefficient μ is calculated using the D'Angola law. Thermal Fourier coefficient λ is calculated according to Equation (7.2). The Sc_k values may differ from one species to another and may differ from the Prandtl number Pr; they are obtained from complex diffusion laws.

Comparing simulations of group (D1) and (D2) $Le_k = 1$ will characterize the high temperature diffusion effects on MIE prediction. Note that simulations using classical diffusion law, such as the Sutherland's law, are not performed as these laws do not predict the correct diffusivity at high temperatures. Finally, comparing simulations of group (D2) and (D3) will characterize eventual discrepancies of MIE prediction between $Le_k = 1$ and $Le_k \neq 1$.

Groups	laminar viscosity μ	Fourier coefficient λ	Le_k
D1	D'Angola law	D'Angola law	$Le(T)$
D2	D'Angola law	Eq.(7.2)	$Le_k = 1$
D3	D'Angola law	Eq.(7.2)	$Le_k \neq 1$

Table 7.1: The different groups of simulations, corresponding to different Lewis number Le_k.

7.1.2 Parameters of the energy deposit

7.1.2.1 Deposit duration τ_{dep}

The energy deposit duration τ_{dep} is fixed to an unique value for all calculations and corresponds to a short duration, since Cardin et al. (2013) used a Laser beam of 8.2 ns duration (section 6.1.1). The deposit duration τ_{dep} is determined according

to the hypothesis presented in section 3.1.2.2 and to the conclusions established by Frendi and Sibulkin (1990). τ_{dep} is chosen such as:

$$\tau_{dep} = 25\ \mu s \tag{7.4}$$

Main conclusions of Frendi and Sibulkin study justifying this choice are recalled below:

- if $\tau_{dep} < 2 - 5\ \mu s$, then τ_{dep} becomes of the same order of magnitude as the characteristic time of the pressure wave propagation, which dissipates a part of the input energy E_{ign}. As it was assumed that the present ignition simulations do not account for the pressure wave propagation (section 3.1.2.2), the duration τ_d is chosen longer than 5 μs.

- if $\tau_{dep} > 100\ \mu s$, then the deposit duration becomes of the same order of magnitude as the heat diffusion time τ_{diff}. This situation does not correspond to a physical short duration spark ignition. An estimation of τ_{diff} will be proposed in section 7.2.4 to confirm the conclusions of Frendi and Sibulkin. Also, when $\tau_d > 100\ \mu s$, τ_{dep} becomes of the same order of magnitude as the Kolmogorov time τ_k, which smallest value in Cardin et al. (2013) experiments is $\tau_k = 128\ \mu s$ (Table 6.1).

According to these observations, the deposit duration τ_{dep} must verify $10\ \mu s < \tau_{dep} < 100\ \mu s$. The duration $\tau_{dep} = 25\ \mu s$ was finally chosen, after performing additional tests using $\tau_{dep} = 50\ \mu s$ and $\tau_{dep} = 15\ \mu s$, which showed that there was no significant variations of the MIE.

7.1.2.2 Deposit radius r_0

The dependency of the MIE on the deposit radius r_0 was investigated by previous studies, presented in section 3.1.2.2. Despite these existing analysis, parametric studies MIE $= f(r_0)$ are performed because: (i) values of MIE for different deposit radii r_0 must be determined for the present study, (ii) two types of kinetic schemes are compared in the ignition study and the comparison of MIE prediction for different deposit radii r_0 can provide very useful information; (iii) thanks to this parametric study, further understanding of the relation between size of the energy deposit and size of the initial flame kernel is provided (see section 8.2).

The parametric study consists to determine for a given deposit radius r_0 which energy E_{ign} is required to successfully ignite or not. As it will be evidenced in Chapter 8, the range of deposit radius r_0 investigated depends in fact on several factors: equivalence ratio ϕ and temperature in the ignition zone.

7.1.3 Kinetic schemes employed

According to Sloane and Ronney (1992) (section 3.1.2.3), kinetic schemes should recover both the laminar flame speed s_L and the auto-ignition delays τ_{ai} to correctly predict ignition. Simplified kinetic schemes, which are widely used in complex configurations because of their reduced CPU costs, cannot today recover both the correct laminar flame speed and the correct auto-ignition delays. On the other hand,

analytical schemes have a strong potential to predict ignition in complex configurations, because they can reproduce correct auto-ignition delays and laminar flame speeds with affordable CPU costs (section 1.1.5). A problematic which is therefore addressed in the ignition study is to characterize eventual ignition discrepancies (in terms of MIE, flame kernel growth rate), when using an analytical chemistry and a simplified chemistry. The study will help in particular to determine if an accurate prediction of auto-ignition delays and of radicals formation is required to predict ignition. The study will finally provide an useful evaluation of analytical kinetic schemes, which are currently object of high interest for the LES community (Franzelli et al., 2013; Bauerheim et al., 2015), for all problems requiring more precise chemical description (for pollutants formation).

7.1.3.1 Analytical schemes

The analytical scheme used is the present study was proposed in the PhD thesis of T. Jaravel (CERFACS), derived using the code Yarc developed by Pepiot (2008). The reference detailed scheme is the GRImech 2.11 (Bowman et al., 1995) presenting 49 species and 277 reactions. Targets conditions are a set of five laminar freely-propagating premixed flames, of equivalence ratio ranging between $\phi = 0.6$ and $\phi = 1.4$, at atmospheric pressure and temperature. The final skeletal mechanism presents $n_{sk} = 40$ species.
In the final analytical mechanism, 22 species are transported : CH_4, O_2, N_2, CO, CO_2,H_2O, H_2, H, O, OH, HO_2, CH_3, CH_2O, H_2O_2, CH_3OH, C_2H_2, C_2H_6, C_2H_4, NO, NO_2, HCN, N_2O. 15 following species are assumed to be to the QSS : CH_2, CH_2(S), HCO, CH_2OH, C, CH, C_2H_3, C_2H_5, CH_3O, HCCO, NH_2, NCO, HNCO, HNCO, HOCN.

7.1.3.2 Simplified scheme

A 2-step simplified kinetic scheme is used. The pre-exponential Arrhenius constant A and the activation energy E_a coefficients were adjusted in order to recover the laminar flame speed s_L predicted by the detailed mechanism GRImech. The corresponding kinetic parameters are given in Table 7.2.

reaction	A ($cm^3mol^{-1}s^{-1}$)	β	E_a($cal.mol^{-1}$
$CH_4+\frac{3}{2}O_2 \rightarrow CO+2H_2O$ forward coefficients $\nu_{CH_4} = 0.5$, $\nu_{O_2} = 0.65$	$3.6 * 10^9$	0.0	35500
$CO+\frac{1}{2}O_2 \leftrightarrow CO_2$	$2 * 10^8$	0.7	12000

Table 7.2: Parameters for the 2-step simplified scheme for CH_4/air used in the ignition study.

7.1.4 Numerical setup for the laminar 3D ignition case

The size of the calculation domain is constrained by the size of the energy deposit and by the flame kernel growth rate. Two types of domain were used for the simulations of laminar ignition:

- **Domain D1:** 3D square domaine of length $L = 3.2$ mm for ignition cases with a small initial radius $r_0 < 1.6$ mm. Physical simulation time: 3 ms.
- **Domain D2:** 3D square domaine of length $L = 6.4$ mm for ignition cases with large initial radius: $r_0 > 1.6$ mm. Physical simulation time: 6 ms.

The cell size Δx is constrained by the number of points required to:

- discretize the energy deposit.
- discretize the flame front at small radii, and the intermediate and radicals profiles when using the analytical chemistry.

The chosen grid resolutions for the different ignition cases are specified in Table 7.3. Boundary conditions are standard Navier-Stokes boundary conditions (NSCB (Poinsot and Lele, 1992)) of non-reflecting outlet type, with $P_{outlet} = P_{atm}$.

equivalence ratio	simplified scheme	analytical scheme
$\phi = 0.6$ / $\phi = 0.55$	$\Delta_x = 50\ \mu m$	$\Delta_x = 40\ \mu m$
$\phi = 0.85$	$\Delta_x = 25\ \mu m$	$\Delta_x = 25\ \mu m$

Table 7.3: Grid resolution used for the different equivalence ratios and the different kinetic schemes

7.2 Preliminary calculations for the ignition study

The ignition process results of an auto-ignition phenomenon and on the balance between heat diffusion and flame propagation. Accordingly, to characterize ignition, following quantities must be evaluated: the laminar flame speed s_L, the flame thickness δ_L, the auto-ignition delays τ_{ai} and the characteristic heat diffusion time τ_{diff}. Calculations of the auto-ignition delays τ_{ai} are therefore presented in section 7.2.1, calculations of 1D flames in section 7.2.2. In section 7.2.3, a definition of an ignition time τ_{ign} accounting for the temporal variation of temperature during ignition is proposed. Finally, the estimation of the characteristic heat diffusion time τ_{diff} is presented in section 7.2.4.

7.2.1 Auto-ignition delays τ_{ai}

Auto-ignition delays τ_{ai} of the 2-step, analytical scheme and detailed mechanism GRImech are presented in Fig. 7.1, for the equivalence ratio $\phi = 0.6$. Conclusions are similar to the ones established by Sloane and Ronney (1992) (Table 3.1): the simplified kinetic scheme predicts ignition delays much shorter than the ones predicted

by the detailed mechanism. Also, auto-ignition delays predicted by the analytical scheme are in very good agreement with the auto-ignition delays predicted by the detailed mechanism, which is consistent with the conditions of reduction used to derive this scheme.

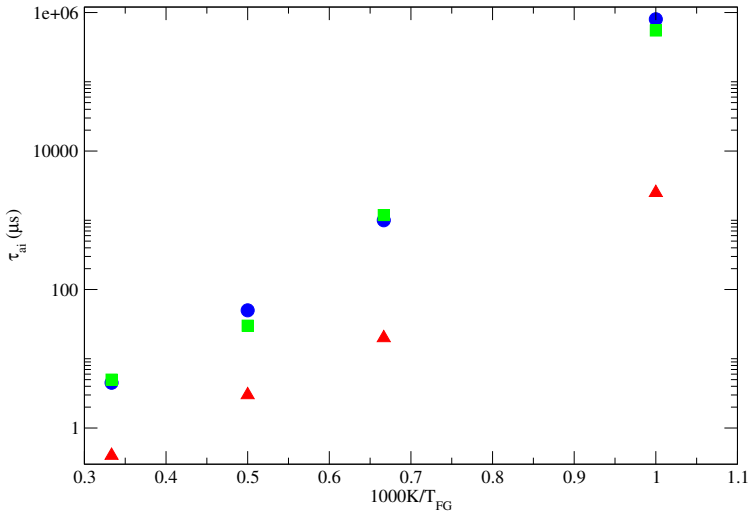

Figure 7.1: Ignition delays τ_{ai} (CHEMKIN calculation). blue circle: GRImech, green square: analytical scheme, red triangle: 2-step simplified scheme.

7.2.2 1D flame calculations

Results of the 1D flames calculation using AVBP are presented below. The computational domain is 2D, of length $L = 20$ mm and of width $l = 20$ cm. The grid cell is $\Delta_x = 50\ \mu m$ for the case $\phi = 0.55$ and $\phi = 0.6$ and $\Delta_x = 25\ \mu m$ for the case $\phi = 0.85$. Boundary conditions are indicated in Fig. 7.2.

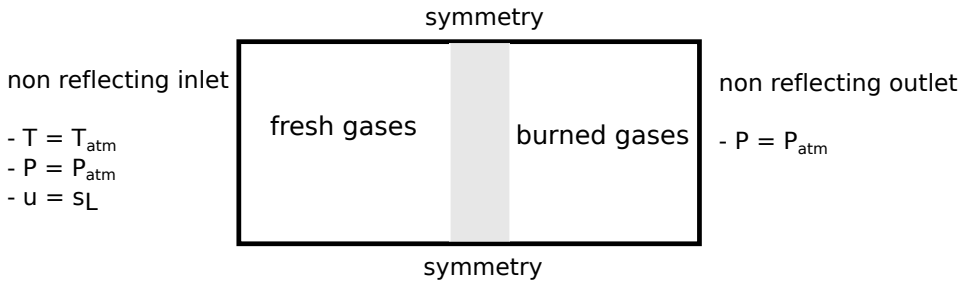

Figure 7.2: Sketch illustrating the 2D computational domain for the 1D flame calculations. Boundary conditions are determined according to the NSCBC method Poinsot and Lele (1992).

Results Figure 7.3 presents 1D temperature profiles obtained using the simplified scheme (plain line) and the analytical scheme (dashed line) and using the detailed mechanism GRImech (dashed line with symbols, CHEMKIN calculation). The profiles obtained for the three equivalence ratios are displayed. Values of the laminar

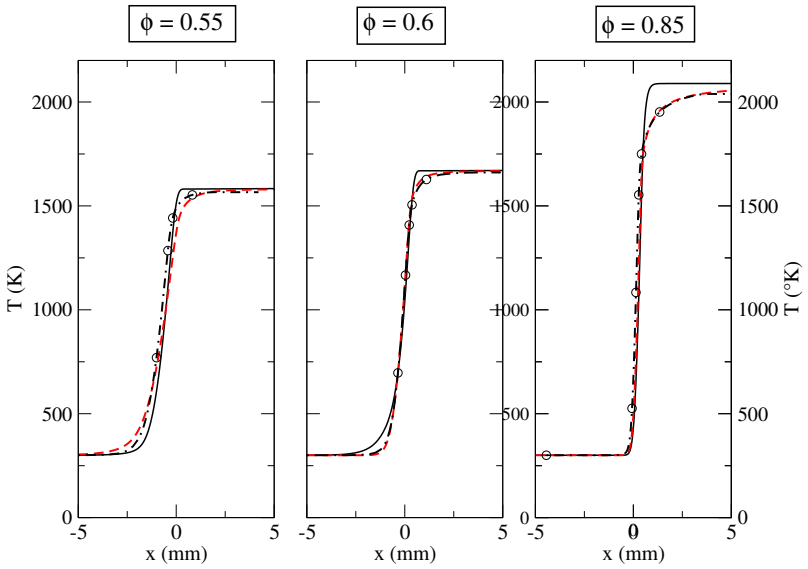

Figure 7.3: 1D temperature profile of planar laminar flame, for equivalence ratios $\phi = 0.55$, $\phi = 0.6$ and $\phi = 0.85$. Plain line: 2-step kinetic scheme (D2), dashed line: analytical scheme (D2), symbols: GRImech mechanism (CHEMKIN calculation).

flame speed s_L and of the laminar flame thickness δ_L obtained for the different schemes and for the equivalence ratios $\phi = 0.6$, $\phi = 0.55$ and $\phi = 0.85$ in Table 7.4, 7.6 and 7.5 respectively. The laminar flame thickness δ_L is calculated according to:

$$\delta_L = \frac{T^{bg} - T^{fg}}{\max\left|\frac{\partial T}{\partial x}\right|} \tag{7.5}$$

while the laminar flame speed s_L is calculated according to:

$$s_L = \frac{-\dot{\Omega}_F}{\rho^u Y_F l} \tag{7.6}$$

where $\dot{\Omega}_F$ is the overall fuel consumption rate and l the width of the simulation domain.

scheme	s_L (cm/s)	δ_L (mm)	Δx_{min} (μm)	n_{res}
GRImech	11.56	0.96	5	200
analytical scheme (D2, $Le_k = 1$)	11	0.95	50	20
simplified scheme (D2, $Le_k = 1$)	11.42	0.93	100	10

Table 7.4: Laminar flame speed calculation CH_4/air, $\phi = 0.6$. Simulations (D2). Δx_{min} indicates the minimal discretization required.

In Fig. 7.3, the analytical scheme very well reproduces the temperature profile of the detailed mechanism GRImech for the three equivalence ratios. The 2-step kinetic scheme shows good agreement with the two other schemes for equivalence

scheme	s_L (cm/s)	δ_L (mm)
GRImech	31.2	0.48
analytical scheme (D2, $Le_k = 1$)	27	0.5
simplified scheme (D2, $Le_k = 1$)	33	0.39

Table 7.5: Laminar flame speed calculation CH_4/air, $\phi = 0.85$

scheme	s_L (cm/s)	δ_L (mm)
GRImech	7.95	1.42
analytical scheme (D2, $Le_k = 1$)	7.06	1.4
simplified scheme (D2, $Le_k = 1$)	8.51	1.18

Table 7.6: Laminar flame speed calculation CH_4/air, $\phi = 0.55$

ratios $\phi = 0.6$ and $\phi = 0.55$, even if the temperature profile is slightly steeper. For the equivalence ratio $\phi = 0.85$, the same laminar flame speed as the one predicted by the GRImech mechanism is recovered but the temperature profile is much steeper.

Lewis effect As the value of the Lewis number of the fuel is close to unity ($Le_{CH_4} = 0.96$), effects of the Lewis number Le_k (between case (D2, $Le_k = 1$) and case (D3, $Le_k \neq 1$)) on the 1D profiles of temperature and main species is not significant. Figure 7.4 presents 1D profiles of CH_4 and H_20 obtained with the analytical scheme, for calculations of group (D2) and (D3).

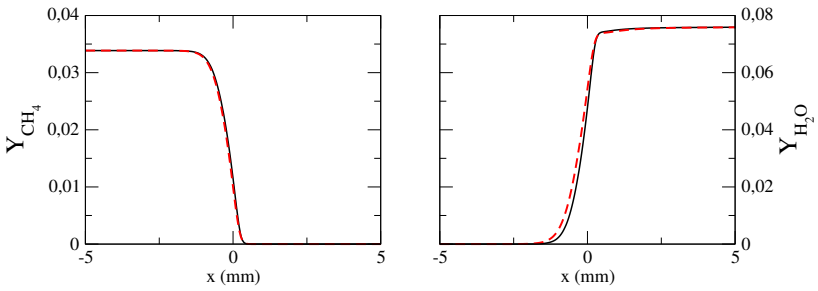

Figure 7.4: 1D profile of CH_4 (left) and H_2O (right) for equivalence ratio $\phi = 0.6$, analytical scheme. Plain line: (D2, $Le_k = 1$), dashed line: (D3, $Le_k \neq 1$).

7.2.3 Ignition time τ_{ign}

7.2.3.1 Definition

In a 3D ignition case, temperature (and pressure) vary both in space and time. Auto-ignition delays τ_{ai} calculated in homogeneous reactors (section 7.2.1) are not sufficient to characterize 3D ignition cases. A better characterization should account for the variation of the temperature with time and space. In the present study, a method to determine the ignition time τ_{ign} is proposed, accounting for the variation

of the temperature with time. The ignition time τ_{ign} is calculated based on the variation of enthalpy in the center of the ignition zone during a 3D ignition case. The calculation procedure is illustrated in Fig. 7.5 and detailed below:

- **Step 1: determination of the total enthalpy in the center of the ignition zone** A 3D ignition case is first considered (equivalence ratio ϕ, initial pressure $P_{ini} = P_{atm}$ and initial temperature $T_{ini} = T_{atm}$). Thermal energy $E_{ign}(r_0, \tau_{dep})$ is deposited, using the ED model. The chemical terms in the species transport equation and in the energy equation are set to zero. Doing so enables to determine the evolution of enthalpy $h(r,t)$ of the mixture, only due to the deposit of energy $E_{ign}(r_0, \tau_{dep})$, and not due to both the energy deposit and the heat released by the combustion reactions. The enthalpy $h(0,t)$ in the center of the deposit are stored versus time in the variable denoted $h_{0,ini}(t)$.

- **Step 2: calculation of the ignition delay in a constant pressure reactor** A constant pressure homogeneous reactor is then considered, with a methane/air mixture at the same equivalence ratio ϕ, at the pressure $P_{HR} = P_{atm}$ and at a enthalpie $h_{HR}(t)$ varying with time, such as $h_{HR}(t) = h_{0,ini}(t)$. The ignition time τ_{ign} is then defined as the time when only 5% of the fuel mass fraction remains:

$$Y_{CH_4}(\tau_{ign}) = 0.05 Y_{CH_4,ini} \tag{7.7}$$

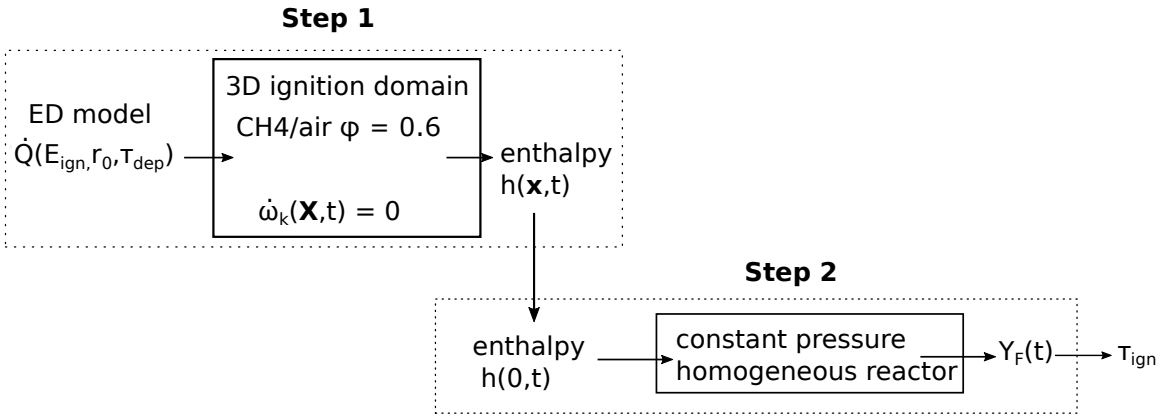

Figure 7.5: Sketch illustrating the calculation procedure of the ignition time τ_{ign}.

7.2.3.2 Results and analysis

An example of the calculation of the ignition time τ_{ign}, using the simplified kinetic scheme, is displayed in Fig. 7.6, showing the evolution of the temperature $T^*(t)$ of the constant pressure reactor (plain line), of $T_{0,ini}(t)$ the temperature corresponding to the enthalpy $h_{0,ini}$ (dashed line) and of the fuel mass fraction $Y_{CH_4}(t)$. The increase of the temperature T^* due to reactions while the fuel is consumed is clearly evidenced.
Using this method, ignition times τ_{ign} were determined for different ignition parameters (E_{ign}, r_0) - corresponding in fact to different energy density E_{ign}/r_0^3 (denoted D) - using the simplified scheme and the analytical scheme. Results are reported

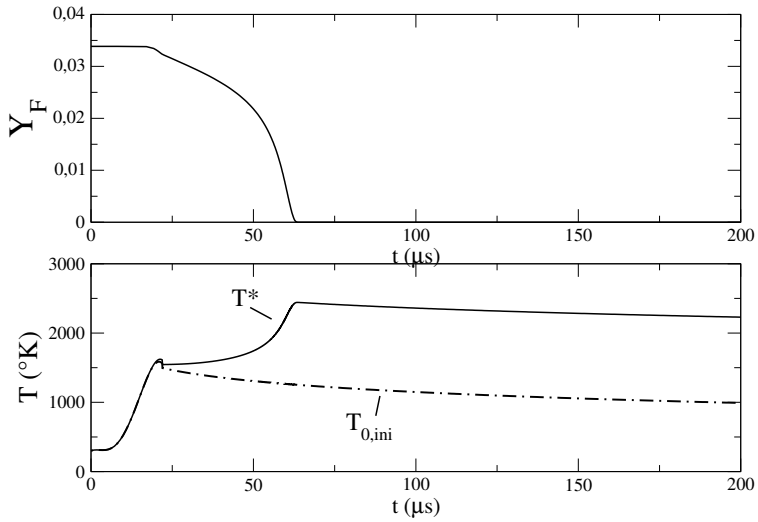

Figure 7.6: Calculation of the ignition time τ_{ign}, for the ignition parameters $E_{ign} = 0.56\ mJ$ and $r_0 = 1.125\ mm$. Top: fuel mass fraction Y_F versus time. Bottom: imposed temperature of the constant pressure homogeneous reactor $T_{0,ini}$ (plain line) and the constant pressure reactor temperature T^* (plain line) versus time.

in Fig. 7.7: the values of τ_{ign} are displayed as a function of the energy density $D = E_{ign}/r_0^3$, which governs the level of temperature. First conclusions can be drawn from this simple analysis:

- There is an asymptotical value of the energy density D_{crit}, for which the ignition time τ_{ign} exponentially increases and tends toward infinity. When the energy density is below the critical value ($D < D_{crit}$), the temperature is not raised to a sufficient level during a sufficient time for the combustion reactions to significantly occur.

- The value of D_{crit} is different when using the simplified scheme and when using the analytical scheme: $D_{crit,analytic} > D_{crit,simplified}$. This difference is related to the difference in terms of auto-ignition delays τ_{ai}, presented in section 7.2.1. Indeed, because the auto-ignition delays of the simplified scheme are shorter than the analytical scheme ones, combustion can occur at lower temperature when using the simplified kinetic scheme.

- when the energy density is higher than the critical energy density of the analytical scheme ($D > D_{crit,analytic}$), the ignition times τ_{ign} obtained using the simplified chemistry and the analytical chemistry are very close, although auto-ignition delays τ_{ai} are very different (see Fig. 7.1). Explanation is as follows: when the energy density is higher than the critical energy density of the analytical scheme ($D > D_{crit,analytic}$), the temperature in the center of the energy deposit is high ($T > 2500\ K$). At this temperature, even if the auto-ignition delays predicted by the simplified scheme and the analytical scheme are different ($\tau_{ai,simplified}(T = 3000\ K) = 0.4\ \mu s$, while $\tau_{ai,simplified}(T = 3000\ K) = 4.4\ \mu s$), auto-ignition delays τ_{ai} are both short enough for combustion reactions to significantly take place during the energy deposit of duration $\tau_{dep} = 25\ \mu s$.

- when the energy density is high ($D > 0.5$ mJ/m^3 in Fig. 7.7), then the ignition

time τ_{ign} is smaller or equal to the deposit duration τ_{dep}, which shows that ignition takes place very quickly, whatever the kinetic scheme.

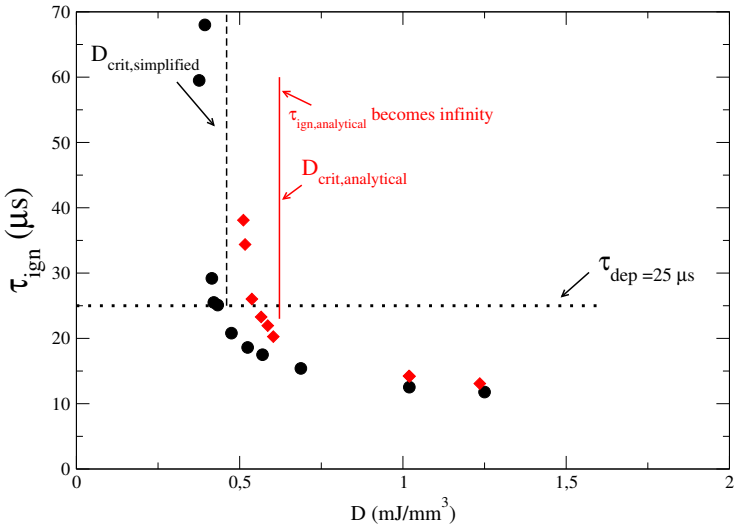

Figure 7.7: ignition time τ_{ign} function of the energy density $D = E_{ign}/r_0^3$ for the simplified scheme (filled circles) and the analytical scheme (filled diamond). The deposit duration τ_d is indicated with the dotted line.

7.2.4 Heat diffusion time τ_{diff}

Considering a sphere of radius R_i maintained to an uniform temperature T_i, the heat diffusion time τ_{diff} is given by solving the heat equation in spherical coordinates. It can be estimated according to:

$$\tau_{diff}(T_i) \sim \frac{R_i^2}{D_{th}(T_i)} \tag{7.8}$$

Practically, the temperature field is not uniform, because of the Gaussian shape of the energy deposit but the approximation can be used in a first analysis. Heat diffusion times $\tau_{diff}(T)$ were estimated for different temperatures T in the ignition zone, using the different thermal diffusivity law of λ for the groups D1, D2 (see Table 7.1). Values are displayed in Fig. 7.8. Diffusion times τ_{diff} are of the order of magnitude of tens of μs for high temperature ($T \gg 2000$), and differ between case D1 and D2. At lower temperature ($T \sim 2000\ K$), close the adiabatic temperature, diffusion times are similar for cases D1 and D2. Values are of the order of magnitude of hundreds of microsecondes, which is much longer than the deposit duration τ_{dep}.

7.2.5 Conclusion

In this chapter parameters and kinetic schemes used in the ignition study were presented. Important physical quantities to analyze the ignition results were determined: laminar flame speed and thickness, auto-ignition delays, heat diffusion time. An ignition time τ_{ign} was also defined, accounting for the variation of temperature with time during ignition. Ignition times were calculated for different energy densities of the energy deposit. A novel and important conclusion concerns the fact that

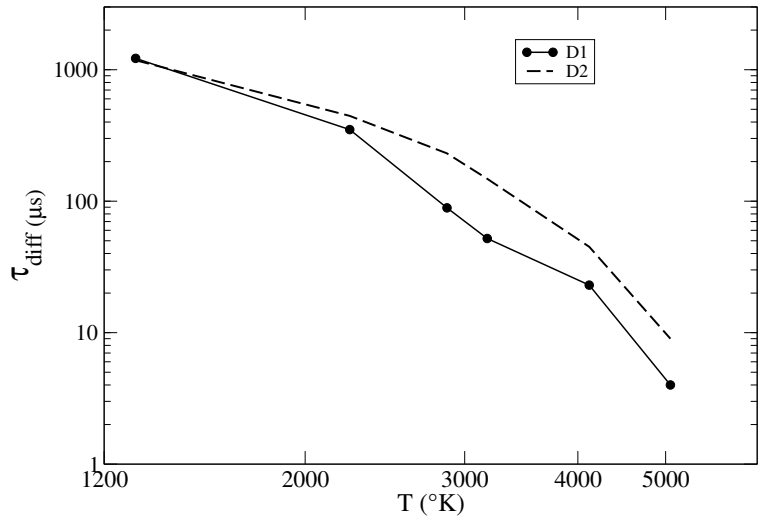

Figure 7.8: characteristic heat diffusion time τ_{diff} as a function of the temperature T, calculated for the different thermal diffusivity law of λ. τ_{diff} is calculated using Relation (7.8), for a methane/air mixture $\phi = 0.6$ and considering an energy deposit $E_{ign} = 0.42$ mJ and $r_0 = 0.75$ mm.

above a certain energy density, the 2-step and the analytical kinetic scheme predict similar values of the ignition time τ_{ign}, although auto-ignition delays are very different. This aspect will play an essential role in the 3D ignition cases (section 8.3.1).

Chapter 8

Laminar ignition cases

Contents

This chapter presents the laminar ignition study. Section 8.1 discusses the results of the different MIE parametric studies, using the 2-step kinetic scheme. Then section 8.2 presents a finer analysis of the process of ignition and extinction observed in the simulations. Section 8.3 is dedicated to the ignition prediction using the analytical scheme. Finally, the results of the simulations are discussed in section 8.4 against the experimental results established by Cardin et al. (2013).

8.1 Global analysis: MIE parametric study using the 2-step kinetic scheme

Following parametric studies establish how MIE varies when: the deposit radius r_0 varies (section 8.1.2), the equivalence ratio ϕ varies (section 8.1.3), the Lewis number varies (section 8.1.4). Analysis enable to define ignition criteria and to better understand the ignition process when using the energy deposit model.
Before presenting the parametric studies, unsuccessful ignition cases are first described in section 8.1.1, as two different types of unsuccessful ignition were observed when determining the MIE and must be distinguished.

8.1.1 Description of unsuccessful ignitions

Two different types of unsuccessful ignition observed when determining the MIE, denoted A and B, are described below:

- **failure A: extinction following the energy deposit (Fig. 8.1)**. The temperature is not raised to a sufficient level during the energy deposit phase, therefore no significant heat released by the combustion is observed, as illustrated in Fig. 8.1. The temperature in the center of the ignition zone is displayed versus time, for a reactive case (red plain line) and for the same case for which chemical terms have been set to zero (blue dotted line). The temperature relaxes the same way for both cases, thus evidencing that the heat released by combustion is not significant.

- **failure B: extinction following a phase of growth of the flame kernel (Fig. 8.2)**. The temperature is locally raised to a sufficient level during the energy deposit phase, combustion successfully initiates and a phase of growth of the flame kernel is observed, before it cools down, as illustrated in Fig. 8.2 (the burned gases radius r_{bg} is calculated as following Eq. (3.10)). In Fig. 8.2-right, the temperature first increases because of the thermal energy deposit, then because of the heat release (the 2-step kinetic scheme which was used in this case is exothermic). Until $t \sim 0.5$ ms, the temperature decreases due to diffusive heat losses, then it relaxes toward the adiabatic flame temperature as the flame kernel grows (Fig. 8.2-left). After $t \sim 1.5$ ms, the temperature in the center of the flame kernel starts decreasing and the flame kernel cools down, corresponding to a decrease of the burned gases radius in Fig. 8.2-left.

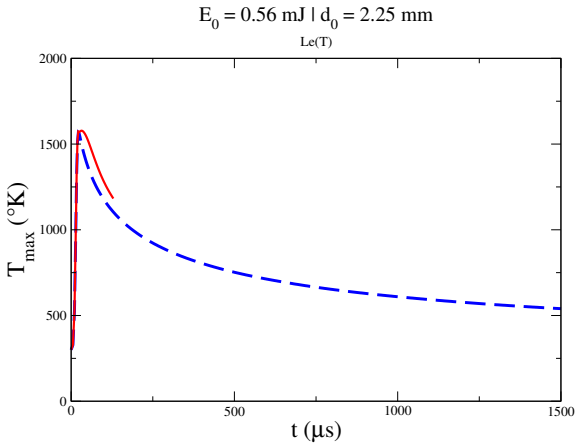

Figure 8.1: Ignition failure A: temperature versus time in the center of the ignition zone. Red plain line: reactive case, blue dotted line: same case with chemical terms set to zero. 2-step kinetic scheme, $\phi = 0.6$. $E_{ign} = 0.56\ mJ$, $d_0 = 2.25\ mm$.

8.1.2 Dependency of the MIE on the deposit radius r_0

To determine the relation between MIE and deposit radius r_0, ignition calculations were run with different sets of ignition parameters (E_{ign}, r_0). Results - e.g. success or failure A or failure B - were then reported in a diagram E_{ign} function of the deposit radius r_0 (Fig. 8.3). Iso-energy density lines, corresponding to $D = E_{ign}/r_0^3 = cst$

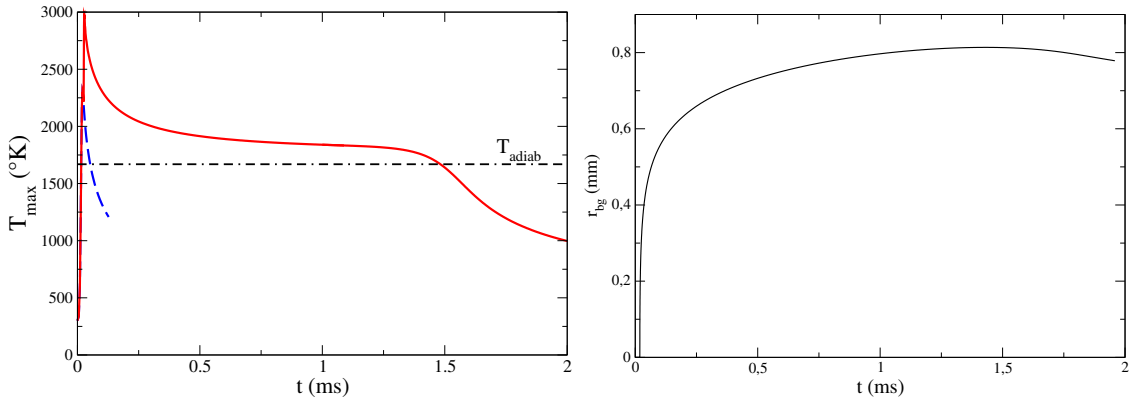

Figure 8.2: Ignition failure B. Left: temperature versus time in the center of the kernel. Red plain line: reactive case, blue dotted line: same case with chemical terms set to zero. Right: burned gases radius r_{bg} versus time. 2-step kinetic scheme, $\phi = 0.6$. $E_{ign} = 0.322$ mJ, $r_0 = 0.85$ mm.

are also displayed in the diagram (dotted and dashed lines). Meaning of the symbols is as follows:

- **Circle symbols**: success.
- **Cross symbols:** ignition failure A (Fig. 8.1).
- **Square symbols:** ignition failure B (Fig. 8.2).

MIE values may be thus estimated by the line passing by circles and square symbols or circles and cross symbols.

8.1.2.1 Description of the diagram

In Fig. 8.3, two zones can be clearly distinguished, as in the results of Sloane and Ronney (1992) or Frendi and Sibulkin (1990) (see Fig. 3.3 and 3.3). These two zones are represented by rectangles and the limit between the two zones, corresponding to $r_0 = r_{0,crit}$, is also drawn.

- **in zone Z1**, corresponding to $r_0 > r_{0,crit}$: MIE is proportional to r_0^3, as evidenced by the iso-energy density line (the red dashed line $D_{ign,crit}$ in Fig. 8.3) exactly passing between points of success and of failure of ignition. In this zone, unsuccessful ignitions are only of type A (cross symbols only, no square symbol). This means that ignition can occur if and only if a critical ignition temperature $T_{ign,crit}$ (corresponding to the critical energy density $D_{ign,crit}$) is reached in a certain ignition volume. Otherwise, the heat release is not significant enough to balance the diffusive heat losses during the energy deposit phase and the kernel starts cooling down just after the energy deposit. These conclusions are similar to previous results, such as the ones established by Wang and Sibulkin (1993). Fig. 8.4 is taken from their study. It shows, as a function of the deposit radius, on the right ordinate the MIE and on the left ordinate, the ignition temperature T_{ign} defined in their study as the temperature in the center of the ignition zone at the end of the energy deposit (that is $T(0, \tau_{dep})$). In the zone $r_0 > r_{0,crit}$, this temperature reaches a constant level

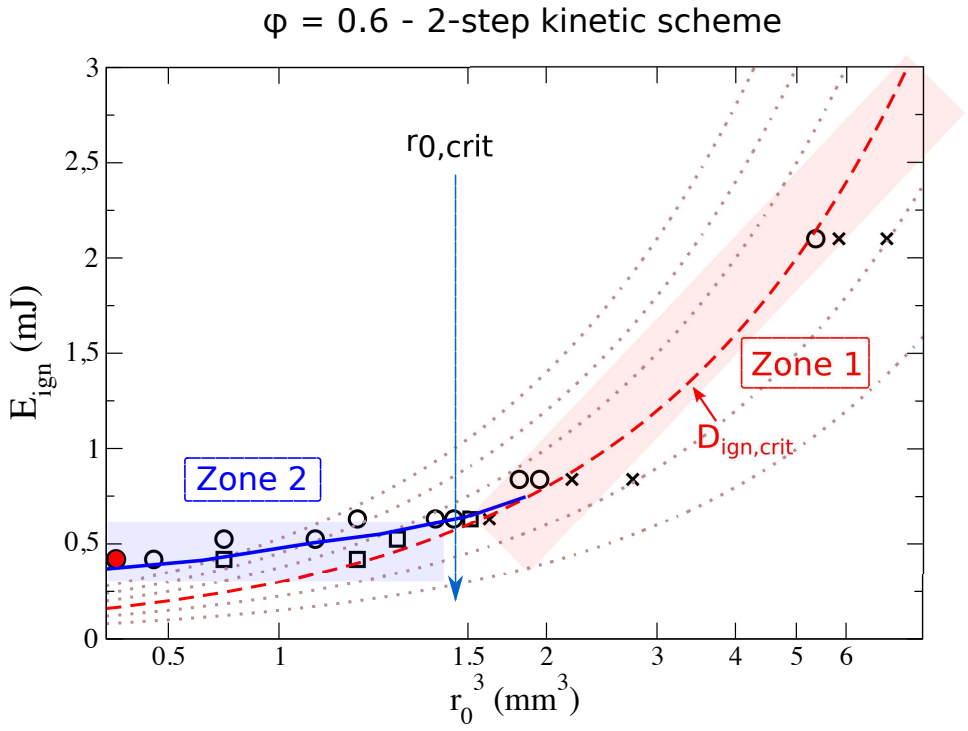

Figure 8.3: Dependency of the MIE on the ignition energy input radius r_0 for the 2-step kinetic scheme. $\phi = 0.6$. Red dashed line and dotted lines: iso-energy density lines $D = E_{ign}/r_0^3 = \text{cst}$. Circle symbols: successful ignition. Cross symbols: unsuccessful ignition A, extinction following the energy deposit. Square symbols: unsuccessful ignition B, extinction following a phase of growth of the flame kernel. Filled red symbol: reference energy density D_{ref} defined in section 8.1.2.3.

($T_{ign}^{min} \approx 1000\ K$), while MIE is proportional to the energy deposit volume. This means that following classical relation can be written:

$$MIE \propto \frac{4}{3}\pi r_0^3 \rho^u C_p \Delta T \tag{8.1}$$

with $\Delta T = (T_{ign,crit} - T_0)$. Wang and Sibulkin (1993) suggest that $T_{ign,crit}$ should not depend on the deposit radius r_0. In our case, because the energy deposit has a Gaussian shape, $T_{ign,crit}$ represents in fact an average temperature within the ignition zone and does depend on the deposit radius r_0 because of the diffusion effects. An estimation of $T_{ign,crit}$ is proposed for the present simulations, comparing the evolution of the temperature in successful and unsuccessful ignition cases. To do so, the temperature in the center of the ignition zone is displayed in Fig.8.5 versus time, for a successful ignition case (left) and an unsuccessful ignition case (right). The evolution of the temperature for the same cases, where chemical terms have been set to zero is also displayed (dashed line). The comparison of these cases provides an estimation of the critical ignition temperature: $T_{ign,crit,simplified} \approx 1600\ K$. Practically, $T_{ign,crit,simplified}$ varies with the radius of the energy deposit r_0 because of the diffusive effects but the order of magnitude of variations is only of a few hundreds of Kelvin.

- **in zone Z2**, corresponding to $r_0 < r_{0,crit}$, MIE remains quasi constant (blue plain line in Fig. 8.3). Ignition can fail even if the energy density D of the deposit is high, i.e. if the ignition temperature is high (unsuccessful ignition case B). This observation is consistent with the previous results of Wang and Sibulkin: in Fig. 8.4 the ignition temperature increases as the deposit radius r_0 decreases. For those unsuccessful ignition cases (case B), the flame kernel starts growing but cannot reach the critical size, as illustrated in Fig. 8.6. The burned gases radius r_{bg} is displayed versus time, for ignition cases of zone Z2 with different ignition energy E_{ign}, but with the same ignition energy density D. The closer the ignition energy E_{ign} is to the MIE, the larger the flame kernel grows, before cooling down. The critical radius $r_{bg,crit}$ can be determined as the last radius reached before extinction. In Fig. 8.6, the critical radius $r_{bg,crit}$ is close to 1.18 mm.

Results also suggest a relation between the critical deposit radius $r_{0,crit}$ and the critical burned radius $r_{bg,crit}$: when $r_0 > r_{0,crit}$, if the ignition energy E_{ign} is sufficient to initiate the combustion, then the flame kernel necessarily reaches the critical radius $r_{bg,crit}$, but when $r_0 < r_{0,crit}$ then the ignition energy must sustain the flame kernel to the critical size of radius $r_{bg,crit}$. Radii r_0 and $r_{bg,crit}$ are not equal, mostly because of the diffusion effects occurring within the ignition zone. However it can be observed in the diagram of Fig. 8.3 that $r_{0,crit} \approx 1.1\ mm$, while in Fig. 8.6, the burned gases radius $r_{bg,crit}$ is close to ≈ 1.18 mm. These two values are close to the laminar flame thickness δ_L (see Table 7.4), which is consistent with the 0D ignition theories (Ballal and Lefebvre, 1974; Champion et al., 1986) (see section 2.3.1) relating the critical ignition volume to the laminar flame thickness.

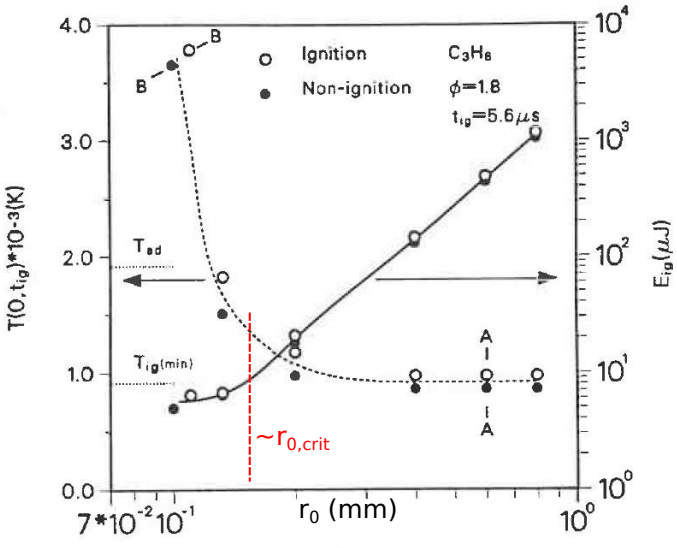

Figure 8.4: Effect of the ignition energy input radius r_0 on the ignition kernel temperature $T(0, t_{ig})$ and on the minimum ignition energy, according to the study of Wang and Sibulkin (1992)

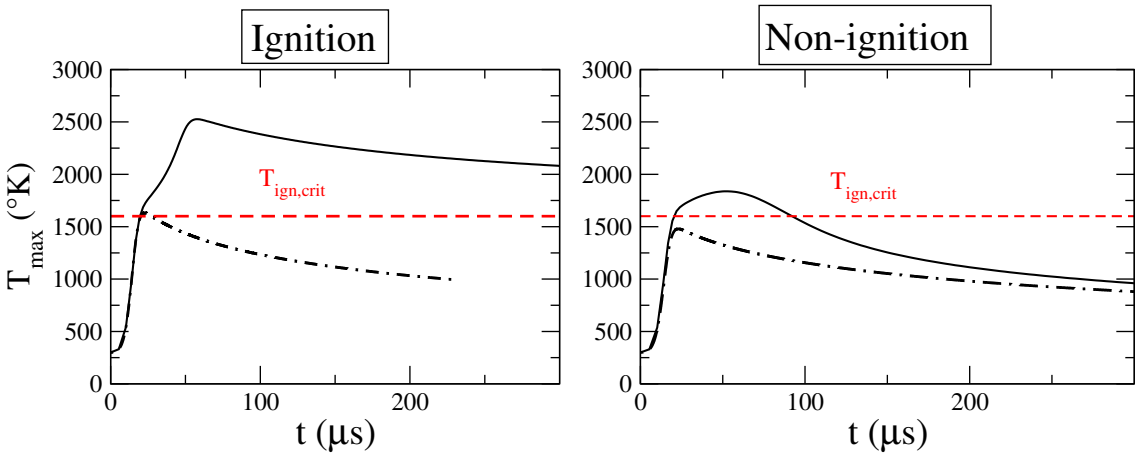

Figure 8.5: Estimation of the critical ignition temperature $T_{ign,crit}$ for the 2-step kinetic scheme. Left: $E_{ign} = 0.7$ mJ, $r_0 = 1.2$ mm; Right: $E_{ign} = 0.65$ mJ, $r_0 = 1.2$ mm (ignition parameters are in zone Z1). Plain line: reactive case, dashed line: same case with chemical terms set to zero.

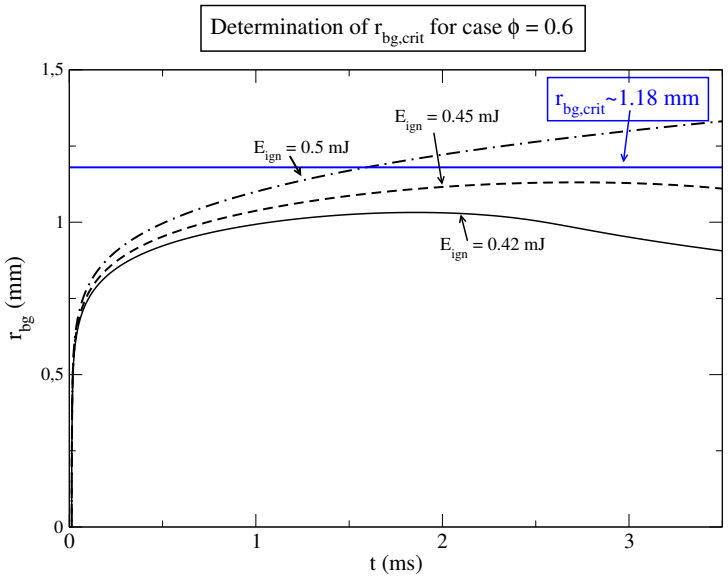

Figure 8.6: Temporal evolution of the burned gases radius r_{bg} for different ignition energy E_{ign} and same ignition energy density $D = E_{ign}/r_0^3$ in zone Z2. 2-step kinetic scheme, (D1). $\phi = 0.6$.

8.1.2.2 Definition of ignition criteria

Based on the analysis of the diagram in Fig. 8.3, two ignition criteria can be defined:

1. **Criterion 1:** E_{ign} must be sufficient for the critical ignition temperature $T_{ign,crit}$ to be reached in the ignition zone. The critical ignition temperature corresponds to the temperature for which the heat release can balance the diffusive heat losses during the energy deposit phase, so that a flame kernel can form and start growing.

2. **Criterion 2:** E_{ign} must be sufficient to sustain the flame kernel until it reaches the critical size of radius $r_{bg,crit}$, which is related to the laminar flame thickness

δ_L.

Practically in a successful ignition case, Criterion 1 is verified before Criterion 2. But depending on the zone of the diagram, only one of the two criteria is required to successfully ignite. The ignition criterion depends on the value of the deposit radius r_0:

- **Zone 1, when $\mathbf{r_0 > r_{0,crit}}$**, the ignition criterion is **Criterion 1**, because in that case verifying Criterion 1 implies that Criterion 2 is also verified. Indeed, when $r_0 > r_{0,crit}$, the part of the ignition volume where the temperature is above the critical ignition temperature (Criterion 1) is large enough to ensure, that once diffusion occurred, the resulting flame kernel is above the critical size of radius $r_{bg,crit}$ (Criterion 2).
- **Zone 2, when $\mathbf{r_0 < r_{0,crit}}$**, the ignition criterion is **Criterion 2**, because in that case verifying Criterion 2 implies that Criterion 1 is also verified. The energy density required to sustain the flame kernel to the critical size $r_{bg,crit}$ (Criterion 2) is higher than the critical energy density D_{crit} required to observe the significant apparition of burned gases (Criterion 1).

8.1.2.3 Choice of a reference energy density D_{ref}

From the diagram of Fig. 8.3, a reference energy density D_{ref} can be defined. D_{ref} will serve to define the ignition parameters of the turbulent ignition cases presented in Chapter 9 and to compare the MIE predicted in simulations to the experimental results of Cardin et al. (2013). D_{ref} is chosen in zone Z2 of the diagram of Fig. 8.3 and is indicated by the red filled circle (value $D_{ref} = 1.0196$ mJ/mm^3). Reason of this choice is that D_{ref} must correspond to a high density energy deposit. Indeed this type of ignition mimics the high temperature peak of the breakdown (in simulations, the maximal temperature can for instance reach 8000 K), followed by a heat relaxation phase and then a phase of growth of the flame kernel. This situation is closer to a physical short duration spark ignition case than an ignition case of zone Z1, of lower energy density.

8.1.3 Effect of the equivalence ratio ϕ on MIE

In order to confirm the analysis presented in section 8.1.2.1 for the equivalence ratio $\phi = 0.6$, a similar parametric study MIE function of the deposit radius r_0 is performed for the equivalence ratio $\phi = 0.85$. Then, MIE values determined with the reference energy density D_{ref} are compared to the experimental values of Cardin et al. (2013) and to the 0D criterion of Ballal and Lefebvre, for equivalence ratios $\phi = 0.55$, $\phi = 0.6$ and $\phi = 0.85$.

8.1.3.1 Diagram MIE function of the deposit radius r_0 for the equivalence ratio $\phi = 0.85$

Results of the parametric study MIE function of the deposit radius r_0 for the equivalence ratio $\phi = 0.85$. are displayed in Fig. 8.7. The MIE estimated for the equivalence ratio $\phi = 0.6$ is also indicated (dashed line). As for the case $\phi = 0.6$ (see Fig. 8.3), zones Z1 and Z2 are clearly identified. Following observations can be also made:

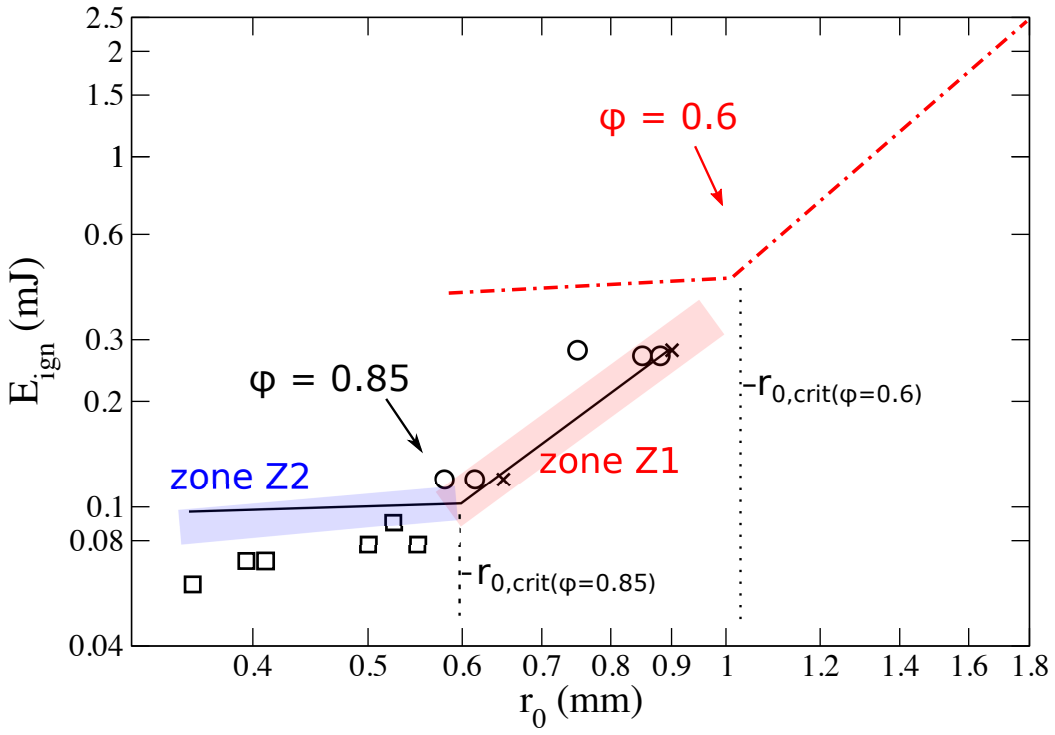

Figure 8.7: Ignition energy E_{ign} as a function of the deposit radius r_0. Symbols (for $\phi = 0.85$) cross: unsuccessful ignition A and square: unsuccessful ignition case B, circle: successful ignition (see section 8.1.1 for the details). Lines estimate the MIE for the case $\phi = 0.85$ (plain line) and $\phi = 0.6$ (dashed line). 2-step kinetic scheme, (D2).

- In zone Z1, the slope of the MIE line is similar for equivalence ratios $\phi = 0.6$ and $\phi = 0.85$, which means that the critical energy density $D_{ign,crit}$ is similar. Reason is that the critical ignition temperature $T_{ign,crit}$ results of the competition between the heat diffusion and the heat released by the combustion reactions during the deposit phase. The heat release is governed by the auto-ignition delays during the deposit phase, which do not vary much from $\phi = 0.6$ to $\phi = 0.85$.

- In zone Z2, MIE values for case $\phi = 0.85$ are smaller than for case $\phi = 0.6$, which is consistent with experimental results (Ballal and Lefebvre, 1974; Champion et al., 1986; Beduneau et al., 2009; Cardin et al., 2013), 0D models predictions(Ballal and Lefebvre, 1974; Champion et al., 1986) and previous simulations (Sloane, 1990). A more quantitative comparison with the results of Cardin et al. (2013) is proposed in next section 8.1.3.2.

- the critical radius $r_{0,crit}$ is smaller for case $\phi = 0.85$ than for case $\phi = 0.6$. This is consistent with the explanation proposed in section 8.1.2, relating $r_{0,crit}$ to the laminar flame thickness (Tab 8.1, values of the critical burned gases radius r_{bg} are also reported).

	$\phi = 0.6$	$\phi = 0.85$
δ_L (mm)	0.93	0.39
$r_{0,crit}$ (mm)	1.1	0.55
$r_{bg,crit}$ (mm)	1.18	0.6

Table 8.1: Comparison of the laminar flame thickness calculated in section. 7.2.2 (first row), the critical deposit radius $r_{0,crit}$ determined in Fig. 8.7 (second row) and the critical burned gases radius r_{bg} determined in Figs. 8.6 and 8.8 (third row).

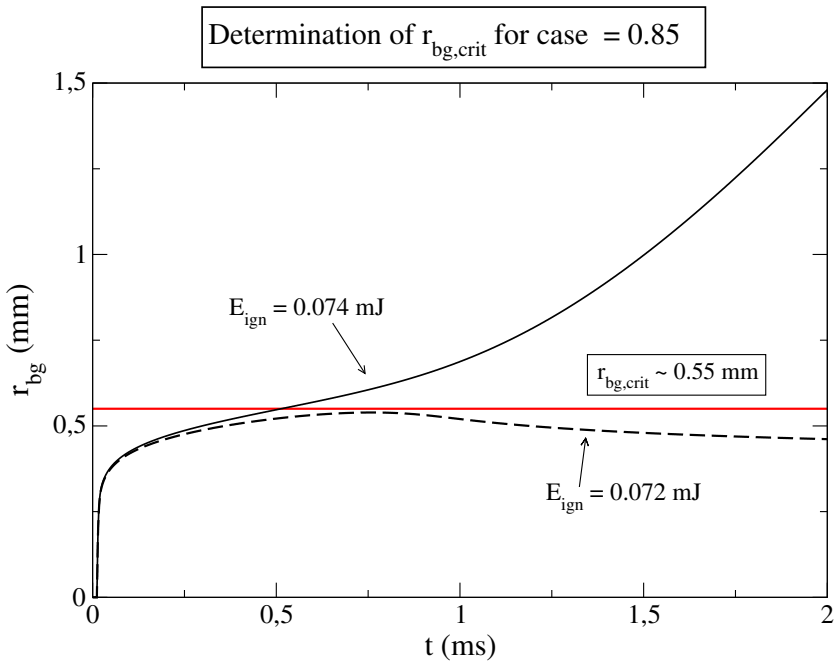

Figure 8.8: Temporal evolution of the burned gases radius r_{bg} for different ignition energy E_{ign} and same ignition energy density $D = E_{ign}/r_0^3 = D_{ref}$. 2-step kinetic scheme, (D2). $\phi = 0.85$.

8.1.3.2 Validation of MIE predicted in simulations

MIE were determined for the three equivalence ratios $\phi = 0.55$, $\phi = 0.6$ and $\phi = 0.85$, for the reference energy density D_{ref} defined in section 8.1.2.3. Values are reported in Table 8.2, with the ones predicted using the correlation of Ballal and Lefebvre (2.13) and the ones extrapolated from the measurements of Cardin (2013). The authors recommend an estimation of the effective MIE value MIE_{eff} such as: $MIE_{eff} = 0.15 * MIE_{Laser}$, because about 85% of the measured Laser energy is dissipated by the propagation of the post-breakdown pressure wave, which is not accounted for in the present simulations. Criterion of Ballal and Lefebvre (1974) is recalled below:

$$MIE = \frac{4}{3}\pi {\delta_L}^3 \rho^u (T_{adiab} - T_0) \tag{8.2}$$

The results of the simulations verify that MIE decreases with the equivalence ratio ϕ, respecting the same trend as the one observed in the experiments of Cardin and as

the one predicted by the 0D criterion of Eq. (8.2)(see also section 2.3.1). Moreover, the values predicted in the simulations are close to the MIE_{eff} values estimated from the measurements. In the correlation (8.2), the laminar flame thickness must be divided by a parameter α set to $\alpha = 2.8$ to recover the same MIE value as the one estimated from the experimental measurements. This highlights that 0D criteria can reproduce the correct physical trend MIE function of the equivalence ratio ϕ but cannot be quantitative.

MIE prediction	$\phi = 0.55$	$\phi = 0.6$	$\phi = 0.85$
simulations (simplified kinetics-(D2))	0.85 mJ	0.47 mJ	0.072 mJ
Correlation (8.2)	1 mJ	0.49 mJ	0.071 mJ
Experiments: $0.15 * MIE_{Laser}$	0.94 mJ	0.49 mJ	0.1 mJ

Table 8.2: MIE calculations (mJ): comparison of the MIE calculated in the simulations (first row), predicted using the correlation of Ballal and Lefebvre (1974) with δ_L divided by $\alpha = 2.58$ (second row) and estimated from the measurements of Cardin et al. (2013) (third row).

8.1.4 Effect of Lewis numbers Le_k on MIE

To characterize the effect of the Lewis numbers Le_k on MIE, MIE obtained in simulations (D1), (D2) and (D3) (Tab. 8.3) are compared for equivalence ratios $\phi = 0.55$, $\phi = 0.6$ and $\phi = 0.85$, with the reference energy density D_{ref}. Then, to characterize the influence of the diffusivity law on the MIE prediction, the diagram MIE function of the deposit radius r_0 is established for simulations (D1) and (D2), for the equivalence ratio $\phi = 0.6$. Differences are analyzed.

Groups	laminar viscosity μ	Fourier coefficient λ	Le_k
D1	D'Angola law	D'Angola law	$Le(T)$
D2	D'Angola law	Eq.(7.2)	$Le_k = 1$
D3	D'Angola law	Eq.(7.2)	$Le_k \neq 1$

Table 8.3: The different groups of simulations, corresponding to different Lewis number Le_k, see section 7.1.1.2.

8.1.4.1 Different equivalence ratios ϕ, reference energy density D_{ref}

MIE values obtained in simulations (D1), (D2) and (D3) are reported in Table 8.4. Results of groups (D2) and (D3) are first commented. For these groups, the law to calculate the Fourier thermal coefficient λ is the same ($\lambda = \mu C_p/Pr$), only the species Schmidt numbers Sc_k differ. According to the results gathered in Table 8.4:

$$MIE_{(D2)} > MIE_{(D3)} \tag{8.3}$$

Groups as def. in Table 8.3	Le_k	$\phi = 0.55$	$\phi = 0.6$	$\phi = 0.85$
(D1)	$Le_k(T)$	x	0.28	0.035
(D2)	$Le_k = 1$	0.85	0.47	0.072
(D3)	$Le_k \neq 1$	0.75	0.4	x

Table 8.4: MIE calculations (mJ): effect of Lewis numbers Le_k. for different equivalence ratios ϕ and different Lewis numbers Le_k (see Tab. 8.3). Reference energy density D_{ref} (see section 8.1.2.3). 2-step simplified kinetic scheme. Cross symbols corresponds to cases that were not simulated.

Differences observed between simulations (D2) ($Le_k = 1$) and simulations (D3) ($Le_k \neq 1$ with $Le_{CH_4} = 0.98$) are consistent with previous results (Champion et al., 1986; Tromans and Furzeland, 1986). These studies explain that when $Le_F < 1$, then MIE decreases and vice versa (which is verified in the relation (8.3)). Indeed, when $Le_F < 1$, then $D_{th} < D_k$: species, in particular the fuel, diffuse faster than the heat, accordingly the MIE decreases. When $Le_F > 1$, then $D_{th} > D_k$, heat diffuses faster than the species, accordingly MIE increases.
To explain the difference of MIE predictions between group (D1) and the two other groups (D2, D3), Fig. 8.9 displays a profile of the Lewis number $Le_{(D3)}(T)$ for an ignition case of group (D1), at different timings of the ignition. At $t = 20\ \mu s$, that is during the energy deposit, the Lewis number is very high: $Le_{(D1)}(T) \gg 1$. Then, at longer time $t > 100\ \mu s$, $Le_{(D1)}(T)$ becomes smaller than unity. To complete the analysis, it is recalled that the reference energy density D_{ref} chosen for these ignition cases is situated in **zone Z2** ($r_0 < r_{0,crit}$). In that case, the ignition criterion is **Criterion 2**: the ignition energy E_{ign} must be sufficient to sustain the flame kernel until it reaches the critical size. Thus, the key phase is the phase of growth of the flame kernel. This implies that the key parameter is not the value of Lewis numbers Le_k during the energy deposit phase, but during the phase of the flame kernel growth. During this phase, according to Fig. 8.9, $Le_{(D1)}(T) < 1$, that is $Le_{(D1)} < Le_{(D2)}$, which is consistent with the MIE results: MIE predicted in case (D1) is smaller than MIE predicted in case (D2).

8.1.4.2 Variable energy density D, equivalence ratio $\phi = 0.6$

A parametric study MIE function of the deposit radius r_0 is performed for groups (D1) and (D2), for the equivalence ratio $\phi = 0.6$. Results are reported in Fig. 8.10:

- **In zone Z1**: results do not depend on the diffusivity law, because the energy density, that is the ignition temperature T_{ign}, are low ($T_{ign} < 2000K$). Explanations are detailed in the following. When $r_0 > r_{0,crit}$, the ignition criterion is **Criterion 1**, the ignition temperature must be higher than the critical ignition temperature ($T_{ign} > T_{ign,crit}$). The critical temperature $T_{ign,crit}$ results from the balance between the chemical heat release - that depends on kinetics - and the diffusive heat losses - that depend on thermal diffusivity law. It was established in section 8.1.2.1 that $T_{ign,crit} \approx 1600\ K$. At this temperature, the thermal diffusivity predicted by the D'Angola law and Equation (7.2) are

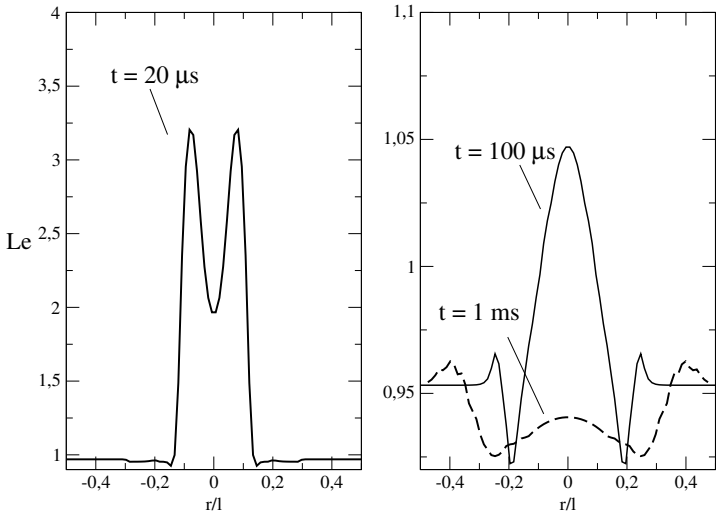

Figure 8.9: cut of the Lewis number $Le(T)$ inside the flame kernel at $t = 20\ \mu s$, $t = 100\ \mu s$ and $t = 1\ ms$. Simulation (D1), ignition parameters $E_{ign} = 0.42$ mJ, $r_0 = 0.75$ mJ.

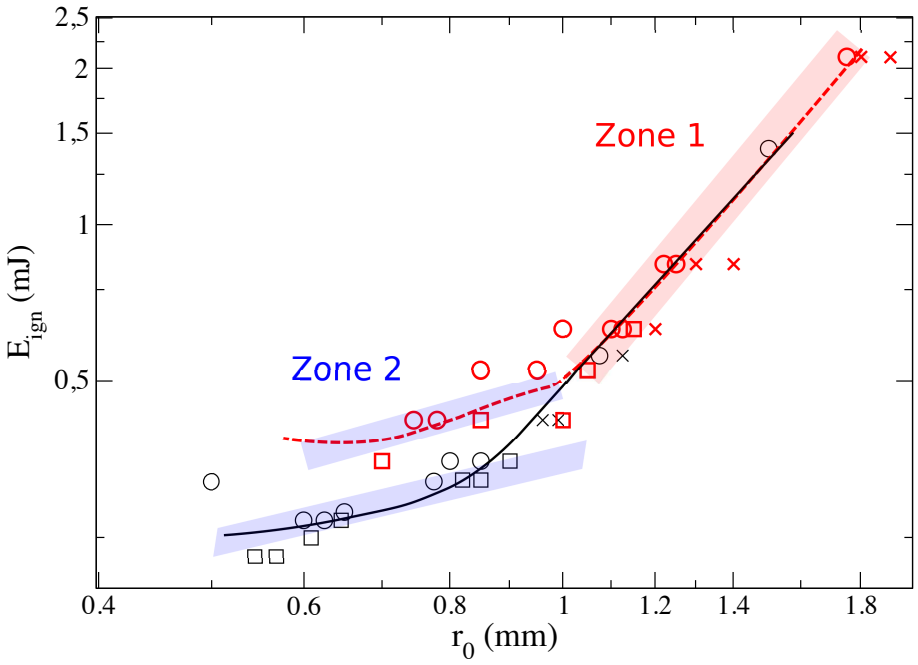

Figure 8.10: Effect of the thermal diffusivity law on the MIE prediction. Black plain line: simulations (D1). Red dotted line: simulations (D2). Cross symbols: unsuccessful ignition A, square symbols: unsuccessful ignition B, circle symbols: successful ignition (see section 8.1.2 for details)

very similar, as illustrated in Fig. 8.11. The thermal diffusivity coefficient D_{th} is displayed versus temperature, for the two different diffusivity law of simulations (D1) and (D2). When $T < 1500\ K$, the diffusivity coefficients are very similar. When $T > 1500\ K$, D'Angola law predicts a slightly higher diffusivity coefficient. The difference becomes significant only when $T > 2500\ K$, which

is much higher than the critical ignition temperature $T_{ign,crit}$. Accordingly, in zone Z2, MIE predictions do not depend on the thermal diffusivity law.

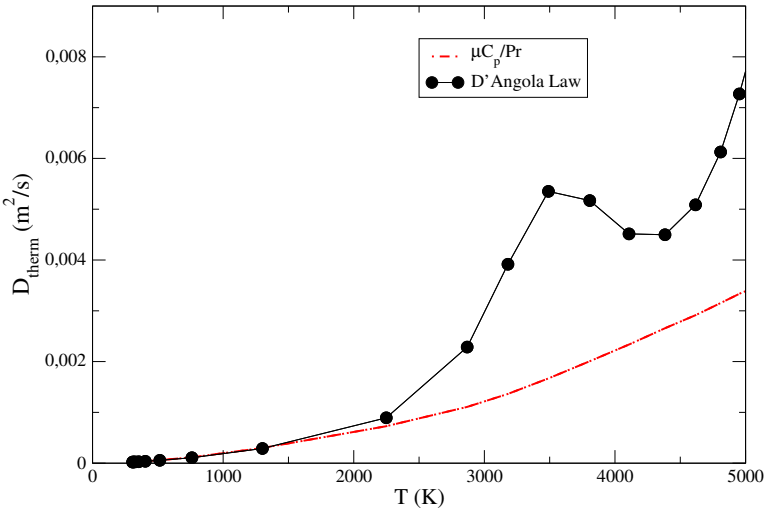

Figure 8.11: Diffusivity coefficient D_{th} as a function of the temperature, for two different laws of the thermal diffusivity coefficient λ.

- **In zone Z2**: MIE values obtained using the D'Angola law are smaller than the MIE values obtained using Equation (7.2) from a factor ≈ 2. This difference was explained in section 8.1.4.1. To provide an additional illustration of these results, Fig. 8.12 displays the temporal evolution of the temperature in the center of the ignition zone for an ignition case (D1) and for an ignition case (D2). Both simulations were performed with the same ignition parameters (E_{ign}, r_0). Although the D'Angola Law predicts a higher thermal diffusivity coefficient at high temperature (circle symbols in Fig. 8.11), therefore leading to a lower temperature peak at $t \sim 25\ \mu s$ (dashed line in Fig. 8.12), the flame kernel of simulation (D1) becomes a self-propagating flame kernel. On the contrary, Eq. (7.2) predicts a lower thermal diffusivity coefficient at high temperature (red line in Fig. 8.11), therefore leading to a higher temperature peak at $t \sim 25\ \mu s$ (plain line in Fig. 8.12), but the flame kernel of simulation (D2) does not become a self-propagating flame kernel and cools down after 1 ms, because its fuel Lewis number Le_F is higher than the fuel Lewis number of (D1), $Le_{F,(D2)} > Le_{F,(D1)}$. These observations confirm the previous analysis: when $r_0 < r_{0,crit}$, the key phase for the ignition is the phase of growth of the flame kernel, governed by the balance between heat release and heat losses, thus governed by the Lewis number.

The analysis of the influence of the diffusivity law on MIE prediction bring new elements: for large deposit radii ($r_0 > r_{0,crit}$), the diffusivity law has not significant influence on MIE prediction, as the ignition temperature is low ($T_{ign} \sim 2000\ K$). For small deposit radii ($r_0 < r_{0,crit}$) corresponding to high ignition temperature ($T_{ign} \gg 2000K$), the diffusivity law influences MIE prediction. However, this is not due to the heat diffusion effects during the high temperature phase (which last about 100 μs), but to heat diffusion effects during the phase of growth of the flame kernel, when temperature is lower.

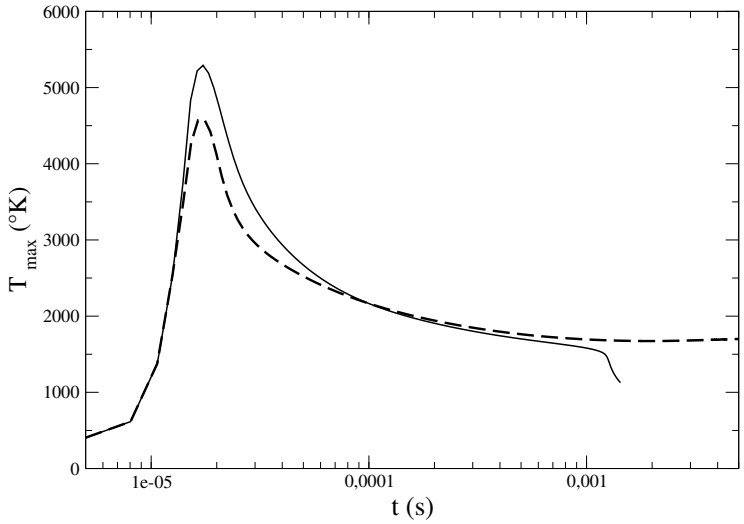

Figure 8.12: Influence of the λ thermal Fourier coefficient on the flame kernel formation and propagation: evolution of the temperature in the center of the flame kernel. Black plain line: Simulations (D1). Black dotted line: Simulations (D2). Energy deposit parameters (E_{ign} = 0.42 mJ, r_0 = 0.75 mm). Simplified kinetic scheme, $\phi = 0.6$.

8.2 Analysis of the ignition process

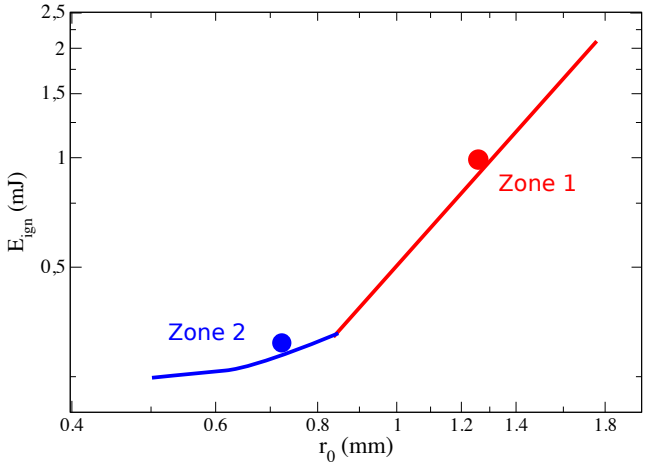

Figure 8.13: sketch of the diagram MIE function of the deposit radius r_0, indicating the ignition case of zone Z1 (blue), analyzed in section 8.2.1 and of zone Z2 (red), analyzed in section 8.2.2.

In this section, successful ignitions are described in more details, for ignition cases of zones Z1 (section 8.1.2.1) and Z2 (section 8.2.2), indicated in Fig. 8.13. Focus is on the time required to form burned gases in the zone of width r_0.

8.2.1 Ignition in zone Z1

Figure 8.14-top shows the temporal evolution of the fuel mass fraction Y_F in different locations of the ignition zone, for a successful ignition case. Corresponding temper-

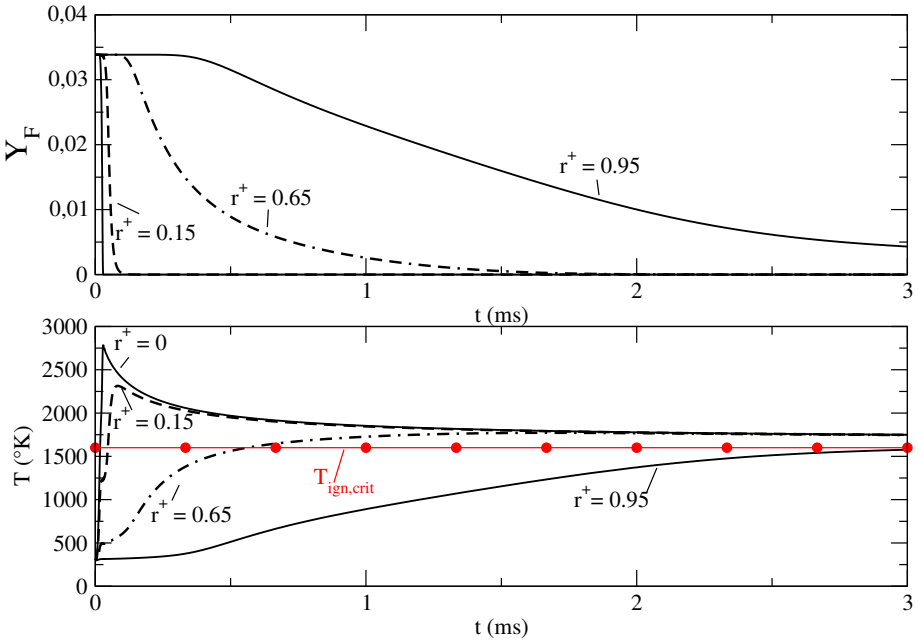

Figure 8.14: Zone Z1: temporal evolution of the fuel mass fraction Y_f (top) and of the temperature T (bottom) in different locations of the ignition zone. $r^+ = r/r_0$ where r is the distance to the center of the ignition zone and r_0 is the deposit radius. $E_{ign} = 0.84$ mJ, $r_0 = 1.25$ mm. $\phi = 0.6$, 2-step kinetic scheme.

atures are displayed in Fig. 8.14-bottom. The fuel consumption time $\tau_{cons,F}(r)$ is defined as the time required to consume 95% of the fuel in a given location of the ignition zone:

$$Y_F(r, \tau_{cons,F}) = 0.05 Y_{F,ini} \tag{8.4}$$

The values of $\tau_{cons,F}(r)$ in different locations of the ignition zone are reported in Table 8.5. In locations $r/r_0 \leq 0.15$, fuel is consumed before $t = 100$ μs, because temperature is higher than the critical ignition temperature (Fig. 8.14-bottom). In locations $r/r_0 > 0.15$, fuel is consumed after $t > 1$ ms. In this latter case, the temperature becomes higher than the critical ignition temperature only once the diffusion of temperature and species have become significant (Fig. 8.14-bottom). A practical consequence is that the size of the flame kernel at the end of the energy deposit (radius $r_{bg}(\tau_{dep})$) is much smaller than the input parameter r_0 of the ignition model. In fact, $r_{bg}(\tau_{dep})$ can even be equal to zero, because first burned gases appear just after the end of the energy deposit (as in Tab. 8.5). The flame kernel reaches the size r_0 only after several hundreds of μs, as illustrated in Fig. 8.15.

r/r_0	0	0.15	0.65	0.95
$\tau_{cons,F}(\mu s)$	27	76	1171	> 3000

Table 8.5: Values of $\tau_{cons,F}$ as defined in Eq. (8.4), for different locations $r^+ = r/r_0$ in the ignition zone. $E_{ign} = 0.84$ mJ, $r_0 = 1.25$ mm. $\phi = 0.6$, 2-step kinetic scheme.

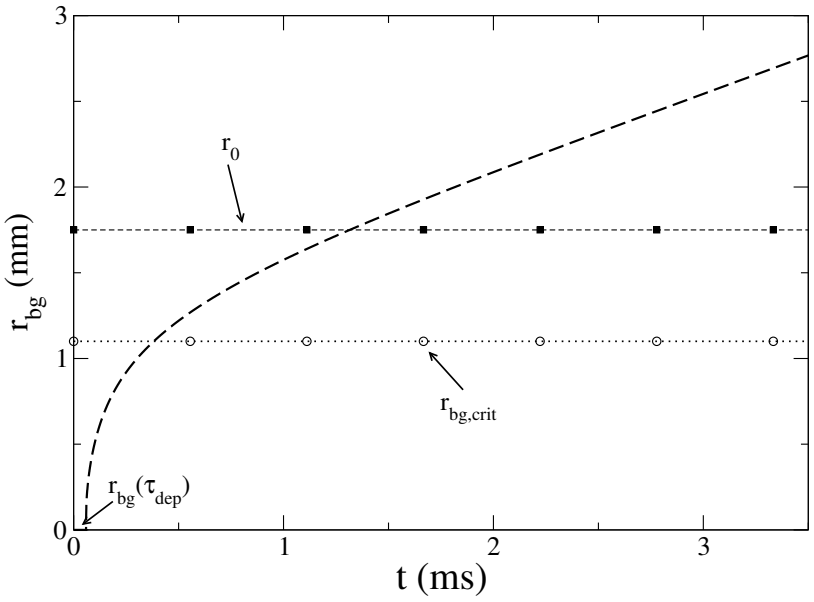

Figure 8.15: Time evolution of the burned gases radius r_{bg} for an ignition case of zone Z1. $E_{ign} = 2.1$ mJ and $r_0 = 1.75$ mm. (D3), 2-step kinetic scheme. $\phi = 0.6$.

8.2.2 Ignition in zone Z2

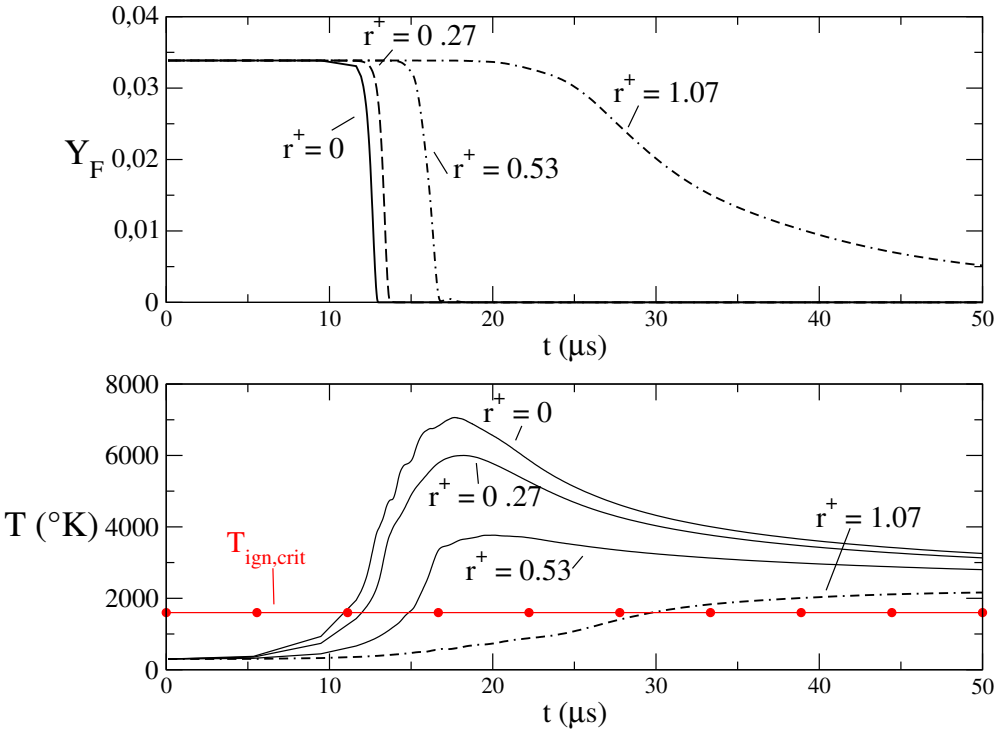

Figure 8.16: Zone 2. Top: temporal evolution of the fuel mass fraction Y_F in different locations of the ignition zone $r^+ = r/r_0$, r is the distance to the center of the ignition zone and r_0 the deposit radius. Bottom: temporal evolution of the temperature in different locations r^+ of the ignition zone. 2-step kinetic scheme, (D3), $E_{ign} = 0.42$ mJ, $r_0 = 0.745$ mm.

Figure 8.16-top displays the temporal evolution of the fuel mass fraction Y_F in

different locations of the ignition zone. Temporal evolutions of the corresponding temperature are displayed in Fig. 8.16-bottom. The fuel is consumed within the ignition zone between $\tau_{cons,F}(0) = 13\ \mu s$ (center of the ignition zone, $r = 0$) and $\tau_{cons,F}(r_0) \approx 50\ \mu s$ (limit of the ignition zone $r = r_0$). In fact, values $\tau_{cons,F}(r = 0)$ and $\tau_{cons,F}(r = r_0)$ are very similar and are of the order of magnitude of the deposit duration τ_{dep}. This means that ignition occurs much faster than the heat diffusion within the whole ignition zone:

$$\tau_{cons,F}(r \leq r_0) \ll \tau_{diff}(r \leq r_0) \tag{8.5}$$

Relation (8.5) is due to the fact that the ignition temperature is much higher than the critical ignition temperature ($T_{ign} \gg 1600\ K$) in the whole ignition zone (Fig. 8.16-bottom). A practical consequence is that the radius of the flame kernel at the end of the energy deposit $r_{bg}(\tau_{dep})$ is very close to the deposit radius r_0, as illustrated in Fig. 8.17.

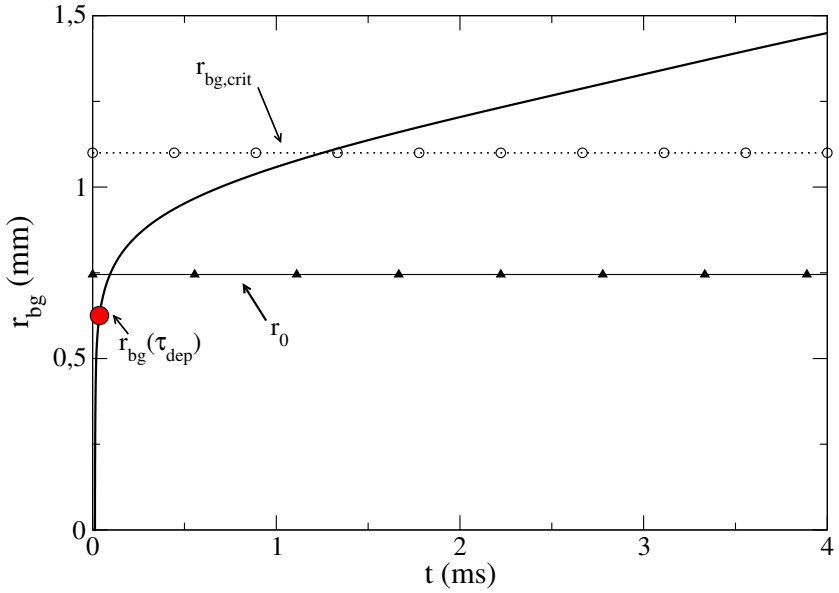

Figure 8.17: Zone Z2, successful ignition: time evolution of the burned gases radius r_{bg}. $E_{ign} = 0.42$ mJ and $r_0 = 0.745$ mm. $\phi = 0.6$, (D3), 2-step kinetic scheme.

8.3 Influence of the kinetics: ignition prediction using the analytical scheme

The purpose of this section is to characterize the differences in terms of MIE prediction between the simplified and the analytical scheme and to understand in which measure the use of the analytical scheme coupled to the energy deposit model can better describe ignition. To do so, MIE predictions using the analytical and the 2-step kinetics scheme are compared for different energy densities in section 8.3.1. Then results obtained in the present study are confronted to results of Sloane and Ronney in 8.3.2. Finally the evolution of the radicals concentration during ignition is described in section 8.3.3.

8.3.1 Global analysis: comparison of the MIE prediction using the 2-step kinetic scheme and the analytic scheme

A parametric study MIE function of the deposit radius r_0 was performed using the analytic scheme. Results are reported with the results obtained using the 2-step kinetic scheme (section 8.1.2) on the same diagram E_{ign} function of the deposit radius r_0, for the equivalence ratios $\phi = 0.6$ (Fig. 8.18-left) and $\phi = 0.85$ (Fig. 8.18-right). Similar trends are obtained using the analytical scheme and the 2-step kinetic scheme, for both equivalence ratios. Thus, in zone Z1 ($r_0 > r_{0,crit}$), MIE is proportional to the energy deposit volume, while in zone Z2 ($r_0 < r_{0,crit}$) MIE is quasi constant. The two parts of the diagram are detailed below:

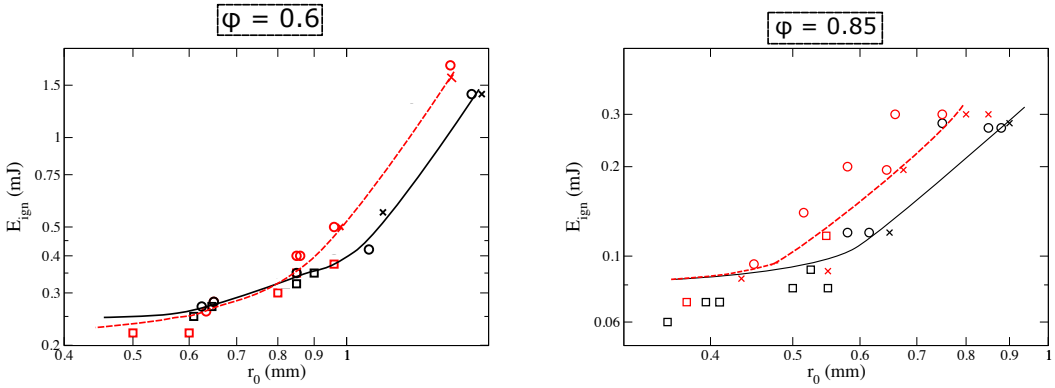

Figure 8.18: MIE as a function of the energy deposit radius r_0, using the 2-step kinetic scheme (black) and the analytic scheme (red). $\phi = 0.6$ (left) and $\phi = 0.85$ (right). Simulations (D2).

zone Z1 ($\mathbf{r_0 > r_{0,crit}}$): for a given deposit radius r_0, the MIE values predicted using the analytical scheme are higher than the MIE values predicted using the 2-step kinetic scheme. This implies that the energy density required to ignite using the analytical scheme is higher than the one required to ignite using the 2-step kinetic scheme. This result was already evidenced when calculating the ignition time τ_{ign} on homogeneous reactor, as presented in section 7.2.3.2 (see Fig. 7.6). These results can also be interpreted in terms of critical ignition temperature $T_{ign,crit}$:

$$T_{ign,crit,analytic} > T_{ign,crit,simplified} \tag{8.6}$$

where $T_{ign,crit,simplified}$ is the critical ignition temperature of the 2-step kinetic scheme as defined in section 8.1.2.1. $T_{ign,crit,analytic}$ can be equivalently determined for the analytical scheme. Thus, Fig. 8.19 shows the temporal evolution of the temperature in the center of the ignition zone for a successful ignition case (left) and an unsuccessful ignition case (right), using the analytical scheme. Successful and unsuccessful ignition cases have the same energy deposit radius r_0 and close ignition energy E_{ign}. The evolution of the temperature for the same cases for which chemical terms are set to zero is also displayed (dashed line). This gives an estimation of the critical ignition temperature in the center of the ignition zone: $T_{ign,crit,analytic} \approx 2400\ K$. This result confirms Relation (8.6), since it was established in section 8.1.2.1 that

$T_{ign,crit,simplified} \approx 1600\ K$, using an energy deposit with the same deposit radius r_0.

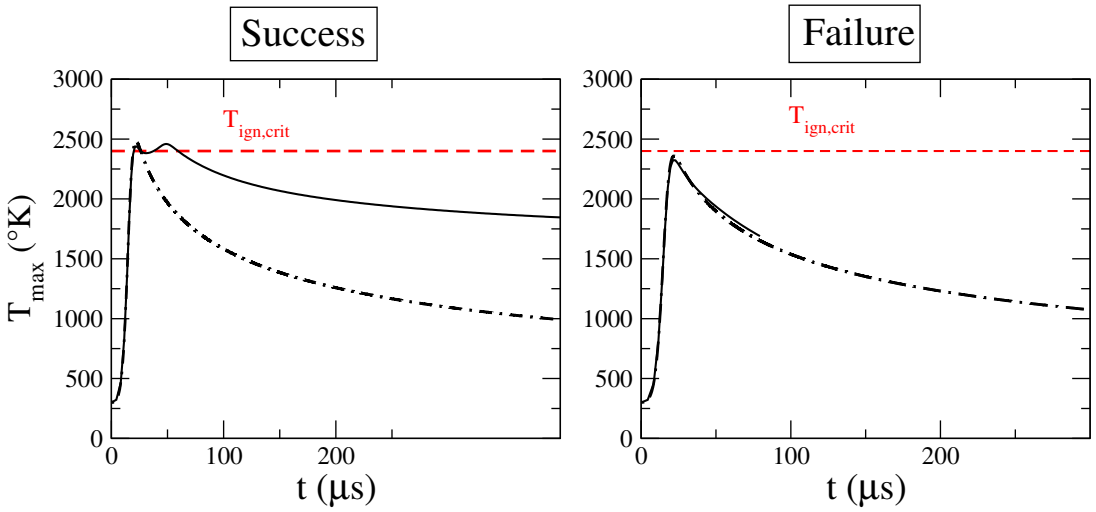

Figure 8.19: Estimation of the critical ignition temperature for the analytical scheme $T_{ign,crit,analytic}$. Temperature in the center of the ignition zone versus time. Left: $E_{ign} = 0.93$ mJ, $r_0 = 1.2$ mm; Right: $E_{ign} = 0.9$ mJ, $r_0 = 1.2$ mm. Plain line: reactive case, dashed line: same case with chemical terms set to zero. Analytical scheme. $\phi = 0.6$. Diffusion law (D3).

Zone 2 ($\mathbf{r_0 < r_{0,crit}}$): The analytical scheme and the 2-step kinetic schemes predict very close values of MIE. This is because, when $r_0 < r_{0,crit}$, the ignition temperature T_{ign} is high (in practice above 2500 K), higher than both the critical temperature $T_{ign,crit}$ of the 2-step kinetic and the critical temperature $T_{ign,crit}$ of the analytical scheme. Accordingly, both kinetic schemes predict a heat release important enough to balance the diffusive effects during the energy deposit phase and a phase of growth of the flame kernel is observed. These observations are once again consistent with the calculation of the ignition time τ_{ign} presented in section 7.2.3.2: it was established that, when the energy density $D = E_{ign}/r_0^3$ is above the critical energy density of the analytical scheme $D_{crit,analytic}$ (that is when $T_{ign} > T_{ign,crit,analytic}$), then the ignition times τ_{ign} obtained using the simplified and analytical chemistry are similar and are close to the deposit duration τ_{dep} (see Fig. 7.7).
Once the flame kernel is formed, it must reach the critical size to become a self propagating flame kernel. Because the critical size is related to the laminar flame thickness δ_L and that both kinetic schemes predict the same laminar flame thickness, the MIE values predicted by the two kinetic schemes are similar.

Results are now confronted in next section 8.3.2 to the results obtained by Sloane and Ronney (1992), who compared simplified and detailed chemistry (3.1.2.3).

8.3.2 Discussion of the results established by Sloane and Ronney

Conclusions established in the previous section differ from the ones of Sloane and Ronney (1992). In the following, elements to explain this discrepancy are proposed.

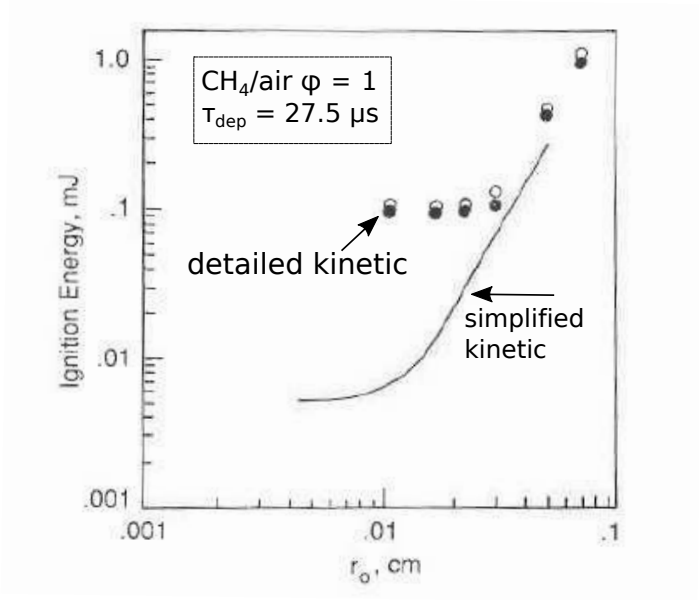

Figure 8.20: MIE as a function of the energy deposit radius r_0. Symbols: results obtained by Sloane and Ronney (1992) using the detailed kinetic scheme of Sloane (1989). Open circles: ignition occurred, filled circles: ignition failed to occur. Solid line: results of Frendi and Sibulkin (1990) using the simplified kinetic scheme of Coffee et al. (1983).

Figure 8.20 displays the MIE values obtained by Sloane and Ronney as a function of the deposit radius r_0. Main conclusions of the study of Sloane and Ronney are summarized (see also section 3.1.2.3):

- when $r_0 < 0.01$ cm, MIE predicted using the detailed chemistry (circle symbols in Fig. 8.20) is higher by a factor 20 that the one predicted using the simplified chemistry (solid line).

- when $r_0 > 0.03$ cm, there is only a factor ≈ 2 between the MIE predicted using the detailed chemistry and the MIE predicted using the simplified chemistry.

In order to discuss these results, it must be first recalled that Sloane and Ronney (1992) simulated the ignition of a methane/air mixture for the equivalence ratio $\phi = 1$. Then, following observations can be made:

- when $r_0 > 0.03$ cm (Fig. 8.20), the difference observed between the MIE predicted using the detailed mechanism and the simplified mechanism is similar to the one observed in the present ignition study (factor ≈ 2 of difference, see Fig. 8.18). It was explained in section 8.3.1 that this difference is due to the difference in terms of critical ignition temperature $T_{ign,crit}$, the critical ignition temperature of the analytical scheme being higher than the one of the simplified scheme. Even if Sloane and Ronney (1992) did not establish similar conclusions regarding the existence of a critical ignition temperature, they also observed that during ignition, temperature obtained using the detailed scheme is lower than the temperature obtained using a simplified scheme, for the same ignition parameters (E_{ign}, r_0) (Fig. 3.7).

- when $r_0 < 0.01$ cm, the deposit radius is very small. Very small deposit radius implies, as suggested by Sloane and Ronney, that the characteristic heat diffusion time τ_{diff} (Eq. (7.8)) becomes short enough to compete with auto-ignition during the energy deposit phase, even when the ignition temperature is high ($T_{ign} > 2000\ K$). Accordingly, auto-ignition delays prediction is essential to determine the MIE.

  This phenomenon is not observed in the present simulations, because leaner equivalence ratios are considered. As the ignition volume is related to the laminar flame thickness (see Fig. 8.18), the ignition volume increases for leaner equivalence ratios. For instance the smallest deposit radius r_0 considered in the present simulations is $r_{0,min} = 0.4$ mm. Accordingly, characteristic diffusion times are longer and there is no competition between heat diffusion and auto-ignition during the energy deposit phase.
  Further investigations would be required to confirm this hypothesis, e.g. to determine the MIE using analytical and simplified scheme for the equivalence ratio $\phi = 1$. However, stoichiometric ignition cases (presenting high laminar flame speed and very small ignition volume) are no object of particular interest, because then, MIE is very low and ignition is always successful with the current ignition devices.

8.3.3 Analysis of the radicals production during ignition

In this section, the evolution of the concentration of radicals during ignition is analyzed, for different cases of successful and unsuccessful ignitions. The evolution of the burned gases radius r_{bg} (see section 8.2) is not commented, because mechanisms of ignition are the same as the 2-step kinetic scheme ones (section 8.3.1,). The radicals description is the key difference. In the following, the critical ignition temperature $T_{ign,crit,analytic}$ is related to the production of the radicals. The critical ignition temperature of the analytical scheme $T_{ign,crit,analytic}$ is directly related to the production of a sufficient amount of radicals to initiate the combustion via the chain branching reactions. These radicals are typically radicals OH, H or O. To evidence this phenomenon, Fig. 8.21 presents the time evolution of the average mass fraction of these radicals, in a successful and in an unsuccessful ignition cases, with the same deposit radius r_0 and close ignition energy E_{ign}. (These two ignition cases are the same as the ones illustrated in Fig. 8.19). The mean mass fraction $[R_i]$ of the radical R_i is defined by:

$$[R_i] = \frac{\int_\Omega Y_{R_i} \mathrm{d}V}{V} \tag{8.7}$$

where Y_{R_i} is the mass fraction of radical R_i and V the volume of the domain of simulation.
Figure 8.21 shows that a slight change of energy density can trigger a significant apparition of these radicals: for the same deposit radius r_0, $E_{ign} = 0.9$ mJ is not sufficient to ignite, while $E_{ign} = 0.93$ mJ is sufficient. There is a dramatic difference between the radicals mean mass fractions of the successful (dashed line) and unsuccessful (plain line) ignitions. The concentration of radicals in the unsuccessful ignition case vanishes in a hundred μs, while in the successful ignition case, the amount of radical generated during the first 100 μs is large enough to initiate the chemical chain branching reactions. This on-off behavior is fully consistent with

the analysis performed in section 7.2.3.2, when calculating the ignition time τ_{ign} on homogeneous reactors: as the energy density D decreases toward $D_{crit,analytic}$, the ignition time τ_{ign} exponentially increases until it becomes infinity: no ignition takes place. This behavior somehow brings a more physical interpretation of the critical ignition temperature than the one of the simplified scheme, which is purely governed by the balance between the exothermic heat release and the diffusive heat losses.

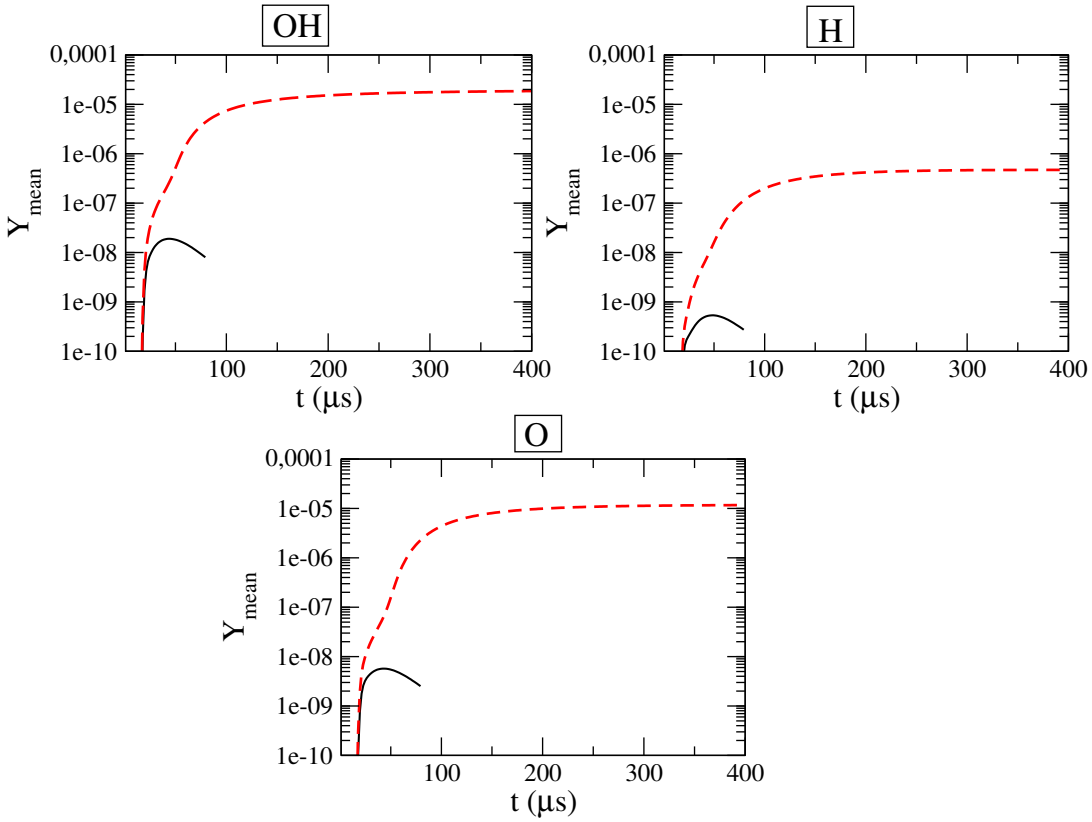

Figure 8.21: Evolution of the mean mass fractions of different radicals versus time, predicted by the analytical scheme. Dashed line (successful ignition): $E_{ign} = 0.93$ mJ, $r_0 = 1.2$ mm; plain line (unsuccessful ignition): $E_{ign} = 0.9$ mJ, $r_0 = 1.2$ mm (Zone Z2).

8.4 Comparison of simulations results against experimental data and analysis

In this section, simulations results are compared against the experimental results of Cardin et al.. The MIE values determined in the simulations were compared in Tab. 8.2 for three different equivalence ratios against the experimental values. A good agreement with the values measured by Cardin et al. was found. However, several other important experimental results must be discussed. In particular Cardin et al. define a chemical time τ_{CB} from their measurement in the laminar case (see section 6.2.1.2); authors base their analysis of the turbulent ignition regimes on the comparison between the time τ_{CB} with the Kolmogorov time τ_k. It is therefore essential to well understand the physical meaning of the characteristic time τ_{CB}: this aspect is discussed in section 8.4.1. This enables to determine in section 8.4.2

if a similar characteristic time can be defined in simulations. A second important result extracted from the experiments concerns the size of the flame kernel. As pointed out in the study of Klein et al. (2006), the size of the initial flame kernel determines kernel-turbulence interactions. Therefore this aspect is discussed in last section 8.4.3.

8.4.1 Chain branching time τ_{CB}

Cardin et al. define a chain branching time τ_{CB} as the duration required to observe an increase of the mean emission intensity of the flame kernel (see Fig. 6.9). Authors interpret τ_{CB} as a chemical time, corresponding to the initiation of the chain-branching reactions. Cardin (2013) suggests that this relation may be explained by the dependency of the MIE on the equivalence ratio but do not provide any further details. In order to better understand this aspect, an interpretation of the time τ_{CB} is proposed in the following. Figure 8.22 displays two of the mean emission intensity curves presented in section 6.2.1.2, for the equivalence ratios $\phi = 0.58$ and $\phi = 0.75$, respectively. For each case, the two parts of the curve are clearly indicated (τ_{CB} was determined as the intersection of the left exponential part, in blue, and of the right linear part, in red). For each part, a dominant mechanism governing the evolution of the kernel emissions is proposed:

- in the left part (blue line), the decrease of the emissions intensity is governed by the plasma relaxation. The corresponding characteristic time is larger for $\phi = 0.58$ than for $\phi = 0.75$. In fact, the four emissions intensity curves displayed in Fig. 6.9 suggest that the relaxation time increases when the equivalence ratio ϕ decreases. An explanation could be: because the deposited energy E_d increases when ϕ decreases, the relaxation time increases when ϕ decreases. Indeed, when the deposited energy E_d (equal to the MIE of the corresponding equivalence ratio) increases, the spark is then larger (see Fig. 6.7, showing the dimensions of the spark for different deposited energy E_d): it can be then reasonably assumed that the relaxation time of the flame kernel emissions, denoted $\tau_{diff,em}$, increases.

- in the right part (red part), the increase of the emissions is governed by the rate of growth of the flame kernel. The increase of the emissions is clearly more important for $\phi = 0.75$ than for $\phi = 0.58$ as confirmed by Fig. 6.9. As the rate of growth of the flame kernel is related to the flame time τ_c (Eq. 1.41), a simple way to verify these observations is to estimate the flame time τ_c for the different equivalence ratios. Values of the flame time τ_c are reported in Tab. 8.6 and displayed in Fig. 8.23 against the equivalence ratio ϕ. Values of the chain-branching time τ_{CB} are also displayed. Both characteristic times follow the same trend, strongly increasing for leaner equivalence ratios, thus confirming the proposed analysis.

Following interpretation of the time τ_{CB} is thus suggested: the time τ_{CB} results of the equilibrium between, on one hand the plasma (characteristic time $\tau_{diff,em}$) and on the other hand the growth of the flame kernel (characteristic time related to the flame time τ_c). Once the time τ_{CB} is reached, the combustion reactions

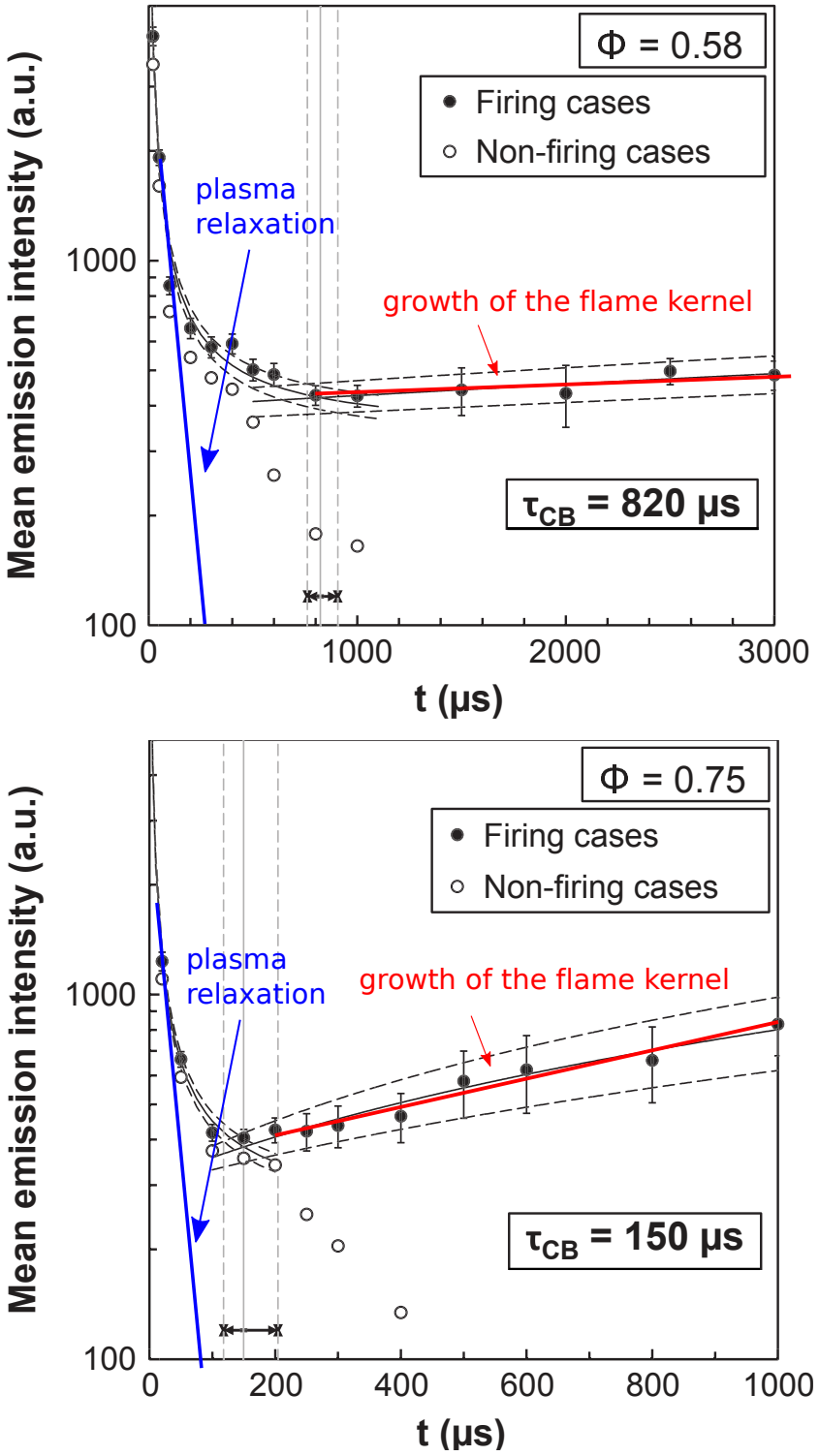

Figure 8.22: Temporal evolution of the mean emission intensity of the flame kernel for firing and nonfiring cases, for two different equivalence ratios, $\phi = 0.58$ and $\phi = 0.75$. The deposited energy is the MIE_0 value of the corresponding equivalence ratio. Cardin et al. (2013).

generate more heat (respectively more radicals) than heat is diffused by the post-breakdown relaxation and by the thermal diffusive losses at the flame kernel surface

equivalence ratio ϕ	0.55	0.6	0.63	0.65	0.7	0.75	0.8	0.85
τ_{CB} (μs)	927	711	567	304	167	150	140	148
τ_c (ms)	1623	830	619	514	345	252	202	165

Table 8.6: Values of the chain branching time τ_{CB} determined by Cardin et al. (2013) and of the flame time τ_c (Eq. 1.41), for different equivalence ratios ϕ.

(respectively radicals recombination). This interpretation is consistent with the 0D theories of ignition, as the one proposed by Ballal and Lefebvre (1974): when the deposited energy is the minimum ignition energy, the characteristic time of diffusion and of reaction are at equilibrium. If such an interpretation is correct, then the time τ_{CB} is equivalent to a diffusion time or to a reaction time, such as:

$$\tau_{CB} \propto \frac{\delta_L^2}{D_{th}} \tag{8.8}$$

Assuming that the minimum ignition energy and the ignition volume are related by the criterion (2.3), $MIE \propto \delta_L^3$, then τ_{CB} should verify:

$$\tau_{CB} \propto (MIE)^{2/3} \tag{8.9}$$

To verify this, experimental values of MIE_0 are displayed against the τ_{CB} values in Fig. 8.24 for the different equivalence ratios ϕ (values of τ_{CB} and of MIE are reported in Tab. 6.3). In Fig. 8.24, Eq.(8.9) is well verified for all equivalence ratios between $\phi = 0.58$ and $\phi = 0.7$, which confirms the proposed interpretation of the time. For $\phi = 0.55$, the measured value of MIE is higher than the one predicted by Eq. (8.9). A possible explanation is that this equivalence ratio is very close to the lean flammability limit and more energy than predicted by theory is required for ignition. For larger equivalence ratios $\phi > 0.7$, values of τ_{CB} reach a plateau ($\tau_{CB} \approx 150$ μs), while according to Eq. (8.9), values of τ_{CB} should keep decreasing as MIE decreases. A possible explanation is that a minimal relaxation time of the plasma is required. It would correspond to the duration required for excited species to relax and radicals to recombine, even if the ignition volume keeps decreasing.

8.4.2 Definition of an ignition characteristic time in simulations

This section proposes to determine if a characteristic time related to τ_{CB} can be defined in the simulations, although no breakdown is accounted for in simulation. This will also help to confirm the interpretation of the time τ_{CB} proposed in the previous section 8.4.1.

The issue is to be able to define from simulations a physical quantity, which temporal evolution would present the same characteristics as the mean emissions intensity of the flame kernel. As a preliminary step, a very simple approach is proposed, based on the following consideration: the mean emissions correspond to the full radiation spectrum emitted by the kernel (see section 6.1.1). It is thus assumed that the evolution of the kernel emissions is similar to the evolution of the

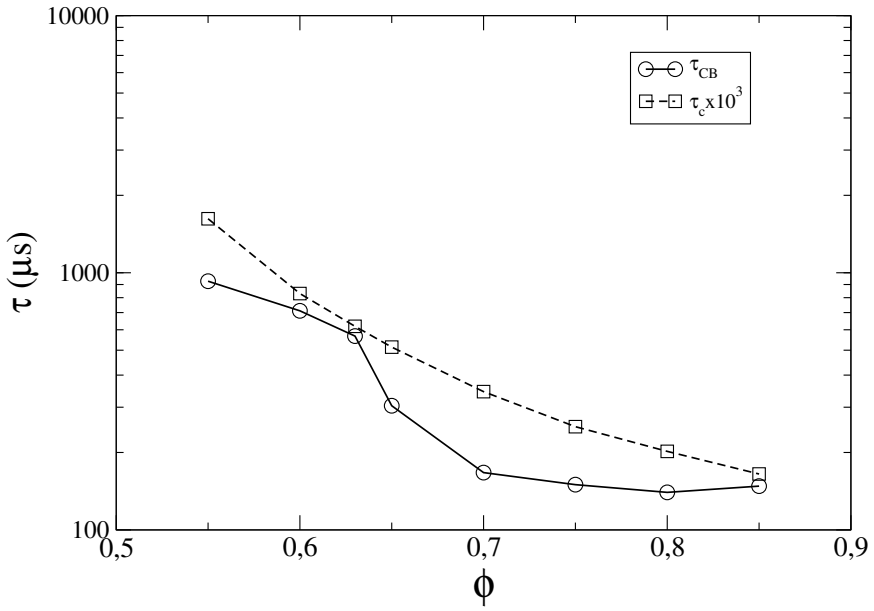

Figure 8.23: Different characteristic times plotted as a function of the equivalence ratio ϕ. Circle symbols: chain branching time τ_{CB}, square symbols: flame time τ_c.

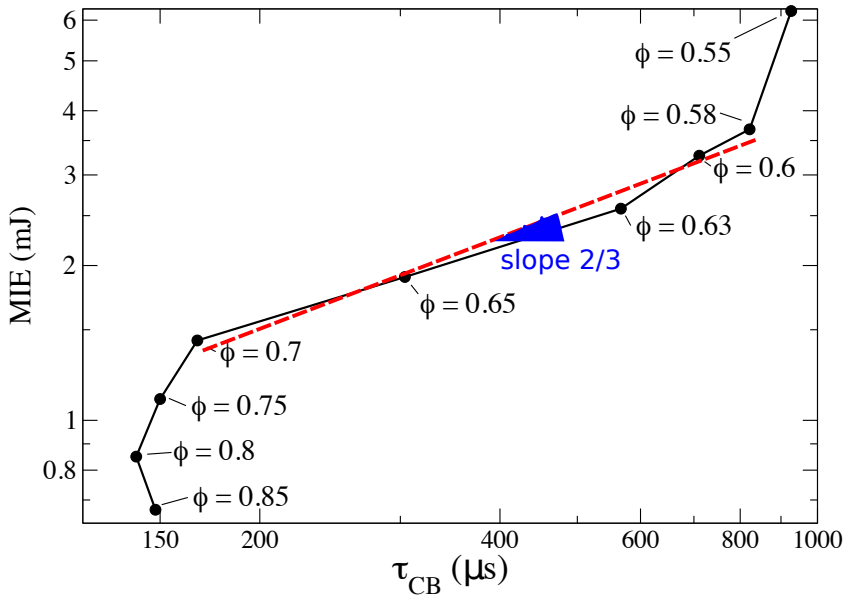

Figure 8.24: MIE (measurements of Cardin *et al.*) plotted as a function of the chain branching time τ_{CB} as defined by Cardin *et al.*, for equivalence ratios $\phi = 0.55$ to $\phi = 0.85$ (see Table 6.3).

heat produced by the kernel. Accordingly a mean temperature of the kernel, denoted T_{ave} and defined hereafter, is calculated. T_{ave} represents an average temperature within a zone of "hot" gases, accounting both for the growth of the hot zone and

for the diffusion effects within this zone. $T_{ave}(t)$ is calculated according to:

$$T_{ave}(t) = \frac{\int_{T>T_s} T(\mathbf{X},t)\mathrm{d}V}{\int_{T>T_s} \mathrm{d}V} \tag{8.10}$$

where T_s is an arbitrary level of temperature, chosen here as $T_s = 310\ K$ (the choice of T_s changes the value of T_{ave} but not its temporal evolution). Fig. 8.25 shows the evolution of T_{ave} with time, for the equivalence ratios $\phi = 0.6$ and $\phi = 0.85$. For each equivalence ratio, T_{ave} was calculated in a case of successful and unsuccessful ignition, for very close ignition energy E_{ign} (see the ignition parameters in Tab 8.7). In Fig. 8.25, a peak of T_{ave} can be observed, corresponding to the rise of temperature induced by the energy deposit and by the exothermic heat release of the combustion reactions during the first 50 μs. Note that the peak of T_{ave} is higher for the case $\phi = 0.6$ than for the case $\phi = 0.85$. This is because the energy E_{ign} is higher in the case $\phi = 0.6$ than in the case $\phi = 0.85$. Also diffusion effects within the ignition zone are more important in the case $\phi = 0.85$ than in the case $\phi = 0.6$, because the deposit radius r_0 in the case $\phi = 0.85$ is twice smaller than the deposit radius r_0 in the case $\phi = 0.6$ (see ignition parameters in Tab. 8.7). Then, the temperature T_{ave} decreases, because of heat diffusion. After a certain time, denoted τ_{crit} and indicated in the Fig 8.25, T_{ave} increases in the case of successful ignition, while T_{ave} keeps decreasing in the case of unsuccessful ignition. Note that the curves of T_{ave} show a similar trend as the experimental emission intensity curves of Fig. 6.9: a peak of temperature/emissions, followed by a relaxation and then an new increase of temperature/emissions, after a characteristic time (τ_{crit} or τ_{CB}) that varies with the equivalence ratio ϕ. Moreover, values of the characteristic time τ_{crit} for the equivalence ratios $\phi = 0.6$ and $\phi = 0.85$ are close to the values of τ_{CB} (see Tab. 8.8). Besides, in the case of successful ignition, the temperature T_{ave} grows faster (once $t > \tau_{crit}$) for the equivalence ratio $\phi = 0.85$ than for $\phi = 0.6$. Similar conclusions were established when describing the mean emission intensity curves in Fig. 8.22 : the rate of growth of the emissions when $t > \tau_{CB}$ increases with the equivalence ratio. The increase of the rate of growth of T_{ave} with the equivalence ratio is easily explained by the fact that the adiabatic temperature T_{adiab} for $\phi = 0.85$ is higher than the one for $\phi = 0.6$ and that $s_L(\phi = 0.85)$ is higher than $s_L(\phi = 0.6)$.

A similar characteristic time of ignition seems to be observed in the simulations and in the experiments. A last important feature of the ignition remains to be evaluated in order to fully assess the results of the laminar simulation studies: it concerned the size of the flame kernel, which is discussed in the next section 8.4.3.

8.4.3 Shape and size of the flame kernel

Simulations predict a MIE value and a characteristic time of successful ignition similar to the ones measured in the experiments. Recovering the correct size of the initial kernel in the laminar case is also essential to predict the ignition in the turbulent case: interactions between the vortices of the turbulence and the flame kernel change depending on the size of the flame kernel.
Images of the kernel at different times are displayed in Fig. 6.8. Assuming a spherical shape, the radius r_{kernel} of the kernel can be estimated, for instance at $t = 50\ \mu s$, for different equivalence ratios. The values of r_{kernel} are reported for the equivalence

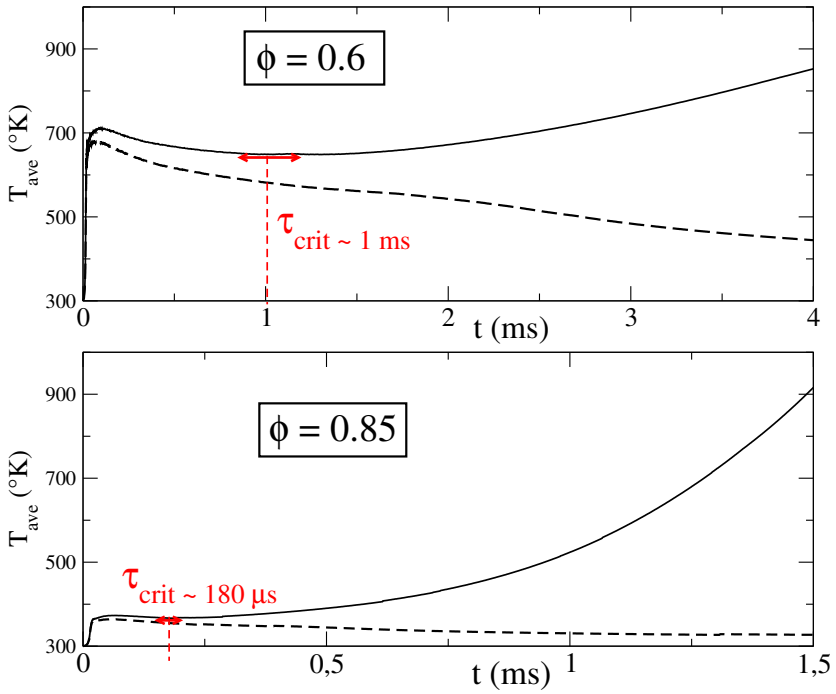

Figure 8.25: Left: $\phi = 0.6$, Right $\phi = 0.85$. Plain line: successful ignition. Dashed line: unsuccessful ignition. Ignition parameters are detailed in Tab. 8.7.

ratios $\phi = 0.55$, $\phi = 0.6$ and $\phi = 0.85$ in Tab. 8.9. Values of the burned gases radius r_{bg} at the instant $t = 50\ \mu s$ determined in the simulations are also reported, along with the values of the laminar flame thickness δ_L. Values of $r_{bg}(t = 50\ \mu s)$ were determined for the successful ignition cases described in section 8.1.3 (with the reference energy density D_{ref}). For all considered equivalence ratios:

$$r_{bg}(t = 50\ \mu s) < \delta_L < r_{kernel}(t = 50\ \mu s) \tag{8.11}$$

Besides, comparing burned gases radius r_{bg} with estimated experimental values of the kernel radius at longer times evidences a growing difference, as illustrated in Fig. 8.26. This large discrepancy between simulation and experiments does not depend on the kinetic scheme. According to these observations, the correct MIE is recovered but the volume of the flame kernel in the simulations is much smaller than the volume of the flame kernel estimated from the experimental images of Fig. 6.8.

		E_{ign} (mJ)	r_0 (mm)
$\phi = 0.6$	success	0.42	0.745
	failure	0.35	0.7
$\phi = 0.85$	success	0.084	0.87
	failure	0.078	0.84

Table 8.7: Ignition parameters (E_{ign}, r_0) for the ignition cases displayed in Fig. 8.25 2-step kinetics. (D2).

equivalence ratio ϕ	0.6	0.85
τ_{CB} (μs)	711	148
τ_{crit} (μs)	1000	180

Table 8.8: Values of the chain branching time τ_{CB} determined by Cardin et al. (2013) and of the critical time τ_{crit} determined in the simulations in Fig. 8.25

A possible explanation would be that the ignition volume (or which is equivalent, the reference energy density D_{ref}) was not correctly chosen in the simulations. To verify this, a very simple test was conducted for the equivalence ratio $\phi = 0.6$: ignition parameters (r_0, E_{ign}) were determined to obtain a flame kernel of same size than the size of the real flame kernel measured in Fig. 6.8 at $t = 50$ μs: $r_{bg}(t = 50\ \mu s) \approx r_{kernel}(t = 50\ \mu s)$, with E_{ign} being the minimum ignition energy. Ignition parameters were determined for both the 2-step kinetic scheme and the analytical scheme and are reported in Tab. 8.10. Note that for this range of deposit radius r_0 ($r_0 \gg r_{0,crit}$), the ignition simulations cases are now situated in zone Z1 in the diagram MIE function of the deposit radius r_0 (see Fig. 8.3). According to Tab. 8.10 and recalling that for $\phi = 0.6$, $MIE_{Cardin} = 3.42$ mJ:

$$0.15 * MIE_{Cardin} \ll MIE_{2,step} \ll MIE_{analytical} \tag{8.12}$$

As explained in section 8.1.3, the experimental value of MIE_{Cardin} is multiplied by a factor 0.15 to be compared against the MIE values determined in the simulations, because simulations do not account for the energy losses due to the pressure wave propagation. Relation $MIE_{2,step} \ll MIE_{analytical}$ is easily explained by the fact that the ignition temperature of the analytical scheme is larger than the ignition temperature of the simplified scheme (see section 8.3). Relation $0.15 * MIE_{Cardin} \ll MIE_{2,step}$ demonstrates that both the correct MIE and the correct ignition volume cannot be recovered in the simulations, and this whatever the chosen energy density E_{ign}/r_0^3. Either the MIE is correct but the flame kernel is too small compared to experiments, either the flame kernel is comparable to experiments and the MIE is too large. Several possibilities to explain this discrepancy are proposed hereafter.

equivalence ratio ϕ	0.55	0.6	0.85
$r_{kernel}(t = 50\ \mu s)$ (mm)	1.8	1.5	X
$r_{bg}(t = 50\ \mu s)$ (mm)	0.96	0.75	0.45
δ_L (mm)	1.29	0.96	0.5

Table 8.9: Comparison of the value of kernel radius r_{kern} at $t = 50$ μs (experiments), of the burned gases radius r_{bg} at $t = 50$ μs (simulations) and of the laminar flame thickness δ_L (1D flame calculations using the GRI 3.0 mechanism). The cross corresponds to non-available experimental data.

Plasma chemistry effects No radicals pool is accounted for in the simulations. In a real spark ignition, highly reactive radicals are generated by the breakdown

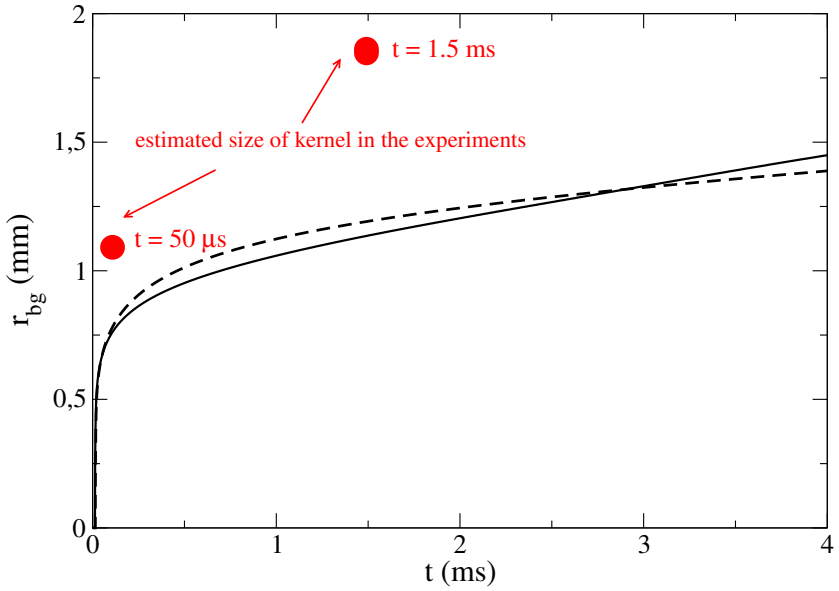

Figure 8.26: Evolution of the burned gases radius r_{bg}: plain line: 2-step kinetic, dashed line: analytical scheme. Reference energy density D_{ref} and E_{ign} =MIE. Filled circles correspond to the estimation, at the time $t = 50\ \mu s$ and $t = 1.5$ ms, of the radius of the kernel based on the experimental images displayed in Fig. 6.8.

ignition parameters	E_{ign}	r_0
2-step kinetics scheme	3.5 mJ	3 mm
analytical kinetic scheme	8 mJ	3 mm

Table 8.10: Determination of the MIE when imposing the values of $r_{bg}(t = 50\ \mu s) \approx r_{kernel}$, for the 2-step kinetic scheme and the analytical scheme. $\phi = 0.6$.

and represent a chemical source to sustain combustion. In the simulations, these radicals are replaced by thermal energy (2-step kinetic scheme) or by radicals generated via a thermal path (analytical scheme). A possible explanation to the fact that the MIE found in simulation is higher than the extrapolated value from the experimental measurements ($0.15 * MIE_{cardin}$), would be due to the radicals generated by the breakdown, promoting combustion. Unfortunately this point cannot be easily verified as the composition of the radical pool is unknown.

Pressure wave effects In the energy deposit model, a spherical shape of the flame kernel is assumed. The sphericity assumption is also used to determine the values of r_{kernel} in the kernel images of Fig. 6.8. In fact, this assumption is not valide: the kernel does not develop as a sphere. As illustrated in Fig. 6.6, just after the breakdown, the plasma presents a non-symmetrical ellipsoidal shape. Then, the post-breakdown pressure wave induces gas dynamic effects, strongly affecting the development of the gas kernel (Spiglanin et al., 1995; Morsy and Chung, 2002; Bradley et al., 2004), that is non-spherical. For instance it can be seen in Fig. 8.27 that the spark takes first an ellipsoidal shape (instants $t = 5\ \mu s$ on the right and instant $t = 5 = 3\ \mu s$ on the left). Then it develops orthogonally to the Laser direction

(between $t > 5$ μs and $t \sim 50$ μs), while the pressure wave expands (Fig. 8.27-left). Bradley et al. mention a form of doughnut: the flame kernel is not spherical but presents a toroidal shape. Around $t \sim 90$ μs, a third-lobe structure appears in the front of the flame kernel, that keeps growing at longer times (Fig. 8.27 right and left). Bradley et al. explain that these complex shapes of the kernel results from the initial non-symmetrical ellipsoidal shape of the plasma. Now coming back to the images of the flame kernel recored in the study of Cardin displayed in Fig. 6.8, the flame kernel appears there to be spherical, because these images were taken in the same direction as the Laser beam, which is the direction of the torus axis and not perpendicular to it. Therefore, the toroidal shape and the structure of the third-lobe cannot be observed. Note that in the images of Fig. 6.8, a hole in the center of the kernel can be observed, that should correspond to the center of the torus. According to these observations, a guess is that the characteristic length in experiments to be compared with the deposit radius r_0 in simulations is not the length r_{kernel} (length of the torus), but rather the height of the torus, denoted h. From there, it can be reasonably assumed than the height h of the torus is smaller than the length r_{kernel}. If this assumption is verified, then this would explain why, when the deposit radius r_0 is chosen to verify $r_{bg}(t = 50\ \mu s) = r_{kernel}$, the value of the MIE found is simulation is larger than the experimental value: the volume of the sphere of radius r_{kernel} is larger than the volume of the torus of length r_{kernel} and of height $h \ll r_{kernel}$, therefore more energy is required to ignite the sphere of radius r_{kernel} than the tore.
Unfortunately, verifying these assumptions from the available experimental data is not possible. From a simulation point of view it would be also delicate to verify it. Initial conditions of the spark channel (pressure, temperature, shape, dimensions) are primordial to accurately predict the gas motions: the exact shape and dimensions of the kernel depend on these conditions (Bradley et al., 2004). Furthermore, CPU resources are today limited to perform both the calculation of the plasma channel expansion, resolving the complex gas motions and determining the MIE. No such study exists to our knowledge, but this would be an interesting path to investigate.

8.5 Conclusions

In this chapter, LES of ignition in quiescent laminar lean methane/air mixtures were performed, using the ED model (Lacaze et al., 2009) and setting the thickening factor of the TF-LES approach to unity. Several parametric studies were conducted, to determine the numerical and physical ignition parameters.
Focus was first on the influence of equivalence ratio ϕ, deposit radius r_0 and Lewis numbers Le_k on MIE prediction, when using a 2-step kinetic scheme. Corresponding parametric studies enabled to clearly define two ignition criteria and to relate them to the size of the deposit radius r_0. Thus, when the radius r_0 is larger than the critical value $r_{0,crit}$, related to the laminar flame thickness δ_L, the mixture ignites if and only if a critical ignition temperature is reached. The critical ignition temperature is governed by the balance between heat diffusion and heat released by combustion during the deposit phase. Accordingly the critical ignition temperature was found to be independent of equivalence ratio and Lewis numbers, which have no significant effect on the auto-ignition of the mixture during the deposit phase. When the radius r_0 is smaller than the critical value $r_{0,crit}$, the ignition energy E_{ign} must be sufficient

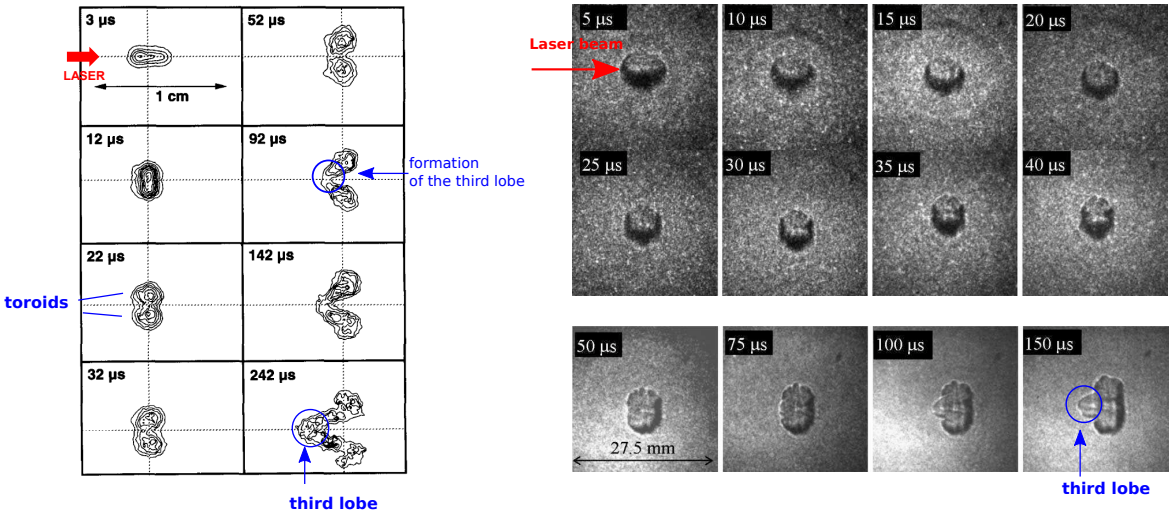

Figure 8.27: Right: Iso-contours of the fluorescence signal (OH radical) of the kernel at different instants after the breakdown (mixture H2/O2/Ar) Spiglanin et al. (1995). Left: Imacon schlieren images of non-igniting propane-air mixture, $\phi = 0.45$. Incident Laser energy: 224 mJ. Bradley et al. (2004)

to sustain the flame kernel until it self-propagates. A critical burned gases r_{bg} was defined, corresponding to the size above which the flame kernel is self-sustained. Values were found to be related to the laminar flame thickness δ_L, in agreement with previous literature results. Finally the high-temperature effects during the energy deposit phase were characterized: accounting for the correct diffusivity using the D'Angola law during the high temperature phase ($T > 2000\ K$) has in fact a limited effect on ignition. The key phase is the flame kernel growth phase, when the temperature is lower ($T < 2000K$).

In a second part, a more detailed analysis of the ignition mechanism in simulations was proposed and highlighted the differences of the ignition process, according to the size of the deposit radius r_0. When the deposit radius r_0 is smaller than the critical radius r_0, ignition occurs fast in the zone of width r_0, in a time close to the deposit duration τ_{dep}. For larger deposit radii ($r_0 > r_{0,crit}$), ignition is still fast in the center of the ignition zone, where burned gases appear after a time close the deposit duration τ_{dep}, but at larger radii, diffusion effects become significant and ignition occurs later.

In a third section, ignition simulations were performed with an analytical scheme. MIE values obtained with this scheme and the 2-step simplified scheme were compared. The analytical scheme was found to behave the same way as the 2-step kinetic scheme: once the critical ignition temperature is reached, chemical reactions quantitatively take place in a few μs. The critical size above which the flame kernel becomes self-sustained was found to be close to the one predicted by the 2-step kinetic scheme. The major difference between the two schemes concerns the value of the critical ignition temperature which is higher for the analytical scheme, because this scheme accounts for the creation of a radicals pool following the thermal energy deposit. This results in different MIE prediction, the MIE predicted by the analytical scheme being higher than the one predicted by the 2-step kinetic scheme by about a factor 2-3, when the energy density of the deposit is lower.

Finally, simulations results were confronted to the experimental results of Cardin

et al. (2013). MIE values determined in simulations were found to be in good agreement with experimental values. A new interpretation of the characteristic time τ_{CB} defined in experiments by Cardin et al. (2013) was proposed, based on a balance between the plasma relaxation process and the growth of the flame kernel. This interpretation was confirmed by the simulations, where a time similar to τ_{CB} can be defined. However, an important element of discrepancy between simulations and experiments concerns the shape and size of the flame kernel. On the experimental images of kernel emissions, the kernel appears spherical, and with a radius about twice larger as the radius found in simulations. In fact, the kernel is not spherical but develops with a toroidal shape, which volume could possibly be similar to the volume of the flame kernel in simulations. This could be an element of explanation to the fact that the size of the kernel is smaller in simulations than in experiments, although the MIE and the characteristic time τ_{CB} are similar. To verify this, future simulations should account for the non-spherical kernel development, that can be predicted only by describing the initially cylindrical or ellipsoidal spark expansion. In this context, the first tests of turbulent ignition cases presented in next Chapter 9 will provide additional elements to serve this discussion: as shape and size of the flame kernel are essential in flame-turbulence interactions, the difference in terms of shape between simulation and experiments could result in differences in terms of MIE in the turbulent case.

Chapter 9

Toward DNS of turbulent ignition cases

Contents

In this chapter, first simulations of the turbulent ignition cases experimentally characterized by Cardin et al. (2013) are presented. The laminar ignition study presented in Chapter 8 enabled to determine the reference ignition parameters (E_{ign}, r_0) and to highlight the governing mechanisms in the laminar case. Conclusions established in the laminar case will help to analyze the results of the turbulent tests. Only a reduced number of turbulence conditions could be investigated, they are first presented, along with the method of generation of the initial homogeneous isotropic turbulence field. Ignition results are then detailed and elements of discussions proposed.

9.1 Cases considered

Among the different turbulence conditions investigated by Cardin et al. (see section 6.1.2), two conditions of turbulence were chosen, indicated in Fig. 9.1:

- **Condition 1** corresponds to a low turbulence intensity: $u' = 0.68$ m/s, before the ignition transition for the lean equivalence ratio $\phi = 0.6$ (left part of the MIE diagram in Fig. 9.1).
- **Condition 2** corresponds to a high turbulence intensity: $u' = 1.43$ m/s, after the ignition transition for the lean equivalence ratio $\phi = 0.6$ (right part of the MIE diagram in Fig. 9.1).

Turbulence characteristics (turbulence intensity u', kinetic energy dissipation rate ϵ and integral length scale l_t) are reported in Tab. 9.2. Values of the integral scale l_t were calculated based on the experimental value of the dissipation rate ϵ, more precise than the measure of the integral length scale (see Mazellier et al. (2010)) such as:

$$l_t = \frac{u'^3}{\epsilon} \tag{9.1}$$

In those first tests, attention is paid in particular:

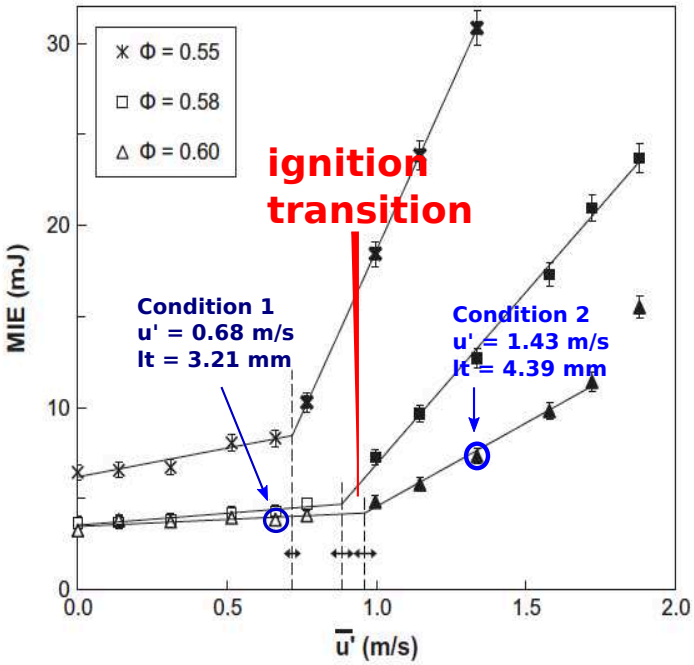

Figure 9.1: Measured MIE in the experiments of Cardin et al. (2013), for the equivalence ratios $\phi = 0.55$, $\phi = 0.58$ and $\phi = 0.6$. Conditions 1 and 2 correspond to the conditions chosen for the simulations.

	Condition 1	**Condition 2**
u' (m/s)	0.68	1.43
ϵ ($m^2.s^{-1}$)	96	668
l_t (mm) Eq. (9.1)	3.21	4.39

Table 9.1: turbulence properties of the initial flow field for simulations

- to assess whether ratios MIE/MIE_0 follow experimental trends.
- to investigate changes in flame kernel shapes with turbulence conditions. (see Fig. 2.18) .

The energy density of the energy deposit $D = E_{ign}/r_0^3$ is the reference energy density D_{ref} defined in section 8.1.2.3. A few parametric studies were performed, to investigate possible causes of variations in the turbulent flame kernel development:

1. Lewis number Le_k: calculations were performed for unity (group (D2), see Tab. 7.1) and non-unity (group (D3)) Lewis numbers Le_k.
2. kinetics: calculations were performed using the 2-step and the analytical schemes.

Before presenting the results of the different tests in section 9.3.1, the numerical set-up is described in next section 9.2.

9.2 Numerical set-up

9.2.1 Calculation domain

The parameters of the calculation domain are summarized in Tab. 9.2. Cells are hexahedrons and the mesh resolution is set to $\Delta_x = 50\ \mu m$ (see section 7.1.4). According to the estimations of the turbulent properties provided in the study of Cardin et al. (2013) (see Tab 6.1), the Kolmogorov scale η_k ranges between 50 μm and 94 μm, thus the cell size Δ_x is not small enough to discretize the Kolmogorov structures (2 points of resolution are required according to the Nyquist criterion). However the resolution of the LES remains very close to a DNS. The calculation is a square 3D domaine of length $L = 12$ mm, containing thus 13.4 millions nodes. The domain must contain at least 2 to 3 times the integral length scale to capture the whole range of turbulence structures.

Hexahedrons size Δ_x	length of the domain L	Boundary conditions
50 μm	12 mm	periodic

Table 9.2: Parameters of the calculation domain used for the turbulent ignition cases

9.2.2 Generation of the homogeneous isotropic turbulence velocity field

To obtain the same turbulence properties as in the experiments, two solutions can be used. The first one consists to calculate the whole experimental device, e.g. the wind tunnel and the turbulence grids. But doing so requires specific cold flow calculations and very important CPU resources. Besides nothing ensures that the calculated turbulence flow field will have exactly the same properties as in the experiments. The second solution consists to generate a homogeneous isotropic turbulence (HIT) flow field, using a synthetic initial turbulence spectrum, with the turbulence properties (turbulence intensity u', dissipation rate ϵ) measured in experiments (see Tab. 9.2). Note that in simulations the turbulence is a temporally decaying turbulence, the simulation domain being convected at the mean velocity U_0. In experiments the turbulence is temporally and spatially decaying (see section 6.1.2).
The HIT is initialized with a Passot-Pouquet spectrum (Passot and Pouquet, 1987). As the initial Passot-Pouquet spectrum is not a solution of the Navier-Stokes equations, cold flow calculations were performed to obtain the turbulence flow field with the desired turbulence properties (u', ϵ). Calculations must last an eddy turnover time which corresponds here to 1 for condition 1 and 3 ms for condition 2. As an illustration, the evolution of the cold flow turbulence characteristics (u', ϵ) are displayed in Fig. 9.2. The red point at time $t = t_{ini}$ indicates the initial solution for the ignition calculations. Until the time t_{ini}, the dissipation rate ϵ increases, as the turbulence spectrum fills with smaller scales. At time $t = t_{ini}$, the dissipation rate reaches a minimal value, corresponding to the instant when the turbulence spectrum is filled with all scales until the cell cut-off scale $2\Delta_x$. Then the dissipation rate ϵ decreases, because turbulence dissipates. As complementary information, Fig. 9.3 displays the turbulence spectrum for different times between $t = 0$ and $t = t_{ini}$,

showing the spectrum filling with smaller scales, while the turbulence intensity decreases.

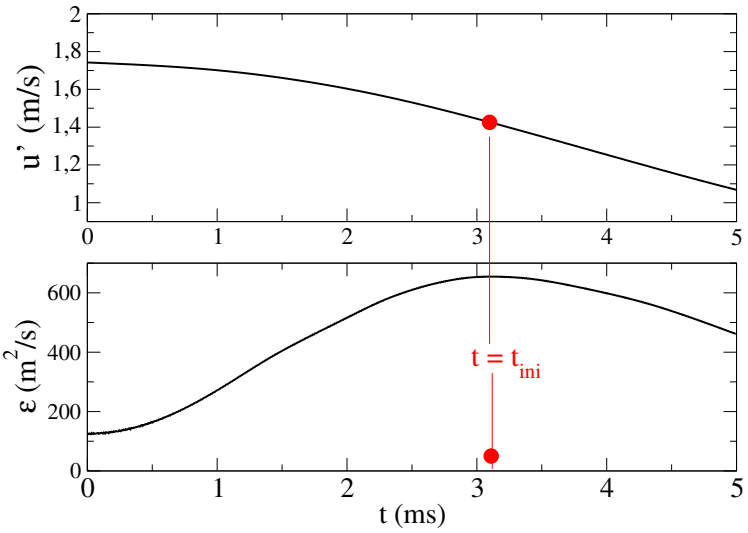

Figure 9.2: Cold flow calculation of the turbulence (Condition 2) initialized by the Passot-Pouquet spectrum. Top: turbulence intensity u' versus time. Bottom: dissipation rate $\epsilon = -d\kappa/dt$ versus time, where κ is the total kinetic energy in the calculation domain. Red point: initial solution for the calculation of ignition .

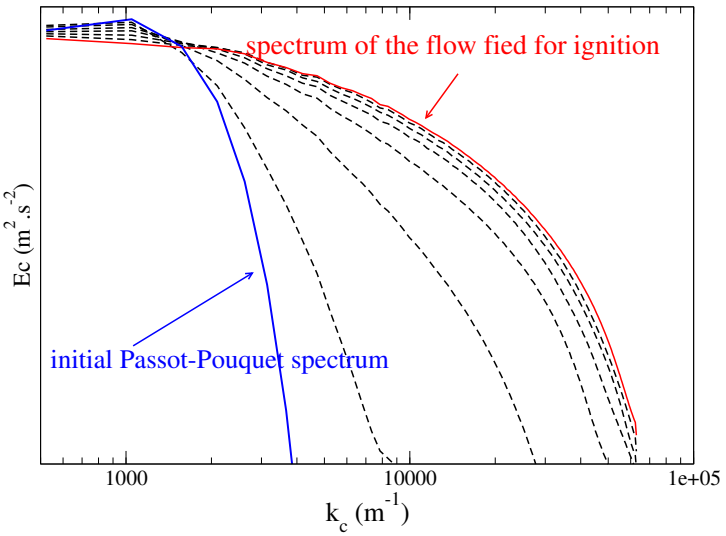

Figure 9.3: Turbulence spectrum at different times of the cold flow calculation presented in Fig. 9.2, between timing $t = 0$ and $t = t_{ini}$.

9.3 Results and discussions

9.3.1 Results of the simulations

Fig. 9.3.1 displays the ratios E_{ign}/MIE_0 calculated in the simulations using the 2-step kinetic scheme, the analytical scheme and different Lewis number values. The MIE_0 value corresponds to the values of the MIE determined in the laminar case (see

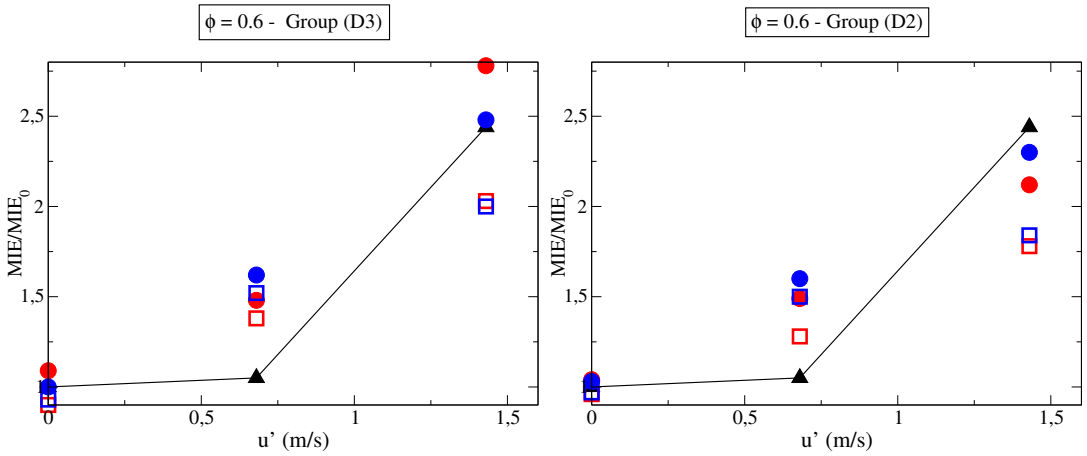

Figure 9.4: E_{ign}/MIE_0 values obtained in simulations using the 2-step kinetic scheme (red) and the analytical scheme (blue). Circle: successful ignition. Squares: unsuccessful ignition. Triangle: experimental measurements of the ratio MIE/MIE_0, Cardin et al. (2013). $\phi = 0.6$. Left: group (D3) simulations. Right: group (D2) simulations .

Tab. 8.2). As in the laminar case, circle symbols denote a successful ignition, while square symbols denote unsuccessful ignition where the flame kernel extinguishes after a phase of growth that can last several ms (see section 8.1.2). The ratio MIE/MIE_0 determined in simulations is then situated in-between the circle and square symbols, for each turbulence conditions. Experimental values of the ratio MIE/MIE_0 are also reported. Following observations can be made:

- Simulations results do not vary much with Lewis numbers nor with the type of kinetics. This may be explained by the fact that in simulations, kinetics behave as in the laminar case: because auto-ignition occurs very quickly ($\sim 20\ \mu s$), it is not affected by turbulence. The characteristic time of ignition is much smaller than the Kolmogorov time τ_k and turbulence acts only during the phase of growth of the flame kernel. Even if the response of the flame to the strain depends on kinetic scheme and Lewis numbers, they seem to have in practice a limited effect on the prediction of the ratio MIE/MIE_0.

- In simulations, the ratio MIE/MIE_0 linearly increases with the turbulence. On the contrary, a plateau is observed in experiments, which predict that the ratios MIE/MIE_0 are equal to unity until a certain value of turbulence intensity u'_{crit} (see also Fig. 2.17 displaying all turbulence conditions investigated in experiments).

- Same order of magnitude of the ratio MIE/MIE_0 for the high turbulence intensity case (condition 2) is predicted in simulations and in experiments. However, when simulating the same ignition case with the turbulence conditions 2 but at the equivalence ratio $\phi = 0.55$, then the difference between the ratio MIE/MIE_0 predicted in simulations and the one measured experimentally becomes important: as seen in Fig. 9.5, the ratio MIE/MIE_0 predicted in simulations is twice smaller than the one measured experimentally for the equivalence ratio $\phi = 0.55$.

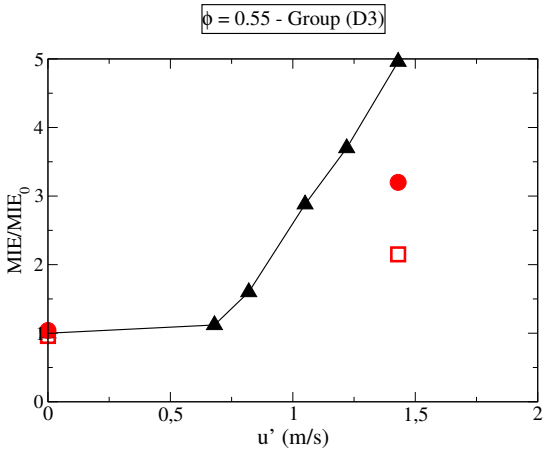

Figure 9.5: E_{ign}/MIE_0 values obtained in simulations using the 2-step kinetic scheme. Circle: successful ignition. Square: unsuccessful ignition. Triangle: experimental measurements of the ratio MIE/MIE_0 Cardin et al. (2013). $\phi = 0.55$, group (D3).

Additional information are provided by 3D fields observations. Figure 9.6 displays 3D isosurfaces of temperature, for the turbulence conditions 1 and 2, at three different times after ignition. The flame kernel is less wrinkled for the low (u' = 0.68 m/s, before ignition transition) than for high (u' = 1.43 m/s, after ignition transition) turbulence conditions. But in this latter case, the aspect of the flame kernel is very different from experimental findings. Simulations predict that the flame front remains continuous, even though it is wrinkled. According to the experimental observations, the flame is disrupted, from early timings ($t < 700\ \mu s$), as seen in Fig. 2.18, right column. Possible elements of explanations will be discussed in section 9.3.2. However the differences in terms of flame kernel aspect are consistent with numerically under-predicted MIE in the high turbulence intensity case (condition 2): when the flame front remains continuous, diffusive heat losses are less important than when the flame front is disrupted, therefore less energy is required to ignite.
Simulating ignitions with higher turbulence intensity and different equivalence ratios would be necessary to confirm these findings, in particular to confirm that simulations under-predict the minimum ignition energy in the high turbulence intensity regime. Note that to generate the turbulence corresponding to higher turbulence intensity cases (for instance $u' > 1.43$ m/s for the equivalence ratio $\phi = 0.6$), a larger simulation domain would be required, because then the integral length scale l_t increases. For reasons of CPU resources and time, such calculations were not performed. However, the results of these first tests are already sufficient to conclude that the simulation approach adopted here is not predictive enough.

9.3.2 Discussions

The previous results are now discussed.

Shape and size of the initial flame kernel A first possible explanation is based on finding that in the laminar case, the development of the flame kernel also dif-

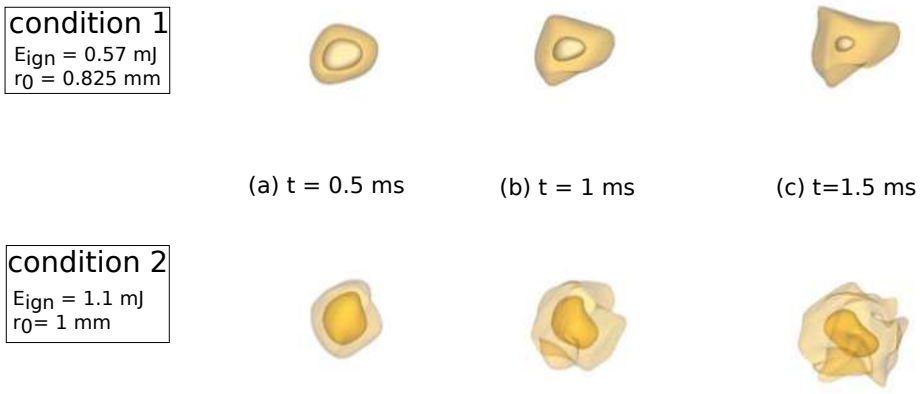

Figure 9.6: Isosurfaces of temperature ($T = T_{adiab}$ and $T = 450$ K), at three different timings after ignition. Top: Condition 1 ($u' = 0.68$ m/s). Bottom: Condition 2 ($u' = 1.43$ m/s). $\phi = 0.6$, 2-step kinetics, simulations (D3).

fers in simulations and experiments (see section 8.4.3). Instead of developing as a sphere, as in simulations, the kernel develops with a toroidal shape, then with a third-lobe structure, without relaxing toward a spherical shape even at longer times (see Fig. 8.27). Shape and size of the kernel are essential parameters for flame-turbulence interactions. It can be reasonably assumed that, for high turbulence intensity cases, a toroidal flame kernel is more deformed by turbulence than a spherical flame kernel. Unfortunately, as explained in section 8.4.3, the images of the kernel recorded in the study of Cardin et al. (2013) (Fig. 2.18) were taken in the same direction as the Laser beam, therefore these cannot help to validate this hypothesis: the toroidal shape of the flame kernel and the third-lobe can be observed only if images are recorded perpendicular to the Laser beam. In their Laser-ignition study, Mulla et al. (2015) recorded such images: Fig. 9.7 displays instantaneous OH-PLIF of the flame kernel developing in a turbulent flow of various Reynolds number Re, recorded in the direction perpendicular to the Laser beam. In these experiments, a methane/air mixture coming out of a Bunsen burner is ignited at a given distance above the burner lips. The Reynolds number in the left image ($Re = 575$) corresponds to the laminar flow regime for pipe flow. In this image, the two toroids (upstream and downstream parts) of the kernel and the third-lobe can be well identified. For the higher Reynolds number corresponding to the turbulent flow regime (middle and right images), the three segments can still be observed but the toroids are stretched and the third lobe appears disintegrated. These effects become stronger when the Reynolds number increases. Such observations could explain why in the images of Fig. 2.18-right column recorded by Cardin et al. (2013), the flame kernel is so fragmented and disrupted: images show the planar projection of the tore and of the third-lobe. If the tore is stretched and the front-lobe torn apart, then their projection in a plan perpendicular to the axis of the torus may present this fragmented aspect. If these explanations are correct, then they also enable to understand why the minimum ignition energy so drastically increases for high turbulence intensity: very fragmented flame kernels require much higher ignition energy, because their heat losses are drastically increased.

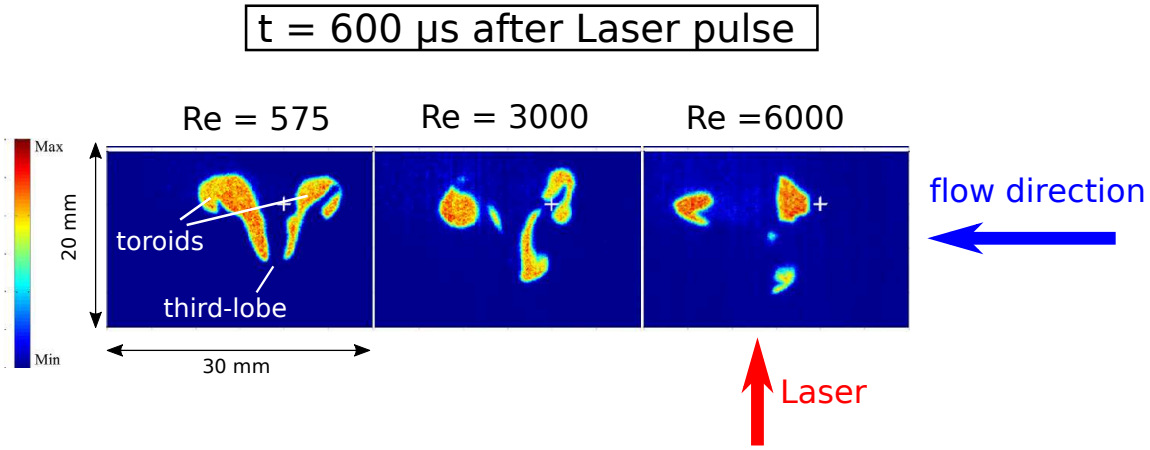

Figure 9.7: Instantaneous OH-PLIF images of igniting methane/air mixture at $\phi = 0.6$, for different Reynolds number, study of Mulla et al. (2015). The white cross mark indicates the approximate location of focus of the ignition-laser beam. Mean pulse energy of the Laser: $E = 138$ mJ.

If this analysis is correct, future works should then understand how to precisely relate the deformations of the flame kernel described above to the evolution of the ratio MIE/MIE_0 with the turbulence intensity u' and with the equivalence ratio ϕ.

To complete the discussions, other possible causes of the discrepancy between simulations and experiments are proposed.

Turbulence properties turbulence properties may not be exactly the same as in the experiments. The procedure of generation of the initial turbulence flow field can be trusted to recover very close turbulence intensity u' and integral length scale l_t to the ones of the experiment. But nothing enables to verify the turbulence properties at longer times. Also a more precise technique could be used to generate the turbulence flow field: a rigorous DNS could be performed, using a more elaborate initial spectrum than the Passot-Pouquet spectrum to generate the homogeneous isotropic turbulence. However such procedure would be at the expense of increased CPU costs. Besides, according to the analysis presented above, possible imprecisions of the turbulence properties alone cannot explain the discrepancies between simulations and experiments and it is believed that the kernel shape is the first order explanation.

Plasma chemistry effects as proposed by Cardin et al. (2013), chemical effects may play the key role and the ignition regimes may result of the competition between initiation of the chain-branching reaction (characteristic time τ_{CB}) and turbulence. In that case a more advanced modeling of the breakdown process would be required, such as the description of an initial radical pool

9.4 Conclusions

This chapter was devoted to preliminary simulations of turbulent ignition cases experimentally characterized by Cardin et al. (2013). The energy deposit model

(Lacaze et al., 2009) was used to simulate the ignition in a homogeneous isotropic turbulence flow field. Only two turbulence conditions were investigated, for reasons of CPU resources and of time. The comparison to experimental results led to the conclusion that both minimum ignition energy prediction and flame kernel aspect are not correctly predicted in simulations. A probable explanation was proposed, different from the analysis proposed by Cardin et al. (2013). The exponential increase of MIE in the high turbulence intensity regime was attributed not to the Kolmogorov time τ_k becoming smaller than the chain branching time τ_{CB} (Cardin et al., 2013), but to the very important wrinkling of the flame kernel, presenting a three-segments shape that is very easily stretched and torn apart at high Karlovitz number ($Ka > 20$ in the present study). Neglecting in simulations the non-spherical flame kernel development caused by the post-breakdown pressure wave propagation distorts the flame-turbulence interactions, resulting in a incorrect prediction of the minimum ignition energy and of the flame kernel aspect. Further investigations are required to validate this hypothesis. For instance, numerical simulations accounting for the ellipsoidal or cylindrical shape of the spark, with initial conditions of temperature and pressure characteristic of the post-breakdown state, should be performed in turbulent flows, for longer times of the order of one milliseconde. Only then the toroidal development of the flame kernel could be described, its impact on the flame turbulence interactions characterized and its influence on the minimum ignition energy determined. However performing such simulations are not only very CPU demanding but also very delicate because, as already mentioned in section 8.5, initial conditions for the spark are essential to predict how the kernel will develop. No clear rule exists today to set these initial conditions. But if such simulations could be performed, results will represent a consequent progress in the understanding of ignition and of its modeling in LES. For instance, if it is found out that the toroidal development of the kernel is a reasonable explanation to the ignition regimes, then no advanced modeling to account for the radicals generated by the breakdown would be required. Reduced chemistry would be then sufficient to describe the ignition. On the contrary, if the toroidal development of the flame kernel cannot explain the ignition regime, then plasma chemical effects should be closely investigated.

Conclusions & Perspectives

This thesis contributed to the improvement of LES modeling tools for the prediction of cycle-to-cycle variability induced by ignitions in spark ignition engines, when the combustion regime is lean or stoichiometric diluted. The existing TF-LES approach was chosen. During the early stages of the combustion phase, the flame kernel must be fully resolved until it reaches a certain size, to correctly predict the diffusive processes that are essential to ignition. Then, a sub-grid wrinkling model can be used to predict the turbulent flame propagation but the model should describe the out-of-equilibrium flame development. In this context, two distinct issues were addressed: the ignition prediction and the prediction of the sub-grid wrinkling factor during the turbulent propagation phase.

Dynamic wrinkling modeling

The dynamic wrinkling model of Wang et al. (2012) was studied in a first part. Practical difficulties were identified when using the dynamic model in the SI engine configurations. First, a numerical problem due to test-filter implementation was evidenced. Then, a problem in the wrinkling factor definition when fronts interact at a distance shorter than the test-filtering scale was pointed out. Modifications of the initial wrinkling model were proposed and tested in academical configurations. Then, first validations of the modified dynamic model were performed in the SI engine configuration and results compared against simulations performed with the ECFM-LES model. The study demonstrated the potential of the dynamic approach to reproduce the out-of-equilibrium flame behavior and to account for the cycle-to-cycle variability without any model parameter adjustment.

Coupling the modified dynamic wrinkling model with the TF-LES model should provide a model at least as predictive as ECFM-LES.
In a future work, coupling the dynamic model with the ignition phase will enable to simulate the full combustion phase in the engine. However, as the dynamic procedure assumes an already established flame front at the effective scale $\widehat{\Delta}$, the duration of the ignition phase if using the dynamic model is larger than the duration of the ignition phase when using no dynamic wrinkling model because the transition to the fully established flame front at scale Δ takes place before the transition to the fully established flame front at scale $\widehat{\Delta}$. This implies to refine the mesh in the ignition zone until the flame kernel reaches a size close to $\widehat{\Delta}$, at the expense of CPU time.

Ignition prediction

In a second part, LES of turbulent spark ignitions in lean methane/air mixtures at atmospheric conditions were performed, setting the thickening factor F to unity. The ignition is modeled by a heat source term (ED model) and reduced chemistry was used. The propagation of the pressure wave induced by the intense breakdown deposit was not accounted for. Simulations were compared to recent experimental data of Cardin et al. (2013), who characterized the ignition regimes by measuring the minimum ignition energy for different turbulence properties.
Parametric studies to determine the numerical and physical ignition parameters of the ED model were first performed in the laminar case. Results highlighted that the chosen ignition approach could predict reasonable values of MIE in the laminar case, if the ignition parameters are correctly chosen. In particular, energy density and ignition volume appeared as key parameters. Then, ignition predictions obtained with a 2-step and an analytical kinetic mechanism were compared, enabling not only to further understand the role of the kinetics when modeling ignition with a heat source term but also to propose a novel validation of an analytical kinetic scheme. An important conclusion concerns the fact that, in the case of high density modeled energy deposit and for lean equivalence ratios ($\phi < 0.9$), the 2-step and the analytical kinetic schemes predict very similar MIE. Analysis of the ignition process suggested that in those conditions, simplified kinetic schemes are as much adequate as schemes predicting both the correct auto-ignition delays and laminar flame speed. However, for lower energy density deposit, corresponding for instance to the glow phase, the 2-step kinetic scheme underestimated MIE, confirming that kinetic schemes predicting the correct auto-ignition delays, like analytical schemes, must be used. This may be also the case for stoichiometric equivalence ratios, as evidenced by Sloane and Ronney (1992).
In the turbulent case, the ignition approach was found not to be sufficient to capture the transition from low to high turbulence intensity evidenced in Cardin et al. experiments. The MIE predicted in simulations linearly increases with the turbulent intensity, whatever the kinetic scheme or the parameters of the energy deposit, unlike to experimental MIE which exponentially increases with the turbulence intensity, from a critical turbulence intensity. In addition to this, simulations predict a continuous although wrinkled flame front, while the kernel appears in experiments fragmented in high turbulence intensity cases. Results analysis showed that a more accurate description of the spark deposit is required to describe ignition. Two investigation paths were proposed, to help determining first-order mechanisms leading to the different ignition regimes: (i) to account for the plasma chemistry effects in the modeling of the spark energy deposit, for instance by describing an initial radicals pool. This implies to determine an initial chemical composition representative of the post-breakdown state and to use adequate kinetic mechanisms, which is not straightforward. (ii) To account for the post-breakdown pressure wave propagation which induces the development of the flame kernel into a donut shape. This implies to determine the initial conditions of the spark just after breakdown in terms of pressure, temperature and size, which is also a question of debate.

In addition to these fundamental aspects, the following issues could be addressed to help deriving fully predictive ignition models:

- To set up practical tools to simulate ignition in real engine configurations. In particular a strategy of mesh refinement in the ignition zone must be defined, for instance by coupling the ignition calculation domain corresponding to the refined zone in the vicinity of the spark plug to the whole calculation domain of the engine combustion chamber, as proposed by Bonhomme et al. (2014). Determining the size of the refined zone and the duration when it needs to be refined will demand specific studies, to find the best compromise between CPU time and ignition prediction. Concerning kinetics, results obtained with the analytical scheme should be confirmed for heavier fuels, such as isooctane. As analytical schemes are very recent, systematic reduction methods are currently developed and an open question is to determine if this type of scheme still allows affordable CPU time for heavier fuels.

- To account for the deposit of energy along the electrical arc in the case of long-duration spark ignition. As existing ignition models assume a spherical shape of the initial flame kernel, this should represent a consequent improvement, both for the TF-LES and FSD ignition models. A solution consists to use Lagrangian particles to track the position of the arc deformed by the flow, the ignition energy can be then deposited along the arc path.

- To study ignition in two phase flow conditions and to determine ignition probabilities. Simulations could be performed in configurations close to real configurations conditions, such as the KIAI burner of CORIA laboratory.

Appendix A: Dynamic wrinkling model

Numerical implementation of the test-filter operator

The implementation method retained for the test-filter $\widehat{\Delta}$ is proposed by Moureau et al. (2011), based on the resolution of a diffusion equation. This kind of implementation is well adapted to unstructured meshes and for massively parallel calculations. The filtering procedure is detailed in the following, as one of the problems which was encountered when using the dynamic wrinkling model in the engine configuration concerns the nature of the filter (centered operator).

Moureau et al. propose to approximate the filtering of any scalar ϕ when filtered with a 1D Gaussian shape filtering, using the Taylor series development of the filtering function, truncated to the first non zero term:

$$\widehat{\phi} = \phi + \frac{\widehat{\Delta}^2}{24}\frac{\partial^2\phi}{\partial x^2} \tag{2}$$

Equation (2) is then generalized to multidimensional cases, such as:

$$\widehat{\phi} = \phi + \frac{\widehat{\Delta}^2}{24}\Delta\phi \tag{3}$$

Resolving Eq. (3) is equivalent to resolving a diffusion equation, introducing the diffusivity coefficient ν_{eff}:

$$\frac{\partial\phi}{\partial t} = \nu_{\text{eff}}\frac{\partial^2\phi}{\partial x^2} \tag{4}$$

Time discretizing Eq. (4) gives:

$$\frac{\phi^{\text{n}+1} - \phi^{\text{n}}}{\Delta\text{t}} = \nu_{\text{eff}}\frac{\partial^2\phi}{\partial x^2} \tag{5}$$

where Δt is the time-step of the numerical calculation. Then:

$$\phi^{\text{n}+1} = \phi^{\text{n}} + \nu_{\text{eff}}\Delta\text{t}\frac{\partial^2\phi}{\partial x^2} \tag{6}$$

The filtering Eq. (2) is thus equivalent to diffusion Eq. (6) and diffusivity coefficient ν_{eff} can be calculated according to:

$$\frac{\widehat{\Delta}^2}{24} = \nu_{\text{eff}}\Delta\text{t} \tag{7}$$

When explicitly solving the diffusion equation (6), stability is governed by the Fourier number criterion $\mathscr{F}$ defined by:

$$\mathscr{F} = \frac{\nu_{\text{eff}} \Delta \text{t}}{\Delta_x^2} \tag{8}$$

For the diffusion equation to be numerically stable, the Fourier number $\mathscr{F}$ must be smaller than unity: $\mathscr{F} < 1$. In practice, the resolution of Eq. (6) is resolved in n_{it} sub-steps. Then, diffusivity coefficient becomes $\nu_{\text{eff}}/n_{\text{it}}$ and n_{it} must verify:

$$\mathscr{F} = \frac{1}{24}\left(\frac{\widehat{\Delta}}{\Delta x}\right)^2 \frac{1}{n_{\text{it}}} < 1 \tag{9}$$

For a given Fourier number $\mathscr{F}$, a criterion defining the minimal number of iterations $n_{\text{it,min}}$ required to resolve the equation can be defined:

$$\begin{aligned} n_{\text{it,min}} &= 1 + \text{E}\left[\frac{1}{\mathscr{F}}\frac{1}{24}\left(\frac{\widehat{\Delta}}{\Delta_x}\right)^2\right] \\ &= 1 + \text{E}\left[\frac{1}{\mathscr{F}}\frac{1}{24}(\alpha_t n_{res})^2\right] \end{aligned} \tag{10}$$

where $\alpha_t = \widehat{\Delta}/\Delta$ (Eq. (4.2)), n_{res} is the number of resolution points ($\Delta = n_{res}\Delta_x$) and E refers to the integer part operator.
Introducing the following definition for ψ_{eff}:

$$\psi_{\text{eff}} = \frac{\widehat{\Delta}^2}{24} \tag{11}$$

The numerical system of equations reads:

$$\begin{aligned}
\widehat{\phi}^{(0)} &= \phi + \frac{\psi_{\text{eff}}}{n_{\text{it,min}}}\Delta\phi \\
\widehat{\phi}^{(1)} &= \widehat{\phi}^{(0)} + \frac{\psi_{\text{eff}}}{n_{\text{it,min}}}\Delta\widehat{\phi}^{(0)} \\
.. &= .. + .. \\
.. &= .. + .. \\
\widehat{\phi}^{(n_{\text{it,min}})} &= \widehat{\phi}^{(n_{\text{it,min}}-1)} + \frac{\psi_{\text{eff}}}{n_{\text{it,min}}}\Delta\widehat{\phi}^{(n_{\text{it,min}}-1)}
\end{aligned}$$

The minimal number of iterations $n_{\text{it,min}}$ depends on the number of grid points of resolution n_{res} and the Fourier number $\mathscr{F}$, which depends in practice on the

steepness of the profil and on the cell size Δ_x. The minimal number of iterations required for the filtering is at least $n_{it} = 2$. Indeed, considering a maximal value of Fourier number $\mathscr{F} = 1$, a minimal value of parameter $\alpha_t = 1$ (corresponding to a test-filter of size $\widehat{\Delta} = \Delta$) and a minimal number of grid points in the flame front such as $n_{res} = 7$, then Eq. (10) gives $n_{it,min} = 2$.
Using the dynamic procedure implies an additional CPU cost, due to the filtering operation, which is not the case when using algebraic closures for the sgs wrinkling. However results obtained using the dynamic wrinkling model represent a consequent progress and it is possible to optimize in the simulations the frequency of the dynamic calculation: chapter 5 will demonstrate the interest of the dynamic model for SI engine configurations, which additional CPU cost remains below 20%.

Numerical calculations of the filtering procedure using the diffusion operator proposed by Moureau et al.

The analytical expression of the equations system of the test-filtering operation $\mathscr{T}$ is first recalled:

$$\begin{aligned}
\widehat{\phi}^{(0)} &= \phi + \frac{\psi_{\text{eff}}}{n_{\text{it,min}}}\Delta\phi \\
\widehat{\phi}^{(1)} &= \widehat{\phi}^{(0)} + \frac{\psi_{\text{eff}}}{n_{\text{it,min}}}\Delta\widehat{\phi}^{(0)} \\
.. &= .. + .. \\
.. &= .. + .. \\
\widehat{\phi}^{(n_{\text{it,min}})} &= \widehat{\phi}^{(n_{\text{it,min}}-1)} + \frac{\psi_{\text{eff}}}{n_{\text{it,min}}}\Delta\widehat{\phi}^{(n_{\text{it,min}}-1)}
\end{aligned}$$

Denoting ψ_{eff} such as:

$$\psi_{\text{eff}} = \frac{\widehat{\Delta}^2}{24} \tag{12}$$

and $n_{\text{it,min}}$ given by:

$$n_{\text{it,min}} = 1 + \text{E}\left(\frac{1}{\mathscr{F}}\frac{1}{24}\left(\frac{\widehat{\Delta}}{\Delta_x}\right)^2\right) \tag{13}$$

Notations introduced in 4.4.2 are recalled. $\mathscr{R}_1 = \mathscr{T} * \mathscr{G}$ is the numerical operator obtained when calculating the gradient (operator $\mathscr{G}$) and then test-filtering (operator $\mathscr{T}$), while $\mathscr{R}_2 = \mathscr{G} * \mathscr{T}$ is the numerical operator obtained when test-filtering

(operator $\mathscr{T}$) and then calculating the gradient (operator $\mathscr{G}$). For clarity's sake, case $n_{\text{it,min}} = 1$ is considered. A 2D calculation domain with hexahedrons is considered. The problem is mono dimensional in the x dimension. The different calculation steps are described in the following:

1. when the flame front is "far" from the border of the computational domain, that is when all stencils $\mathscr{S}_i$ are complete (all nodes of the stencil are in the calculation domain)

2. when the scalar is "close" to the border of the computational domain, that is when stencils $\mathscr{S}_i$ are incomplete.

The purpose is to demonstrate that when the flame front is situated at a distance $d < \mathscr{S}_i$, then the commutativity between the numerical operators derivative and filter is no more verified so that $\mathscr{R}_1 \neq \mathscr{R}_2$.

Calculation "far from the border"

1. calculation of the gradient $\nabla\phi|_i$ In AVBP, the calculation of gradients use the cell-vertex approach. Gradients are first calculated in the cells, using approximation (16) (**Step 1** in Fig. 8):

$$\iiint_{\Omega} \nabla\phi \mathrm{dV} \approx \oiint_{\Omega} \phi_i \; n_i \mathrm{dS} \tag{14}$$

where $\mathbf{n_i}$ is the normal to the cell face. In the present case $\mathbf{n_i} = \mathbf{e_x}$. This gives for instance in cell a in Fig. 8:

$$\nabla\phi|_a (\Delta_x)^3 \approx (\phi_{i-1} - \phi_i)(\Delta_x)^2 \tag{15}$$

Gradient in the node i is calculated using the gradient values calculated in the neighbor cells which are scattered back to the nodes (**step 2** in Fig. 8).
Final value in the node i of $\nabla\phi|_i$ is:

$$\nabla\tilde{c}|_i = \frac{\phi_{i-1} - \phi_{i+1}}{2\Delta_x} \tag{16}$$

2. Calculation of $\nabla\cdot(\psi_{\text{eff}}\nabla\phi)$ To calculate the divergence $\nabla\cdot\mathbf{F}$, Green-Ostrogradsky theorem is applied:

$$\iiint_{\Omega} \nabla\cdot\mathbf{F} \mathrm{dV} = \oiint_{\Omega} \mathbf{F}.\mathbf{n} \mathrm{dS} \tag{17}$$

Divergence in the node i results of the sum of fluxes in each neighbor cells. See Fig. **??** for the calculation of $\nabla\cdot(\psi_{\text{eff}}\nabla\phi)$:

Divergence of $\nabla\cdot(\psi_{\text{eff}}\nabla\phi)$ in the node i is thus given by:

$$\nabla\cdot(\psi_{\text{eff}}\nabla\phi)|_i = \psi_{\text{eff}} \frac{\nabla\phi|_{i-1} - \nabla\phi|_{i+1}}{2\Delta_x} \tag{18}$$

$$= \psi_{\text{eff}} \left(\frac{1}{2\Delta_x}\right)^2 (\phi_{i-2} - \phi_i + \phi_{i+2}) \tag{19}$$

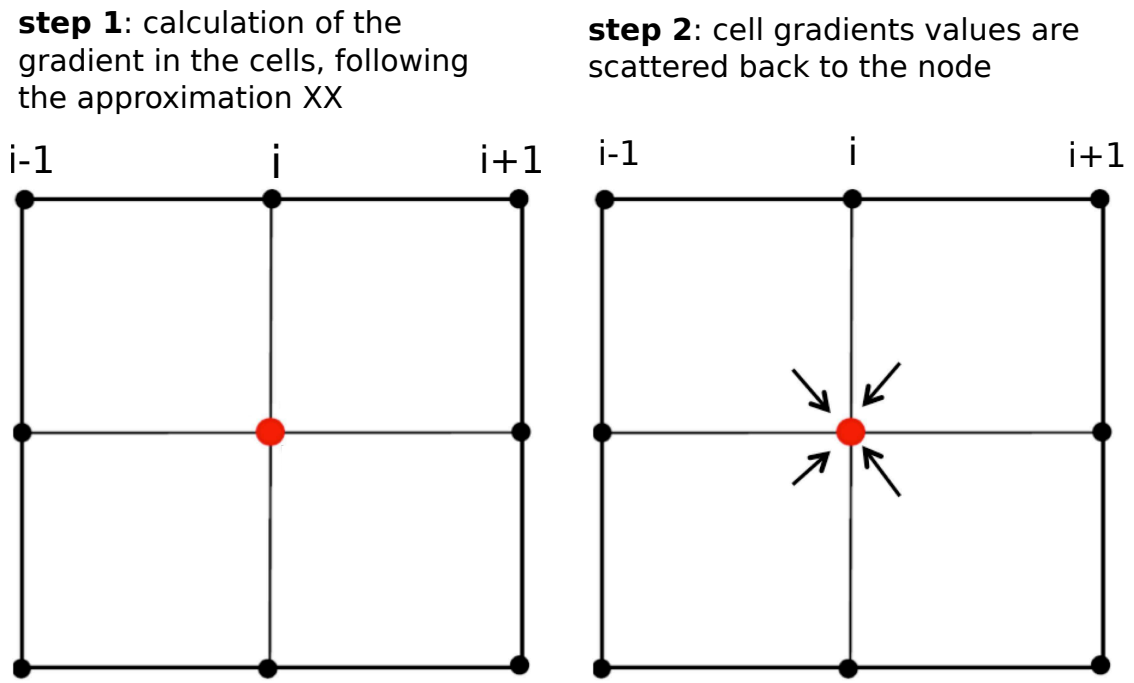

Figure 8: numerical calculation of gradients ($\nabla\phi$) in AVBP: gradients values calculated in the celles are redistributed to the nodes.

3. Calculation of the filtering function Using Eq. (16) and (19), $\widehat{\phi}$ in the node i reads:

$$\widehat{\phi_i} = \phi_i + \psi_{\text{eff}}\left(\frac{1}{2\Delta_x}\right)^2 (\phi_{i-2} - 2\phi_i + \phi_{i+2}) \tag{20}$$

4. Calculation of $\nabla\widehat{\tilde{c}}$ Equation (20) is applied for $\phi = \tilde{c}$, which gives:

$$\widehat{\tilde{c}}_i = \tilde{c}_i + \psi_{\text{eff}}\left(\frac{1}{2\Delta_x}\right)^2 (\tilde{c}_{i-2} - 2\tilde{c}_i + \tilde{c}_{i+2}) \tag{21}$$

Then $\nabla\widehat{\tilde{c}}\big|_i$ can be calculated using Equation (21) according to:

$$\begin{aligned} \nabla\widehat{\tilde{c}}\big|_i &= \frac{1}{2\Delta_x}\left(\widehat{\tilde{c}}_{i-1} - \widehat{\tilde{c}}_{i+1}\right) \\ &= \frac{\tilde{c}_{i-1} - \tilde{c}_{i+1}}{2\Delta_x} + \frac{\psi_{\text{eff}}}{2\Delta_x}\left(\frac{1}{2\Delta_x}\right)^2 (\tilde{c}_{i-3} - 3\tilde{c}_{i-1} + 3\tilde{c}_{i+1} - \tilde{c}_{i+3}) \end{aligned} \tag{22}$$

5. Calculation of $\widehat{\nabla\tilde{c}}$ Applying $\phi = \nabla\tilde{c}$ in Equation (20) gives:

$$\widehat{\nabla\tilde{c}|_i} = \nabla\tilde{c}|_i + \psi_{\text{eff}}\left(\frac{1}{2\Delta_x}\right)^2 \left(\nabla\tilde{c}|_{i-2} - 2\,\nabla\tilde{c}|_i + \nabla\tilde{c}|_{i+2}\right) \tag{23}$$

Replacing $\nabla\tilde{c}|_i$ by its expression (16):

$$\widehat{\nabla\tilde{c}|_i} = \frac{\tilde{c}_{i-1} - \tilde{c}_{i+1}}{2\Delta_x} + \frac{\psi_{\text{eff}}}{2\Delta_x}\left(\frac{1}{2\Delta_x}\right)^2 (\tilde{c}_{i-3} - 3\tilde{c}_{i-1} + 3\tilde{c}_{i+1} - \tilde{c}_{i+3}) \tag{24}$$

Commutativity between test-filter operator $\widetilde{\ }$ and derivative is verified, as Eq. (22) and (22) are equal:

$$\widetilde{\nabla\tilde{c}|_i} = \nabla\widehat{\tilde{c}}\Big|_i \tag{25}$$

Finally it can be noted that the stencil of the operation "derivative convoluted to filtering" (or "filtering convoluted to derivative") when $n_{\text{it}} = 1$ is $3\Delta_x$.

Calculation "close" to the border

According to Eqs. (24) and (22), when $n_{it} = 1$ the stencil of the numerical operator $\mathscr{R}_i$ is $\mathscr{S}_i = 3\Delta_x$. Accordingly, when the calculation of $\Sigma_{1,x}$ or $\Sigma_{2,x}$ is performed at a distance $d < 3\Delta_x$ from the border of the domain, Eqs (24) and (22) can not be used. In the following, expressions of $\Sigma_{1,x}$ and $\Sigma_{2,x}$ are established, when $d < 3\Delta_x$ (for $n_{it} = 1$), demonstrating that $\Sigma_{1,x} > \Sigma_{2,x}$. To do so, the situation of Fig. 9 is considered: node i is situated at $d = 3\Delta_x$ from the border of the computational domain. Calculations of $\Sigma_{1,x}$ and $\Sigma_{2,x}$ in the node $(i-2)$ (blue point) are detailed step by step.

1. Calculation of the gradient at the border Because the stencil of the gradient operator is equal to Δ_x, the expression of the gradient in the node situated at the border (blue point $i-2$ in Fig. 9) is changed. Values in the nodes $i-1$, i, etc..are unchanged. Calculation of the gradient in point $i-2$ (blue point) is presented in Fig. 9:

$$\nabla\phi|_{i-2} = \frac{\phi_{i-2} - \phi_{i-1}}{\Delta_x} \tag{26}$$

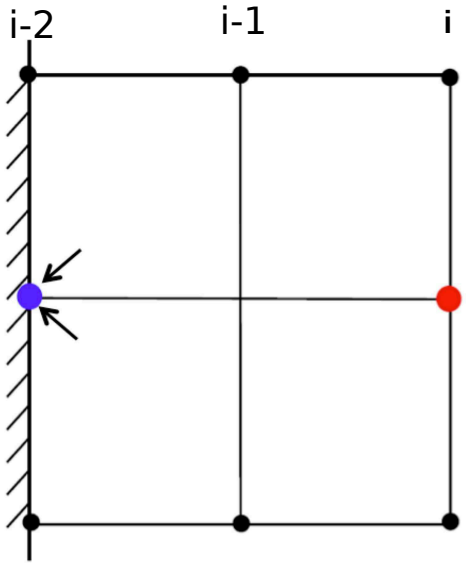

Figure 9: calculation of $\nabla\phi$ at the border (blue point, denoted by index $i-2$): gradient is not centered anymore but degenerates in forward difference. red point corresponds to the nodes in which quantities Σ_1 and Σ_2 are calculated (denoted by index i).

Calculation of $\nabla \cdot (\psi_{\text{eff}} \nabla \phi)$ at the border Because the stencil of the diffusivity operator is $2\Delta_x$ (see Eq. (19)), the calculation of $\nabla \cdot (\psi_{\text{eff}} \nabla \phi)$ is changed in the nodes $i-2$ and $i-1$.

Fig. 10 illustrates the calculation in the node $i-2$: as for the gradient calculation presented above, the expression of the divergence in node $i-2$ is changed and is given by:

$$\nabla \cdot (\psi_{\text{eff}} \nabla \phi)|_{i-2} = \psi_{\text{eff}} \frac{\nabla \phi|_{i-2} - \nabla \phi|_{i-1}}{\Delta_x} \tag{27}$$

Replacing $\nabla \phi|_{i-2}$ by its expression established in Eq. (26), while $\nabla \phi|_{i-1}$ is replaced using Eq. (16), leads to:

$$\nabla \cdot (\psi_{\text{eff}} \nabla \phi)|_{i-2} = \psi_{\text{eff}} \left(\frac{1}{\Delta_x} \right)^2 \left(\frac{\phi_i + \phi_{i-2}}{2} - \phi_{i-1} \right) \tag{28}$$

In the node $i-1$, the expression of divergence (18) is unchanged and reads:

$$\nabla \cdot (\psi_{\text{eff}} \nabla \phi)|_{i-1} = \psi_{\text{eff}} \frac{\nabla \phi|_{i-2} - \nabla \phi|_{i}}{2\Delta_x} \tag{29}$$

Replacing the value of $\nabla \phi|_{i-2}$ by its changed expression (26), the final expression for the diffusive flux in the node $i-1$ reads:

$$\nabla \cdot (\psi_{\text{eff}} \nabla \phi)|_{i-1} = \frac{\psi_{\text{eff}}}{2} \left(\frac{1}{\Delta_x} \right)^2 \left(\phi_{i-2} + \phi_{i+1} - \frac{3}{2} \phi_{i-1} \right) \tag{30}$$

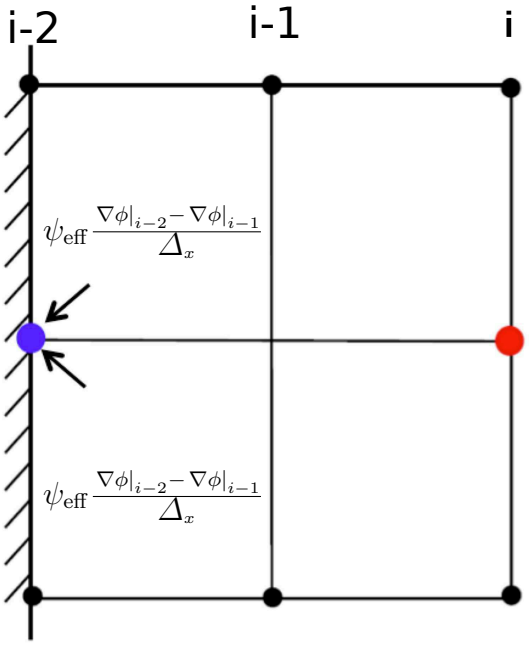

Figure 10: Calculation of the divergence at the border

Calculation of $\nabla\widehat{\tilde{c}}$ at the border (node $i-2$) Replacing $\phi = \hat{\tilde{c}}$ in Expression (26) gives:

$$\nabla\widehat{\tilde{c}}\Big|_{i-2} = \frac{1}{\Delta_x}\left(\widehat{\tilde{c}}_{i-2} - \widehat{\tilde{c}}_{i-1}\right) \tag{31}$$

$\widehat{\tilde{c}}_{i-2}$ and $\widehat{\tilde{c}}_{i-1}$ are expressed using respectively Eq. (30) and Eq. (28):

$$\widehat{\tilde{c}}_{i-2} = \tilde{c}_{i-2} + \psi_{\text{eff}}\left(\frac{1}{\Delta_x}\right)^2\left(\frac{\tilde{c}_i + \tilde{c}_{i-2}}{2} - \tilde{c}_{i-1}\right) \tag{32}$$

$$\widehat{\tilde{c}}_{i-1} = \tilde{c}_{i-1} + \frac{\psi_{\text{eff}}}{2}\left(\frac{1}{\Delta_x}\right)^2\left(\tilde{c}_{i-2} + \tilde{c}_{i+1} - \frac{3}{2}\tilde{c}_{i-1}\right) \tag{33}$$

which gives:

$$\nabla\widehat{\tilde{c}}\Big|_{i-2} = \frac{\tilde{c}_{i-2} - \tilde{c}_{i-1}}{\Delta_x} + \frac{\psi_{\text{eff}}}{2\Delta_x}\left(\frac{1}{\Delta_x}\right)^2\left(\tilde{c}_i - \tilde{c}_{i+1} - \frac{1}{2}\tilde{c}_{i-1}\right) \tag{34}$$

Calculation of $\widehat{\nabla\tilde{c}}$ at the border (node $i-2$) Using Expression (28) with $\phi = \nabla\tilde{c}|_{i-2}$ gives:

$$\widehat{\nabla\tilde{c}}\Big|_{i-2} = \nabla\tilde{c}|_{i-2} + \psi_{\text{eff}}\left(\frac{1}{\Delta_x}\right)^2\left(\frac{\nabla\tilde{c}|_i + \nabla\tilde{c}|_{i-2}}{2} - \nabla\tilde{c}|_{i-1}\right) \tag{35}$$

Using Eq. (26) for $\nabla\tilde{c}|_{i-2}$, Eq. (16) for $\nabla\tilde{c}|_{i-1}$ and $\nabla\tilde{c}|_i$ leads to:

$$\widehat{\nabla\tilde{c}}\Big|_{i-2} = \frac{\tilde{c}_{i-2} - \tilde{c}_{i-1}}{\Delta_x} + \frac{1}{2\Delta_x}\left(\frac{\psi_{\text{eff}}}{2\Delta_x}\right)^2\left(\tilde{c}_{i-2} - \frac{3}{2}\tilde{c}_{i-1} - \frac{1}{2}\tilde{c}_{i+1} + \tilde{c}_i\right) \tag{36}$$

We remark that Eq. (34) and Eq. (36) are not equivalent, e.g.:

$$\widehat{\nabla\tilde{c}}\Big|_{i-2} \neq \nabla\widehat{\tilde{c}}\Big|_{i-2} \tag{37}$$

Values of $\widehat{\nabla\tilde{c}}|_{i-1}$, $\widehat{\nabla\tilde{c}}|_i$, $\nabla\widehat{\tilde{c}}\big|_{i-1}$ and $\nabla\widehat{\tilde{c}}\big|_i$ can also be calculated from a similar manner and it is then easily demonstrated that $\widehat{\nabla\tilde{c}}|_{i-1} \neq \nabla\widehat{\tilde{c}}\big|_{i-1}$ and $\widehat{\nabla\tilde{c}}|_i \neq \nabla\widehat{\tilde{c}}\big|_i$.

The demonstration was performed for $n_{\text{it}} = 1$. In practice $n_{\text{it}} > 1$ (see section 9.4). When $n_{\text{it}} = 1$, then $\mathscr{S}_i = 3\Delta_x$ (see Eq. (24) or Eq. (22)). In the general case, as the stencil of the test-filtering operator $\mathscr{T}$ is equal to $2\Delta_x$ (see Eq. 20), $\mathscr{S}_i = (2n_{it} + 1)\Delta_x$.

Expression of exponent β in spherical coordinates

This implies to express flames surfaces $\Sigma_1 = |\nabla\widehat{\tilde{c}}|$ and $\Sigma_2 = \widehat{|\nabla\tilde{c}|}$, using the analytical expression of the test-filter given by Equation (3) By obvious symmetry considerations, fields only depend on the radial coordinate r.
Following notations are first introduced:

$$\Sigma_{1,r} = \widehat{\left|\frac{\partial\tilde{c}}{\partial r}\right|} \tag{38}$$

and

$$\Sigma_{2,r} = \left|\frac{\partial\widehat{\tilde{c}}}{\partial r}\right| \tag{39}$$

$\Sigma_{1,r}$ can be expressed, using the filtering Equation (3) applied to the scalar $\left|\frac{\partial\tilde{c}}{\partial r}\right|$:

$$\Sigma_{1,r} = \left|\frac{\partial\tilde{c}}{\partial r}\right| + \psi_{\text{eff}}\left(\frac{\partial^2}{\partial r^2}\left|\frac{\partial\tilde{c}}{\partial r}\right| + \frac{2}{r}\frac{\partial}{\partial r}\left|\frac{\partial\tilde{c}}{\partial r}\right|\right) \tag{40}$$

On the other hand, the analytical expression of $\widehat{\tilde{c}}$ - it is recalled that $\widehat{\tilde{c}}$ is the notation for $\widehat{\tilde{c}}$ - can be written, using the filtering Equation (3) applied to the scalar $\tilde{c}$:

$$\widehat{\tilde{c}} = \tilde{c} + \psi_{\text{eff}}\left(\frac{\partial^2\tilde{c}}{\partial r^2} + \frac{2}{r}\frac{\partial\tilde{c}}{\partial r}\right) \tag{41}$$

$\Sigma_{2,r}$ can be then developed as:

$$\begin{aligned}\Sigma_{2,r} &= \left|\frac{\partial}{\partial r}\left(\tilde{c} + \psi_{\text{eff}}\left(\frac{\partial^2\tilde{c}}{\partial r^2} + \frac{2}{r}\frac{\partial\tilde{c}}{\partial r}\right)\right)\right| \\ &= \left|\left(1 - \frac{2\psi_{\text{eff}}}{r^2}\right)\frac{\partial\tilde{c}}{\partial r} + \psi_{\text{eff}}\left(\frac{\partial^3\tilde{c}}{\partial r^3} + \frac{2}{r}\frac{\partial^2\tilde{c}}{\partial r^2}\right)\right|\end{aligned} \tag{42}$$

Noticing that $\frac{\partial\tilde{c}}{\partial r} = -\left|\frac{\partial\tilde{c}}{\partial r}\right|$, $\overline{\Sigma}_{2,r}$ can be recast such as:

$$\begin{aligned}\Sigma_{2,r} &= \left|-\left(1 - \frac{2\psi_{\text{eff}}}{r^2}\right)\left|\frac{\partial\tilde{c}}{\partial r}\right| - \psi_{\text{eff}}\left(\frac{\partial^2}{\partial r^2}\left|\frac{\partial\tilde{c}}{\partial r}\right| + \frac{2}{r}\frac{\partial}{\partial r}\left|\frac{\partial\tilde{c}}{\partial r}\right|\right)\right| \\ &= \left(1 - \frac{2\psi_{\text{eff}}}{r^2}\right)\left|\frac{\partial\tilde{c}}{\partial r}\right| + \psi_{\text{eff}}\left(\frac{\partial^2}{\partial r^2}\left|\frac{\partial\tilde{c}}{\partial r}\right| + \frac{2}{r}\frac{\partial}{\partial r}\left|\frac{\partial\tilde{c}}{\partial r}\right|\right)\end{aligned} \tag{43}$$

$\Sigma_{1,r}$ and $\Sigma_{2,r}$ are thus related to each other according to:

$$\Sigma_{1,r} = \Sigma_{2,r} + \frac{2\psi_{\text{eff}}}{r^2}\left|\frac{\partial\tilde{c}}{\partial r}\right| \tag{44}$$

Replacing ψ_{eff} by its definition (11), ratio ψ_{eff}/r^2 reads:

$$\frac{\psi_{\text{eff}}}{r^2} = \frac{1}{24}\frac{\widehat{\Delta}^2}{r^2} = \frac{1}{24}\left(\frac{\gamma\Delta}{r}\right)^2 = \frac{1}{24}\frac{\gamma^2-1}{\gamma^2}\left(\frac{\widehat{\Delta}}{r}\right)^2 \tag{45}$$

A non-dimensional curvature c^+ can be then introduced, defined by:

$$c^+ = \frac{\widehat{\Delta}}{r} \tag{46}$$

Replacing c^+ in the expressions of $\overline{\Sigma}_{1,r}$ (40) and of $\overline{\Sigma}_{2,r}$ (43) enables to establish the final expression of exponent $\beta(r)$:

$$\beta(r) = \frac{\log\left(1 + \dfrac{\gamma^2-1}{12\gamma^2}\dfrac{\left\langle (c^+)^2\left|\dfrac{\partial\tilde{c}}{\partial r}\right|\right\rangle}{\langle\Sigma_{2,r}\rangle}\right)}{\log(\gamma)} \tag{47}$$

Appendix B: Experimental method of determination of the MIE

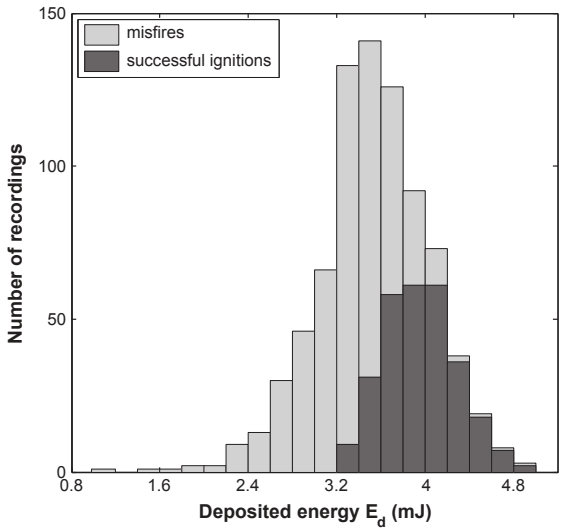

Figure 11: Number of recordings as a function of the deposited energy (energy classes of 0.2 mJ wide). Methane/air flame, $U = 0.60$, $< u' >= 0.66$ m/s.(Cardin et al., 2013) .

Variability of MIE can have several causes: turbulence, mixture inhomogeneities but also the variability induced by the stochastic nature of the Laser breakdown. Even in a laminar flow, variability is observed from the moment of formation of the plasma, which means that a same deposited energy E_d can lead to fire or misfire. To determine the MIE for a given equivalence ratio ϕ and given turbulence conditions, Cardin et al. conducted 800 ignition trials. They varied the energy deposited by the Laser E_d, to observe the ignition probability taking values from 0 to 1. To determine ignition probability, classes of deposited energy E_d were defined, with 20 trials at least within each class. The ignition probability was calculated for each energy class as the ratio of the number of successful ignition trials out of the number of trials in the class. An exemple is shown in Fig. 11. The MIE was then defined as the energy E_d leading to a probability of ignition of 50%. An exemple of an ignition probability curve on which Cardin et al. based their calculations of MIE is displayed in Fig. 12.

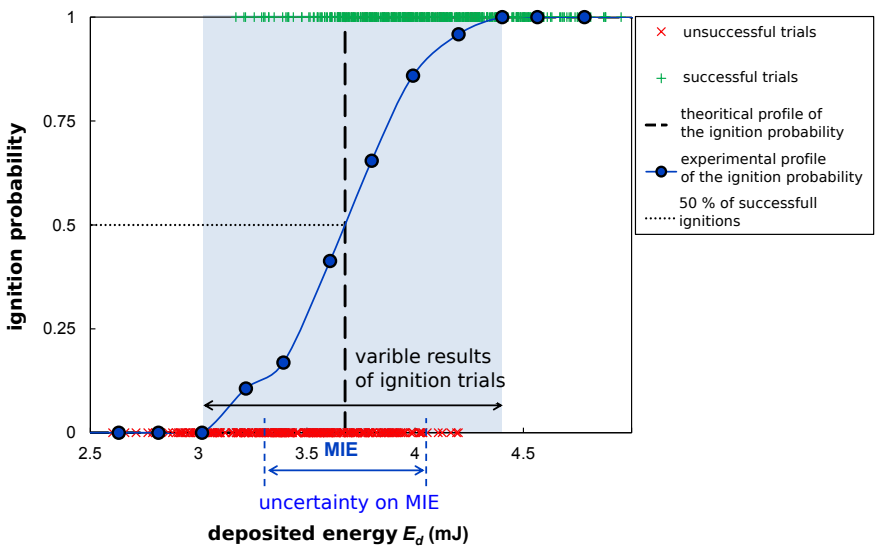

Figure 12: Experimental profile of the ignition probability as a function of the deposited energy. CH_4/air mixture, $\phi = 0.58$. 800 trials. Cardin (2013).

Bibliography

R. Abdel-Gayed and D. Bradley. Combustion regimes and the straining of turbulent premixed flames. *Combustion and Flame*, 76:213–218, 1989.

O. Akindele, D. Bradley, P. Mak, and M. McMahon. Spark ignition of turbulent gases. *Combustion and Flame*, 47:129–155, 1982.

P. G. Aleiferis, A. M. Taylor, J. H. Whitelaw, K. Ishii, and Y. Urata. Cyclic variations of initial flame kernel growth in a honda vtec-e lean-burn spark-ignition engine. Technical report, SAE Technical Paper, 2000.

T. Alger, J. Gingrich, C. Roberts, B. Mangold, and M. Sellnau. A high-energy continuous discharge ignition system for dilute engine applications. *SAE Technical Paper*, pages 01–1628, 2013.

C. Angelberger, D. Veynante, F. Egolfopoulos, and T. Poinsot. Large eddy simulations of combustion instabilities in premixed flames. *CTR Proceedings of the summer Program*, 159:61–82, 1998.

W. P. Attard and P. Parsons. Flame kernel development for a spark initiated prechamber combustion system capable of high load, high efficiency and near zero nox emissions. *SAE International Journal of Engines*, 3(2):408–427, 2010.

D. Ballal and A. Lefebvre. The influence of flow parameters on minimum ignition energy and quanching distance. *Proceedings of the Combustion Institute*, 15:1473–1481, 1974.

D. Ballal and A. Lefevbre. The Influence of Spark Discharge Characteristics on Minimum Ignition Energy in Flowing Gases. *Proceedings of the Combustion Institute*, 24:99–108, 1975.

S. Bane, J. Ziegler, and S. J.E. Investigation of the effect of electrode geometry on spark ignition. *Combustion and Flame*, 162:462–469, 2015.

D. Barré, L. Esclapez, M. Cordier, E. Riber, B. Cuenot, G. Staffelbach, B. Renou, A. Vandel, G. L.Y.M., and G. Cabot. Flame propagation in aeronautical swirled multi-burners: Experimental and numerical investigation. *Combustion and Flame*, 161:2387–2405, 2014.

R. J. Bastiaans, J. A. de Swart, J. A. van Oijen, and L. P. H. de Goey. Analysis of premixed turbulent spherical flame kernels. In *Complex Effects in Large Eddy Simulations*, pages 371–383. Springer, 2007.

M. Bauerheim, T. Jaravel, L. Esclapez, E. Riber, L. Gicquel, B. Cuenot, M. Cazalens, S. Bourgois, and M. Rullaud. Multiphase flow les study of the fuel split effects on combustion instabilities in an ultra low-nox annular combustor. In *ASME Turbo Expo 2015: Turbine Technical Conference and Exposition*, pages V04BT04A069–V04BT04A069. American Society of Mechanical Engineers, 2015.

J. Beduneau, N. Kawahara, T. Nakayama, E. Tomita, and Y. Ikeda. Laser-induced radical generation and evolution to a self-sustaining flame. *Combustion and Flame*, 156(3):642–656, 2009.

J.-L. Beduneau, B. Kim, L. Zimmer, and Y. Ikeda. Measurements of minimum ignition energy in premixed laminar methane/air flow by using laser induced spark. *Combustion and Flame*, 132(132):653–665, 2003.

M. Boger. *Modélisation de sous-maille pour la simulation aux grandes échelles de la combustion turbulente prémélangée*. PhD thesis, Ecole Centrale de Paris, Chatenay-Malabry, France, 2000.

M. Boger, D. Veynante, H. Boughanem, and A. Trouvé. Direct numerical simulation analysis of flame surface density concept for large eddy simulation of turbulent premixed combustion. *Symposium (International) on Combustion*, 27(1):917 – 925, 1998. ISSN 0082-0784. doi: DOI:10.1016/S0082-0784(98)80489-X. URL `http://www.sciencedirect.com/science/article/pii/S008207849880489X`. Twenty-Seventh Sysposium (International) on Combustion Volume One.

M. Boileau, G. Staffelbach, B. Cuenot, T. Poinsot, and C. Bérat. LES of an ignition sequence in a gas turbine engine. *Combustion and Flame*, 154(1-2):2 – 22, 2008. ISSN 0010-2180. doi: DOI:10.1016/j.combustflame.2008.02.006. URL `http://www.sciencedirect.com/science/article/pii/S0010218008000497`.

A. Bonhomme, F. Duchaine, G. Wang, L. Selle, and T. Poinsot. A parallel multidomain strategy to compute turbulent flows in fan-stirred closed vessels. *Computers & Fluids*, 101:183–193, 2014.

R. Borghi. Turbulent combustion modelling. *Progress in energy and combustion science*, 14(4):245–292, 1988.

C. Bowman, R. Hanson, D. Davidson, W. Gardiner Jr, V. Lissianski, G. Smith, D. Golden, M. Frenklach, and M. Goldenberg. Gri-mech 2.11. *URL: http://www.me. berkeley. edu/gri-mech*, 1995.

D. Bradley and F.-K. Lung. Spark Ignition and the Early Stages of Turbulent Flame Propagation. *Combustion and Flame*, 69:71–93, 1987.

D. Bradley, C. Sheppard, I. Suardjaja, and R. Woolley. Fundamentals of High-Energy Spark Ignition With Lasers. *Combustion and Flame*, 138:55–77, 2004.

K. Bray, M. Champion, and P. A. Libby. The turbulent premixed boundary layer with variable enthalpy. *Combustion science and technology*, 55(4-6):139–161, 1987.

T. Briggs, T. Alger, and B. Mangold. Advanced ignition systems evaluations for high-dilution si engines. *SAE International Journal of Engines*, 7(4):1802–1807, 2014.

T. Butler and P. O'Rourke. A numerical method for two dimensional unsteady reacting flows. *Symposium (International) on Combustion*, 16:1503–1515, 1977.

R. Cant, S. Pope, and K. Bray. Modelling of flamelet surface to volume ratio in turbulent premixed combustion. In *23rd Symp. (Int.) on Combustion*, pages 809–815, Orleans, 1990. The Combustion Institute, Pittsburgh.

M. Capitelli, G. Colonna, and A. D'Angola. Thermodynamic properties and transport coefficients of high-temperature air plasma. In *Pulsed Power Plasma Science, 2001. PPPS-2001. Digest of Technical Papers*, volume 1, pages 694–697. IEEE, 2001.

C. Cardin. *Etude expérimentale des phénonomènes physico-chimiques de l'allumage dans les écoulements laminaires et turbulents*. PhD thesis, UMR 6614 CORIA, 2013.

C. Cardin, B. Renou, G. Cabot, and A. M. Boukhalfa. Experimental analysis of laser-induced spark ignition of lean turbulent premixed flames: New insight into ignition transition. *Combustion and Flame*, 160(8):1414–1427, 2013.

N. Chakraborty, E. Mastorakos, and R. Cant. Effects of turbulence on spark ignition in inhomogeneous mixtures: a direct numerical simulation (dns) study. *Combustion Science and Technology*, 179(1-2):293–317, 2007.

M. Champion, B. Deshaies, G. Joulin, and K. Kinoshita. Spherical Flame Initiation: Theory versus Experiments for Lean Propane-Air Mixtures. *Combustion and Flame*, 65:319–337, 1986.

F. Charlette, C. Meneveau, and D. Veynante. A power-law flame wrinkling model for LES of premixed turbulent combustion Part I: non-dynamic formulation and initial tests. *Combustion and Flame*, 131(1-2):159 – 180, 2002a. ISSN 0010-2180. doi: DOI:10.1016/S0010-2180(02)00400-5. URL `http://www.sciencedirect.com/science/article/pii/S0010218002004005`.

F. Charlette, C. Meneveau, and D. Veynante. A power-law flame wrinkling model for LES of premixed turbulent combustion Part II: dynamic formulation. *Combustion and Flame*, 131(1-2):181 – 197, 2002b. ISSN 0010-2180. doi: DOI:10.1016/S0010-2180(02)00401-7. URL `http://www.sciencedirect.com/science/article/pii/S0010218002004017`.

W. Chen, D. Madison, P. Dice, J. Naber, B. Chen, S. Miers, M. Czekala, C. Glugla, Q. Qu, and G. Huberts. Impact of ignition energy phasing and spark gap on combustion in a homogenous direct injection gasoline si engine near the egr limit. Technical report, SAE Technical Paper, 2013.

Y.-C. Chen, N. Peters, G. A. Schneemann, N. Wruck, U. Renz, and M. S. Mansour. The detailed flame structure of highly stretched turbulent premixed methane-air flames. *Combustion and Flame*, 107(3):223 – 226, 1996. ISSN 0010-2180. doi: DOI:10.1016/S0010-2180(96)00070-3. URL `http://www.sciencedirect.com/science/article/pii/S0010218096000703`.

Y.-C. Chen, M. Burke, and Y. Ju. On the critical flame raidus and minimum ignition energy for spherical flame initiation. *Proceedings of the Combustion Institute*, 33: 1219–1226, 2011.

T. P. Coffee, A. J. Kotlar, and M. S. Miller. The overall reaction concept in premixed, laminar, steady-state flames. i. stoichiometries. *Combustion and Flame*, 54(1-3): 155–169, 1983.

O. Colin. *Simulations aux grandes échelles de la combustion turbulente prémélangée dans les statoréacteurs*. PhD thesis, INP Toulouse, 2000.

O. Colin and M. Rudgyard. Development of high-order taylor–galerkin schemes for les. *Journal of Computational Physics*, 162(2):338–371, 2000.

O. Colin and K. Truffin. A spark ignition model for large eddy simulation based on an FSD transport equation (ISSIM-LES). *Proceedings of the Combustion Institute*, 33(2):3097 – 3104, 2011. ISSN 1540-7489. doi: DOI:10.1016/j.proci.2010.07.023. URL `http://www.sciencedirect.com/science/article/pii/S1540748910002555`.

O. Colin, F. Ducros, D. Veynante, and T. Poinsot. A thickened flame model for large eddy simulations of turbulent premixed combustion. *Physics of Fluids*, 12 (7):1843–1863, 2000.

P. Dagaut, M. Reuillon, J.-C. Boettner, and M. Cathonnet. Kerosene combustion at pressures up to 40 atm: Experimental study and detailed chemical kinetic modeling. In *Symposium (International) on Combustion*, volume 25, pages 919–926. Elsevier, 1994.

R. Dahms, T. Fansler, M. Drake, T.-W. Kuo, A. Lippert, and N. Peters. Modeling ignition phenomena in spray-guided spark-ignited engines. *Proceedings of the Combustion Institute*, 32(2):2743 – 2750, 2009. ISSN 1540-7489. doi: DOI: 10.1016/j.proci.2008.05.052. URL `http://www.sciencedirect.com/science/article/pii/S1540748908002587`.

F. Di Mare, W. Jones, and K. Menzies. Large eddy simulation of a model gas turbine combustor. *Combustion and Flame*, 137(3):278–294, 2004.

E. Domingues, M. Burey, B. Lecordier, and P. Vervisch. Ignition in an si engine using nanosecond discharges generated by a spark gap plasma igniter (sgpi). Technical report, SAE Technical Paper, 2008.

J. M. Duclos and O. Colin. Arc and kernel tracking ignition model for 3D spark ignition engine calculations. In *COMODIA*, pages 343–350, Nagoya, Japon, 2001. SparkIg.

T. Dunstan and K. Jenkins. Flame surface density distribution in turbulent flame kernels during the early stages of growth. *Proceedings of the Combustion Institute*, 32(1):1427–1434, 2009.

K. Eisazadeh-Far, F. Parsinejad, H. Metghalchi, and J. C. Keck. On flame kernel formation and propagation in premixed gases. *Combustion and Flame*, 157(12):

2211–2221, Dec. 2010. ISSN 00102180. doi: 10.1016/j.combustflame.2010.07.016. URL http://linkinghub.elsevier.com/retrieve/pii/S001021801000204X.

B. Enaux, V. Granet, O. Vermorel, C. Lacour, C. Pera, C. Angelberger, and T. Poinsot. Les study of cycle-to-cycle variations in a spark ignition engine. *Proceedings of the combustion Institute*, 33(2):3115–3122, 2011.

B. Franzelli, E. Riber, M. Sanjosé, and T. Poinsot. A two-step chemical scheme for kerosene–air premixed flames. *Combustion and Flame*, 157(7):1364–1373, 2010.

B. Franzelli, E. Riber, and B. Cuenot. Impact of the chemical description on a large eddy simulation of a lean partially premixed swirled flame. *Comptes Rendus Mécanique*, 341(1):247–256, 2013.

A. Frendi and M. Sibulkin. Dependence of minimum energy on ignition parameters. *Combustion Science and Technology*, 73:395–413, 1990.

S. Gashi, J. Hult, K. Jenkins, N. Chakraborty, S. Cant, and C. Kaminski. Curvature and wrinkling of premixed flame kernels?comparisons of OH PLIF and DNS data. *Proceedings of the Combustiion Institute*, 30:809–817, 2005.

G. J. Germane, C. G. Wood, and C. C. Hess. Lean combustion in spark-ignited internal combustion engines-a review. Technical report, SAE Technical Paper, 1983.

M. Germano. Turbulence: the filtering approach. *Journal of Fluid Mechanics*, 238: 325–336, 1992.

M. Germano, U. Piomelli, P. Moin, and W. Cabot. A dynamic subgrid-scale eddy viscosity model. *Physics of Fluids*, 3(7):1760–1765, 1991.

F. Ghosal. Analysis and control of errors in the numerical simulation of turbulence. *Fluid Mechanics and its Application*, 66:101–110, 2004.

D. Goryntsev, A. Sadiki, M. Klein, and J. Janicka. Large eddy simulation based analysis of the effects of cycle-to-cycle variations on air–fuel mixing in realistic disi ic-engines. *Proceedings of the Combustion Institute*, 32(2):2759–2766, 2009.

F. Gouldin. An application of fractals to modeling premixed turbulent flames. *Combustion and Flame*, 68(3):249–266, 1987.

V. Granet, O. Vermorel, C. Lacour, B. Enaux, V. Dugué, and T. Poinsot. Large-eddy simulation and experimental study of cycle-to-cycle variations of stable and unstable operating points in a spark ignition engine. *Combustion and Flame*, 159 (4):1562–1575, 2012.

R. Gukelberger, T. Alger, J. Gingrich, and B. Mangold. Impact of operating parameters on ignition system energy consumption. Technical report, SAE Technical Paper, 2014.

O. Gulder. Turbulent premixed combustion modelling using fractal geometry. *Proceedings of the Combustion Institute*, 23:835–842, 1991.

Ö. L. Gülder and G. J. Smallwood. Inner cutoff scale of flame surface wrinkling in turbulent premixed flames. *Combustion and Flame*, 103(1):107–114, 1995.

J. Han, H. Yamashita, and N. Hayashi. Numerical study on the spark ignition characteristics of a methane-air mixture using detailed chemical kinetics: Effect of equivalence ratio, electrode gap distance, and electrode radius on MIE, quenching distance, and ignition delay. *Combustion and Flame*, 157(7):1414 – 1421, 2010. ISSN 0010-2180. doi: DOI:10.1016/j.combustflame.2010.02.021. URL `http://www.sciencedirect.com/science/article/pii/S0010218010000751`.

E. R. Hawkes and R. S. Cant. A flame surface density approach to large-eddy simulation of premixed turbulent combustion. *Proceedings of the Combustion Institute*, 28:51–58, 2000.

J. Hirschfelder, C. Curtiss, and R. Byrd. *Molecular theory of gases and liquids*. John Wiley & Sons, New York, 1969.

A. Hosseinzadeh, T. Schmitt, A. Sadiki, and J. Janicka. Application of the dynamic f-tacles combustion model to a lean premixed turbulent flame. *Flow, Turbulence and Combustion*, 95(2-3):481–500, 2015.

C. Huang, S. Shy, C. Liu, and Y. Yan. A transition on minimum ignition energy for lean turbulent methane combustion in flamelet and distributed regimes. *Proceedings of the Combustion Institute*, 31(1):1401–1409, 2007.

K. Ishii, O. Aoki, Y. Ujiie, and M. Kono. Investigation of ignition by composite sparks under high turbulence intensity conditions. *Symposium (International) on Combustion*, 24(1):1793 – 1798, 1992. ISSN 0082-0784. doi: DOI:10.1016/S0082-0784(06)80210-9. URL `http://www.sciencedirect.com/science/article/pii/S0082078406802109`. Twenty-Fourth Symposium on Combustion.

S. Jerzembeck, N. Peters, P. Pepiot-Desjardins, and H. Pitsch. Laminar burning velocities at high pressure for primary reference fuels and gasoline: Experimental and numerical investigation. *Combustion and Flame*, 156(2):292–301, 2009.

W. Jones and R. Lindstedt. Global reaction schemes for hydrocarbon combustion. *Combustion and flame*, 73(3):233–249, 1988.

W. P. Jones and A. Tyliszczak. Large Eddy Simulation of Spark Ignition in a Gas Turbine Combustor. *Flow Turbulence Combustion*, 85:711–734, 2010.

C. Kaminski, J. Hult, M. Alden, S. Lindenmaier, A. Dreizler, U. Maas, and M. Baum. Spark Ignition of turbulent methane/air mixture revealed by time-resolved planar laser-induced fluorescence and direct numerical simulations. *Proceedings of the Combustiion Institute*, 28:399–405, 2000.

J. Kim and R. W. Anderson. Spark anemometry of bulk gas velocity at the plug gap of a firing engine. Technical report, Society of Automotive Engineers, Inc., Warrendale, PA (United States), 1995.

M. Klein, N. Chakraborty, K. Jenkins, and R. S. Cant. Effects of initial radius on the propagation of premixed flame kernels in a turbulent environment. *Phyics of Fluids*, 18, 2006.

M. Klein, N. Chakraborty, and Cant. Effect of Turbulence on Self-sutained Combustion in Premixed Flame KKernel: A Direct Numerical Simulation (DNS) Study. *Flow T*, 81:583–607, 2008.

M. Kono, K. Niu, T. Tsukamoto, and Y. Ujiie. Mechanism of flame kernel formation produced by short duration sparks. *Proceedings of the Combustion Institute*, 22: 1643?1649, 1989.

T. Kravchik and E. Sher. Numerical Modeling of Spark Ignition and Flame Initiation in a Quiescent Methane-Air Mixture. *Combustion and Flame*, 99:635–643, 1994.

K. Kuo. *Principles of Combustion (2nd ed.)*. John Wiley, New York, 1986.

G. Lacaze, E. Richardson, and T. Poinsot. Large eddy simulation of spark ignition in a turbulent methane jet. *Combustion and Flame*, 156(10):1993 – 2009, 2009. ISSN 0010-2180. doi: DOI:10.1016/j.combustflame.2009.05.006. URL `http://www.sciencedirect.com/science/article/pii/S001021800900128X`.

C. Lacour and C. Pera. An experimental database dedicated to the study and modelling of cyclic variability in spark-ignition engines with les. *SAE paper (2011-01-1282)*, 72, 2011.

B. Lewis and G. von Elbe. Ignition of explosive gas mixtures by electric sparks. ii. theory of the propagation of flame from an instantaneous point source of ignition. 1. *The Journal of Chemical Physics*, 15(11):803–808, 1947.

B. Lewis and G. Von Elbe. *Combustion, Flames and Explosions of Gases*. Academic Press, New York, third edition, 1987.

T. Løvås, P. Amnéus, F. Mauss, and E. Mastorakos. Comparison of automatic reduction procedures for ignition chemistry. *Proceedings of the Combustion Institute*, 29(1):1387–1393, 2002.

T. Lu and C. Law. Systematic Approach To Obtain Analytic Solutions of Quasi Steady State Species in Reduced Mechanisms. *The Journal of Physical Chemistry A*, 110:13202?13208, 2006.

R. Maly. Ignition model for spark discharges and the early phase of flame front growth. In *18th Symp. (Int.) on Combustion*, pages 1747–1754. The Combustion Institute, Pittsburgh, 1981.

R. Maly and M. Vogel. Initiation and propagation of flame fronts in lean CH4-air mixtures by the three modes of the ignition spark. *Symposium (International) on Combustion*, 17(1):821 – 831, 1979. ISSN 0082-0784. doi: DOI:10.1016/S0082-0784(79)80079-X. URL `http://www.sciencedirect.com/science/article/pii/S008207847980079X`. Seventeenth Symposium (International) on Combustion.

N. Mazellier, L. Danaila, and B. Renou. Multi-scale energy injection: a new tool to generate intense homogeneous and isotropic turbulence for premixed combustion. *Journal of Turbulence*, 43:1–30, 2010.

W. Meier, P. Weigand, X. Duan, and R. Giezendanner-Thoben. Detailed characterization of the dynamics of thermoacoustic pulsations in a lean premixed swirl flame. *Combustion and Flame*, 150(1):2–26, 2007.

R. Mercier, T. Schmitt, D. Veynante, and B. Fiorina. The influence of combustion sgs submodels on the resolved flame propagation. application to the les of the cambridge stratified flames. *Proceedings of the Combustion Institute*, 35(2):1259–1267, 2015.

M. Metghalchi and J. C. Keck. Burning velocities of mixtures of air with methanol, isooctane, and indolene at high pressure and temperature. *Combustion and flame*, 48:191–210, 1982.

A. Misdariis. *Schémas cinétiques réduits et couplage thermique pour les simulations aux grandes échelles du cliquetis dans les moteurs à piston.* PhD thesis, 2015.

A. Misdariis, O. Vermorel, and T. Poinsot. A methodology based on reduced schemes to compute autoignition and propagation in internal combustion engines. *Proceedings of the Combustion Institute*, 35:3001–3008, 2015.

M. Morsy and S. Chung. Numerical simulation of front lobe formation in laser-induced spark ignition of CH4/air mixture. *Proceedings of the Combustiion Institute*, 29:1613–1619, 2002.

V. Moureau, G. Lartigue, Y. Sommerer, C. Angelberger, O. Colin, and T. Poinsot. Numerical methods for unsteady compressible multi-component reacting flows on fixed and moving grids. *Journal of Computational Physics*, 202(2):710–736, 2005.

V. Moureau, P. Domingo, and L. Vervisch. From Large-Eddy Simulation to Direct Numerical Simulation of a lean premixed swirl flame: Filtered laminar flame-PDF modeling. *Combustion and Flame*, 158(7):1340 – 1357, 2011. ISSN 0010-2180. doi: DOI:10.1016/j.combustflame.2010.12.004. URL `http://www.sciencedirect.com/science/article/B6V2B-51TW27K-1/2/51b4d8c8466d4e51cd2835d3aa03007b`.

I. A. Mulla, S. R. Chakravarthy, N. Swaminathan, and R. Balachandran. Evolution of flame-kernel in laser-induced spark ignited mixtures: A parametric study. *Combustion and Flame*, 2015.

N. Ozdor, M. Dulger, and E. Sher. Cyclic variability in spark ignition engines a literature survey. Technical report, SAE Technical Paper, 1994.

S. V. Pancheshnyi, D. A. Lacoste, A. Bourdon, and C. O. Laux. Ignition of propane–air mixtures by a repetitively pulsed nanosecond discharge. *Plasma Science, IEEE Transactions on*, 34(6):2478–2487, 2006.

T. Passot and A. Pouquet. Numerical simulation of compressible homogeneous flows in the turbulent regime. *Journal of Fluid Mechanics*, 181:441 – 466, 1987.

D. Patel and N. Chakraborty. Effects of energy deposition characteristics on localised forced ignition of homogeneous mixtures. *International Journal of Spray and Combustion Dynamics*, 7(2):151–174, 2015.

P. Pepiot. *Automatic strategies to model transportation fuel surrogates*. PhD thesis, Stanford University, 2008.

P. Pepiot-Desjardins and H. Pitsch. An efficient error-propagation-based reduction method for large chemical kinetic mechanisms. *Combustion and Flame*, 154(1): 67–81, 2008.

N. Peters. The turbulent burning velocity for large-scale and small-scale turbulence. *Journal of Fluid mechanics*, 384:107–132, 1999.

T. X. Phuoc and F. P. White. Laser-Induced Spark Ignition of CH4/air mixture. *Combustion and Flame*, 119:203–216, 1999.

T. X. Phuoc and F. P. White. An optical and spectroscopic study of laser-induced sparks to determine available ignition energy. *Proceedings of the Combustion Institute*, 29:1621–1628, 2002.

G. Pilla and L. Francqueville. Stabilization of highly diluted gasoline direct injection engine using innovative ignition systems. *SAE International Journal of Engines*, 7(4):1734–1743, 2014.

G. Pilla, D. Galley, D. A. Lacoste, F. Lacas, D. Veynante, and C. O. Laux. Stabilization of a turbulent premixed flame using a nanosecond repetitively pulsed plasma. *Plasma Science, IEEE Transactions on*, 34(6):2471–2477, 2006.

W. F. Piock, P. Weyand, E. Wolf, and V. Heise. Ignition systems for spray-guided stratified combustion. *Combustion*, 1:0598, 2010.

S. Pischinger and J. B. Heywood. A Model for Flame Kernel Development in a Spark-Ignition Eengine. In T. C. Institute, editor, *Twenty-Third Symposium (International) on Combustion*, pages 1033–1040, 1990.

T. Poinsot and D. Veynante. *Theoretical and numerical combustion*. R.T. Edwards, 2nd edition, 2005.

T. J. Poinsot and S. K. Lele. Boundary conditions for direct simulations of compressible viscous flows. *J. Comput. Phys.*, 101(1):104 – 129, 1992. ISSN 0021-9991. doi: DOI:10.1016/0021-9991(92)90046-2. URL `http://www.sciencedirect.com/science/article/pii/0021999192900462`.

S. B. Pope. Turbulent flows, 2001.

R. Reinmann and A. Saitzkoff. Spark energy deposition studies. *Journal of Physics D, Applied Physics*, 1998.

B. Renou, A. Mura, E. Samson, and A. Boukhalfa. Characterization of the local flame structure and the flame surface density for freely propagating premixed flames at various lewis numbers. *Combustion science and technology*, 174(4):143–179, 2002.

S. Richard. *Simulation aux grandes échelles de la combustion dans les moteurs á allumage commandé*. PhD thesis, Ecole Centrale de Paris, 2005.

S. Richard, O. Colin, O. Vermorel, A. Benkenida, C. Angelberger, and D. Veynante. Towards large eddy simulation of combustion in spark ignition engines. *Proceedings of the Combustion Institute*, 31(2):3059 – 3066, 2007. ISSN 1540-7489. doi: DOI:10.1016/j.proci.2006.07.086. URL `http://www.sciencedirect.com/science/article/pii/S1540748906001040`.

A. Robert, S. Richard, O. Colin, L. Martinez, and L. De Francqueville. Les prediction and analysis of knocking combustion in a spark ignition engine. *Proceedings of the Combustion Institute*, 35(3):2941–2948, 2015.

G. Rymer. Analysis and modeling of the mean reaction rate and transport terms in turbulent premixed combustion. *École Centrale Paris*, 2001.

A. Schmitt, T. abd Sadiki, B. Fiorina, and D. Veynante. Impact of dynamic wrinkling model on the prediction accuracy using the F-TACLES combustion model in swirling premixed turbulent flames. *Proceedings of the Combustion Institute*, 34:1261–1268, 2013.

T. Schmitt, M. Boileau, and D. Veynante. Flame Wrinkling Factor Dynamic Modeling for Large Eddy Simulations of Turbulent Premixed Combustion. *Flow Turbulence Combustion*, 94:199:217, 2014.

C. Schneider, A. Dreizler, and J. Janicka. Fluid dynamical analysis of atmospheric reacting and isothermal swirling flows. *Flow, turbulence and combustion*, 74(1): 103–127, 2005.

L. Selle, G. Lartigue, T. Poinsot, R. Koch, K.-U. Schildmacher, W. Krebs, B. Prade, P. Kaufmann, and D. Veynante. Compressible large eddy simulation of turbulent combustion in complex geometry on unstructured meshes. *Combustion and Flame*, 137(4):489–505, 2004.

E. Sher and J. Keck. Spark Ignition of Combustible Gas Mixtures. *Combustion and Flame*, 66:17–25, 1986.

E. Sher, J. Ben-Ya'ish, and T. Kravchik. On the Birth of Spark Channels. *Combustion and Flame*, 89:186–194, 1992.

S. Shy, W. Shih, and C. Liu. More on minimum ignition energy transition for lean premixed turbulent methane combustion in flamelet and distributed regimes. *Combustion Science and Technology*, 180(10-11):1735–1747, 2008.

T. Sloane. Ignition and flame propagation modeling with an improved methane oxidation mechanism. *Combustion science and technology*, 63(4-6):287–313, 1989.

T. Sloane. Energy requirements for spherical ignitions in methane-air mixtures at different equivalence ratios. *Combustion Science and Technology*, 73:351–365, 1990.

T. Sloane and P. Ronney. A Comparison of Ignition Phenomena ModModel with Detailed and Simplified Kinetics. *Combustion Science and Technology*, 88:1–13, 1992.

T. Sloane and A. Schoene. Energy requirements for spherical ignitions in atmospheric-pressure methane-air mixtures: a computational study. *Proceedings of the Combustion Institute*, pages 1669–1676, 1988.

J. Smagorinsky. General circulation experiments with the primitive equations. I: The basic experiment. *Monthly Weather Review*, 91(3):99–164, 1963.

G. P. Smith, D. M. Golden, M. Frenklach, N. W. Moriarty, B. Eiteneer, M. Goldenberg, C. T. Bowman, R. K. Hanson, S. Song, W. C. Gardiner Jr, et al. GRImech 3.0 reaction mechanism, Berkeley, 2012.

T. Spiglanin, A. McIlroy, E. Fournier, R. Cohen, and J. Syage. Time-resolved imaging of flame kernels: laser spark ignition of h 2/o 2/ar mixtures. *Combustion and Flame*, 102(3):310–328, 1995.

G. Staffelbach, L. Gicquel, G. Boudier, and T. Poinsot. Large eddy simulation of self excited azimuthal modes in annular combustors. *Proceedings of the Combustion Institute*, 32(2):2909–2916, 2009.

D. Thévenin. Three-dimensional direct simulations and structure of expanding turbulent methane flames. *Proceedings of the Combustion Institute*, 30(1):629–637, 2005.

M. Thiele, S. Selle, U. Riedel, J. Warnatz, and U. Maas. Numerical Simulation of Spark Ignition Including Ionization. *Proceedings of the Combustion Institute*, 28: 1177–1785, 2000a.

M. Thiele, J. Warnatz, and U. Maas. Geometrical study of spark ignition in two dimensions. *Combustion Theory and Modelling*, 4:413–434, 2000b.

L. Thobois. Intèrêt et faisabilité de la simulation aux grandes échelles dans les moteurs automobiles. 2006.

P. Tromans and R. Furzeland. An analysis of Lewis number and flow effects on the ignition of premixed gases. In *21st Symp. (Int.) on Combustion*, pages 1891–1897. The Combustion Institute, Pittsburgh, 1986.

K. Truffin. Report on coupling the aktim-les spark ignition model with other turbulent combustion models d1. 5c (timecop project). *IFP Energies Nouvelles*, 193, 2006.

K. Truffin, C. Angelberger, S. Richard, and C. Pera. Using large-eddy simulation and multivariate analysis to understand the sources of combustion cyclic variability in a spark-ignition engine. *Combustion and Flame*, 162(12):4371–4390, 2015.

D. Verhoeven. Spark heat transfer measurements in flowing gases. *Revue de l'Institut Francais du Pétrole*, 52(4):453–464, 1997.

O. Vermorel, S. Richard, O. Colin, C. Angelberger, A. Benkenida, and D. Veynante. Towards the understanding of cyclic variability in a spark ignited engine using multi-cycle les. *Combustion and Flame*, 156(8):1525–1541, 2009.

D. Veynante and V. Moureau. Analysis of dynamic models for large eddy simulations of turbulent premixed combustion. *Combustion and Flame*, 162(12):4622–4642, 2015. doi: 10.1016/j.combustflame.2015.09.020. URL `http://www.scopus.com/inward/record.url?eid=2-s2.0-84949570431&partnerID=40&md5=a4c51d2a17f62250dee45cb474d9161f`. cited By 0.

C.-S. Wang and M. Sibulkin. Comparison of Minimum Ignition Energy for 4 Alkanes: Effects of Ignition Kernel Size and Equivalence Ratio. *Combustion Science and Technology*, 91:163–178, 1993.

G. Wang, M. Boileau, and D. Veynante. Implementation of a dynamic thickened flame model for large eddy simulations of turbulent premixed combustion. *Combustion and Flame*, 158(11):2199–2213, 2011.

G. Wang, M. Boileau, D. Veynante, and K. Truffin. Large eddy simulation of a growing turbulent premixed flame kernel using a dynamic flame surface density model. *Combustion and Flame*, 159(8):2742–2754, 2012.

H. Weller, G. Tabor, A. Gosman, and C. Fureby. Application of flame-wrinkling LES combustion model to a turbulent mixing layer. In *27th Symposium (International) on Combustion*, pages 899–907, The Combustion Institute, Pittsburgh, 1998.

F. Williams, editor. *Combustion Theory*. Benjamin Cummings, Menlo Park, 1985.

K. Yoshida and Y. Soma. The effect of corona discharge on pre-mixed combustion. Technical report, SAE Technical Paper, 2009.

M. B. Young. Cyclic dispersion–some quantitative cause-and-effect relationships. Technical report, SAE Technical Paper, 1980.

M. B. Young. Cyclic dispersion in the homogeneous-charge spark-ignition engine?a literature survey. Technical report, SAE Technical Paper, 1981.

T. Yuasa, S. Kadota, M. Tsue, M. Kono, H. Nomura, and Y. Ujiie. EFFECTS OF ENERGY DEPOSITION SCHEDULE ON MINIMUM IGNITION ENERGY IN SPARK IGNITION OF METHANE/AIR MIXTURES. *Proceedings of the Combustion Institute*, 29:743–750, 2002.

M. Zajadatz, N. Zarzalis, and W. Leuckel. Investigation of the turbulent flame speed for natural gas and natural gas/hydrogen mixtures at high turbulence levels and volumetric heat release rates. In *ASME Turbo Expo 2013: Turbine Technical Conference and Exposition*, pages V01BT04A003–V01BT04A003. American Society of Mechanical Engineers, 2013.

G. Ziegler, E. Wagner, and R. Maly. IGNITION OF LEAN METHANE-AIR MIXTURES BY HIGH PRESSURE GLOW AND ARC DISCHARGES. *Proceedings of the Combustion Institute*, 20:1817–1824, 1985.

université PARIS-SACLAY
ÉCOLE DOCTORALE
Sciences mécaniques et énergétiques, matériaux et géosciences (SMEMAG)

Titre: Simulations aux grandes échelles de l'allumage turbulent et de la propagation de la flamme dans les Moteurs à allumage commandé.
Mots-clés: combustion pré-mélangée, allumage, moteur à allumage commandé

Résumé: Le fonctionnement en régime très pauvre ou avec forts taux d'EGR des moteurs à allumage commandé (MAC) permet de réduire efficacement les émissions de CO2 et de Nox ; cependant ces stratégies se heurtent à l'augmentation des variabilités cycliques. Ces dernières sont principalement dues à la phase d'allumage qui devient critique au-delà d'un seuil critique de dilution. Le modèle ECFM-LES actuellement utilisé à IFPEn, basé sur la notion de densité de surface de flamme, est insuffisant pour décrire l'allumage dans ces conditions critiques. Dans ces travaux, l'approche TF-LES est adoptée, l'allumage étant alors décrit par un emballement cinétique des réactions chimiques lors d'une élévation locale de la température. Ces travaux définissent et évaluent une stratégie de simulation pour TF-LES en configuration moteur, qui permette une prédiction fine des allumages critiques et de la propagation turbulente de la flamme, afin de décrire le cycle moteur complet.
Dans une première partie, des DNS d'allumages turbulents ont été réalisées, en modélisant la phase d'allumage par un dépôt d'énergie thermique (Lacaze et al., (2009)). Les calculs ont simulé les expériences d'allumage de Cardin et al. (2013), dans lesquelles l'énergie minimum d'allumage (MIE) d'un mélange méthane-air a été mesurée, pour différentes richesses pauvres et sous différentes intensités turbulentes. L'objectif principal des simulations a été de déterminer les paramètres numériques et physiques du modèle permettant de reproduire les allumages de l'expérience. Deux types de schemas cinétiques ont été évalués : un schéma simplifié et un schéma analytique (ARC), ce dernier reproduisant et les délais d'auto-allumage et la vitesse de flamme laminaire. Les résultats ont permis de définir des critères d'allumage et de mettre en évidence les différences de prédiction d'allumage avec les deux types de schémas cinétiques. Les résultats ont également démontré que l'approche choisie permettait de prédire les bons niveaux d'énergie pour les allumages laminaires et à faibles nombres de Kalovitz (Ka<10). Aux plus hauts nombres de Karlovitz, il a été montré que le modèle ED était insuffisant pour prédire les énergies d'allumage et qu'une description plus fine du dépôt d'énergie est nécessaire.
Dans la seconde partie des travaux, un modèle de plissement dynamique (Wang et al., 2012) a été étudié, afin de décrire le développement hors-équilibre de la flamme dans la phase de propagation turbulente. Des études sur des flammes sphériques laminaires ont d'abord été menées. Ensuite, les premiers tests en configuration moteur ayant révélé des incompatibilités du modèle, des modifications ont été proposées. Le modèle de plissement dynamique modifié a été finalement évalué sur la configuration moteur ICAMDAC. Les résultats obtenus ont été comparés aux résultats obtenus par Robert et al. (2015) avec le modèle ECFM-LES, qui utilise une équation de transport de densité de surface de flamme décrivant le plissement hors-équilibre de la flamme. Les résultats obtenus avec le plissement dynamique sont en très bon accord avec ceux du modèle ECFM-LES, démontrant ainsi la capacité du modèle dynamique à prédire des valeurs de plissement hors-équilibre. D'autre part, le modèle dynamique s'ajustant automatiquement aux conditions de turbulence de l'écoulement, nul besoin n'est d'ajuster la constante de modélisation en fonction du régime moteur, comme c'est le cas pour l'équation de transport de la densité de surface de flamme.

Title: Large Eddy simulation of the turbulent spark ignition and of the flame propagation in spark ignition engines

Keywords: premixed combustion, spark ignition, spark ignition engines

Abstract: The use of lean equivalence ratios or high EGR rates in spark ignition engines (SIE) enables to optimize CO2 and NOx emissions; however too important dilution rates leads to increased cycle-to-cycle variability. These latter are mostly due to the ignition phase, which becomes critical when dilution rates are important. The ECFM-LES model currently used in IFPEN, which is based on the flame surface density concept, is not sufficient to describe ignition in these critical conditions. The TF-LES approach was chosen in this study, principally because it directly resolved chemistry and can thus model ignition via a local raise of the temperature. The present work defines and evaluates a simulation strategy for TF-LES in SIE configurations, that enables a fine prediction of critical ignitions and of the turbulent flame propagation.

In the first part, DNS of turbulent ignition were performed. The ignition phase was modeled using a thermal energy deposit (Lacaze et al. (2009)). Simulations reproduced the ignition experiments of Cardin et al. (2013) in which the minimum ignition energy (MIE) of lean premixed methane/air mixtures was measured, for different turbulence characteristics. The main purpose of the study was to determine the numerical and physical model parameters, which enable to reproduce Cardin et al. experiments. Two types of kinetic schemes were evaluated: a simplified kinetic scheme and an analytical kinetic scheme (ARC) that recovers both the auto-ignition delays and the laminar flame speed. Results analysis enabled to define ignition criteria and to highlight the differences in terms of ignition prediction using the two kinetic schemes. Results also demonstrated that the chosen approach could recover correct levels of ignition energy for laminar and low Karlovitz number cases (Ka<10). For higher Karlovitz number cases, the ED model was found to be insufficient to predict the ignition and a finer description of the energy deposit is required.

In the second part, a dynamic wrinkling model (Wang et al., 2012) was studied to describe the out-of-equilibrium behavior of the flame during the propagation phase. Studies on laminar spherical flames were first performed, to assess the laminar degeneration of the model. Then, as first tests in an engine configuration have revealed incompatibilities of the model, modifications were proposed. The modified dynamic model was finally tested in the ICAMDAC engine configuration. Results of the simulations were compared against previous results obtained with the ECFM-LES model using a transport equation for the flame surface density that can describe the out-of-equilibrium wrinkling of the flame. Results obtained with the dynamic model are in very good agreement with the ECFM-LES model, thus demonstrating the ability of the dynamic model to predict out-of-equilibrium values in the engine configuration. Besides, the dynamic model self-adapts to the turbulence conditions, hence does not require any model parameter adjustment, as is it the case for models based on the flame surface density transport equation.